Offshore Wind-Powered Carbon Dioxide Removal – a Solid Carbon Initiative

by

Gerard Avellaneda Domene
B.Sc., Universitat Autònoma de Barcelona, 2015
M.Sc., Heriot-Watt University, 2019

A Dissertation Submitted in Partial Fulfilment of the
Requirements for the Degree of

DOCTOR OF PHILOSOPHY

in the Department of Mechanical Engineering
Institute for Integrated Energy Systems

We acknowledge and respect the Lək̓ʷəŋən (Songhees and Xʷsepsəm/Esquimalt) Peoples on whose territory the university stands, and the Lək̓ʷəŋən and W̱SÁNEĆ Peoples whose historical relationships with the land continue to this day.

Offshore Wind-Powered Carbon Dioxide Removal – a Solid Carbon Initiative

by

Gerard Avellaneda Domene

B.Sc., Universitat Autònoma de Barcelona, 2015

M.Sc., Heriot-Watt University, 2019

Supervisory Committee

Dr. Curran Crawford, Supervisor

Department of Mechanical Engineering, University of Victoria

Dr. Brad Buckham, Departmental Member

Department of Mechanical Engineering, University of Victoria

Dr. Richard Dewey, External Member

Ocean Networks Canada

Abstract

If societies around the globe are to stabilise Earth's surface temperature and prevent it from rising beyond levels compatible with human and non-human life, they must not only eliminate their current greenhouse gas (GHG) emissions but also remove accumulated emissions from the atmosphere. Of the different anthropogenic GHGs emitted, carbon dioxide (CO_2) has historically and is continuing to contribute the most to the warming of the atmosphere, ocean, and land. For this reason, it is the focus of this investigation.

This dissertation provides insights into and designs for two possible modular system solutions for offshore wind-powered carbon dioxide removal (CDR). The first one takes CO_2 directly from the air (known as direct air capture, or DAC), and the second one draws it out indirectly through the ocean (known as direct ocean capture, or DOC). Although not studied in this work, once captured, the CO_2 can be permanently sequestered via mineral trapping in mafic rocks, such as basalt formations. This is especially convenient as basalt covers most of the upper ocean crust and offers more than enough storage capacity to meet projected CDR needs. The feasibility of CO_2 mineralisation in subseafloor basalt is currently being investigated by the Solid Carbon project, to which this study contributes.

The prospect of storing CO_2 permanently in subseafloor basalt reservoirs motivated the idea to locate the capture of CO_2 offshore as well, where: the constraints on area use are more relaxed than onshore, the process can be powered by local renewable winds, and all required operating equipment can be housed on floating offshore wind turbine (FOWT) platforms. FOWT platforms are rapidly emerging technologies whose costs are less sensitive to water depth variations than more established fixed-bottom turbine platforms. As such, they are better suited for remote offshore applications, such as wind-powered DAC and wind-powered DOC. The integration of the CO_2 capture (whether DAC or DOC) and wind power systems on the same floating platform can reduce operational costs, since part of the maintenance of the two can be carried out together.

For the first proposed system solution, the FOWT-DAC platform, a dynamic analysis is conducted to modify as necessary and ensure that adding the DAC equipment to the moored wind platform disturbs its operation as little as possible. This is done by comparing the FOWT-DAC system's floating stability and its fully coupled motion responses with those of the reference FOWT platform design. The research findings demonstrate good fit between the proposed system and the benchmark, suggesting that the hybrid FOWT-DAC platform behaves in a similar way to the reference system and can serve as a viable modular deployment approach.

For the second proposed system solution, the FOWT-DOC platform, four design scenarios are examined. Each draws seawater from increasingly greater depths – 20 m (Case 0), 100 m (Case 1), 200 m (Case 2), and 300 m (Case 3) - with incrementally higher dissolved inorganic carbon (DIC) concentrations. The energy intensity and cost of carbon capture in each case are then compared. The key finding is that, although Case 3 is the least energy intensive, it is not the most economical. This is explained by the rising linear costs associated with deeper withdrawal outweighing the benefits from seawater with correspondingly increased DIC concentration, which peaks between Cases 0 and 1, and diminishes progressively thereafter. As a result, the estimated cost is lowest for Case 2, which is almost 8% more cost-effective than Case 0.

Direct air capture and direct ocean capture are two emerging CDR methods with high potential to remove CO_2 from the atmosphere and could be coupled with offshore, permanent sequestration in subseafloor basalt. Although DOC is currently at an earlier stage of development than DAC, it could additionally help mitigate local ocean acidification, which together with climate change, is one of the seven planet boundaries currently transgressed. Both DAC and DOC are estimated to have similar costs of implementation, which are comparatively higher than those of many other CDR techniques. This may be an established but unfair comparison as not all CDR methods exhibit the same sequestration permanence (durability), among other key indicators. Future economic assessments should account for these differences and show the true societal cost of carbon removal across different residence times.

Table of contents

Abstract III
Table of contents V
List of Tables VIII
List of Figures X
List of Abbreviations XIII
Nomenclature XVI
Superscripts and subscripts XIX
Acknowledgements XX
Chapter 1. Introduction 1
  1.1. Context 8
  1.2. Objectives and approach 10
  1.3. Structure 12
Chapter 2. Offshore Wind-Powered Direct Air Capture 13
  2.1. Introduction 14
    2.1.1. Context and background 14
    2.1.2. System configuration 15
    2.1.3. Objectives 16
    2.1.4. Paper outline 17
  2.2. Design 17
    2.2.1. Floating offshore wind turbine 17
    2.2.2. Deck 18
    2.2.3. Direct air capture 18
    2.2.4. Ancillary system 18
    2.2.5. Integrated FOWT-DAC system 19
    2.2.6. Inertial properties 22
  2.3. Methods 23
    2.3.1. Floating initial intact stability 23
    2.3.2. Static stability 23
    2.3.3. Dynamic stability 26
    2.3.4. Wave splashing – air gap 26
    2.3.5. Environmental conditions 28

2.3.6. Modelling 29
2.4. Results & discussion 30
2.4.1. Floating stability 30
2.4.2. Hydrodynamics 32
2.4.3. Wave splashing – air gap 35
2.4.4. System loads 35
2.4.5. Power performance 39
2.5. Conclusions 40
2.6. Appendices 41
2.6.1. Direct air capture 41
2.6.2. Ancillary system 41
2.6.3. Wave splashing 45
2.6.4. Results 48
Chapter 3. Design of a carbon dioxide transportation system 53
3.1. Introduction 54
3.1.1. Objectives 54
3.1.2. The similar case of e-fuels 55
3.2. Design 56
3.2.1. FOWT-CO$_2$ capture system 56
3.2.2. Flexible riser 56
3.2.3. Moorings 61
3.3. Methods 61
3.3.1. Riser modelling 62
3.3.2. Site description 67
3.4. Results & discussion 70
3.4.1. Effective tension 70
3.4.2. von Mises stress 72
3.4.3. Curvature 73
3.5. CO$_2$ riser conclusions 74
3.6. Extension to e-fuels risers 75
3.7. Appendices 77
3.7.1. Riser layout 77
3.7.2. Mooring design 77

3.7.3. Pressure losses ... 78
Chapter 4. Offshore Wind-Powered Direct Ocean Capture ... 80
4.1. Introduction ... 81
4.2. Direct ocean capture ... 84
4.2.1. Asymmetric chloride-mediated electrochemical pH swing ... 85
4.3. Methods ... 87
4.3.1. Design approach ... 87
4.3.2. Design scenarios ... 88
4.3.3. Floating wind turbine (FOWT) platform ... 90
4.3.4. Seawater intake system ... 91
4.3.5. FOWT-DOC design ... 92
4.3.6. Cost estimation ... 95
4.4. Results and discussion ... 97
4.4.1. Comparison with FOWT-DAC ... 105
4.5. Conclusions ... 108
4.6. Appendices ... 109
4.6.1. Base electrochemical energy ... 109
4.6.2. Fundamentals of chemical oceanography ... 111
4.6.3. Pressure losses ... 114
4.6.4. Floating wind turbine platform ... 115
4.6.5. Detailed costs ... 116
Chapter 5. Conclusions and future work ... 118
5.1. Summary and contributions ... 118
5.2. Recommendations for future work ... 123
Erratum ... 128
References ... 129

List of Tables

Table 1.1. Main topics retrieved from the refined project proposal, modified for clarity and conciseness, and assigned to the contributors involved in Activity Area 1 of Solid Carbon, including the author of this dissertation. Their respective published research outcomes are referenced for the reader's interest. 10
Table 2.1. Reference design properties[72,74]. 18
Table 2.2. Main DAC and ancillary system configuration for the low, mid, and high scenarios. 20
Table 2.3. Inertial and hydrostatic properties of the reference, low, mid, and high case scenarios. The percentage differences with respect to the reference design are written in parentheses next to the result where relevant. 22
Table 2.4. Metocean data binning conditions. 28
Table 2.5. Design load case matrix 29
Table 2.6. Rigid-body natural frequencies (Hz) for the low, mid, and high scenarios and compared with the reference design (Ref.). 33
Table 2.7. Air gap (in meters) at the different platform points of study for the reference design, and low, mid, and high case scenarios. 35
Table 2.8. Electric storage system sizing for the low, mid, and high case scenarios. 41
Table 2.9. Type IV HT700-103 hydrogen tank unit specifications[105] 42
Table 2.10. CO_2 compression specifics. 44
Table 2.11. CO_2 mass and volume storage for the low, mid, and high case scenarios. This excludes the mass/volume of the storage tanks. 44
Table 2.12. CO_2 storage tanks dimensions. 44
Table 2.13. Final CO_2 storage tanks selection. 45
Table 3.1. Hydrostatic and inertial properties of the FOWT-CO_2 capture platform. 56
Table 3.2. CO_2 conditions at the flexible riser's inlet. 58
Table 3.3. Flexible riser dimensions and mechanical properties. 59
Table 3.4. Bend stiffener mechanical properties and configuration. 61
Table 3.5. Mooring line configuration for the deep-water case. 61
Table 3.6. Shallow water case: riser nodal configurations. 62
Table 3.7. Design load conditions for the flexible riser in the FOWT-CO_2 system. 69
Table 4.1. Oceanographic data from different water depths (20 m, 100 m, 200 m, 300 m) at a point in the Pacific Northeast (47.614°N, -125.771°W)[181,182]. 88
Table 4.2. Thermodynamic values at the platform entry point for the design scenarios, and for the adiabatic (AD) and nonadiabatic (NAD) transports[181,182]. 89
Table 4.3. Base FOWT-DOC main financial and technical assumptions used in the cost estimation. 97
Table 4.4. Carbon capture energy intensities (in kWh/kgCO_2) of the main DOC processes for the design scenarios and for the nonadiabatic transport through the SWIR case. The percentage between parenthesis indicates the energy savings of Cases 1, 2, and 3 with respect to Case 0. 99
Table 4.5. Pressure heads (in bar) across system components for the design scenarios. The percentage between parenthesis indicates the difference with respect to Case 0. 100
Table 4.6. Discounted individual and total costs (in million dollars, $M) for the main FOWT-

DOC system components, and levelized cost of carbon (in \$/tCO_2) for each design scenario, with a gap between cell's electrodes of $\boldsymbol{\delta cell}$ = 1 mm. 103
Table 4.7. Summary of magnitudes used in the estimation of the levelized cost of carbon (LCC) for the FOWT-DAC configuration, presented for a range of possible values (low, mid, and high). 107
Table 5.1. FOWT-DAC and FOWT-DOC unit deployment for three CO_2 removal scenarios by 2050. 122

List of Figures

Figure 1.1. Location of Cascadia Basin, offshore from Washington and British Columbia (with permission from Ocean Networks Canada). The figure also shows ONC's cabled observatory network NEPTUNE. 9

Figure 2.1. Possible offshore wind powered-DACCS system configurations envisioned in Solid Carbon (with permission from Ocean Networks Canada). The configuration developed further in this work appears squared in red. 15

Figure 2.2. Process followed to determine the size of the DAC and ancillary system per platform. 19

Figure 2.3. Left: FOWT-DAC platform with installed deck connecting the three radial columns. Right: top DAC layout view for the a) low, b) mid, and c) high scenarios. Note that the rows with five and six CO$_2$ collectors are two stories high. 21

Figure 2.4. Ancillary system layout per radial column (in yellow) for the a) low, b) mid, and c) high scenarios, and d) shape and colour legend of each ancillary system unit. 21

Figure 2.5. Pitch hydrostatic restoring moment as the reference design platform pitches for the range of operational angles. The blue curve is obtained with equation 2.7, while the orange curve is computed with equation 2.8 using ProteusDS$^{\text{TM}}$. 25

Figure 2.6. Air gap definition in a) still waters, and b) irregular seas. Reproduced from ref.[83]. 27

Figure 2.7. Righting moment for the low (blue line), mid (grey line), and high scenarios (yellow line), and benchmarked with the reference design (orange line). The wind heeling moment is shown in a dash-dotted grey line 31

Figure 2.8. Average maximum pitch platform angles for DLCs 1.3, 6.1 and 6.2 for the low, mid, and high scenarios, and benchmarked with the reference design. 32

Figure 2.9. Added mass coefficient in surge-surge versus frequency evaluated by HAMS for the low, mid, and high scenarios, and benchmarked with the reference design. 32

Figure 2.10. Wave-induced RAOs in surge, heave, and pitch for the reference design, low, mid, and high case scenarios. 34

Figure 2.11. Points of study for the air gap assessment. 35

Figure 2.12. Maximum blade tip flapwise deflection per ECD type and scenario (reference design, low, mid, and high case). 36

Figure 2.13. DLC 1.6 maximum, mean, and minimum platform surge for the a) reference, b) low, c) mid, and d) high case scenarios. 37

Figure 2.14. DLC 1.6 peak fairlead tension (line 1) for the reference design, and low, mid, and high case scenarios. 37

Figure 2.15. DLC 2.3 maximum tower base pitching moment for the reference design, and low, mid, and high case scenarios. 38

Figure 2.16. DLC 6.1 and 6.2: platform heave minimum, maximum, and mean for the reference design, and low, mid, and high case scenarios. 38

Figure 2.17. IFORM resulting $\boldsymbol{Hs}$-$\boldsymbol{Tp}$ contour together with the steepness criterion curve and the air gap design sea state, $\boldsymbol{Hs}$ = 6.49 m, $\boldsymbol{Tp}$ = 7.91 s. 47

Figure 2.18. Added mass coefficients in top) heave-heave, middle) pitch-pitch, and bottom) yaw-yaw. 48

Figure 2.20. Radiation damping coefficients in top) pitch-pitch, and bottom) yaw-yaw versus

frequency evaluated by HAMS for the low, mid, and high scenarios, and benchmarked with the reference design. 50
Figure 2.21. Excitation force coefficients (magnitude) in a) surge, b) heave, and c) pitch versus frequency evaluated by HAMS for the low, mid, and high scenarios, and benchmarked with the reference design. 51
Figure 2.22. Wind turbine power curve for the reference design, and the low, mid, and high case scenarios. 52
Figure 3.1. FOWT-CO_2 capture platform and flexible riser layout configuration (in red) for the: (top) shallow water case, and (bottom) deep water case. 60
Figure 3.2. Bend stiffener profile along the arc length. 61
Figure 3.3. Wind-induced vertical current profile for normal and extreme current models. 68
Figure 3.4. Shallow water: internal pressure along the flexible riser length for (left) zero pressure case, and (right) maximum pressure case. 70
Figure 3.5. Mean riser effective tension for the (left) shallow water case, (right) deep water case. Zero and maximum pressure and flow configurations with 0° wind and current directions, and wind speed of 4 m/s. 72
Figure 3.6. Mean riser von Mises stress for the (left) shallow water case, and (right) deep water case. Zero and maximum pressure and flow configurations with 0° wind and current directions, and wind speed of 4 m/s. 73
Figure 3.7. Mean riser curvature for the (left) shallow water case, and (right) deep water case. Zero and maximum pressure and flow configurations with 0° wind and current directions, and wind speed of 4 m/s. 73
Figure 3.8. Shallow water and H_2 case: mean riser (top left) effective tension, (top right) max von Mises stress, and (bottom) curvature. Zero and maximum pressure and flow configurations with 0° wind and current directions, and wind speed of 4 m/s. 76
Figure 4.1. Bjerrum plot showing the three main species in the ocean carbonate system; carbon dioxide ($CO_2^* = CO_{2(aq)}+H_2CO_3$), bicarbonate ion ($HCO_3^-$), and carbonate ion ($CO_3^{2-}$). 85
Figure 4.2. Asymmetric chloride mediated pH-swing direct ocean capture system concept by Kim et al.[166] 85
Figure 4.3. Depiction of the conceived FOWT-DOC system using (left) seawater from 20 m depth, at the vicinity of the platform bottom (Case 0), and (right) seawater withdrawn from 100, 200, and 300 m water depth (Cases 1, 2, and 3, respectively). The DOC equipment is placed at the base of the hull (with an assumed concrete thickness of one meter), at around 16.6 m water depth. 87
Figure 4.4. Variation of pH and dissolved inorganic carbon (DIC) with water depth for the four cases analysed [181]. 89
Figure 4.5. Schematic illustration of the main DOC system processes integrated into the floating platform. Blue arrows represent seawater flows, while the red arrow indicates captured CO_2 flow. 93
Figure 4.6. Carbon capture seawater intensity as a function of dissolved inorganic carbon (DIC) for the design scenarios. 98
Figure 4.7. (Left) Total system energy expenses, and (right) annual CO_2 captured with different gaps between cell's electrodes ($\boldsymbol{\delta cell}$) per each design scenario. 101

Figure 4.8. (Top) Average system component costs per unit of CO_2 captured across design scenarios. The abbreviated field "Comp." stands for compressor, and the field "Other" comprises the intake system, electrochemical cells, and batteries. (Bottom) Sensitivity of the levelized cost of carbon (LCC, in \$/tCO_2) with ±15% and ±30% percentage changes in the combined cost of the CO_2 riser and seawater intake system for each design scenario. The minimum LCC at every percentage variation across design scenarios is highlighted in red. 104

Figure 4.9. Carbon capture energy intensity for the FOWT-DAC and FOWT-DOC systems studied. The minimum thermodynamic energy required for CO_2 direct air capture and minimum electrochemical energy for CO_2 direct ocean capture are included for reference in red. 107

Figure 4.10. Variation with sea water depth of (left) dissolved inorganic carbon by ocean, and (right) pH in the North Pacific along 152˚W, modified from refs.[225,228]. 112

Figure 4.11. Dissolved oxygen (top) and nitrogen (middle) profiles, and salinity (bottom) for the Pacific Ocean (1984) between Japan and USA (40-50˚N) adapted from Schlitzer[231]. 114

Figure 5.1. (Left) Future projected CapEx for the FOWT platforms (semisubmersible and TLP) used in the FOWT-DAC and FOWT-DOC solutions. (Right) Future projected cost of CO_2 removal via FOWT-DAC and FOWT as a function of the annual CO_2 removal. 122

List of Abbreviations

AD	Adiabatic transport
AEP	Annual energy production
BECCS	Bioenergy with carbon capture and storage
BPMED	Bipolar membrane electrodialysis
CapEx	Capital expenditure
CCS	Carbon capture and storage
CCUS	Carbon capture, utilisation and storage
CDR	Carbon dioxide removal
CDF	Cumulative distribution function
CF	Cartridge filter
CO_2	Carbon dioxide
COP	Coefficient of performance
CSPD	Current speed at sea surface
CTP	Climate tipping point
DAC	Direct air capture
DACCS	Direct air capture with carbon storage
DF	Disc filter
DIC	Dissolved inorganic carbon
DLC	Design load condition
DOC	Direct ocean capture
DOCCS	Direct ocean capture with carbon storage
DOF	Degree of freedom
ECD	Extreme coherent gust with wind direction change
E-CEM	Electrolytic cation exchange module
ECM	Extreme current model
ED	Electrodialysis
EOG	Extreme operating gust
ERW	Enhanced rock weathering
ESS	Extreme sea state, energy storage system
ETM	Extreme turbulent model
EWM	Extreme wind model
FOWT	Floating offshore wind turbine
FOWT-DAC	Floating offshore wind turbine direct air capture
FOWT-DOC	Floating offshore wind turbine direct ocean capture
FPV	Floating photovoltaic
FTE	Full time equivalent
GDP	Gross domestic product
GHG	Greenhouse gas
GMST	Global mean surface air temperature
GWP	Global warming potential
HAMS	Hydrodynamic Analysis of Marine Structures
HDPE	High-density polyethylene

HFM	Hollow fibre membrane
HOP	Hang-off point
IAM	Integrated assessment model
ID	Internal diameter
IEA	International Energy Agency
IFORM	Inverse first order reliability method
IPCC	Intergovernmental Panel on Climate Change
LCA	Life-cycle assessment
LCC	Levelized cost of carbon
LCOE	Levelized cost of electricity
LM	Load management
LWR	Lazy-wave riser
MBL	Minimum breaking load
MBR	Minimum bending radius
MGPS	Marine growth preventive systems
MRV	Measurement, reporting, and verification
NAD	Nonadiabatic transport
NCM	Normal current model
NET	Negative emission technology
NRMSE	Normalized root mean square error
NSS	Normal sea state
NTM	Normal turbulence model
O&G	Oil and gas
O&M	Operations and maintenance
OAE	Ocean alkalinity enhancement
OD	Outer diameter
ODE	Ordinary differential equation
ONC	Ocean Networks Canada
OPB	Out-of-plane bending
OpEx	Operational expenditure
OTEC	Ocean thermal energy conversion
OWF	Offshore wind farm
P2X	Power-to-X
PB	Planet boundaries
PEM	Proton exchange membrane
PFT	Potential flow theory
PPI	Producer Price Index
PRIMED	Pacific Regional Institute for Marine Energy Discovery
RAO	Response amplitude operator
RMSE	Root mean squared error
RNA	Rotor nacelle assembly
RO	Reverse osmosis
RP	Return period
RWT	Reference wind turbine

SAB	Structured adsorbent bed
SRM	Solar radiation management
SSP	Shared socioeconomic pathway
SSS	Severe sea state
SWIR	Seawater intake riser
SWL	Still water level
TDH	Total dynamic head
TDP	Touch down point
TLP	Tension-leg platform
TMP	Transmembrane pressure
UF	Ultrafiltration
UMaine	University of Maine
WSPD	Mean wind speed at hub height

Nomenclature

α	Correction factor
a_0, a	Still or instantaneous water air gap or freeboard
A, A_i	Added mass, inner cross-sectional area
Ag	Silver
A_o	Outer cross-sectional area
A_r	Cross-sectional area for some radial distance r from the pipe’s centre
A_{rotor}	Wind rotor swept area
A_w	Cross-sectional wall area, $A_w = A_o - A_i$
A_{wind}	Wind availability factor
β	Reliability index or standard normal U-space radius
B	Wave radiation damping
Bi	Bismuth
γ	Heat capacity ratio
c_{ij}	Coefficients of the hydrostatic stiffness matrix
C_p	Heat capacity at constant pressure
C_t	Rotor thrust coefficient
C_v	Heat capacity at constant volume
CoB	Centre of buoyancy
CoG	Centre of gravity
δ	Gap between electrodes, vertical motion of the floater
δ_{ij}	Kronecker’s delta function
Δp	Pressure difference
d_0	Reference depth at which wind-induced current speed vanishes
D	Water depth
D_h	Hydraulic diameter
D_t	Percentage annual gross domestic product deflator
ζ	Small floating body displacement from the sea surface
e	Carbon capture energy intensity
ε	Probability distribution location parameter, surface roughness
E	Young’s modulus, experience parameter
EA_w	Axial stiffness
EI	Bending stiffness
$f(x)$	External load
f_D	Darcy friction factor
F	Faraday constant
F_{m,CO_2}	Molar flow rate of saturated CO_2 with water vapor
g	Gravity’s acceleration
G	Generation rate
GM	Metacentric height
H	Pressure head
H_s	Significant wave height

i	Electric current volumetric density
I	Electric current
ID	Internal diameter
I_{ii}	Moment of inertia about the centre of gravity
κ, κ_{CO_2}	Line curvature (reciprocal of bending radius), adiabatic constant of CO_2
k	Wind-current coupling coefficient, probability distribution shape parameter
KG	Vertical height of the centre of gravity above the keel
λ, λ_{ow}	Probability distribution scale parameter, seawater ionic conductivity
μ	Mean of a probability distribution, kinematic viscosity
L	Length of pipe/riser
LR	Learning rate
m_{year}	Annual mass flow rate
$\dot{m}$	Mass flow rate
MBR	Minimum bending radius
M_w	Wind heeling moment
η	Efficiency, free surface elevation
$n, \boldsymbol{n}$	Polytropic path coefficient, normal vector to surface element dS
θ	Angular displacement in pitch
ρ	Fluid density
p	Pressure
p_i	Inner pressure (e.g. inside a pipe)
p_o	External pressure
ppm	Parts per million
p_{T_R}	Failure probability
P_{WT}	Wind turbine power
$Pr(v_i)$	Probability of occurrence of wind speed v_i
$Q, \dot{V}$	Volumetric flow rate
OD	Outer diameter
$\boldsymbol{r}$	Position vector from the body's centre of flotation
r_{T_R}	Reliability
R	Universal gas constant
Re	Reynolds number
S_B	Instantaneous wetted surface
S_{11}	Second moment of area
T	Temperature
TDH	Total dynamic head
T_e	Effective tension
T_p	Peak period
T_{top}	Top tension
T_w	True wall tension
$U_{1h,10m}$	One-hour sustained wind speed at 10 m height
U_{rated}	Rated wind speed
V	Electric potential

V_0	Floating body submerged volume under equilibrium conditions
v	Mean wind speed, flow speed
v_c	Total ocean current velocity
$v_{c,circulation}$	Ocean circulation contribution to current velocity
$v_{c,tidal}$	Tidal contribution to current velocity
$v_{c,wind}$	Wind contribution to current velocity
$v_{erosion}$	Erosional velocity
W_a^{fluid}	Internal fluid apparent weight
W_a^{riser}	Riser apparent weight
$\epsilon_{Poisson}$	Poisson effect axial strain
$\epsilon_{tensile}$	Tensile strain
κ	Curvature
ρ	Volumetric mass density
ρ_i	Inner fluid density
ρ_s	Seawater density
σ	Standard deviation of a probability distribution
σ_b	Bending stress
σ_e	Effective stress
σ_{VM}	von Mises stress
σ_y	Yield strength
τ	Shear stress
T_R	Return period
ν	Poisson effect ratio
x_B, y_B, z_B	Coordinates of the centre of buoyancy
x_G, y_G, z_G	Coordinates of the centre of gravity

Superscripts and subscripts

acid	Acidifying cell
air	Atmospheric air
alkal	Alkalizing cell
aq	Aqueous
cell	Electrochemical cell
degas	Degassing or gas separation
diaphragm	Diaphragm compressor
DIC	Dissolved inorganic carbon
echem	Electrochemical
fab	Fabrication
FE	Faraday efficiency
HFM	Hollow fiber membrane
inst	Installation
motor	Electric motor
Ohmic	Ohmic
ow	Oceanwater
OWI	Oceanwater intake
PF	Pretreatment filters
pump	Water pump
rated	Pertaining to rated wind speed
reciprocating	Reciprocating compressor
riser	Export CO_2 riser
rotor	Wind rotor
screw	Screw compressor
SWIR	Seawater intake riser
VP	Vacuum pump
WT	Wind turbine

Acknowledgements

No person is an island, and this dissertation wouldn't have been possible without the support of many people.

Firstly, I'd like to express my gratitude to my supervisor Dr. Curran Crawford, for his guidance in times of need and his patience throughout this journey. I'm also indebted to my advisors Dr. Brad Buckham and Dr. Richard Dewey, for enriching this dissertation with their expertise and natural curiosity. Dr. Buckham, thank you for always checking in on me whenever we casually bump into each other. Dr. Richard Dewey, thank you for reminding me to put myself first.

To the people who have had to endure the worst of me over these years whilst fighting their own battles. To Spencer, thank you for spreading your contagious optimism and enthusiasm for engineering, and for always being available for a chat. To Rad, I'm thankful for your wisdom and for teaching me what a doctoral program is all about. To Patrick, Heather, and Saeid, thank you for your insightful comments and reviews, and for all the lovely hangouts outside of work.

I'd like to extend my gratitude to Ignacio Beya and Ben Whitby from the Pacific Regional Institute for Marine Energy Discovery, Martin Scherwath from Ocean Networks Canada, and Nikki Forde from Flotation Energy Plc: thank you all for sharing your resources, expertise, and above all, your time. On that front, this PhD project wouldn't have been possible without the financial support of the Pacific Institute for Climate Solutions, a private donor, and the University of Victoria.

To everyone at IESVic, especially the administration team (Pauline and Rachel), for taking care of our social life. A warm mention to Pauline, for going well beyond her duties when proofreading my work, for the countless hours exchanging thoughts on arts, culture, and politics, and for being a true steward of our small community which is IESVic.

My heartfelt and deepest gratitude are dedicated to my family in Spain and to my partner. Als meus pares i a l'Óscar: el vostre carinyo, amor i suport incondicionals són els ciments sobre els quals tota la meva vida s'ha construït, i sense els quals no m'hauria estat possible fer un doctorat. A la meva germana, al meu cunyat i al meu nebot, moltes gràcies per recordar-me la importància de la familia, present sempre que decideixo marxar de nou. To Agatha, thank you for your conscious belief in me, the unconscious positive influence you've had on me, and for being a constant in this ever-changing world.

This dissertation is dedicated to those who refuse to accept the *status quo* in the conviction that a more just world is within reach.

“Three passions, simple but overwhelmingly strong, have governed my life: the longing for love, the search for knowledge, and unbearable pity for the suffering of mankind.

I have sought love, first, because it brings ecstasy - ecstasy so great that I would often have sacrificed all the rest of life for a few hours of this joy. I have sought it, next, because it relieves loneliness - that terrible loneliness in which one shivering consciousness looks over the rim of the world into the cold unfathomable lifeless abyss. I have sought it, finally, because in the union of love I have seen, in a mystic miniature, the prefiguring vision of the heaven that saints and poets have imagined. This is what I sought, and though it might seem too good for human life, this is what - at last - I have found.

With equal passion I have sought knowledge. I have wished to understand the hearts of men. I have wished to know why the stars shine. And I have tried to apprehend the Pythagorean power by which number holds sway above the flux. A little of this, but not much, I have achieved.

Love and knowledge, so far as they were possible, led upward toward the heavens. But always pity brought me back to earth. Echoes of cries of pain reverberate in my heart. Children in famine, victims tortured by oppressors, helpless old people a hated burden to their sons, and the whole world of loneliness, poverty, and pain make a mockery of what human life should be. I long to alleviate the evil, but I cannot, and I too suffer.”

Prologue to the autobiography of Bertrand Russell, July 25th, 1956

Chapter 1.

Introduction

> "*Let's get this on the table right away, without mincing words. With regard to the climate crisis, yes, it's time to panic. We are in deep trouble. To understand why, it is necessary to understand something about carbon budgets*."
>
> Raymond Pierrehumbert, Halley Professor of Physics at the University of Oxford, lead author of the Intergovernmental Panel on Climate Change (IPCC) Third Assessment Report

This first section seeks to orient the reader to the scientific foundations that motivate this dissertation – namely, climate change and the need for carbon dioxide removal (CDR) – and the rationale behind the specific path chosen to contribute to that effort: offshore wind-powered CDR sequestered in deep-sea basalt. At the same time, a sincere effort has been made to uphold the "no silver bullet" philosophy, which cautions against the inherent human tendency to seek a single – often technological - saviour for our problems. If I have failed to reflect this, I apologise. Lastly, in an attempt to offer some clarity in this era of misinformation, I devoted equal consideration to precision, retaining much of the technical terminology used in IPCC reports. I fear this may come at the expense of accessibility or readability at times, and for that, I also apologise.

ANTHROPOGENIC CLIMATE CHANGE AND CARBON DIOXIDE REMOVAL

Human activities, such as energy and land use, land use change, and unsustainable patterns of lifestyle, consumption, and production, have unequivocally induced a change in the climate system, warming the atmosphere, ocean, and land[1]. Between 1850-1900 and 2013-2022, the global mean surface air temperature (GMST) increased 1.15 [1.00 to 1.25]°C, ocean temperatures 0.93 [0.73 to 1.04]°C, and land temperatures 1.65 [1.36 to 1.90]°C, ref.[1]. This warming has already had major consequences worldwide, with rises in mean sea level of 0.20 [0.15 to 0.25] m between 1901 and 2018 (*high confidence*[i]), and more frequent and more intense hot extremes (*virtually certain*) and heavy precipitations (*high confidence*) since the 1950s, ref.[1]. These extremes have reduced food and water security for millions of people across different regions in Africa, Asia, Central and South

---

[i] Following the IPCC confidence qualifiers and likelihood terminology, evidence with a medium and high confidence level have a 50% and 80% chance of being correct, respectively, whereas very likely and virtually certain events have a likelihood of occurrence equal to 90-100% and 99-100%, respectively. For clarity, when used in this section, this terminology is italicised.

America, Small Island Developing States and the Arctic, and across communities of Indigenous Peoples, low-income households, and small-scale producers[1].

It is *very likely* that the main drivers behind this human-induced warming are greenhouse gas (GHG) emissions, primarily carbon dioxide (CO_2)[ii] which contributed to 0.8°C of warming between 1850-1900 and 2010-2019, ref.[2]. The sixth IPCC assessment cycle reaffirmed the near-linear relationship between anthropogenic cumulative CO_2 emissions and global warming (*high confidence*), see Figure SPM.10, ref.[3]. Indeed, for each 1,000 $GtCO_2$ of cumulative CO_2 emissions, the GMST increases 0.45 [0.27 to 0.63]°C. More importantly, "this relationship implies that reaching net zero anthropogenic CO_2 emissions is a requirement to stabilise human-induced global temperature increase at any level, but that limiting global temperature increase to a specific level would imply limiting cumulative CO_2 emissions to within a carbon budget", ref.[3].

Every increase in GMST raises the risks and severity of impacts associated with climate change. At the 2013-2022 warming above pre-industrial levels of 1.15 [1.00 to 1.25]°C, five climate tipping points (CTPs) had already become likely: the collapse of the Greenland and West Antarctic ice sheets, the collapse of the Labrador-Irminger subpolar gyre, the die-off of low-latitude coral reefs, and the abrupt thaw of boreal permafrost[4]. Limiting any further warming is necessary to preserve a liveable planet[1]. However, with the climate policies in place by 2019, projections by the IPCC showed that the global net median GHG emissions would remain roughly the same as in 2019 until 2100 (Figure SPM.5 in ref.[1])[iii]. At these levels, the effects of the accumulated anthropogenic GHGs on the atmosphere – referred to as historical emissions – could lead to a GMST of 3.2 [2.2 to 3.5]°C (*medium confidence*) by 2100 relative to the 1850-1900 period[1].

In an effort to define legally binding temperature targets and spur countries to reduce their GHG emissions, the 2015 Paris Agreement sought to keep the GMST well below 2°C, preferably to 1.5°C above pre-industrial levels[iv]. To attain this, it is necessary to achieve net zero CO_2 emissions between the early 2050s and the early 2070s, as shown by all IPCC global modelled pathways (see e.g. Figure 3.6 in ref.[1]). First and foremost, this requires profound reductions in CO_2 emissions, achieved mainly through the replacement of carbon intensive energy sources and technologies by

---

[ii] In 2019, the concentration of CO_2 in the atmosphere was higher than any time over the past two million years (high confidence), with an unprecedented increase seen since 1750 which transcends natural multi-millennial variations between glacial and interglacial periods over at least the last 800,000 years[1]. Methane is the second largest contributor to the observed warming of the atmosphere, causing a 0.5°C increase between 1850-1900 and 2010-2019, ref.[2]. Although most of the world efforts have been focused on reducing CO_2, it is becoming increasingly clear that resources devoted to methane mitigation must be stepped up[254], as only ~2% of global climate financial resources are destined to methane abatement[255] and actions to reduce CO_2 emissions have fallen short.

[iii] In 2019, the global net anthropogenic GHG emissions were 59 ± 6.6 $GtCO_2$-equivalent, 54% higher than in 1990, ref.[1]. Aggregated GHG emissions from different GHGs are stated in CO_2-equivalents (CO_2e), which are calculated based on their global warming potential (GWP) over 100 years. The GWP measures the infrared thermal radiation GHGs would absorb over a given time frame (often taken as 100 years).

[iv] Between 1.5-2°C, nine additional CTPs become possible: the collapse of the East Antarctic subglacial basins and the Atlantic Meridional Overturning Circulation, the dieback of the Amazon rainforest and the southern boreal forest, the abrupt loss of the Barents Sea ice, the loss of mountain glaciers, the greening, of the Sahel and West African monsoon, and the northern expansion of the boreal forest[4].

low-carbon ones (commonly known as decarbonisation), the reduction and change of energy demand through improvements in technological efficiency and socio-cultural and behavioural changes, and the protection and restoration of ecosystems (*high confidence*)[1]. In addition, historical emissions must be offset by carbon dioxide removal (CDR) methods, which aim to lower the concentration of CO_2 in the atmosphere. Estimates suggest[5] that achieving the 1.5°C with limited or no overshoot requires removal of 100 to 1,000 $GtCO_2$ by 2100[v]. Beyond compensating for past emissions, CDR is essential for counterbalancing emissions from sectors which are by nature harder to decarbonise, such as agriculture, aviation, shipping, road transportation (i.e. heavy-duty trucks), and iron and steel production[6].

Despite the unavoidable necessity to upscale CDR (currently at around 2.1 $GtCO_2$/year, ref.[7]), if we are to meet the targets of the 2015 Paris Agreement, I find it important to emphasise the next statement from the IPCC[5] that, to my mind, remains true today and underscores the order of priorities:

> “Limits to our understanding of how the carbon cycle responds to net negative emissions increase the uncertainty about the effectiveness of CDR to decline temperatures after a peak. CDR deployed at scale is unproven, and reliance on such technology is a major risk in the ability to limit warming to 1.5°C. CDR is needed less in pathways with particularly strong emphasis on energy efficiency and low demand.”, page 34, ref.[5].

CDR is not a replacement for decarbonisation efforts or an excuse to continue promoting carbon intensive practices. CDR and decarbonisation need to take place in parallel, but the former cannot slow down or limit the pace of the latter.

Several CDR methods currently exist[vi], each exhibiting their own sustainability, readiness levels, CO_2 removal potential, and permanence[vii] (see comparison and summary of CDR methods in Table 1 in ref.[8]). Given the uncertainties around their risks, benefits, and the scale of CDR deployment

---

[v] The required range of 100-1,000 $GtCO_2$ reflects an estimation based on the carbon budget at the time (2018-2019), and accounts for uncertainties that consider the speed of decarbonisation. It assumed that CO_2 emissions would peak around 2020, which did not happen and are still increasing every year, reaching a record high of 38.1 $GtCO_2$ in 2025, ref.[256]. Consequently, the lower boundary of 100 $GtCO_2$ of cumulative removal by 2100 is no longer compatible with staying within 1.5°C with limited or no overshoot, and the true amount required is likely higher. The integrated assessment models (IAMs) used by ref.[5] to derive the required levels of CDR are based on the Shared Socioeconomic Pathways (SSPs) framework[257], comprised of five main scenarios. Each scenario has a defined qualitative narrative that translates into quantitative demographic and economic markers employed by the IAMs. The economic marker used across all SSPs is the gross domestic product (GDP) and, notably, in all SSPs projections of GDP to the year 2100, this indicator never ceases to grow (Figure 2 in ref.[257]). To be compatible with a GHG emission cap, such growth assumptions can only be justified insofar as a full decoupling of emissions and GDP is achievable, which may not have been achieved as of yet[258–261]. I will leave the divisive debate between growth supporters and growth critics aside for now, but before doing so, I propose the following (provocative) question: how would the well-known cumulative required levels of CDR by 2100 (100-1,000 $GtCO_2$) change if the SSPs had considered a non-growing (i.e. steady) or even declining GDP? I hope the reader will forgive this brief detour.

[vi] E.g. afforestation, reforestation, and improved forest management, enhanced rock weathering, ocean fertilisation, coastal blue carbon, increased soil carbon sequestration, bioenergy with carbon capture and storage.

[vii] Permanence may be defined as the time CO_2 can be locked away from the atmosphere.

required, all CDR approaches should ultimately be developed to ensure a more robust system, although some are likelier to play a larger role in the near term than others. Certainly, conventional and more inexpensive CDR solutions but with *insufficient* permanence – such as afforestation, reforestation, and forest management practices, which currently comprise 99.9% of the existing CDR deployed[7] and have permanence scales of decades to centuries – can "buy us some valuable time while more durable forms of CDR are developed", ref.[9]. However, because models of global carbon cycling strongly agree that fossil fuel-CO_2 emissions can affect the climate for thousands of years[10], solutions with equivalent permanence may be the most desirable, which explains why the approaches above with shorter storage durations were referred to as insufficient. In comparison, CO_2 stored in minerals and geologic formations can be locked in for thousands of years, making it the most preferred option for sequestering CO_2.

CLARIFICATION NOTES: CDR, CCS, CCUS, and SRM

CDR is not to be confused with carbon capture and storage (CCS) or carbon capture, utilisation and storage (CCUS). As opposed to CDR, which captures CO_2 from the atmosphere, CCS and CCUS capture it from large emitters (often called point sources), such as power plants or industrial facilities, which use fossil fuels or biomass as fuel. Consequently, CCS and CCUS only balance current emissions and do not reduce further atmospheric CO_2 concentration. After the CO_2 is captured from point sources, it may be stored away in reservoirs (CCS) or used in a range of applications (CCUS).

Solar radiation management (SRM) or solar geoengineering is a set of non-CDR strategies which rely on increasing the amount of sunlight reflected back to space, thereby reducing the heat trapped by Earth and addressing global warming. Without ignoring the challenges posed to achieve a fair and inclusive global governance of planetary-scale SRM[11], solar geoengineering does not tackle the root of climate change (i.e. CO_2 emissions), only one of the effects caused by it (i.e. global warming), effectively just "kicking the can down the road"[12].

CARBON DIOXIDE SEQUESTRATION IN DEEP-SEA BASALT – A TIMELY AND SAFE MINERALISATION

There are different mechanisms by which CO_2 can be retained in minerals and geologic formations, which can be categorized as physical (structural, stratigraphic, residual, and hydrodynamic) and geochemical trapping (solubility, and mineral)[viii]. Among these, mineral trapping is the most stable and long-term mechanism, in which CO_2 reacts with rocks rich in calcium, magnesium, and iron oxides, and forms carbonate minerals in an exothermic process known as carbonation.

$$CaO + CO_2 \rightarrow CaCO_3 \tag{1.1}$$

[viii] Physical traps consist of impervious stratum, or put simply, a layer or series of layers of rock that do not allow the CO_2 to pass. Structural traps are formed by tectonic forces (e.g. folding or faulting of rocks), while stratigraphic traps occur due to changes in rock properties (e.g. porosity or permeability). Residual trapping refers to CO_2 confined inside the tiny pores of a structure due to capillary forces, and hydrodynamic trapping happens "when the residence or travel time of CO_2 in low permeability regional aquifers is of the order of thousands to a million years", ref.[19].

$$MgO + CO_2 \rightarrow MgCO_3 \tag{1.2}$$

$$FeO + CO_2 \rightarrow FeCO_3 \tag{1.3}$$

Carbonation in onshore silicates, akin to the natural weathering of silicates to carbonates in the carbonate-silicate cycle, was first suggested by Seifritz[13] as a means of CO_2 disposal. They noted, nevertheless, that the slow kinetics of the reaction (i.e. the long timescale to mineralisation) might make the process impractical. Indeed, Kelemen et al.[14] estimated the carbonation rate of open peridotite formations in Samail Ophiolite (Oman) as 10^4 tCO_2/year, much slower than the rate at which anthropogenic CO_2 emissions are added to the atmosphere (10^{10} tCO_2/year). However, they also modelled how drilling and injecting high-pressure, dissolved CO_2 at depth could speed up the carbonation reaction kinetics, calculating an increase of six orders of magnitude in the rate of CO_2 mineralised, or 10^{10} tCO_2/year. Certainly, as gaseous CO_2 is hydrated, and one bicarbonate ion (HCO_3^-) and proton (H^+) form (see eq. 1.4), the enhanced acidic environment induces the dissolution of minerals from the host silicates, which react with the dissolved bicarbonate and result in the precipitation of carbonates (eqs. 1.5 to 1.7). Further, the dissolution of CO_2 in water under unsaturated conditions prevents it from degassing as the CO_2 is no longer buoyant, known as solubility trapping. The advantages conferred by these injection conditions were later confirmed by the CarbFix pilot project, which demonstrated that 95% of the injected and dissolved CO_2 in land basaltic formations mineralised within two years[15].

$$CO_2(aq) + H_2O \leftrightarrows H_2CO_3 \leftrightarrows HCO_3^- + H^+ \tag{1.4}$$

$$Ca^{2+} + HCO_3^- \rightarrow CaCO_3(s) + H^+ \tag{1.5}$$

$$Mg^{2+} + HCO_3^- \rightarrow MgCO_3(s) + H^+ \tag{1.6}$$

$$Fe^{2+} + HCO_3^- \rightarrow FeCO_3(s) + H^+ \tag{1.7}$$

In nature, mafic and ultramafic rocks, such as basalt and peridotite, are the richest sources of calcium, magnesium, and iron, and the preferred rock formations for CO_2 mineralisation[ix]. Of these, basaltic rocks are one of the most widespread rock types on Earth, covering approximately 10% of the continental surface and most of the upper ocean crust[16]. Subseafloor basalt alone is estimated to have a capacity over 30,000 $GtCO_2$, ref.[17].

Goldberg and Slagle[17] assessed the global CO_2 storage capacity of subseafloor basalt in deep waters (at a minimum of 2,700 m depth), sealed by an upper sediment layer of 200 m thickness or

---

[ix] The calcium, magnesium, and iron content in many sedimentary rocks is lower than in basalt rocks, and thus their capacity and rate of mineral trapping is also lower[262,263]. That said, the vast majority of the current CO_2 storage projects inject CO_2 in underground sedimentary basins, where the CO_2 remains in gas, liquid or supercritical phase for a long time (e.g. see Figure 1 in ref.[64]). Although the likelihood of leakage is estimated to be negligible[264], the requirement of long-term monitoring may not be feasible considering e.g. current levels of political commitments. Together with the need for new site identification, these factors encourage the assessment of alternative CO_2 storage methods, such as mineralisation in basalts.

more. The impermeable sediment layer provides a first stratigraphical trap after the CO_2 is injected, impeding its migration to the surface. If the buoyant CO_2 gas were still to permeate through and leak into seawater, the high hydrostatic pressure would prevent it from ascending any further, what is known as gravitational trapping. Moreover, at such water depths, deep-ocean waters take centuries to mix with surface waters, so the CO_2 could be sequestered for hundreds of years[18], what is known as deep ocean disposal[19].

The high prevalence and location away from human activities, combined with multiple trapping mechanisms (physical and geochemical) and large storage capacity for disposal (estimates suggest dozens of teratons of CO_2, ref.[17]), make deep-sea basalt rock a strong candidate for safe and permanent CO_2 storage. These advantages motivated the Solid Carbon team, within which this PhD research is conducted, to investigate and advance CO_2 sequestration in deep-sea basalt formations.

CARBON DIOXIDE REMOVAL VIA DIRECT AIR CAPTURE AND DIRECT OCEAN CAPTURE

Before CO_2 can be sequestered in geologic reservoirs such as deep-sea basalt, it needs to be captured from the atmosphere; one way is by direct removal from ambient air, or direct air capture (DAC). Another way is by extracting CO_2 dissolved in seawater, thereby enabling further indirect atmospheric uptake by the ocean, which is known as direct ocean capture (DOC). The two processes have a comparable annual removal potential of 5 to 40 $GtCO_2$/year by 2050[20], among the highest identified by Cross et al.[8]. Most importantly, both DAC and DOC can be coupled to geologic CO_2 sequestration (such as deep-sea basalt), thus becoming direct air carbon capture and storage (DACCS), and direct ocean carbon capture and storage (DOCCS), respectively.

The removal of CO_2 from ambient air and seawater are energy intensive processes and are thus contingent upon the availability of reliable and abundant sources of energy. For example, DAC requires 1.4-2.8 kWh per kilogram of CO_2 (kWh/$kgCO_2$) sequestered, while DOC needs 5.8 kWh/$kgCO_2$, refs.[21,22]. If all CDR by 2050 were to come from DAC – estimated at 6 $GtCO_2$/year to remain within a 2°C warming[23] – it would consume between 8.4-16.8 petawatt-hours (PWh) per year. For comparison, global electricity consumption in 2024 was approximately 30 PWh[24]. In Canada, where the GHG intensity of the electricity grid is among the lowest globally (100 gCO_2e/kWh in 2022, compared to 258 gCO_2e/kWh in the European Union, and 390 gCO_2e/kWh in the United States[25]), the annual emissions associated with grid powered DAC would be 0.84-1.68 $GtCO_2e$, equivalent to 14-28% of the 2050 CDR target. Although these are rough estimates, they underscore the importance that if DAC and DOC are to contribute to offsetting CO_2 emissions, their energy demand should be met with low-carbon sources[x] (e.g. see refs.[26–29]). To this end – and to avoid competition for land-use and grid energy with other sustainable activities, which could be a deterrent for CDR deployment – an offshore, off-grid renewable energy system is proposed. This approach can

---

[x] Wind and solar energy are the most mature and inexpensive renewable, low-carbon energy sources; between 2014 and 2023, the world's wind power installed capacity (both onshore and offshore) almost tripled, while solar power (concentrated solar and solar photovoltaics) nearly grew eightfold[265]. As a result, their levelized cost of electricity (LCOE) experienced equally notable improvements, declining 70% for onshore wind and a remarkable 90% for solar photovoltaics[266].

be co-located with deep-sea basalt reservoirs, thus offering a fully autonomous, safe, and permanent CDR solution.

Among the possible offshore energy source candidates – namely, offshore wind, floating solar, tidal, wave, and ocean thermal energy conversion (OTEC) – generally offshore wind exhibits the highest market readiness and remains the most cost-effective solution[30]. In particular, in the Pacific Northeast – around Cascadia Basin (**Figure 1.1**) where the Solid Carbon team is assessing CO_2 sequestration in deep-sea basalt – the environmental conditions (slow currents and reduced temperature gradient along the vertical water column) are not ideally suited for tidal energy or OTEC. Despite the fact that floating solar platforms and wave energy converters are possible alternatives – especially given the strong expertise in the latter of near institutions such as the Pacific Regional Institute for Marine Energy Discovery (PRIMED) and the Pacific Northwest National Laboratory – offshore wind continues to be the most economically viable option and the least likely to face resistance or scepticism from developers and funding agencies. Some authors claim that, in the absence of decarbonised grid electricity, DAC (and equivalently DOC) are unlikely to be economical unless paired with high-capacity factor renewables, such as offshore wind[31]. These considerations make offshore wind energy the most compelling offshore renewable energy source. Accordingly, this dissertation investigates the integration of offshore wind-powered DAC and, separately, offshore wind-powered DOC.

A MULTIFACETED OPPORTUNITY FOR CANADA

Although Canada has vast offshore wind resources and is host to companies involved in several offshore wind farms worldwide[xi], the offshore wind power installed capacity in the country is currently zero (late 2025). Efforts to change this are underway in multiple sectoral areas, from regional resource assessments and spatial planning[32,33], workplans for future market and grid integration studies[34], to roadmaps detailing required legislative and regulatory frameworks[35], and recommendations to establish an inclusive and sustainable supply chain[36]. Thus far, such interest has all been focused on the Canadian Atlantic coast, with Nova Scotia leading the way and offering leases for 5 GW of offshore wind by 2030 to support the green hydrogen industry[xii], ref.[37]. If developed, this could provide 14,500 full time equivalent (FTE) jobs[xiii], or 3.4% of the number of FTE jobs in the region in 2024, ref.[38]. Nevertheless, as the electrification required to reach net zero CO_2 emissions by 2050 is anticipated to double the demand for electricity in Canada, new wind power capacity is expected to be installed nation-wide, with some scenarios estimating 3.8 GW of additional capacity annually[39]. While most of this new capacity will sit onshore, the opportunity presented by more

---

[xi] E.g. Northland Power Inc. with three operating offshore wind farms in the North Sea, and partial ownership of two more under construction in Taiwan (1,022 MW)[267].

[xii] On 29 July 2025, four areas that will be included in the first call for bids were officially designated. These are located at the French Bank, Middle Bank and Sable Island Bank off mainland Nova Scotia, and Sydney Bight off Cape Breton[268]. These are the first areas ever designated for offshore wind development in Canada, marking a significant step forward to unlock Canada's offshore wind potential.

[xiii] These figures are based on the UK's offshore wind industry[269]. In 2017, the offshore wind installed capacity of approximately 7 GW supported a total of 30,000 FTE jobs (the sum of direct, indirect, and induced employment, or Type II impact). By 2032, the industry is forecasted to grow to 20 GW, resulting in 58,000 FTE jobs. From this, it can be derived that, by 2032, every gigawatt of capacity installed sustains 2,900 FTE jobs.

powerful and reliable winds offshore with fewer social and regulatory constraints has already been recognized in Canadian reports[40]. Therefore, if the Canadian industries and markets follow the patterns shown in Europe, we can expect further offshore deployment in the future.

Despite that in its nascent state the Canadian offshore wind industry and markets may lack the capacity and infrastructure to support the implementation of the solutions explored in this dissertation – namely, offshore wind-powered DAC and DOC – this should not be viewed as a limitation to their value. First, as David T. Ho wrote, "CDR is not a current climate solution ... and [to] remove CO_2 from the atmosphere is pointless unless society has almost completely eliminated its polluting activities"[41]. And second, the Solid Carbon team has demonstrated that many regions worldwide, with a total CO_2 storage capacity of 4,300 Gt (lower bound estimation), possess the desired characteristics for these solutions to be applied – namely, deep-sea reactive basalt (mineral and gravitational trapping), sitting below an impermeable 200 m thick sediment layer (stratigraphic trapping), and located in proximity to port infrastructures and offshore wind resource[42]. Therefore, while this dissertation and the Solid Carbon project use Cascadia Basin as a case study to explore the feasibility of offshore wind-powered CDR (via DAC and DOC) in deep-sea basalt, the relevance of these solutions is not restricted to this location. In principle, these solutions can be exported to dozens of regions worldwide, and Solid Carbon is playing a part in its progress.

1.1. Context

This dissertation is conducted as part of the Solid Carbon project[43] and is aligned with its goals. The research directions pursued since its inception in May 2020 have been motivated by and are consistent with broader project endeavours. To better understand these, the origins of Solid Carbon and its project objectives are presented.

Solid Carbon was formed by a consortium of universities and industry partners led by Ocean Networks Canada (ONC), the University of Victoria, and the University of British Columbia. The initiative officially launched in 2019, and it was funded by the Pacific Institute for Climate Solutions. The first phase of the project (2019-2024) culminated in a feasibility study published in April 2024[44], to which the work of the author contributed. Solid Carbon built on earlier work by Goldberg et al.[17] among others, who modelled the CO_2 storage capacity of deep-sea basalt at a site in Cascadia Basin (estimated as 750 $GtCO_2$ approximately), on the eastern side of the northern Juan de Fuca Ridge, offshore from Washington State and British Columbia (**Figure 1.1**). Subsequent findings by the USA-funded CarbonSAFE program confirmed the viability of Cascadia Basin as a region suitable for carbon mineralisation[45]. Located at a water depth of approximately 2,700 m and capped by an ocean sedimentary layer 200-300 m thick[46], Cascadia Basin offers both gravitational and stratigraphic trapping. Further, the young basalt rock (less than 15 million years old[16]) is highly reactive and porous, with the potential of a fast mineralisation process. Cascadia Basin is also integrated into ONC's cabled observatory network NEPTUNE (**Figure 1.1**), featuring in-place and real-time monitoring since 2009 with hundreds of sensors on site. These provisions make the deep-sea basalt of Cascadia Basin an ideal location for CO_2 sequestration and motivated the formation of the Solid Carbon team.

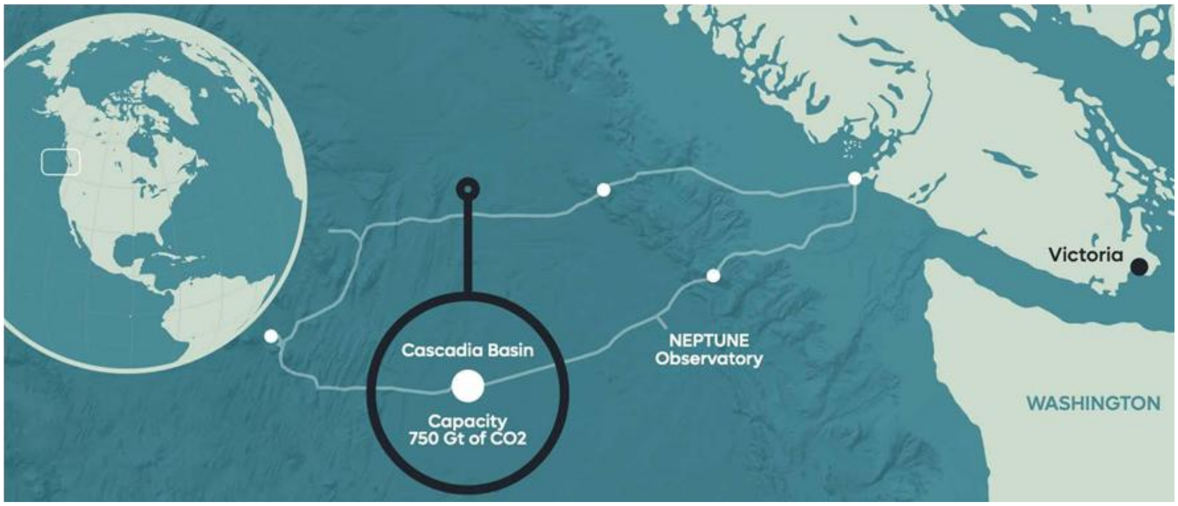

Figure 1.1. Location of Cascadia Basin, offshore from Washington and British Columbia (with permission from Ocean Networks Canada). The figure also shows ONC's cabled observatory network NEPTUNE.

Solid Carbon's mission, shared with this dissertation and reflecting the advantages conferred by deep-sea basalt, can be quoted from the project proposal document as:

> "Solid Carbon aims to reverse the effects of anthropogenic global warming and climate change by permanently removing excess CO_2 from the atmosphere via a scalable Negative Emissions Technologies[xiv] solution. Solid Carbon makes use of the world's largest possible reservoir for CO_2 sequestration—ocean basalt, which reacts with the CO_2 to turn it into carbonate rock."

To pursue this mission, the Solid Carbon project proposal document identified three main areas of activity and their focuses:

- Activity area 1: offshore CO_2 direct capture feasibility,
- Activity area 2: a carbon mineralisation demonstration project plan, and
- Activity area 3: advancement of social, regulatory, and investor acceptance.

This dissertation contributes to Activity Area 1, which is developed around a baseline scenario and two alternative options. The baseline scenario is the preferred option and is characterised by an integrated, ocean-based CO_2 capture platform. The two alternative options are: (1) shore/nearshore-based capture with [CO_2] pipeline delivery to seafloor injection, and (2) shore/nearshore-based capture and floating production storage offloading delivery. This research study supports the work undertaken within the baseline scenario and complements and informs the systems-level optimisation being carried out by other members of the Solid Carbon team, which includes the two alternative options. For completeness, the main tasks assigned to past and present

---

[xiv] Negative Emissions Technologies (or NETs) are nature- and engineering-based solutions that ultimately reduce the total amount of CO_2 from the atmosphere. The term NETs is often interchangeably used with CDR methods.

participants in Activity Area 1 are presented in **Table 1.1**. Included in it are the topics given to the author, which draw on previous work by Goldberg et al.[47,48] and form the core of the research presented in this dissertation.

Table 1.1. Main topics retrieved from the refined project proposal, modified for clarity and conciseness, and assigned to the contributors involved in Activity Area 1 of Solid Carbon, including the author of this dissertation. Their respective published research outcomes are referenced for the reader's interest.

Contributor(s)	Topics studied	Outcomes
Ryan Foxall, Haris Ishaq	• Existing terrestrial technologies for CO_2 DAC and their adaptations to perform offshore. • Sources for process heat for the DAC process.	Refs. [49,50]
Haris Ishaq, Muhammad Faisal Shehzad	• Potential for by-products of the CO_2 capture process and any excess renewable generation to be used for synergistic production of e.g. synthetic fuels to improve the overall economics of carbon sequestration.	Refs.[51–55]
Muhammad Faisal Shehzad	• Control strategies for the integration of wind powered-DAC.	Ref.[56]
Gerard Avellaneda Domene (author)	• System design options for delivering CO_2 into ocean basalt using DAC and DOC powered with offshore wind energy. • System design options for CO_2 transportation from a floating CO_2 capture platform.	Refs.[57,58]
Heather Norton	• Shore-based CO_2 capture with pipeline delivery to subsea wellhead(s). • Technical assessment of the full system components, their feasibility, identification of any roadblocks to their system integration, and the full system costs per $MtCO_2$.	Refs.[42,59]
Patrick Connolly	• Novel design concepts for production of offshore wind-powered synthetic fuels.	Refs.[60,61]
Mehar U Nisa	• CO_2 capture from seawater as a potentially more concentrated source.	Ref.[62]

1.2. Objectives and approach

The objectives of this dissertation were presented briefly in **Table 1.1** and are further developed next. The principal goal is to investigate and design potential *system solutions* for offshore wind-powered CO_2 capture, either directly from the atmosphere or indirectly through the ocean (explored in Chapters 2 and 4, respectively). It is not concerned with the CO_2 injection process into subseafloor basalt (which partly lies within the scope of Activity Area 2), although the CO_2 captured is processed and compressed to high pressures thus reflecting typical energy expenses associated with transport pre-conditioning. It is, however, interested in the design options for the retrieval and transport of the captured CO_2 from the ocean surface to the seabed (analysed in Chapter 3).

Chapter 2 is a fundamental part of this dissertation. It is concerned with exploring plausible ways an offshore wind-powered CO_2 capture plant can be arranged. It draws inspiration from system typologies proposed in offshore wind Power-to-X applications to argue that a decentralised configuration is most appropriate for offshore wind-powered DAC, mostly due to its modularity and reduced infrastructure. Additionally, it proposes to integrate the DAC system onto a floating offshore wind turbine (FOWT) platform rather than the more prevalent (and cheaper) fixed-bottom turbines. This preference is justified by the comparatively lower cost-depth sensitivity of FOWTs beyond the 50-60 m depth range, making them more suitable in deeper waters. This is particularly advantageous for locations with deep bathymetries close to shore, such as the Cascadia Basin case study. These design choices lay the foundations for subsequent chapters and are carried forward into Chapter 4 when investigating offshore wind-powered DOC. The rest of Chapter 2 seeks to examine the impact the addition of the DAC system has on the dynamics of the FOWT platform.

Chapter 3 begins by briefly discussing the two main transport options to deliver the captured CO_2 to the injection site: pipelines and vessels. Given the expected distance between the capture and injection locations in the Cascadia Basin case study, among other factors, a pipeline is considered as the most suitable option, and the remainder of Chapter 3 focuses on its design. But Chapter 3 goes beyond this, and it investigates possible modelling simplifications of CO_2 risers. At this point, the reader may question how these simplifications fit within the broader structure of the dissertation. This becomes clearer when noting that, at the time Chapter 3 was initiated, the intended scope of Chapter 4 differed from what it eventually became. Chapter 4 was conceived not to analyse DOC, but to study the upscaling of the offshore wind-powered DAC unit system (investigated in Chapter 2) into a farm of units. Part of the planned research for Chapter 4 was then devised as a farm layout optimisation of the CO_2 riser/piping/manifold system presented in Chapter 3. To enable an accurate yet computationally efficient farm layout optimisation in Chapter 4, Chapter 3 therefore sought to simplify the modelling of each CO_2 pipe. That said, upon completing Chapter 3, the objectives of Chapter 4 were reconsidered. The appeal of DOC as a more convenient method of CO_2 capture in the offshore environment, thus better suited with the aims of Solid Carbon, compelled us to reimagine Chapter 4. Not simply as an extension of Chapter 2 and its offshore wind-powered DAC concept, but as an exploration of another CDR method - admittedly less established and less researched than DAC - offering potentially simpler architectures and additional environmental benefits (i.e. local mitigation of ocean acidification).

The italicised term above *system solutions* denotes the holistic and interdisciplinary nature of this study. It is holistic in that it takes a wide stance and considers all the main functional elements that compose the system. This approach is particularly useful given the early stage of development of offshore, renewably-powered CDR solutions, as it prevents the premature exclusion of potentially important system elements. It is also interdisciplinary since, by combining the offshore wind power and CO_2 capture systems, it brings multiple fields together, such as wind energy, CO_2 capture technologies and chemistry, and oceanography.

From this system engineering view, this dissertation lays emphasis on:

- Identifying design system solutions for the offshore wind-powered CO_2 capture systems, whether via DAC or DOC,
- Exploring possible cost-reduction pathways and synergies, and

- Screening less appropriate designs and advancing more suitable ones.

The performance of each identified design system solution is evaluated and compared in terms of CO_2 capture capacity per unit time and energy intensity (i.e. the energy required per unit of CO_2 captured). Chapter 4 complements and finalises the analysis by estimating the economic cost per unit of CO_2 captured for the design solutions presented in Chapters 2 and 4. Owing to the novelty of these systems and the inherent uncertainties associated with first-of-a-kind projects, access to reliable information for accurate costs assessment is limited. Consequently, the cost estimates presented should be regarded with appropriate caution. Nevertheless, they can still inform present and future studies and be compared with alternative CDR methods.

1.3. Structure

This dissertation adopts a paper-based format. This means that Chapters 2 to 4 are presented, with only noted exceptions, verbatim from their referenced journal articles, either in progress or published. I resized and reformatted some figures to fit the dissertation's layout and typography, and homogenised the spelling to British English, as it is more natural to me. Since Chapters 2 to 4 are co-authored with my supervisor, Dr. Curran Crawford, there are instances in which I use the first person of the plural ("we") to acknowledge his contributions. In the remaining chapters, whenever I do not refer to the work co-authored with him, I use the first person of the singular ("I") to reflect my independent work.

Each chapter is a self-contained piece of research structured, in general, with an introduction, design and methods, results and discussion, and conclusions. Since each chapter is independent of one another, it includes contextual information (e.g. about CDR or the Solid Carbon project) which the reader may see repeated at different times throughout the dissertation. Chapter 5 finalises by summarising the research presented in Chapters 2 to 4, underscoring their contributions, and recommends future avenues of investigation.

Chapter 2.

Offshore Wind-Powered Direct Air Capture

This chapter was first published in the Ocean Engineering journal as:

G. Avellaneda Domene and C. Crawford, “Dynamic analysis of a floating wind turbine platform with on-board CO_2 direct air capture,” *Ocean Engineering*, vol. 308, p. 118205, Sep. 2024, doi: 10.1016/j.oceaneng.2024.118205. This is an open access article distributed under the terms of the Creative Commons Attribution Non-Commercial License CC BY 4.0.

After publication, we identified notation errors in **Table 2.3** which have been corrected in the present version. We also added a new graphic description, **Figure 2.4**, to improve the understanding of the ancillary system layout inside the floater’s radial columns.

Author contribution

Gerard Avellaneda Domene: conceptualisation, methodology, investigation, modelling, analysis, writing & editing. Curran Crawford: conceptualisation, analysis, supervision, review & editing.

Abstract

Development of negative emission technologies is key in meeting climate change targets. Offshore wind-powered CO_2 direct air capture (DAC) coupled with deepwater, submarine basalt reservoirs have the potential to offer a reliable way to permanently store CO_2 while avoiding grid-energy and land-use competition. This paper analyses the incorporation of a DAC system into a reference floating offshore wind turbine (FOWT) concept, the IEA 15 MW RWT atop the UMaine VolturnUS-S semi-submersible. The resulting FOWT-DAC platform’s total mass and its distribution is adapted as needed to preserve floating stability, prevent any wave splashing on the DAC system, and ensure minimum power production disturbances. The system’s fully coupled motion responses are analysed for relevant design load conditions and compared to those from the reference design demonstrating good agreement with the benchmark. The research findings suggest that the hybrid FOWT-DAC platform behaves in a similar way to the reference one and can serve as a viable modular deployment approach.

2.1. Introduction

2.1.1. Context and background

It is widely acknowledged that to remain below or return to a 1.5°C mean global temperature rise and also meet the targets of the Paris Agreement, negative emission technologies (NETs) are necessary to remove historical emissions[5]**.** One such technology is direct air capture (DAC), which extracts carbon dioxide (CO_2) directly from ambient air. The captured CO_2 can be stored later in geologic reservoirs, such as basalt rock, thus achieving negative emissions (known as DAC with carbon storage, or DACCS). Currently, there are 18 DAC plants in operation globally capturing ~0.01 $MtCO_2$/year, but only two of them store the CO_2 in permanent reservoirs, while the rest utilise it in industrial applications[63] which are unlikely to be true NETs.

Traditionally, sedimentary basins have been used in carbon storage applications for enhanced oil recovery. However, this type of rock presents some challenges for large scale CO_2 storage, such as limited mineral trapping, the need for identification of new reservoirs, and the considerable risk for the CO_2 to migrate back to the surface[64]. In contrast, basalt rock, acting as a natural, weathering reactor, offers a thermodynamically stable and environmentally favourable CO_2 mineralisation storage mechanism[65,66], with global capacity to store many teratons of carbon, orders of magnitude more than the global requirement[17]**.**

Although basalt is found both onshore and offshore, the storage of CO_2 offshore in deep waters benefits from additional levels of security provided by geochemical and hydrostatic trapping[17]. The low molecular concentration of CO_2 in ambient air means that DAC requires both a significant power input to separate CO_2 from air (1.9-23.1 PJ/$MtCO_2$), as well as a substantial capture area to filter high volumes of air (0.037–0.25 $km^2/MtCO_2$, assuming a volumetric flow rate of $\geq$ 58,000 m^3/s)[17]. With the aim of capturing and sequestering of CO_2, while avoiding competition for grid-energy and land-use, the Canadian Solid Carbon project is working towards the development of an offshore wind-powered CO_2 DACCS system, with CO_2 storage in offshore basalt at Cascadia Basin, off the west coast of British Columbia, Canada. To the best of our knowledge, such an initiative has not been considered before, and no previous studies exist. However, possible offshore wind powered-DACCS system configurations share many commonalities with typologies proposed in offshore wind Power-to-X (P2X) applications[67–69]. For example, a DAC plant may be placed onshore or offshore and depending on the distance from the CO_2 injection site, pipes or vessels can be used to transport the CO_2. Moreover, the offshore wind farm can be located independently from the DAC plant, co-located with it, or even physically integrated together. These solutions, represented in **Figure 2.1**, are being analysed in a larger multi-disciplinary analysis and optimisation framework. This paper, however, specifically considers one of these configurations in-depth, the so-called “offshore” modular solution.

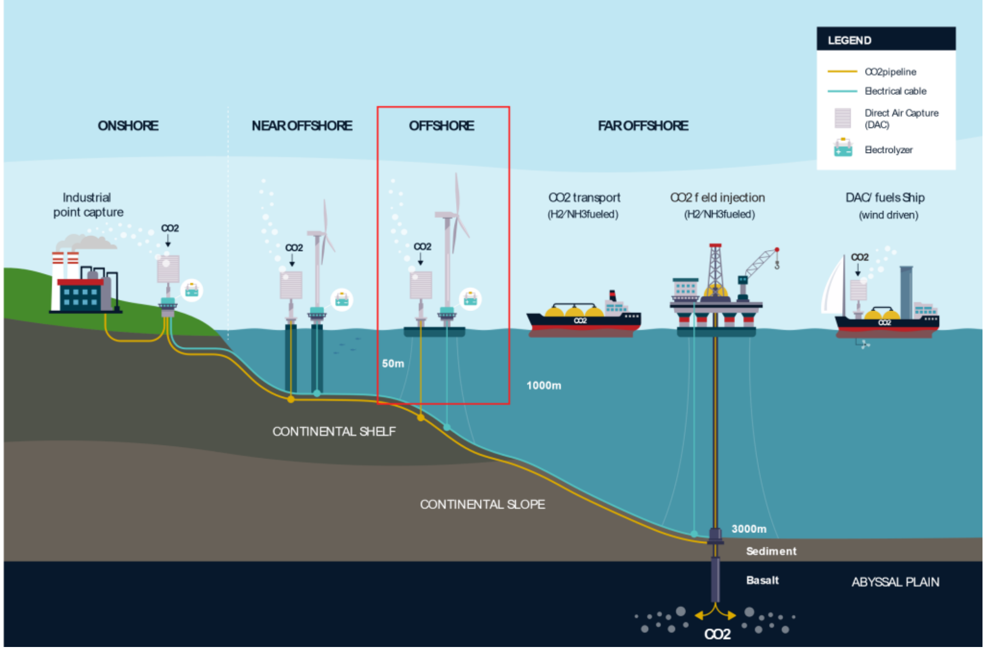

Figure 2.1. Possible offshore wind powered-DACCS system configurations envisioned in Solid Carbon (with permission from Ocean Networks Canada). The configuration developed further in this work appears squared in red.

2.1.2. System configuration

2.1.2.1. Centralised and decentralised typologies

In the "offshore" configuration, the entire DAC system may be placed offshore on one or a few floating platforms powered by nearby wind turbines, an option we refer herein as centralised. Alternatively, the DAC units may be integrated with and powered by co-located wind turbines, a configuration we refer to as decentralised (modular). In both configurations, the captured CO_2 may later be transported via vessel or pipe to the injection site, but this lays outside the scope of this paper. The merits and limitations of both centralised and decentralised scenarios have been discussed in various offshore wind P2X studies[67–69], with some transferable conclusions applicable to the offshore wind-powered DAC system. For example, centralisation of DAC units onto one large or several floating platforms may bring some cost savings resulting from reduced installation, operations and maintenance (O&M), and decommissioning expenditures. Certainly, by having all DAC infrastructure centralised in a smaller area, the required personnel, vessel transportation time fees and fuel consumption would be reduced. However, a decentralised configuration could also bring benefits:

- Increased flexibility and expandability because of an almost modular configuration[69]. Further, as more modular units are produced, the greater the cost reductions as a result of economies of scale, similar to those of historical solar developments.
- Key to the decentralised scenario is the reduced infrastructure required to house the DAC system. CO_2 direct air capture has not only a considerable capture area perpendicular to airflow (0.037–0.25 $km^2/MtCO_2$)[17], but an even larger plan-view projected footprint (0.7–5.3

km^2/MtCO$_2$)[xv], ref.[70]. Because the decentralised configuration may be physically integrated together with offshore wind, there is no need for additional offshore platforms to house the DAC units. Since both systems are co-located, overlapping their respective O&M scheduling and support infrastructure (e.g. vessels, technicians) may lead to significant operational cost reductions.

- Potential for time-saving benefits, whereby individual unit down-time and repairs do not stop completely the process of CO_2 capture.

Due to these various considerations and inspired by previous detailed offshore wind P2X initiatives which opted for a decentralised configuration[xvi], we decided to co-locate and physically integrate both DAC and offshore wind systems in a decentralised configuration (see **Figure 2.3** for physical embodiment).

2.1.2.2. Fixed-bottom and floating support structures

Beyond water depths of 50-80 m, conventional fixed-bottom wind turbines become prohibitively expensive, and floating offshore wind turbines (FOWTs) have emerged as an economical alternative in deep waters. Despite FOWTs now reaching full commercial maturity, we chose FOWTs for our offshore wind powered-DACCS system (referred to as FOWT-DAC system) partly because of the limited availability of shallow water areas around Cascadia Basin, and partly to minimise interference with local shipping lanes and other sea users. We believe this argument holds true for many other offshore basalt reservoirs worldwide with potential to apply our concept[71].

Different floating platform types which were inherited from the oil and gas (O&G) industry may be used for the FOWT-DAC system. While adjustments to accommodate the DAC system on-board can most likely be made with little difficulty in all three traditional platform types (i.e. semi-submersible, spar and tension-leg platform, or TLP), the semi-submersible platforms are the most straightforward option. Indeed, unlike spars or TLPs, semi-submersibles typically have a large waterplane area which they rely on for floating stability. This space can easily and inexpensively be made available for use by the DAC system by simply adding a solid deck across the platform's radial columns. Furthermore, the deck height can be modified to prevent any wave splashing onto the on-board equipment, and the whole platform can be fully assembled in port and towed to the site. For these reasons and supported by the aforementioned offshore wind P2X Dolphyn Project[67], we decided to mount our DAC system on a FOWT semi-submersible (**Figure 2.3**).

2.1.3. Objectives

In this paper we introduce an offshore wind-powered DAC system assembled on-board a FOWT platform. In previous offshore wind P2X studies which opted for a similar layout configuration[67], the inertial properties of the added P2X system were negligible when compared to those of the floating

---

[xv] This area is taken by the DAC collectors directly, but consideration should also be given for the spacing required between collectors to ensure an optimal operation (i.e. with sufficient aerial mixing to maintain a CO_2 concentration as close to the atmospheric as possible to limit energy expense).

[xvi] E.g. Dolphyn Project, in which the industry partner ERM is integrating a hydrogen production on-board the deck of the WindFloat floating wind turbine semi-submersible[67].

platform. In contrast, and as discussed in section **2.2**, the weight of the on-board DAC system may represent 3-16% of the floating structure mass and therefore merits its own analysis if we are to ensure the stability and safe optimal operation of the FOWT-DAC platform. To guarantee the integrity of the DAC units, it is also necessary to model the system against possible environmental effects, with special attention to wave splashing. Additionally, loads on structural components, such as blades, nacelle, and moorings, are computed for different environmental conditions and compared to the loads experienced by the reference FOWT without the DAC system.

Summarising, this work is focused on the most critical elements of design analysis of the FOWT-DAC system. The objectives are to investigate the potential effects that the addition of the DAC units would produce on the dynamics of the floating platform with the aim to de-risk the concept on a deeper technical level. This paper therefore complements and informs the systems-level optimisation undertaken by the Solid Carbon team. Future work will extend the individual platform work to array configurations including CO_2 riser design and integrity verification.

2.1.4. Paper outline

The paper is organised as follows: section **2.2** introduces the reference FOWT concept used, the DAC device and ancillary system components, and shows how the integrated FOWT-DAC designs look. Section **2.3** describes the methods followed to analyse the floating stability and wave splashing on the deck of the FOWT-DAC system, and defines the specific environmental and design load conditions used in this work. Section **2.4** presents and discusses the results of this paper; it begins by analysing the floating stability and hydrodynamic database (i.e. hydrodynamic coefficients, rigid-body natural frequencies, and wave-induced response amplitude operators), and follows by assessing potential wave splashing. It concludes with examining the loads and displacements of different system components. Finally, section **2.5** summarises the findings of this paper.

2.2. Design

In this section, we introduce the two main components of the FOWT-DAC system: the FOWT platform and DAC device. The role of ancillary systems, comprised of energy storage, CO_2 compressor, and CO_2 storage is also mentioned. The system is designed for three scenarios (low, mid, and high) accounting for possible ranges of project variables, such as annual electricity production and number of DAC units, and different equipment sizes, such as CO_2 storage capacity. This is intended to account for project uncertainties and to enhance the usefulness of our results by providing a broader solution space.

2.2.1. Floating offshore wind turbine

The University of Maine (UMaine) VolturnUS-S reference FOWT design coupled with the International Energy Agency (IEA) 15 MW reference wind turbine (RWT) is selected[72,73]. At the time of writing this, the IEA 15 MW RWT atop the UMaine VolturnUS-S is the largest published reference design, although global efforts are already looking at turbine ratings of 22 MW. From now on, a shortform we use to refer to the IEA 15 MW RWT atop the UMaine VolturnUS-S is *reference design*. **Table 2.1** shows selected properties from the reference design. Note that the platform includes two types of ballast: a solid fixed of 2,540 tons placed inside the radial columns, and a seawater variable ballast of 11,300 tons inside the lower pontoons structure. Both ballast types are evenly distributed inside their structures to guarantee the platform's centre of gravity lays somewhere along the tower's vertical axis.

Table 2.1. Reference design properties[72,74].

Parameter	Units	Value
RNA mass	tons	991
Tower mass	tons	1,263
Moorings pretension	kN	6,065
Mooring line breaking strength	kN	22,286
Hull steel mass	tons	3,914
Ballast mass (fixed/variable)	tons	2,540/11,300
Fixed ballast density	kg/m^3	5,000
Floater mass	tons	17,839
Total system mass	tons	20,711

2.2.2. Deck

The reference design does not have a deck for the DAC system; however, one can be easily incorporated by connecting the three radial columns (as similarly suggested by refs.[67,69]). The addition of the deck gives us an approximate usable floor area of 4,600 m^2. The weight and distribution of the DAC equipment, given in section **2.2.5.2**, determine the structural requirements of the deck, which itself has an approximate weight of 34 tons which could be optimised in future work to integrate further with the DAC.

2.2.3. Direct air capture

The unit DAC adopted is representative of Climeworks' modular technology[75]. Each CO_2 modular collector has a nominal capacity of 500 tCO_2/year, with a capture efficiency of 90% and requires 2,006 kWh of energy per ton of CO_2 absorbed[76,77]. It is assumed to have roughly the same size and weight as a typical shipping container (12.19 m long, 2.44 m wide, and 2.90 m tall), with a mass of 4.4-25.9 tons, respectively. The mass range given reflects the uncertainty in the solid sorbent used per collector to trap the CO_2[78].

2.2.4. Ancillary system

The ancillary system includes additional equipment necessary to operate the FOWT-DAC. Firstly, to maximise the annual CO_2 capture, energy storage is required to balance out wind power fluctuations. To that end, lithium-ion batteries and hydrogen fuel cells can be used to deal with short- and longer-term variations, respectively. Secondly, the captured CO_2 may be transported via vessel or pipe to the injection site. Although this process lays outside the scope of this paper, some amount of on-board CO_2 storage is assumed to accommodate either option. Thirdly, regardless of the CO_2 transportation mechanism, a CO_2 compressor is required before storing or piping the captured CO_2 to reduce space claims, and achieve the required piping pressure and CO_2 phase.

2.2.5. Integrated FOWT-DAC system

2.2.5.1. Sizing

Sizing and technical specifics are determined following the process outlined in **Figure 2.2**. We started with Solid Carbon's nominal per-array annual CO_2 capture goal (1 $MtCO_2$/year), the FOWT and DAC technology characteristics as defined above, and the deployment site capacity factor to determine the number of Climeworks' CO_2 collectors per platform. This is then used to estimate the specifics of the ancillary system[xvii]. The same nominal platform may then be scaled to other per-project array sizes.

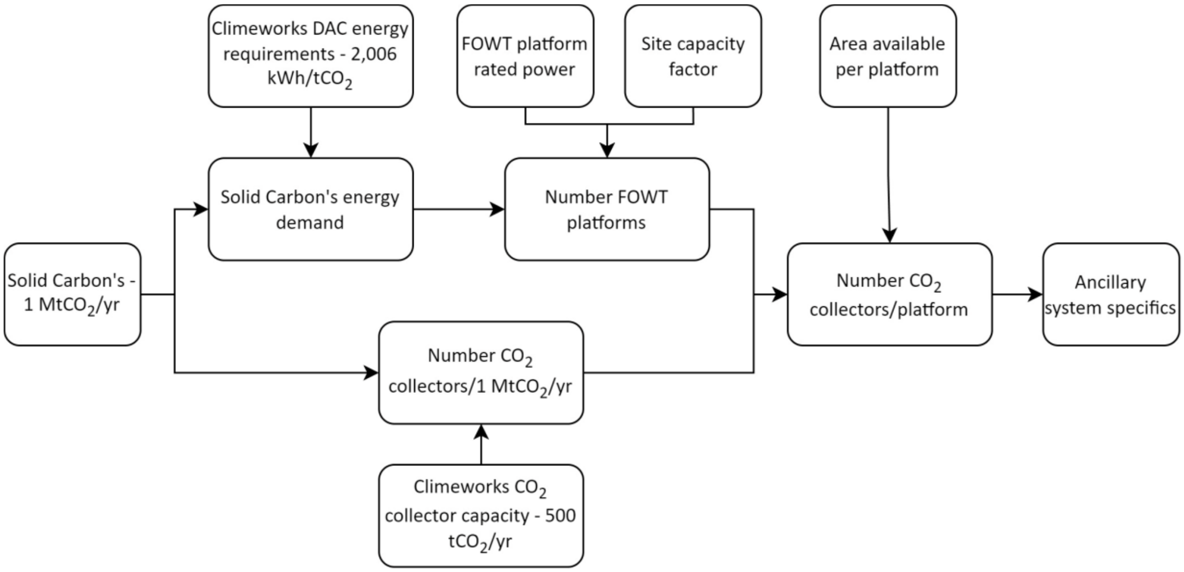

Figure 2.2. Process followed to determine the size of the DAC and ancillary system per platform.

The analysis is done for three scenarios (low, mid, high) and benchmarked against the reference FOWT design. The main configuration differences between these scenarios can be seen in **Table 2.2**. For example, each scenario has a different wind capacity factor, spanning 53% to 65%, calculated by from the nominal Solid Carbon site's average annual wind resource (section **2.3.5**). This range determines the annual energy production and limits the amount of CO_2 that can be captured by one FOWT-DAC platform. The estimated additional mass from the DAC and ancillary system is 523-3,278 tons, depending on the scenario, which represents 3-16% of the reference design mass. The mass contribution of each component varies between scenarios; however, it is worth noting that the largest variations are seen for the sorbent mass and CO_2 storage.

[xvii] For further details about the ancillary system, see Appendices, section **2.6.2. Ancillary system**.

Table 2.2. Main DAC and ancillary system configuration for the low, mid, and high scenarios.

Variables/Scenarios	Units	Low	Mid	High
Wind capacity factor	-	53%	58%	65%
Number of CO$_2$ collectors/platform	-	63	69	78
Horizontal surface taken by the CO$_2$ collectors	m^2	1,881	2,058	2,307
Annual captured CO$_2$/platform	tCO$_2$/year	31,620	34,603	38,779
CO$_2$ collector mass (without sorbent)/platform	tons	247	270	302
Sorbent mass per CO$_2$ collector	tons	0.5	11.4	22.2
Sorbent mass/platform	tons	32	786	1,724
CO$_2$ storage capacity (days' worth of production)/platform	days	1	4	7
CO$_2$ storage[1]/platform	tons	137	405	1,076
Battery capacity/platform	kWh	5,898	6,454	7,233
Battery banks mass/platform	tons	91	122	152
H$_2$ electrolyzer units and storage mass[xviii]	tons	2	2	2
CO$_2$ compressor power	kW	412	451	506
CO$_2$ compressor mass	tons	14.6	17.1	21.2
Total DAC and ancillary services mass	tons	523	1,603	3,278
Fraction of added mass with respect to reference design	-	3%	8%	16%
Total FOWT-DAC and ancillary system mass	tons	20,511	20,611	20,711

2.2.5.2. DAC layout

Adding a deck which connects the three radial FOWT columns, DAC units are placed so that the overall horizontal position of the centre of gravity is preserved – located along the tower vertical axis. The same strategy is applied to the ancillary system (mainly batteries, CO$_2$ and H$_2$ storage, and CO$_2$ compressors), although distributed inside the radial columns. The rationale is to counteract part of the DAC equipment placed on deck and to keep the system's vertical centre of gravity (z_G) as close as possible to the original reference design. To determine the available space inside a radial column, each hollow column was assumed to have a wall thickness of 0.05 m, as stated in ref.[74]. The volume occupied by the fixed ballast per column, assumed to have a cylindrical-like shape, was taken as 169 m^3, ref.[74]. Finally, to balance the addition of the DAC and ancillary system and preserve the overall hydrostatic similarity with the reference design, a corresponding amount of variable ballast was removed for each scenario.

The layout of the DAC and ancillary system units on the floater deck and radial columns for the different scenarios (low, mid, and high) is shown in **Figure 2.3** and **Figure 2.4** (note this may be subject to further refinement in the future). Recall that each DAC unit has the same dimensions as a shipping container, 12.19 m long, 2.44 m wide, and 2.90 m tall. To optimise the limited onboard space, most CO$_2$ collectors are placed in rows of five to six units (depending on the scenario) and two stories high. The smaller rows of one and three DAC units are only one story high. For each scenario (low, mid, and high), the innermost DAC row (i.e. closest to the tower) is 20 m away from the tower's vertical centreline. The distance between DAC rows is equal to 2.44 m, which is also the distance left between DAC units along the same row.

[xviii] Includes mass of storage tanks. See Appendices, section **2.6.2. Ancillary system**, for further details about the CO$_2$ and H$_2$ tanks.

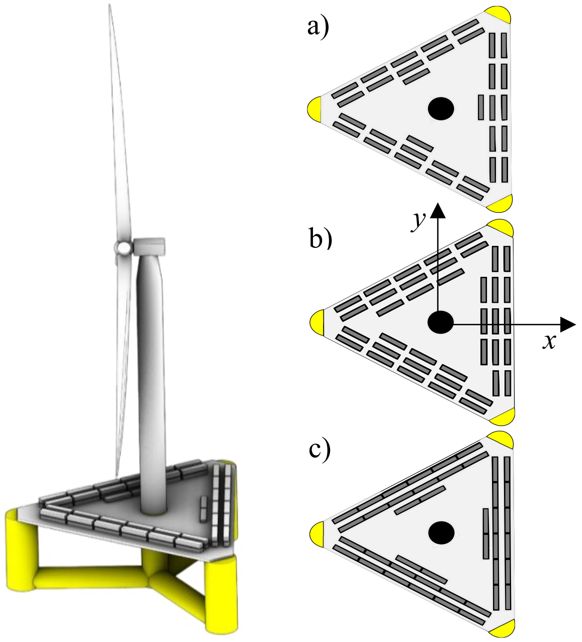

Figure 2.3. Left: FOWT-DAC platform with installed deck connecting the three radial columns. Right: top DAC layout view for the a) low, b) mid, and c) high scenarios. Note that the rows with five and six CO_2 collectors are two stories high.

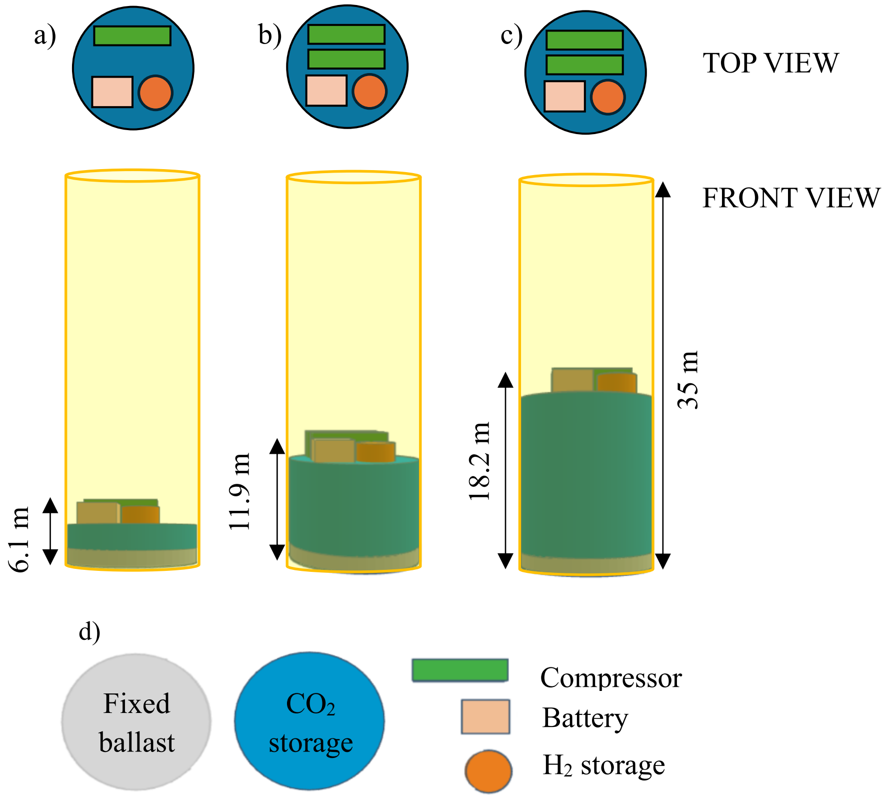

Figure 2.4. Ancillary system layout per radial column (in yellow) for the a) low, b) mid, and c) high scenarios, and d) shape and colour legend of each ancillary system unit.

2.2.6. Inertial properties

Each scenario ensured that the FOWT-DAC platform's z_G was as close as possible to the reference design. To estimate the system's z_G, we determined the location of each component and subcomponent's z_G, assuming for those elements where we could not find data that their z_G was at their geometric centre. For example, from ref.[72], we know the reference design floater's z_G=-14.94 m and that it is comprised of three radial columns, a central one, and three pontoons and three struts, connecting the radial columns with the central at the base and at the top, respectively. Moreover, each radial column includes 847 tons of fixed ballast, and each pontoon has over 3,766 tons of seawater ballast. Because the inner weight of these columns changes with respect to the reference design and between scenarios, the columns' z_G and thus floater's z_G also do, **Table 2.3**.

Table 2.3. Inertial and hydrostatic properties of the reference, low, mid, and high case scenarios. The percentage differences with respect to the reference design are written in parentheses next to the result where relevant.

Parameter	Units	Reference	Low	Mid	High
DAC mass	tons	-	278	1,056	2,026
Ancillary system mass	tons	-	245	546	1,252
Draft	m	20	19.57	19.79	20
DAC z_G	m	-	18.34	18.12	17.90
Radial columns z_G	m	-15.69	-14.26	-14.48	-14.69
Pontoons z_G	m	-17.93	-17.57	-18.03	-18.63
Floater z_G	m	-14.94	-16.45	-17.03	-17.61
Total z_G	m	-2.66	-2.74	-2.74	-2.61
KG	m	18.77	18.26	18.48	18.82
Platform z_B	m	-13.63	-13.19	-13.41	-13.63
Moment of inertia I_{xx}	kg·m^2	1.250E+10	1.265E+10 (1.2%)	1.333E+10 (6.2%)	1.479E+10 (15%)
Moment of inertia I_{yy}	kg·m^2	1.250E+10	1.241E+10 (0.7%)	1.287E+10 (2.9%)	1.566E+10 (20%)
Moment of inertia I_{zz}	kg·m^2	2.367E+10	2.364E+10 (0.1%)	2.399E+10 (1.3%)	2.754E+10 (14%)

Aside from impacting the global location of the system's z_G, the addition of the DAC and ancillary system also affects its rigid body mass distribution. To account for this, we computed the tensor of inertia for the different scenarios. Firstly, to simplify the calculation of the DAC and ancillary system equipment, we assumed each had either a cylindrical or cubic shape. Secondly, to add the individual contribution from each component to the global tensor of inertia, we applied the parallel axis theorem, which was also used to account for the removed ballast. The resulting global moments of inertias about the centre of gravity (I_{xx}, I_{yy}, I_{zz}) are given in **Table 2.3**. Note that the asymmetry between I_{xx} and I_{yy} is a result of the DAC geometry and mass distribution on the deck, with the DAC units having higher moments of inertia about its transversal axis. The change in displaced volume due to the addition of the DAC and ancillary system masses also changes the platform draft. This is accounted by adjusting the vertical location of the mooring fairleads along the floater. In the results section, the effect of these inertial and hydrostatic changes on the FOWT-DAC rigid-body natural frequencies and wave-induced response amplitude operators (RAOs) are discussed.

2.3. Methods

To verify that the inertial and hydrostatic changes presented in **Table 2.3** have no negative effect on the FOWT-DAC platforms', this work assesses their floating stability. The approach followed is discussed in subsection **2.3.1**. In addition, the method used to study the possible wave splashing on the FOWT-DAC floaters' deck, where the DAC system is located, is explained in subsection **2.3.4**. The environmental conditions at the project site and the modelling framework employed throughout the paper are presented in subsections **2.3.5** and **2.3.6**, respectively. The design load conditions employed to assess the system structural loads and displacements are also given in subsection **2.3.5**.

2.3.1. Floating initial intact stability

To maintain the integrity and ensure the successful operation of our FOWT-DAC system in the ocean environment, the platform's floating stability must be demonstrated. Since the platform operates without a crew on site, and most FOWTs are limited to work at maximum roll and pitch angles of 10°, ref.[79], the scope was limited to initial intact stability[80]. That is, it is assumed the structure has not suffered any significant damage, and the stability is studied under small displacements from its equilibrium position.

2.3.2. Static stability

As a first inexpensive test, we started by studying the stability in the absence of time-varying environmental forces (static analysis). For self-stabilized structures such as our FOWT-DAC semi-submersible, this is checked without including the restoring effects from the moorings[79,80], a condition known as freely floating.

2.3.2.1. Linearized hydrostatic restoring force

For a freely floating body subjected to small displacements (ζ_j) – small enough that the body's submerged volume can be considered constant (V_0) – the total hydrostatic force (moment) can be written as a linear restoring force (moment) with ζ_j, equation (2.1), ref.[81],

$$F_i = (\rho V_0 - m) g \delta_{i3} - \left(m y_{G_0} - \rho V_0 y_{B_0}\right) g \delta_{i4} + \left(m x_{G_0} - \rho V_0 x_{B_0}\right) g \delta_{i5} - \sum_{j=1}^{6} c_{ij} \zeta_j \qquad (2.1)$$

where i = 1, 2, …, 6 refers to the six rigid-body degrees of freedom (DOF): surge, sway, heave, roll, pitch, yaw, respectively. The first three F_i values refer to forces arising from translational motions, and the last three to moments resulting from rotational motions. Seawater density, taken as 1,025 kg/m^3, is represented as ρ, the body's total mass as m, gravity's acceleration as g, Kronecker's delta function as δ_{ij}, the coordinates of the centre of gravity and buoyancy at the undisplaced position as ($x_{G_0}, y_{G_0}, z_{G_0}$) and ($x_{B_0}, y_{B_0}, z_{B_0}$), respectively, and c_{ij} are the coefficients of the hydrostatic stiffness matrix.

In stable equilibrium, for $\zeta_j = 0$, the sum of the forces and moments acting on the body are zero, and the zero-order terms with ζ_j in (2.1) must vanish. This implies that the centre of gravity and the centre of buoyancy must lie along the same vertical line,

$$x_{B_0} = x_{G_0} \tag{2.2}$$

$$y_{B_0} = y_{G_0} \tag{2.3}$$

For equilibrium of the vertical force ($i = 3$), Archimedes principle states that the mass of the body must equal the mass of the displaced fluid,

$$m = \rho V_0 \tag{2.4}$$

Now, let $\zeta_5 = \theta$ be a pure small angular displacement in pitch ($i, j = 5$). After applying expressions (2.2)-(2.4) to it, equation (2.1) becomes,

$$F_5 = -c_{55}\theta \tag{2.5}$$

where the linearized hydrostatic stiffness coefficient in pitch-pitch c_{55} is

$$c_{55} = \rho g V_0 \left[\left(\frac{S_{11}}{V_0}\right) + z_{B_0} - z_{G_0}\right] \tag{2.6}$$

with S_{11} as the waterplane moment. The term inside square brackets in (2.6) is the well-known *metacentric height*, denoted as GM, which allows rewriting (2.5) into its more familiar form in naval architecture,

$$F_5 = -\rho g V_0 GM\theta \tag{2.7}$$

This linearized approach developed in (2.1) to (2.7), valid for small displacements, is consistent with assumptions made in potential flow theory (PFT) and linear (Airy) water-wave theory, which most radiation/diffraction solvers (e.g. WAMIT, NEMOH, or HAMS) employ to model ocean waves and wave-structure interactions and to compute c_{ij}. Further, note that the operational regime of FOWTs is typically restricted to maximum roll and pitch rotations of 10°, ref.[79]. This helps to maintain structural integrity, keeping proper clearance between the rotor blades and other system elements, and ensuring optimal levels of power production. Consequently, one may surmise that the (linearized) small angle modelling approximation used by these solvers may suffice to accurately represent the hydrostatic force (moment) in the range of working conditions for our FOWT-DAC. However, this depends on whether the change from its (equilibrium) submerged volume is negligible within this range of angles. One way to verify this is to compare the restoring moment computed using the undisplaced volume (equation (2.7)) with the one calculated using the instantaneous wetted surface, S_B (equation (2.8))[81]. The latter method involves making use of some higher fidelity software, like DSA Ocean's ProteusDS™ [82], which sums the hydrostatic pressure over S_B.

$$F_i = -\rho g \iint_{S_B} (\boldsymbol{r} \times \boldsymbol{n}) z dS, \qquad i = 4, 5, 6 \tag{2.8}$$

In equation 2.8, $\boldsymbol{r}$ is the position vector from the body's centre of flotation to the surface element dS, $\boldsymbol{n}$ is the normal vector to dS pointing outside the body, and z is the vertical coordinate to the surface element dS. The centre of flotation is the body's point of rotation when subjected to only horizontal moments[81].

The comparison for the hydrostatic restoring moment in pitch for the reference design is presented in **Figure 2.5**. To quantify their similarity, the normalized root mean square error (NRMSE) was calculated using the mean of the values given from equation 2.8. Both curves are notably similar (NRMSE = 0.016%), with slight differences towards larger angles, which is expected in the small angle approximation. This demonstrates that, with a negligible margin of error, we can apply the linearized hydrostatic stiffness coefficients to determine the hydrostatic force (moments) of the reference design for its operational conditions.

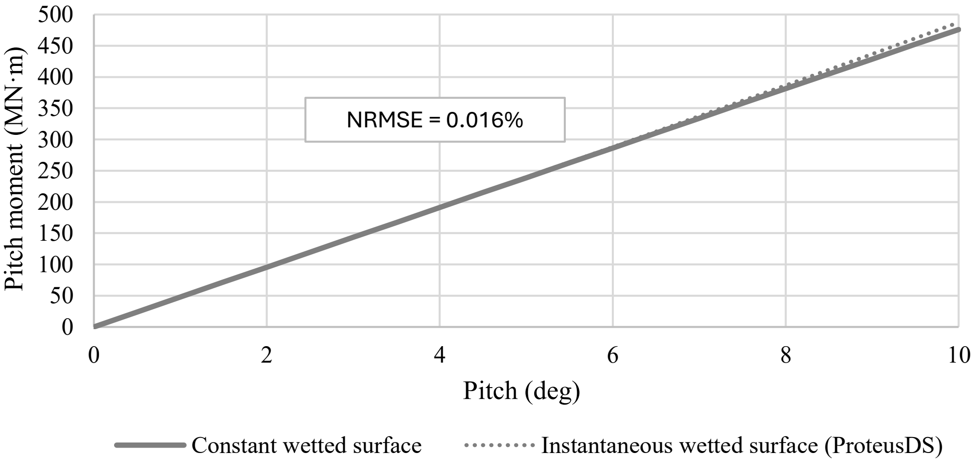

Figure 2.5. Pitch hydrostatic restoring moment as the reference design platform pitches for the range of operational angles. The blue curve is obtained with equation 2.7, while the orange curve is computed with equation 2.8 using ProteusDS™.

2.3.2.2. Stability criterion

A common way to assess the stability of a floating body is through a curve of stability[80], in which the hydrostatic restoring moment (also known as righting moment) is plotted and compared with the environmental heeling moment for a range of angles. If the environmental forces can be assumed to be steady (i.e. static stability), the criteria determining the body's stability under a heeling force are simply derived by comparing the righting and heeling moments. Moreover, as mentioned before and following ref.[79], we use 10° as the serviceability limit for our FOWT cases.

As advised in ref.[80], the platform's stability must be checked along its least stable or critical heeling axis, along which the platform yields the minimum righting moment. In the dynamic case, the righting moment is a function of the mass moment of inertia, the added mass and the radiation damping moments of inertia. Because the platform has surge-sway plane symmetry, the added mass (radiation damping) matrix, which in general is a 6x6 symmetric matrix, only has 12 non-zero, independent coefficients. The crossed terms between (surge, heave, pitch) and (sway, roll, yaw) disappear, and the remaining non-zero crossed terms are then coupled motions in different DOFs. Ultimately, these complex couplings are the mechanisms behind the existence of the critical heeling axis for our platform.

We determined the critical heeling axis by simulating the FOWT platform in OpenFAST and checking its motion with co-directional wind and waves at different orientations (0° to 120° with respect to the X axis as defined in **Figure 2.3**, in 15° intervals). We ran simulations of 600 s with six wave seeds for every orientation. Note that due to the platform geometry, the 0°, 120° and 240° cases are identical. For the reference design, it was found that the platform experiences greater heeling angles (i.e. exhibits minimum righting moment) when the external forces are directed along the 45° line. The same was found for the low, mid, and high case scenarios.

Because the rotor's thrust is the largest contributor to the platform's heeling motion, and it is maximum at the rated wind speed (U_{rated}) when the blades are fully engaged, we computed the wind heeling moment (M_w) at rated conditions for different heeling angles (θ), equation (2.9):

$$M_w = \frac{1}{2}\rho_{air} C_t A_{rotor} U_{rated}^2 r_{flot} \cos\theta \qquad (2.9)$$

where $\rho_{air} = 1.225\ kg/m^3$ is the density of air, $C_t = 0.769$ is the rotor's thrust coefficient at rated conditions[xix], $A_{rotor} = \pi R^2$ is the swept area of the rotor ($R = 120\ m$), and r_{flot} is the moment arm (calculated from the rotor hub height to the centre of flotation, at mean sea water level).

2.3.3. Dynamic stability

Environmental forces are dynamic in nature, with wind and waves fluctuating over time. In addition, the dynamic movement of massive bodies presents unique phenomena which cannot be accounted in a static analysis but that still play an important role in the stability of a floating body, such as the rotational momentum of a FOWT pitching back and forth. To account for these effects, the last part of the stability analysis runs a set of dynamic simulations using OpenFAST. Note that, in contrast to the method followed in the static analysis, in this section the heeling effect from the waves is accounted, as well as the restoring effect from the mooring lines. This was decided to better reflect the reality of moored FOWTs in operating conditions, which is, after all, what we are concerned with.

2.3.4. Wave splashing – air gap

In the absence of waves, the still water air gap (freeboard) $a_0(x, y)$ is defined as the distance between the still water level (SWL) and the under-deck of the platform at horizontal position (x, y) when the floater is in normal trim and in the absence of environmental conditions, **Figure 2.6 a).**

[xix] Withdrawn from the National Renewable Energy Laboratory GitHub site for the IEA 15 MW RWT: https://github.com/NREL/turbine-models/blob/master/Offshore/IEA_15MW_240_RWT.csv

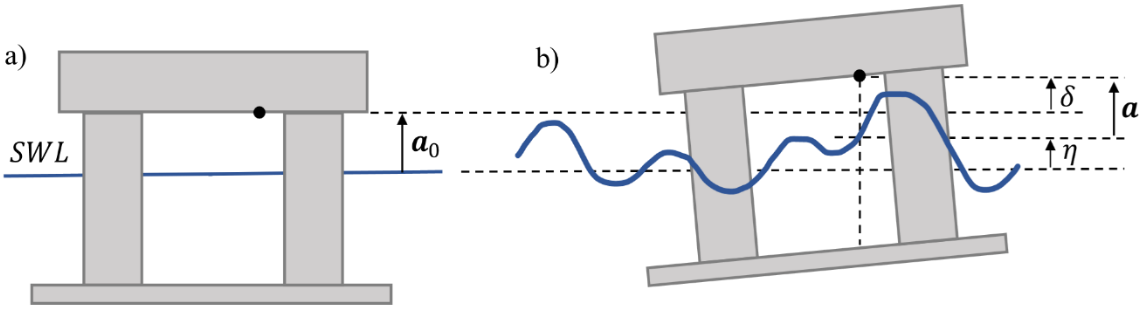

Figure 2.6. Air gap definition in a) still waters, and b) irregular seas. Reproduced from ref.[83].

An insufficient air gap may lead to an undesired wave impact on the deck's equipment (i.e. DAC system) for which it may not be designed for[xx]. Conversely, an excessive air gap may reduce the platform's stability, hinder global performance, reduce payload capacity, and increase capital costs. In the presence of wind and waves, the instantaneous air gap, $a(x, y, t)$, depends on the free surface elevation, $\eta(x, y, t)$, and the vertical motion of the floater, $\delta(x, y, t)$, at the same horizontal position (x, y), **Figure 2.6 b)**.

$$a(x, y, t) = a_0(x, y) - [\eta(x, y, t) - \delta(x, y, t)] \tag{2.10}$$

Note that to avoid all deck wave impacts, $a(x, y, t)$ must be always positive. In linear theory, the free surface elevation is approximated as an Airy wave, which is sufficient to explain low steepness waves and small body motions around its mean position. When looking at the air gap between SWL and the floating body, however, the non-linear, asymmetric wave effects become too important to be ignored. Indeed, steep moderate sea states are more likely to cause wave splashing than non-steep extreme sea states. To model these wave non-linearities, higher-order wave methods are normally employed. In the absence of these, alternatively, it is common practice to use a correction factor (α) accounting for non-linear incident and diffracted wave asymmetry and run-up effects[84], equation (2.11).

$$a(x, y, t) = a_0(x, y) - [\alpha\eta(x, y, t) - \delta(x, y, t)] \tag{2.11}$$

When assessing the air gap, DNV GL recommends looking at the steep wave part of the 100-year return period (RP) significant wave height-peak period (H_s-T_p) contour[84]. Given that existing site metocean data does not extend that far in the past, a typical way to determine these extreme sea states based on comparatively short-term data is through IFORM, or Inverse First Order Reliability Method[85].

The Appendices section **2.6.3** shows the derivation of the 100-year RP contour through IFORM (subsection **2.6.3.1**) and the resulting steep extreme sea state obtained from the wave steepness criterion curve[86] (subsection **2.6.3.2**). To complete the set of metocean conditions for the

---

[xx] Given that we are not aware of previous DAC systems specifically designed to operate offshore, here it is assumed that all wave impacts on the platform must be avoided.

wave splashing analysis (given in **Table 2.5**), a wind regime reflecting the same probability of occurrence was calculated[84], yielding a mean wind speed of 47.5 m/s.

2.3.5. Environmental conditions

2.3.5.1. Site description

Cascadia Basin, off Vancouver Island (British Columbia, Canada), has been highly studied and characterised as a site for CO_2 storage in deep ocean basalt[87,88]. It has also been selected by Solid Carbon as a test site for a demonstration project in 2025. For these reasons, here we also chose Cascadia Basin (-125.59° longitude and 48° latitude, 200 m water depth) to study our FOWT-DAC platform stability and performance.

2.3.5.2. Metocean data analysis

Wave data (significant wave height, peak period, and wave direction) generated by the Wave Watch III global wave model was facilitated by the Pacific Regional Institute of Marine Energy Discovery and obtained from the Marine Energy Resource Atlas Canada[89]. Two horizontal wind speed components at 10 m height were produced by fifth generation ECMWF reanalysis ERA5 and downloaded from the Copernicus program Climate Data Store[90]. Both datasets covered the period from January 1st, 2004, to December 31st, 2016.

To convert the mean wind speed from 10 m to the reference design rotor hub height (at 150 m), we used the power law with a shear exponent of 0.14, ref.[91]. To reduce the burden of environmental variables to deal with, following ref.[92], we defined the wind-wave misalignment as the difference between the wind and wave directions. Then, we binned the data to produce conditional probabilities of mean wind speed, significant wave height, peak period, and wind-wave misalignment (see binning conditions in **Table 2.4**).

Table 2.4. Metocean data binning conditions.

Parameter	Units	Range	Bin width
Mean wind speed	m/s	4-24	2
Significant wave height	m	0.5-10.5	0.5
Peak period	s	3.5-23.5	1
Wind-wave misalignment	-	-180° to 180°	10

Finally, following ref.[93], the conditional probabilities allowed us to define normal, severe, and extreme sea states, which are commonly used in the definition of design load conditions (DLCs).

2.3.5.3. Design load conditions

The selection of an appropriate set of DLCs depends on the purpose and magnitudes of interest. On one hand, we want to assess the floating stability of the FOWT-DAC platform; for that, we take DLCs 1.3, 6.1 and 6.2 as previously done by ref.[79]. In DLCs 1.3, the turbine is running and operating in normal power conditions, while in DLC 6.1 and 6.2, it is parked and experiencing extreme 50-year wind and wave events. Further, in DLCs 1.3, 6.1 and 6.2, extreme turbulence conditions produce errors in the yaw controller which causes deviations from optimum operating conditions. To represent this situation, initial yaw misalignments with respect to the wind direction are set and the RNA yaw DOF is disabled in OpenFAST.

On the other hand, we are interested in studying maximum dynamic values of components of typical concern in FOWT design – these are tower bending moment, blade tip displacement, fairlead tension, platform excursions – and ensuring their values do not diverge dangerously from the reference design. Looking at ref.[72], we can see that, in addition to the DLCs listed above, DLCs 1.4, 1.6, and 2.3 resulted in extremes for our magnitudes of interest. DLC 1.4 represents normal power production transient events in the life of the turbine; DLC 1.6 is used to simulate normal operational conditions with normal wind turbulence (NTM) but under severe sea states (SSS). In DLC 2.3, the turbine is also operating but an extreme gust causes a temporary power loss.

Our analysis (**Table 2.5**) includes all the aforementioned DLCs in addition to the sea state determined for the wave splashing analysis in section **2.3.4**.

Table 2.5. Design load case matrix.

DLC	Wind condition	WSPD (m/s)	Wave condition	H_s (m)	T_p (s)	Settings
1.3	ETM	4	NSS	2.14	5.93	RNA +/- 10°
		6		2.16	5.95	
		8		2.14	5.93	
		10		2.11	5.89	
		12		2.13	5.92	
		14		2.36	6.23	
		16		2.72	6.69	
		18		3.42	7.50	
		20		4.10	8.21	
		22		4.79	8.87	
		24		5.79	9.76	
1.4	ECD+/-R-2.0	8	NSS	2.14	5.93	Rotor azimuth: 0°, 30°, 60°, 90°
	ECD+/-R	10		2.11	5.89	
	ECD+/-R+2.0	12		2.13	5.92	
1.6	NTM	4	SSS	3.47	7.55	
		6		3.70	7.80	
		8		3.92	8.03	
		10		4.22	8.33	
		12		4.58	8.68	
		14		4.86	8.94	
		16		5.20	9.25	
		18		5.68	9.66	
		20		6.18	10.08	
		22		6.74	10.53	
		24		8.59	11.88	
2.3	EOG	8	NSS	2.14	5.93	Rotor parked and pitched after gust
		10		2.11	5.89	
		12		2.13	5.92	
		24		5.79	9.76	
6.1	EWM 50 yr	47.5	ESS,50	11.83	13.95	RNA Yaw +/- 8°
6.2	EWM 50 yr	47.5	ESS,50	11.83	13.95	RNA Yaw +/- 180°
Air gap	EWM 50 yr	47.5	Steep ESS,100	6.49	7.91	

2.3.6. Modelling

To model the FOWT-DAC platform, we first compute the radiation/diffraction hydrodynamic coefficients of the floating structure for each of the scenarios (low, mid, and high) using the opensource potential flow solver HAMS[94]. These are then inputted to OpenFAST and are run for the DLC matrix (**Table 2.5**). To quantify impacts arising from the DAC and ancillary systems, the results of the FOWT-DAC platform for each scenario are benchmarked against the reference design.

Note that to reduce the complexity of the FOWT-DAC platform modelling, we neglect aerodynamic drag effects from the DAC system itself. Although non-intuitive, this simplification is appropriate since the drag from the rotor and tower were calculated as more than four orders of magnitude greater than the drag from the DAC contactors. In addition, the definition of the UMaine VolturnUS-S in the OpenFAST reference files from the IEA Github repository[xxi] does not model the pontoons as filled members. Basically, the seawater ballast is not accounted as a dynamic mass within the pontoons' compartments and it only contributes to the system's inertial properties through its mass distribution (i.e. centre of gravity and moment of inertia).

2.4. Results & discussion

The first two subsections compare the hydrostatics (static and dynamic stability) and hydrodynamics (coefficients, rigid-body natural frequencies, and wave-induced RAOs) from each scenario with the reference design. These comparisons help determine if the proposed FOWT-DAC platform designs (i.e. low, mid, and high case scenarios) preserve hydrostatic and hydrodynamic similarity to the reference design. If so, this implies that the changes we made to adapt the reference design and turn it into different FOWT-DAC platforms was sufficient to ensure the systems' response is kept within the boundaries of the validated reference design performance. The third subsection assesses the wave splashing on the FOWT-DAC platform's deck. Finally, the last two subsections compare the loads experienced by different components of the FOWT platform and the turbine's power performance for each design scenario.

2.4.1. Floating stability

This section presents the results of the static and dynamic stability assessment. Recall that the former does not include, among other phenomena, the restoring effects from the moorings. However, these still serve as a first computationally inexpensive verification of the platform's stability.

2.4.1.1. Static stability

The static stability of the FOWT-DAC platform for the reference design, low, mid, and high scenarios is verified here. The righting and wind heeling (pitch) moments for each case are computed using equations 2.7 and 2.9, respectively, and plotted in a curve of stability in **Figure 2.7.**

[xxi] https://github.com/IEAWindTask37/IEA-15-240-RWT

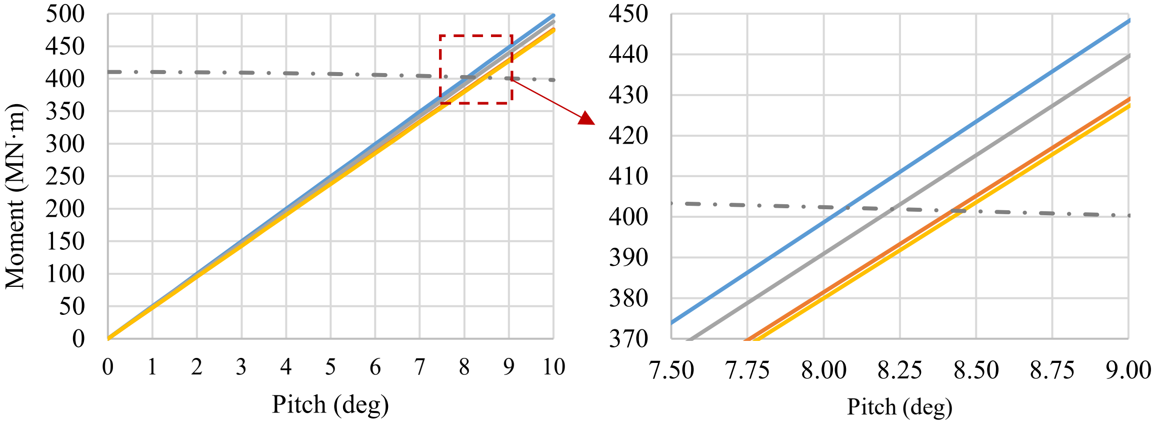

Figure 2.7. Righting moment for the low (blue line), mid (grey line), and high scenarios (yellow line), and benchmarked with the reference design (orange line). The wind heeling moment is shown in a dash-dotted grey line.

As one may observe, the righting moment for the four cases is very similar, with the low and mid scenarios showing a higher restoring capacity. This can be understood by looking at the expression for the hydrostatic stiffness coefficient in pitch (equation (2.6)) and realizing that the ratio between the second moment of area (S_{11}) and V_0 is larger for the low and mid scenarios given their lower submerged volume in comparison to the reference design. In addition, **Figure 2.7** shows that the wind heeling moment crosses the righting moment between 8-8.4°. This means that, under the worst wind conditions causing the maximum rotor thrust (rated wind speed), the reference design and the FOWT-DAC cases manage to remain below 10°, which is the platform serviceability limit we set for FOWTs[79].

2.4.1.2. Dynamic stability

Next, the dynamic stability of the FOWT-DAC platform along its critical heeling axis is examined here for the reference design, low, mid, and high scenarios, and for DLCs 1.3, 6.1 and 6.2, ref.[79]. The average of the extreme platform pitch angle is plotted for these DLCs in **Figure 2.8**. All the simulations show that the maximum pitch angle stays below the 10° operational limit, which means that the reference and the proposed FOWT-DAC designs meet the stability criterion. With the rotor shutdown and the blades pitched out in DLCs 6.1 and 6.2, the platform heeled significantly much less than in DLC 1.3. Notably, the maximum pitch angle for the reference design is consistently the largest, and progressively decreases from the low, to the mid and high cases across DLCs. Given the minor hydrostatic differences between scenarios, we suspect this trend is partly a result of the variations in the pitch moment of inertia. Indeed, as shown in **Table 2.3**, the reference design exhibits the lowest pitch rotational resistance, and increases from there to the low, mid, and high scenarios.

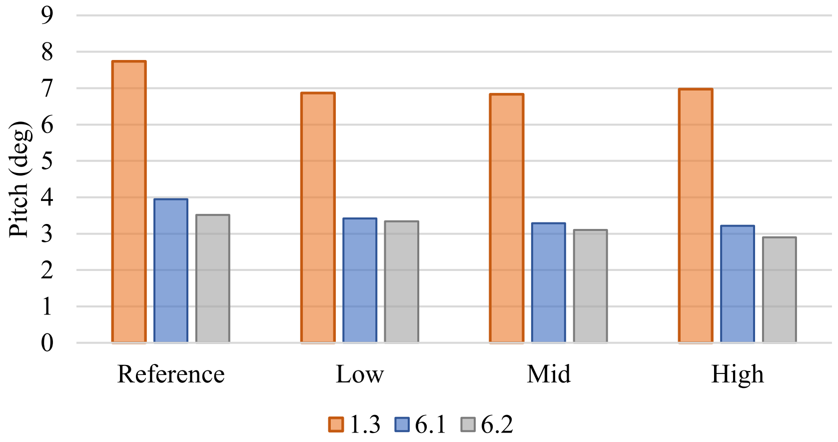

Figure 2.8. Average maximum pitch platform angles for DLCs 1.3, 6.1 and 6.2 for the low, mid, and high scenarios, and benchmarked with the reference design.

2.4.2. Hydrodynamics

2.4.2.1. Hydrodynamic coefficients

Figure 2.9 shows the added mass coefficients in surge-surge (A_{11}). As expected, because the geometry and draft in the reference design and high case scenario are the same, A_{11} also look identical in both. Because the FOWT-DAC platform in the low scenario is not as submerged as in the other cases, its added mass is consistently the lowest across frequencies. Responses for the radiation damping and excitation force coefficients in different DOFs were also analysed and found to be almost identical between scenarios (see **Appendices, Wave splashing**).

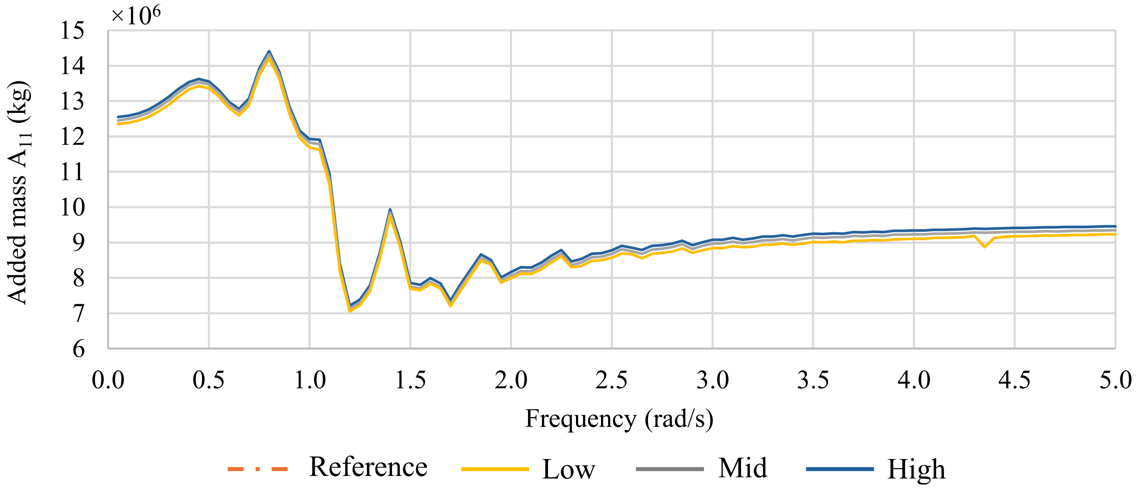

Figure 2.9. Added mass coefficient in surge-surge versus frequency evaluated by HAMS for the low, mid, and high scenarios, and benchmarked with the reference design.

2.4.2.2. Rigid-body natural frequencies

We conduct free decay tests for each rigid-body DOF to compute the rigid-body natural frequencies. Under still environmental conditions, an initial displacement from the platform's equilibrium position is set per DOF, and the natural frequency is calculated by taking the maximum frequency out of the power spectral density over the decay. **Table 2.6** shows the results of these simulations; the values for the three translational DOFs are the same across scenarios and with respect to the reference design, however, slight differences in the three rotational DOFs result from changes in the moments of inertia (**Table 2.3**).

Table 2.6. Rigid-body natural frequencies (Hz) for the low, mid, and high scenarios and compared with the reference design (Ref.).

DOF	Ref.[xxii]	Low	Mid	High
Surge	0.007	0.007	0.007	0.007
Sway	0.007	0.007	0.007	0.007
Heave	0.048	0.048	0.048	0.048
Roll	0.035	0.037	0.037	0.037
Pitch	0.035	0.037	0.037	0.037
Yaw	0.012	0.010	0.012	0.010

2.4.2.3. Wave-induced response amplitude operators

To conclude the hydrodynamic study of the FOWT-DAC platform cases and assess whether these maintain hydrodynamic similarity with the reference design, we present the wave-induced RAOs for the main rigid-body DOFs. Each case was simulated in still air with all structural DOFs disabled except for the six rigid-body ones. Following Ramachandran et al.[95], we ran six seeds of 8,000 s for a two-meter-high white-noise wave spectrum (i.e. with equal wave frequency probability) with periods ranging 0.64-15.9 s. Then, for each DOF, we computed the RAO as the ratio of the cross-spectral density of the platform response and the auto-spectral density of the surface elevation.

The results for the surge, heave, and pitch RAOs are shown in **Figure 2.10.** Because of the zero-degree wave heading and the platform symmetry about the x-axis, the responses in the other DOFs are significantly lower and are therefore not included here. Overall, the peaks shown occur at or very close to the corresponding rigid-body natural frequencies, with notable differences in the pitch RAO consistent with the values seen in **Table 2.6.** In heave, the RAO tends to unity when the wavelengths are much larger than the body dimensions (at low wave frequencies). This causes the system to produce no diffracted waves and thus follow the incoming ones (i.e. output response equal to input signal).

Given that the FOWT system is nonlinear and we used white noise as input waves, the signal amplitude values do not provide a reliable insight about the platform's expected motions. Having said that, one may see that globally all scenarios closely resemble each other and the reference design. This, together with the similarities already presented from the hydrodynamic coefficients and the natural frequencies in the two previous sections, lead us to state that the proposed FOWT-DAC platform designs demonstrate a high degree of hydrodynamic similarity with the reference design.

[xxii] Estimated values following the same procedure as for the low, mid, and high scenarios. Our calculations differ slightly from the values reported in ref.[72], possibly because of different computational methods used.

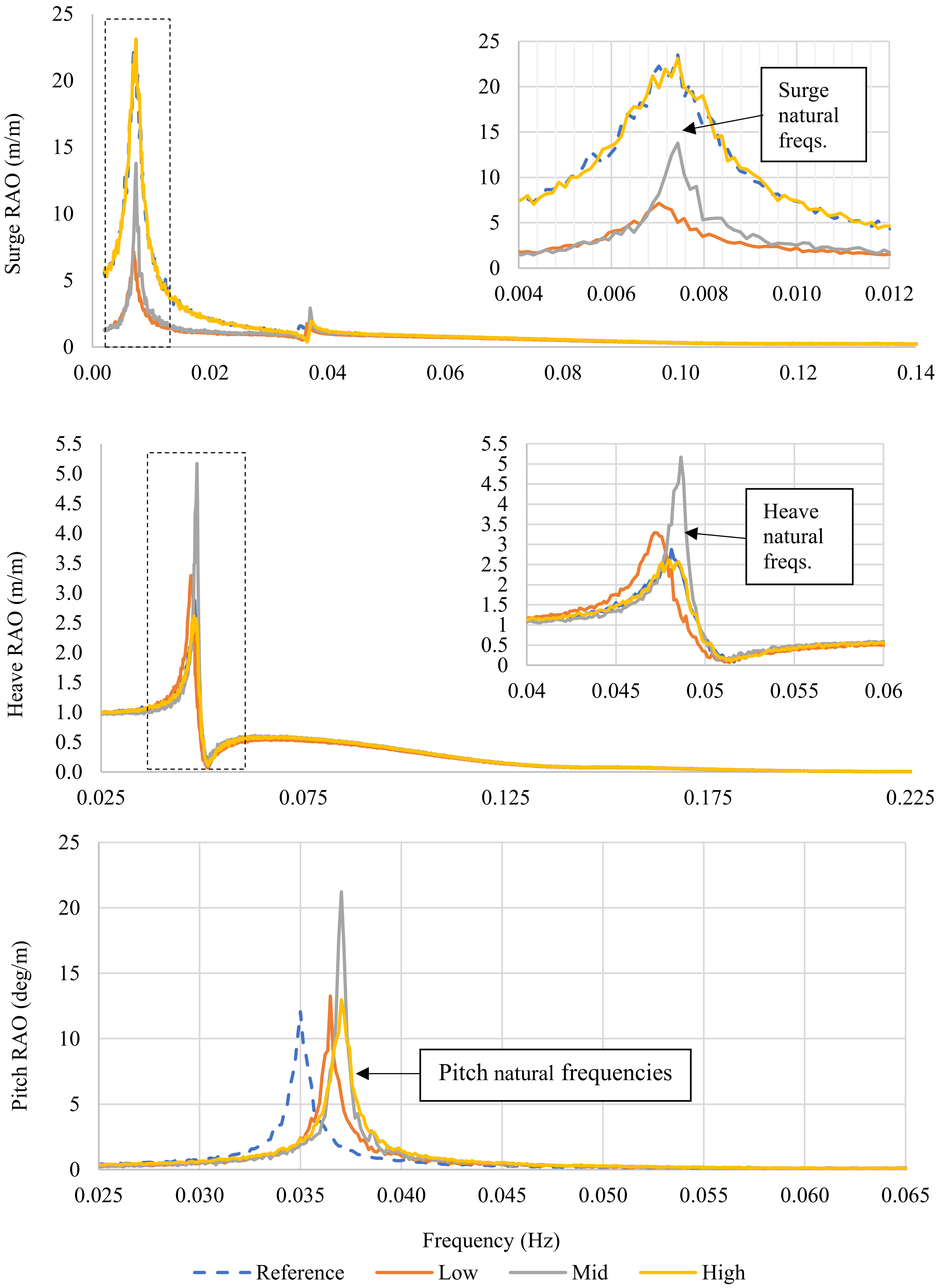

Figure 2.10. Wave-induced RAOs in surge, heave, and pitch for the reference design, low, mid, and high case scenarios.

2.4.3. Wave splashing – air gap

To prevent damage to the FOWT-DAC platform deck equipment, we assumed all wave splashing on the deck had to be avoided. To ensure that is the case even in the most adverse situations, we studied the air gap following the method explained in section **2.3.4** and assessed it using equation (2.11), where the sea surface elevation and the platform heave must be determined at each platform's point of concern. We checked the air gap at eight different points on the platform, **Figure 2.11.**

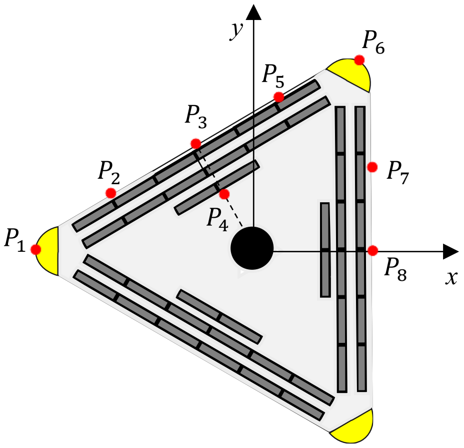

Figure 2.11. Points of study for the air gap assessment.

Given the platform symmetry about the x axis and the wave alignment along the same axis, the chosen points only cover half of the platform. The air gap DLC (**Table 2.5**) is run for six wind seeds, each with six different wave seeds (i.e. 36 simulations in total) for 4,600 s. To be conservative, we take the maximum wave elevation and the minimum heave displacement, shown in **Table 2.7**. The air gap is positive and larger than 1.5 m (as recommended by ref.[96]) at all points of study for all cases, which implies that when subjected to Cascadia Basin conditions, the proposed FOWT-DAC platform designs would not experience any dangerous water splashing on the deck equipment.

Table 2.7. Air gap (in meters) at the different platform points of study for the reference design, and low, mid, and high case scenarios.

Point	Reference (m)	Low (m)	Mid (m)	High (m)
P1	5.8	6.2	4.9	4.5
P2	5.8	5.9	5.7	3.9
P3	5.8	4.8	4.7	4.7
P4	5.7	5.8	5.1	4.9
P5	5.8	5.5	5.0	4.7
P6	5.6	4.9	5.0	4.7
P7	5.6	4.9	5.0	4.7
P8	5.6	4.9	5.0	4.7

2.4.4. System loads

In this section, we check the displacements and loads of different FOWT components (nacelle, blades, tower, floater) for DLCs in **Table 2.5.**

2.4.4.1. DLC 1.4

This DLC specifies a transient load with an extreme coherent gust with wind direction change and normal sea states. The gust starts at 300 s, has a duration of 10 s and peaks at 310 s. Simulations of 360 s are run close to rated wind speed (ECD+/-r), below rated wind speed (ECD+/-r-2), and above rated wind speed (ECD+/-r+2), where +/-r indicates positive and negative wind speeds, respectively. Following refs.[93,97], rotor azimuths of 0°, 30°, 60°, and 90° are considered to account for load differences due to the relative orientation between the wind direction and the blades. The characteristic magnitude (displacement/load) is estimated as the mean of these distinct azimuth positions. A total of 144 simulations, with six seeds per rotor azimuth and wind speed configuration, are analysed. These conditions are selected to capture extreme blade tip flapwise deflections (**Figure 2.12**).

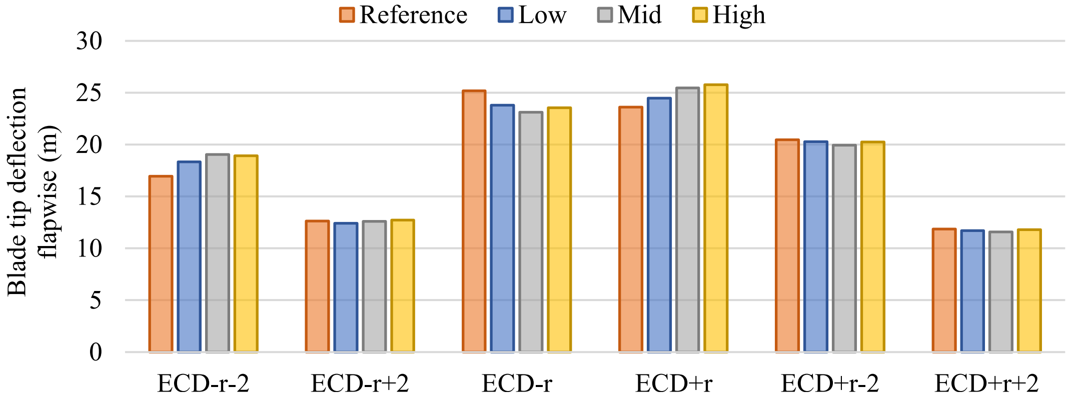

Figure 2.12. Maximum blade tip flapwise deflection per ECD type and scenario (reference design, low, mid, and high case).

2.4.4.2. DLC 1.6

The response of the system under normal turbulence conditions and severe sea states is analysed in DLC 1.6. Because severe sea states are defined for a joint wind-wave probability distribution of 50-year return period, simulations with longer times (4,600 s) are required. All operational wind speeds (4-24 m/s) are considered, each with six seeds, amounting to a total of 66 simulations. The highest values for the platform surge (**Figure 2.13**) and fairlead tension (**Figure 2.14**) are observed in this DLC.

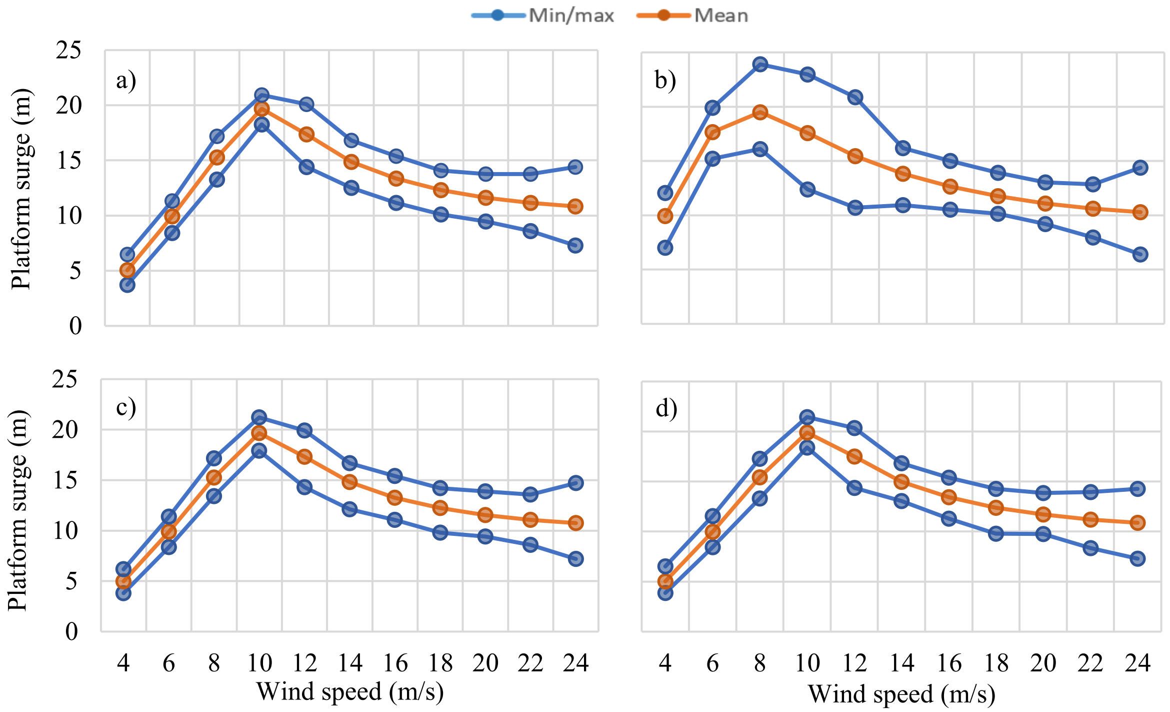

Figure 2.13. DLC 1.6 maximum, mean, and minimum platform surge for the a) reference, b) low, c) mid, and d) high case scenarios.

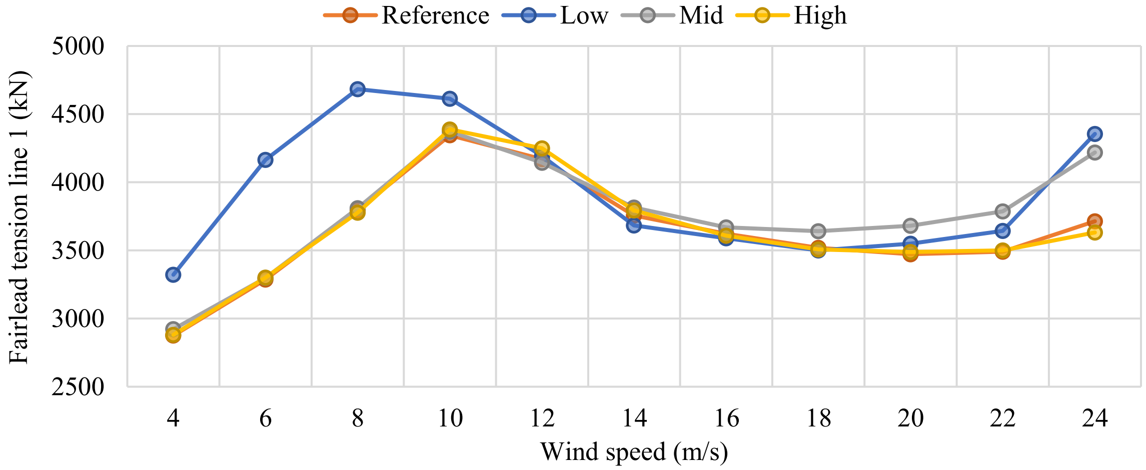

Figure 2.14. DLC 1.6 peak fairlead tension (line 1) for the reference design, and low, mid, and high case scenarios.

2.4.4.3. DLC 2.3

In DLC 2.3, a fault due to a wind gust occurs while the turbine is operating in normal sea states. To prevent damage to the rotor, the blades are completely pitched (90°) immediately after the event, with a 0.2 s delay. Simulations of 600 s are run close to rated wind speed (EOGr), below rated wind speed (EOGr-2), above rated wind speed (EOGr+2), and at the cut-out wind speed (EOGo). The highest absolute value for the tower base pitching (fore-aft) moment is observed in this DLC (**Figure 2.15**).

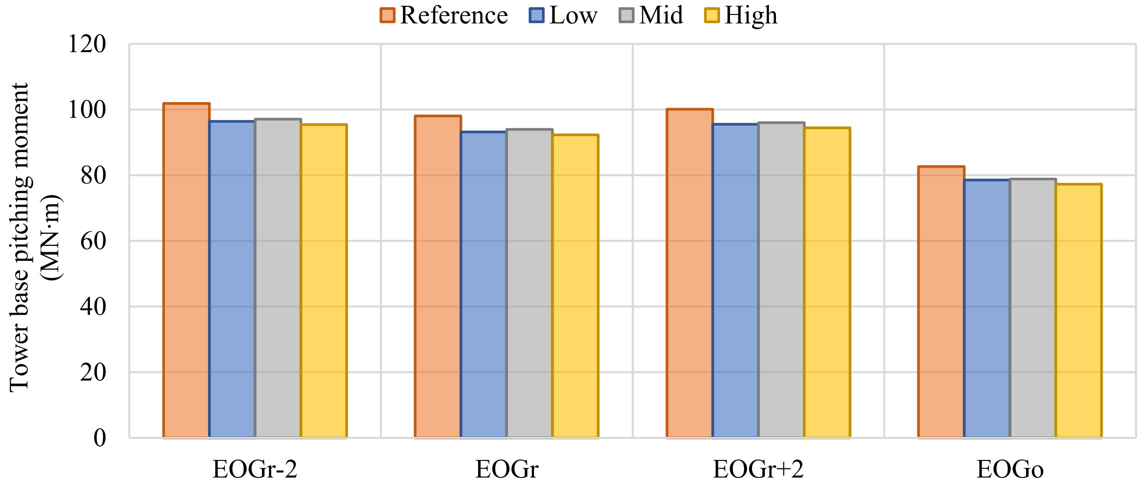

Figure 2.15. DLC 2.3 maximum tower base pitching moment for the reference design, and low, mid, and high case scenarios.

2.4.4.4. DLCs 6.1 and 6.2

In DLCs 6.1 and 6.2, 50-year return period wind and waves conditions are applied, and the turbine is forced to shut down or idle to preserve the rotor's integrity. As noted in ref.[97], given that the EWM wind model cannot be used for simulations longer than 600 s, a normal turbulent model with a turbulence intensity equal to 11% is used instead. The extreme wind and waves are simulated during 4,600 s for different nacelle yaw orientations (-8°, 0°, and 8° in DLC 6.1, and -180°, 0°, and 180° in DLC 6.2) and with the RNA yaw DOF disabled to represent errors in the yaw controller. Maximum platform heave displacements, calculated as the average of the extreme values, occur in these DLCs (**Figure 2.16**).

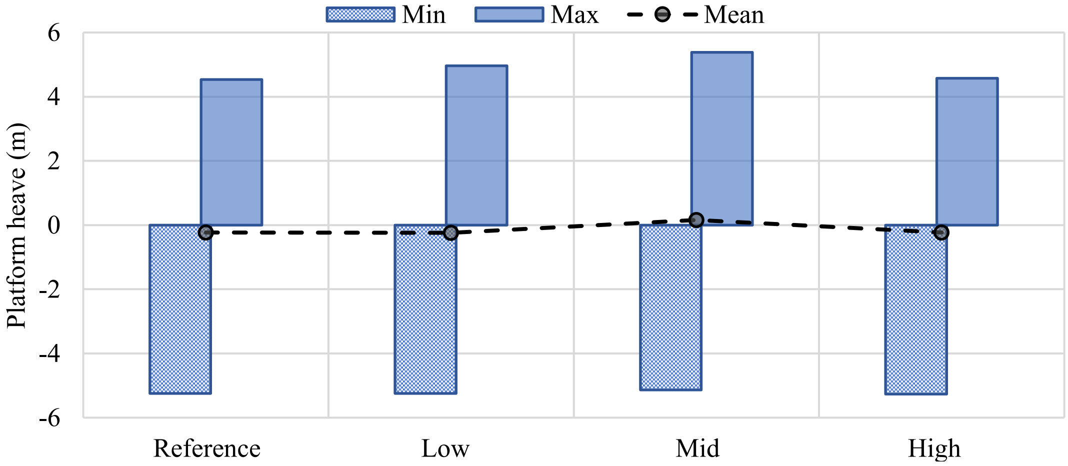

Figure 2.16. DLC 6.1 and 6.2: platform heave minimum, maximum, and mean for the reference design, and low, mid, and high case scenarios.

2.4.4.5. Discussion

As could be seen from figures 4.6 to 4.10, the dynamic displacements and loads observed per DLC for the FOWT reference design (without the DAC) show overall strong agreement with those from each FOWT-DAC scenario (low, mid, and high case). In DLC 1.4, the maximum blade tip deflections (flapwise) between the reference design and the low, mid, and high case scenarios differ a maximum of 11%. While the maximums seen for the ECD+/-r-2 and ECD+/-r+2 cases do not exceed the 23 m value shown in the design report of the IEA 15 MW RWT[73], the same is not true for the ECD+/-r cases, with a maximum deflection of 26 m experienced. Nevertheless, because the maximum blade tip deflections (flapwise) for the reference design is also larger than 23 m**,** the results for the low, mid, and high case scenarios are then considered adequate, and the differences with ref.[73] deemed as acceptable given that different metocean conditions were used here.

In all scenarios of DLC 1.6, the surge displacement is limited to below 25 m (**Figure 2.13**); this may be a useful constraint in future work when designing a flexible pipeline to extract and transport the captured CO_2 from the FOWT-DAC. The FOWT-DAC low case experiences a higher positive surge excursion than the rest, also causing a stronger fairlead tension response of line 1 (**Figure 2.14**). Although subtle, this could be explained by the change in the system mass (displacement volume) of that case with respect to the reference design and the other FOWT-DAC scenarios (see **Table 2.2**). Further, in DLC 1.6 it was shown that the peak fairlead tension stayed below the mooring line breaking strength (**Table 2.1**).

In all cases in DLC 2.3, the reference design shows a bigger tower base pitching moment. Certainly, the reference design is not only heavier than the low and mid cases (**Table 2.1** and **Table 2.3**), but its comparatively smaller pitch moment of inertia means that less force is required per unit of angular acceleration. This explains why the tower base fore-aft moment in the high case scenario, which has the same mass as the reference design but a 20% larger pitch moment of inertia (**Table 2.3**), is smaller than the reference's. The differences between the reference design and the FOWT-DAC cases (low, mid, and high) are 10% at most.

DLCs 6.1 and 6.2 depict the minimum, maximum and mean heave displacements. Despite that the air gap was studied in section **2.4.3**, in DLCs 6.1 and 6.2 we checked the minimum, maximum and mean heave displacements of the floating platform (**Figure 2.16**) to show that no significant differences arise as a result of the DAC system.

2.4.5. Power performance

Lastly, we investigated the wind turbine's power performance for all the scenarios using steady wind speeds covering the whole operational range and in the absence of ocean waves. The results, omitted from the main body but provided in the Appendices (section **2.6.4.2**), show that the power produced in each case (low, mid, and high) is comparatively the same as that generated by the reference design.

2.5. Conclusions

This paper introduced a concept for a co-located and integrated design of an offshore wind-powered CO_2 direct air capture system as part of the Solid Carbon project. The DAC and ancillary system dimensions and power requirements were sized for the IEA 15 MW RWT atop the UMaine VolturnUS-S floating offshore wind turbine semi-submersible. While the CO_2 DAC collectors were placed outside and on top of the designed deck, the ancillary system was distributed inside the floater radial columns. Three design scenarios (low, mid, and high) were defined to represent project, equipment, and deployment site uncertainties. This was done such that hydrostatic and hydrodynamic similarity were kept between the scenarios and the reference design. Mainly, the total system mass and its distribution were adjusted so that the centre of gravity remained as close to the reference's as possible. The principal contributions from this research are summarised below:

- The hydrostatic and hydrodynamic properties of the scenarios (hydrodynamic coefficients, rigid-body natural frequencies, and wave-induced response amplitude operators) were studied and compared with the reference design (i.e. the FOWT without the DAC system) showing minimal variances.
- The floating intact initial stability was assessed for pure pitch rotations. For the static analysis under maximum heeling moment, the righting moment of the unmoored platforms was large enough to stay below the 10° operational limit. For the dynamic analysis, the scenarios were successfully run using DLCs 1.3, 6.1, and 6.2, with maximum pitch angles well below the 10° criterion.
- The distance between the mean water level and the semi-submersible deck, also known as air gap, was computed showing no wave splashing occurring to the onboard DAC units.
- A dynamic analysis using DLCs 1.4, 1.6, 2.3, 6.1 and 6.2 was carried out to investigate and compare the FOWT-DAC system responses with that of the reference design. The displacements and loads seen per DLC for the FOWT reference design (without the DAC) showed strong agreement with those from the FOWT-DAC scenarios.
- Finally, the FOWT power curve for all design scenarios was computed proving again minimal differences with the reference turbine.

Solid Carbon aims to capture and store CO_2 into offshore basalt, however, our scope here was limited to the wind-powered CO_2 DAC process alone. Future work will continue by studying how the addition of a piping system to the FOWT-DAC platform to transport the captured CO_2 to the basalt injection site may affect the system dynamics.

Acknowledgements

The authors would like to thank Ocean Networks Canada for their support, as well as Heather Norton for her input on the DAC and ancillary systems, Rad Haghi for his guidance in selecting appropriate DLCs for the analysis, and Spencer Funk and Patrick Connolly for providing valuable discussions.

2.6. Appendices

2.6.1. Direct air capture

Carbon Engineering and Climeworks are two well-known DAC developer companies, and representative of the two most common DAC techniques. Carbon Engineering uses an aqueous solvent-based DAC system and requires high temperatures (~900 ℃), while Climeworks uses a solid sorbent-based DAC system and works with low temperatures, between 80-130 ℃ [75,98]. In an offshore context and without the use of a fossil-fueled boiler, Carbon Engineering's high-temperature requirements are difficult to provide; electric resistive heaters could be an alternative, but their electricity demand is significantly higher than that of e.g. heat pumps. By comparison, Climeworks' DAC low-temperature heat needs can be met with heat pumps (≤ 100 ℃). Climeworks' DAC technology has a focus on modularity, while Carbon Engineering is better suited for large industrial purposes. That is why in this work we adopted a generic DAC technology representative of Climeworks' low temperature solid sorbent approach.

2.6.2. Ancillary system

This section expands on the procedure followed to size and determine the ancillary system, comprised of energy storage, a CO_2 compressor, and CO_2 storage.

2.6.2.1. Energy storage

The energy storage system is to provide electrical power to the CO_2 capture and ancillary system processes at times when the wind turbines are not producing enough power. These low-power periods are split into two different timescales; a short-term hourly based, which uses electric lithium-ion batteries, and a long-term monthly/seasonally based, which assumes the use of H_2 fuel cells.

To size the battery system, we assume the wind turbine is not producing any power at all for a continuous period, which may be two hours in the best case, or four hours in the worst case. Note these cases are independent of the low, mid, and high configuration scenarios we have used throughout this work. Considering our DAC and ancillary units' mean hourly energy requirements for the low, mid, and high scenarios, and choosing Tesla's lithium-ion Megapack battery (which conveniently comes in two- and four-hour duration modules)[99], we determined the number of Megapacks needed, **Table 2.8**.

Table 2.8. Electric storage system sizing for the low, mid, and high case scenarios.

	Units	Low	Mid	High
FOWT-DAC power load	kW	2,949	3,172	3,617
FOWT-DAC energy load	kWh	5,898	6,343	7,233
# 2-h Megapacks	-	3	3	4
# 4-h Megapacks	-	4	5	5
Total 2-h Megapacks mass	tons	91	91	91
Total 4-h Megapacks mass	tons	122	152	152

Each Megapack module is 7.26 m long, 1.65 m wide, 2.51 m tall, and weighs 30.4 tons. The two-hour module has a power/energy nameplate rating of 1,295 kW/2,570 kWh, respectively, and a round-trip efficiency of 92%. The four-hour module has a power/energy nameplate rating of 775 kW/3,101 kWh, respectively, and a round-trip efficiency of 93.5%, ref.[99].

Because of their low energy density, limited cycle life and cost, lithium-ion batteries are not suitable for long-term storage in grid-scale projects. That is why we opted for a hydrogen-based energy storage system. In short, at times of excess wind power, this is used to run an electrolyzer and store the resulting H_2. Then, at times of deficit power, the H_2 is fed into a fuel cell and converted back into electricity. Although typical roundtrip efficiencies are at present notably low (32-35%, ref.[100]), there is room for improvement both in water electrolysis and H_2 fuel cells.

In offshore applications such as ours, water electrolysis is preceded with a desalination process to turn seawater into fresh and purified water[xxiii]. There are different types of desalination techniques, of which reverse osmosis (RO) is the most popular one, accounting for approximately 70% of all global volume in 2020. In RO, high-pressurised seawater is forced through semi-permeable membranes, capturing dissolved salts and other impurities.

The electrolyzer technology selection depends on the application of use[68]. For an offshore wind-powered H_2 system, refs.[69,101] chose a Proton Exchange Membrane (PEM) electrolyzer type from Siemens Energy used in conjunction with RO. Here, we also opted for the same technology, with the newest model currently available being the Silyzer 300 PEM[102]. A Silyzer 300 half 12-module array has a production of 165 kgH_2/h at a rated power of 8.7 MW, which is enough to meet our estimated hydrogen demands of 106-128 kgH_2/h. Each half 12-module array weighs approximately 2.1 tons, which includes the water storage tanks. The FOWT-DAC hourly hydrogen required was calculated, as a first rough approximation, as the cumulative below-the-monthly mean energy production over an average year for the 2004 to 2016 period.

Once produced, hydrogen must be stored onboard until the time it is needed to be reconverted back to electricity. Hydrogen can be stored in various forms, with cryogenic (liquified) and compressed (gaseous) being the most mature ways. Because of the high cost and complexity of transforming and keeping liquid hydrogen in cryogenic conditions (below 20°K, ref.[103]), and the simplicity and technology readiness of compressed gas storage, the latter is preferred here. For compressed gas storage applications, hydrogen is kept between -40°C to 30°C, and at pressures between 350 to 700 bar. Due to these high pressures, specially designed tanks known as pressure vessels are used. Because our concern revolves around minimising the platform impact from the DAC and ancillary system, we select type IV tanks based on their lightness in comparison with the other types[104]. **Table 2.9** gives the unit specifications.

Table 2.9. Type IV HT700-103 hydrogen tank unit specifications[105].

Magnitude	Units	Value
Weight	kg	66
Dimensions	cm	165

[xxiii] Total dissolved units in water should not exceed 0.5 ppm in electrolysis applications[270].

Max storage	kgH_2	4
External diameter	cm	35
Nominal operating pressure	bar	700
Volume water equivalent	L	103
Recharges	-	45,000

2.6.2.2. CO_2 compressor

To reduce the storing space needs of the onboard CO_2 and ensure appropriate pressure and temperature conditions for a successful injection into basalt, we use a CO_2 compressor. The power of a compressor is the product of the head developed (H) and the volumetric flow rate (Q),

$$P = \eta \frac{\gamma Q p_1}{\gamma - 1}\left[\left(\frac{p_2}{p_1}\right)^{\frac{\gamma-1}{\gamma}} - 1\right] \tag{2.12}$$

Where η is the compressor (adiabatic) efficiency (equation (2.13)), $\gamma = \frac{C_p}{C_v}$ is the heat capacity ratio, and p_1 and p_2 are the CO_2 pressures entering and leaving the compressor, respectively.

$$\eta = \left[\frac{\left(\frac{P_2}{P_1}\right)^{\frac{\gamma-1}{\gamma}} - 1}{\left(\frac{P_2}{P_1}\right)^{\frac{n-1}{n}} - 1}\right] \tag{2.13}$$

The adiabatic efficiency depends on γ, p_1 and p_2, as well as on the polytropic path coefficient, n,

$$n = \left[1 - \frac{\left(\frac{T_2}{T_1}\right)}{\left(\frac{P_2}{P_1}\right)}\right]^{-1} \tag{2.14}$$

With T_1 and T_2 being the CO_2 temperatures entering and leaving the compressor. Assuming p_1= 101 kPa, T_1 = 25°C, and p_2 = 7,380 kPa, T_2 = 2°C, the compressor power can be determined, **Table 2.10**. Further, thanks to ref.[106], one can use the compressor power as a proxy to its transportation weight.

Table 2.10. CO_2 compression specifics.

	Units	Low	Mid	High
Polytropic path coefficient	-	1.0	1.0	1.0
Heat capacity ratio	-	1.3	1.3	1.3
CO_2 flow rate	tCO_2/h	3.6	3.9	4.4
Compressor power	kW	412	443	506
Compressor mass	tons	15	17	21

2.6.2.3. CO_2 storage

Now that the captured CO_2 has been compressed, we can determine the storing space it takes. To do that, we assume that the onboard capacity in the low, mid, and high scenarios is enough to store one-, four- and seven-days' worth of production, respectively. This is done to account for the fact that the CO_2 may be transported by vessel to the injection site, and thus it may be necessary to temporarily store some of it onboard until the vessel retrieves it. Then, knowing the CO_2 conditions of storage (T_2 = 2°C, p_2 = 7,380 kPa), we can determine its density (ρ_{CO_2}= 0.9467 kg/m^3) and hence its volume (**Table 2.11**).

Table 2.11. CO_2 mass and volume storage for the low, mid, and high case scenarios. This excludes the mass/volume of the storage tanks.

	Units	Low	Mid	High
Mass	tons	87	373	744
Volume	m^3	92	394	786

Fluid storage tanks, such as those used for CO_2, are built in different shapes, and exhibit varied levels of protection and insulation. To have an idea of common industrial CO_2 storage tanks, we took *Chart Industries Inc.* bulk solutions as a reference[107]. **Table 2.12** presents the specifications of different *Chart Industries Inc.* tank models that meet our needs.

Table 2.12. CO_2 storage tanks dimensions.

Model	Net capacity (m^3)	Mass (tons)	Length (m)	Width (m)	Height (m)
HS-6000SC	21.8	10.0	9.8	2.2	2.4
HS-9000SC	34.0	14.7	8.8	3.2	3.2
HS-11000SC	41.5	17.6	10.4	3.2	3.2
HS-13000SC	49.4	20.6	11.9	3.2	3.2
HS-15000SC	57.0	23.7	13.4	3.2	3.2

Finally, a possible tank selection to store the CO_2 of the low, mid, and high case scenarios is given in **Table 2.13**. This also indicates the total CO_2 storage mass (content plus container) and the total volume the tanks occupy. Recall that all ancillary system equipment is placed inside the floater radial columns; only the CO_2 collectors (DAC units) are put on the deck.

Table 2.13. Final CO_2 storage tanks selection.

Model	# units	Total mass (tons)	Total volume (m^3)
HS-6000SC	5	137	258
HS-13000SC	8	398	972
HS-15000SC	14	1,076	1,740

2.6.3. Wave splashing

2.6.3.1. Inverse First Order Reliability Method (IFORM)

IFORM was first defined by Winterstein et al.[85] as a method to define extreme environmental contours. Basically, IFORM's premise is that the environmental variables under consideration (e.g. H_s and T_p) are correlated in an undetermined way. IFORM models this correlation as the product of an independent probability distribution of H_s and a conditional one of T_p, where the former usually is taken to be a Weibull distribution, $f_{H_s}(h_s)$, and the latter a lognormal distribution, $f_{T_p|H_s}(t_p|h_s)$, equations (2.15) and (2.16). The lowercase variables h_s and t_p denote the q-quantiles of the continuous distributions.

$$f_{H_s}(h_s) = \frac{k}{\lambda}\left(\frac{h_s - \varepsilon}{\lambda}\right)^{k-1} \exp\left[-\left(\frac{h_s - \varepsilon}{\lambda}\right)^{k}\right] \tag{2.15}$$

$$f_{T_p|H_s}(t_p|h_s) = \frac{1}{\sqrt{2\pi}\sigma_{T_p|H_s}} \exp\left[\frac{\left(ln(t_p|h_s) - \mu_{T_p|H_s}\right)^2}{2\sigma^2_{T_p|H_s}}\right] \tag{2.16}$$

By extrapolating the marginal distribution of H_s, one can determine extreme H_s values for certain return periods, T_R, and input those values into the inverse cumulative distribution function (CDF) of $f_{T_p|H_s}(t_p|h_s)$ to find the corresponding extreme T_p value.

Next, we outline the steps we made using IFORM to determine extreme steep sea states to be used later for the air gap analysis. More information on IFORM can be found in refs.[85,108–110].

In the first step, a joint H_s-T_p probability distribution, $f_{H_sT_p}(h_s, t_p)$, is defined as the product of $f_{H_s}(h_s)$ and $f_{T_p|H_s}(t_p|h_s)$, equation (2.17).

$$f_{H_sT_p}(h_s, t_p) = f_{H_s}(h_s)f_{T_p|H_s}(t_p|h_s) \tag{2.17}$$

The $f_{H_s}(h_s)$ distribution parameters $\varepsilon = 0.93, \lambda = 1.39, k = 1.87$ are the location, scale, and shape parameters, and are found by fitting the short-term H_s data into $F_{H_s}(h_s)$, which is the CDF of $f_{H_s}(h_s)$. The terms $\mu_{T_p|H_s}$ and $\sigma_{T_p|H_s}$ in equation (2.16) are the mean and standard deviation of T_p given H_s in the lognormal distribution and can also be computed for each H_s using the site environmental data. Further, $\mu_{T_p|H_s}$ and $\sigma_{T_p|H_s}$ can be parametrized as a function of h_s, ref.[109], equations (2.18) and (2.19), where their coefficients $a_i, b_i, i = 0, 1, 2$ can be curve fitted using e.g.

the least-squares method[110]. After computing an extreme value of H_s for a given T_R, $\mu_{T_p|H_s}$ and $\sigma_{T_p|H_s}$ can be extrapolated beyond the environmental dataset.

$$\mu_{T_p|H_s} = a_0 + a_1 h_s^{a_2} \tag{2.18}$$

$$\sigma_{T_p|H_s} = b_0 + b_1 \exp(-b_2 h_s) \tag{2.19}$$

With the desired return period, in our case T_R = 100 years based on ref.[84], we can calculate the failure probability, p_{T_R}, the reliability, $r_{T_R} = 1 - p_{T_R}$, and the reliability index, $\beta = \Phi^{-1}(r)$, also known as the standard normal U-space radius, equations (2.20)-(2.22),

$$p_{T_R} = \frac{t_s}{365 \cdot 24 \cdot T_R} \tag{2.20}$$

$$U_{1_i} = \beta \cos\left(\frac{2\pi i}{j}\right) \tag{2.21}$$

$$U_{2_i} = \beta \sin\left(\frac{2\pi i}{j}\right), \qquad \mathrm{i} = 1, 2, \dots, \mathrm{j}-1, \mathrm{j} \tag{2.22}$$

where t_s is the time interval for the recorded environmental data (t_s = 1 h), and Φ^{-1} is the inverse CDF of the standard normal distribution. The radius β allows us to produce points U_{1_i}, U_{2_i} in the U-space which can then be transformed back to the H_s-T_p space through Rosenblatt's transformation[111]:

$$H_s = F_{H_s}^{-1}\big(\Phi(U_1)\big) \tag{2.23}$$

$$T_p = F_{T_p|H_s}^{-1}\big(\Phi(U_2)\big) \tag{2.24}$$

2.6.3.2. Steepness criterion curve

Equations (2.23) and (2.24) provide H_s-T_p pairs of extreme sea states with a return period T_R = 100 years. However, as required by ref.[84], only those extreme sea states crossing the wave steepness criterion curve[86] (equations (2.25)-(2.27)) can be used in the air gap assessment. The 100-year H_s-T_p contour together with the steepness criterion curve and the resulting air gap design sea state (H_s = 6.49 m, T_p = 7.91 s) after applying equations (2.25)-(2.27) can be seen in **Figure 2.17**.

$$H_s = \frac{g T_p^2}{30\pi} \qquad for\ \ T_p \leq 8\,s \tag{2.25}$$

$$H_s = \frac{g T_p^2}{30\pi}\left(\frac{51}{35} - \frac{2T_p}{35}\right) \qquad for\ \ 8\,s < T_p < 15\,s \tag{2.26}$$

$$H_s = \frac{g T_p^2}{50\pi} \qquad for\ \ T_p \geq 15\,s \tag{2.27}$$

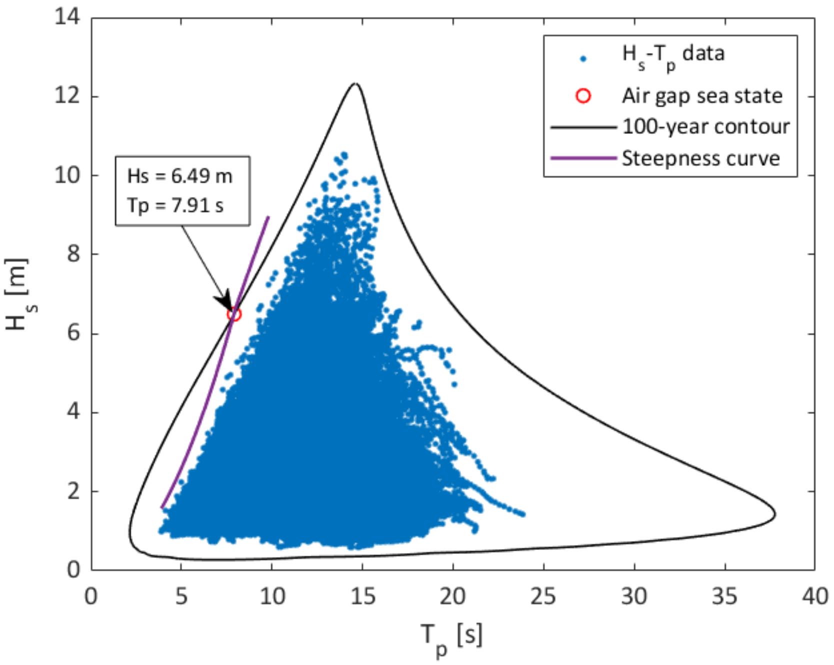

Figure 2.17. IFORM resulting H_s-T_p contour together with the steepness criterion curve and the air gap design sea state, H_s = 6.49 m, T_p = 7.91 s.

2.6.4. Results

2.6.4.1. Hydrodynamic coefficients

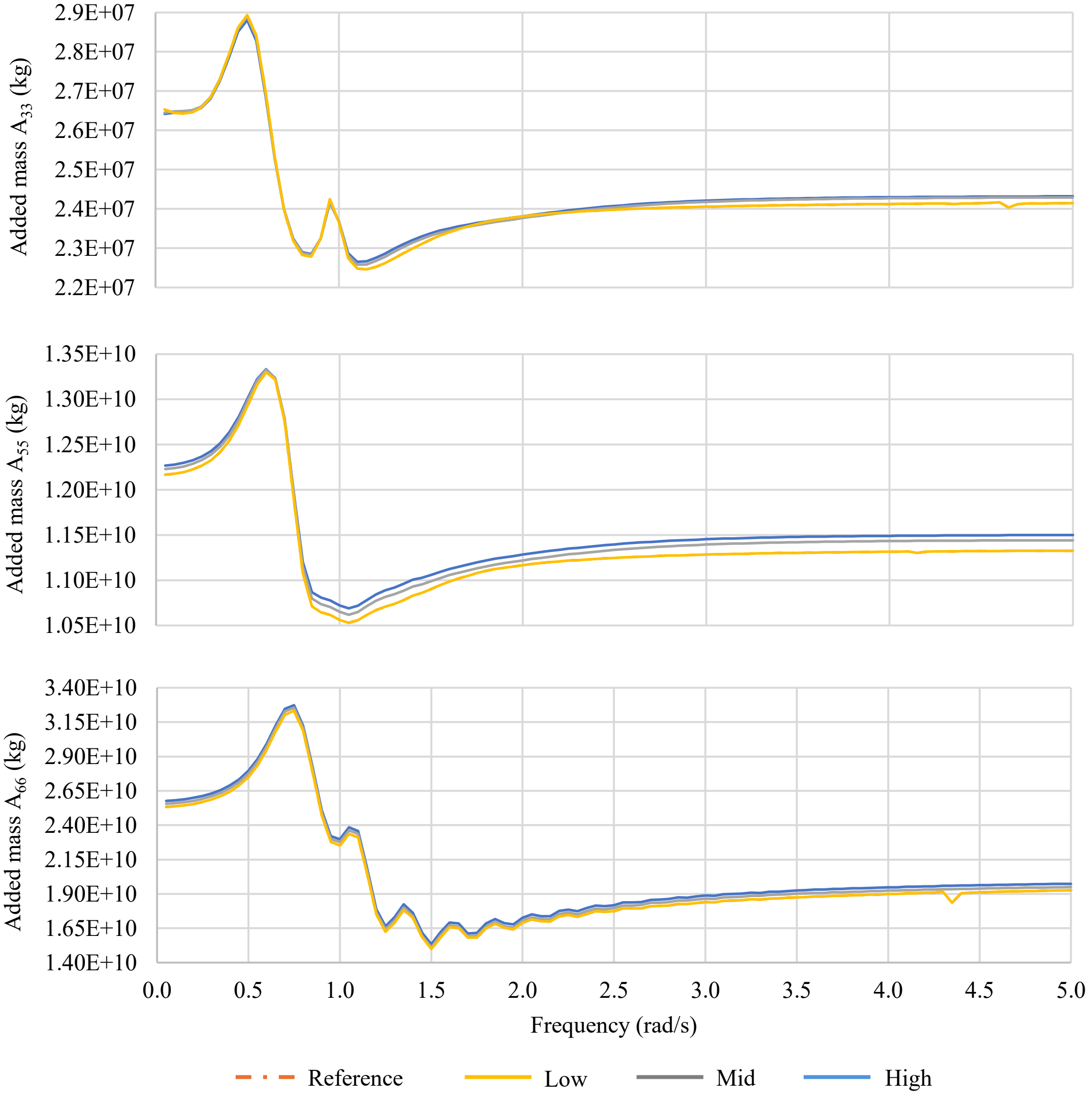

Figure 2.18. Added mass coefficients in top) heave-heave, middle) pitch-pitch, and bottom) yaw-yaw.

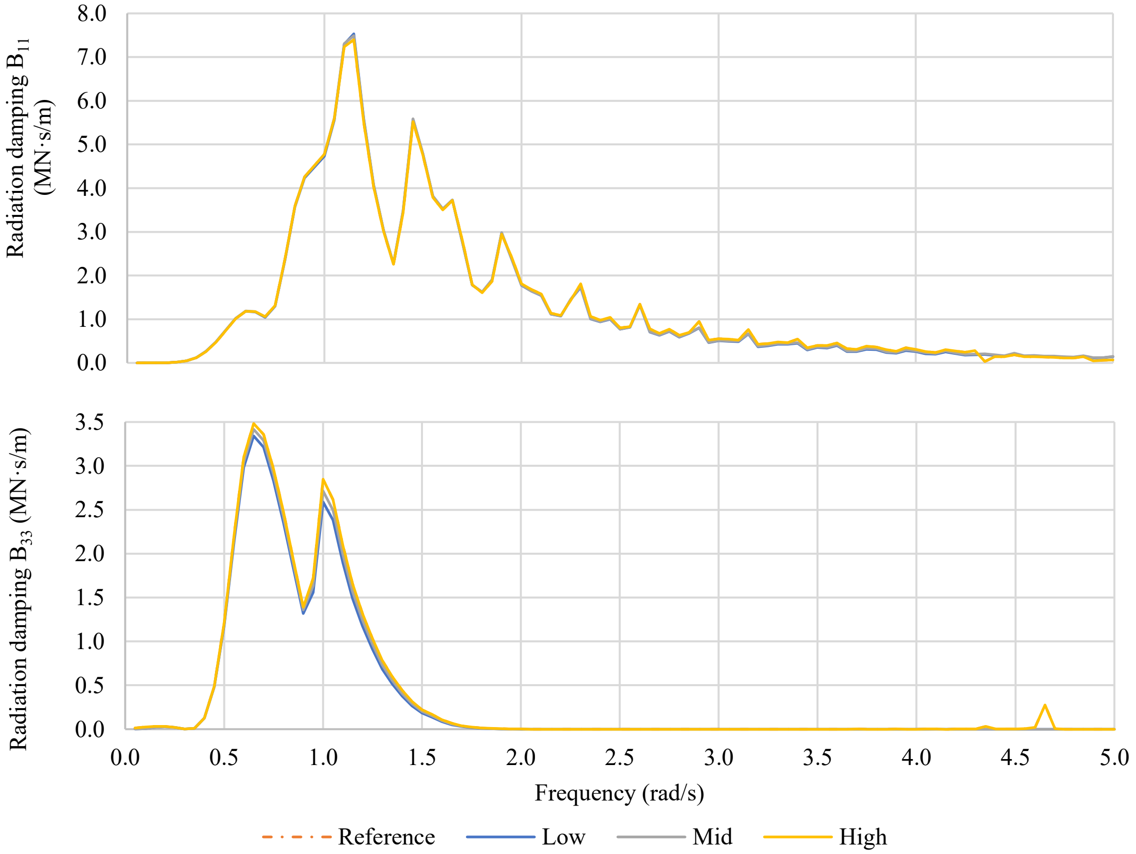

Figure 2.19. Radiation damping coefficients in top) surge-surge, and bottom) heave-heave versus frequency evaluated by HAMS for the low, mid, and high scenarios, and benchmarked with the reference design.

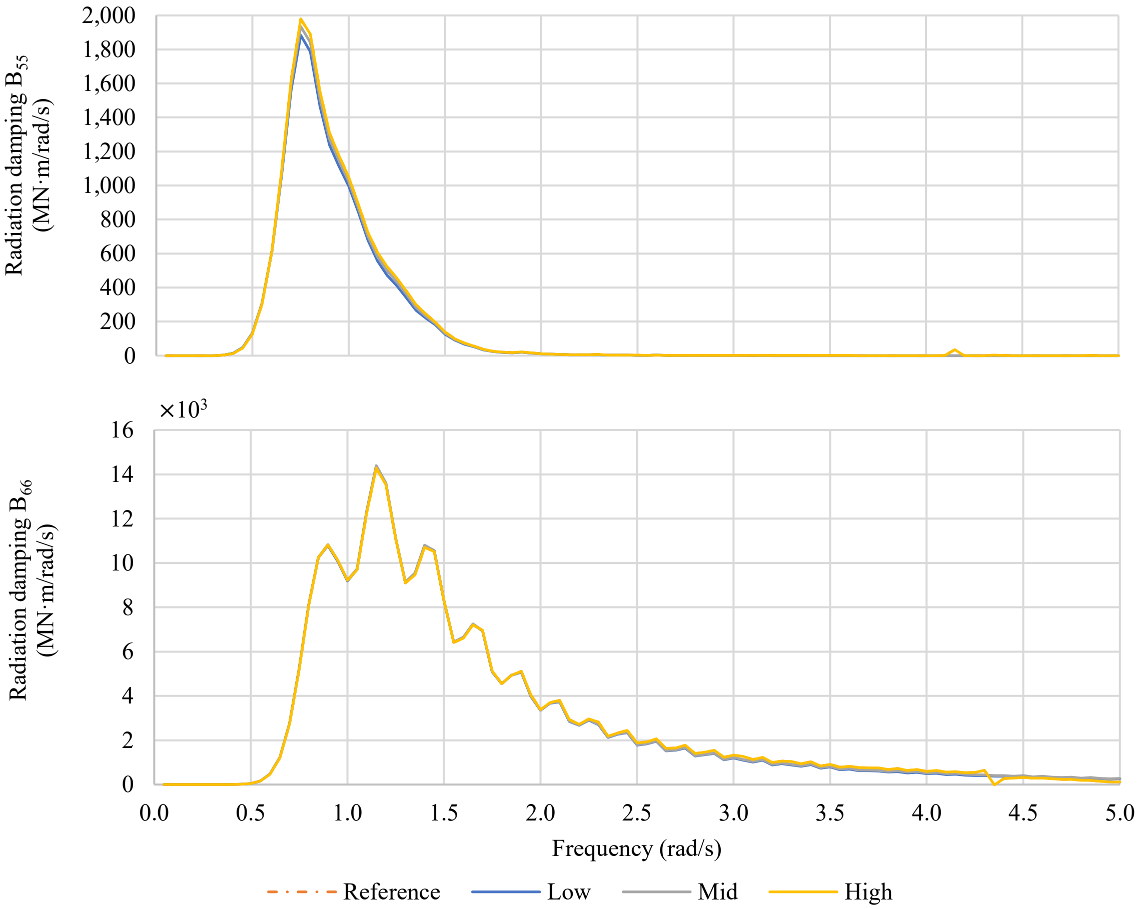

Figure 2.20. Radiation damping coefficients in top) pitch-pitch, and bottom) yaw-yaw versus frequency evaluated by HAMS for the low, mid, and high scenarios, and benchmarked with the reference design.

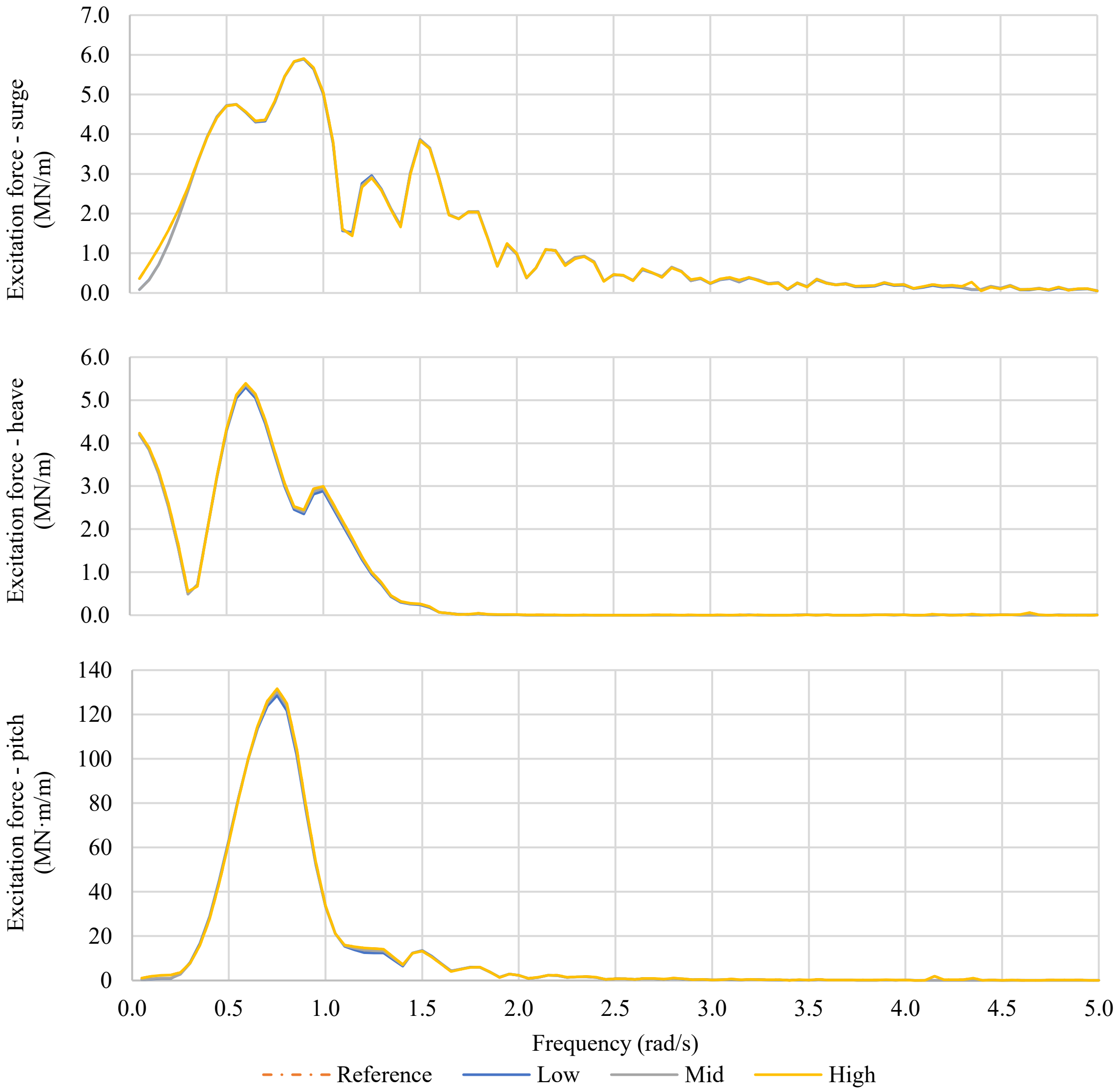

Figure 2.21. Excitation force coefficients (magnitude) in a) surge, b) heave, and c) pitch versus frequency evaluated by HAMS for the low, mid, and high scenarios, and benchmarked with the reference design.

2.6.4.2. Power curve

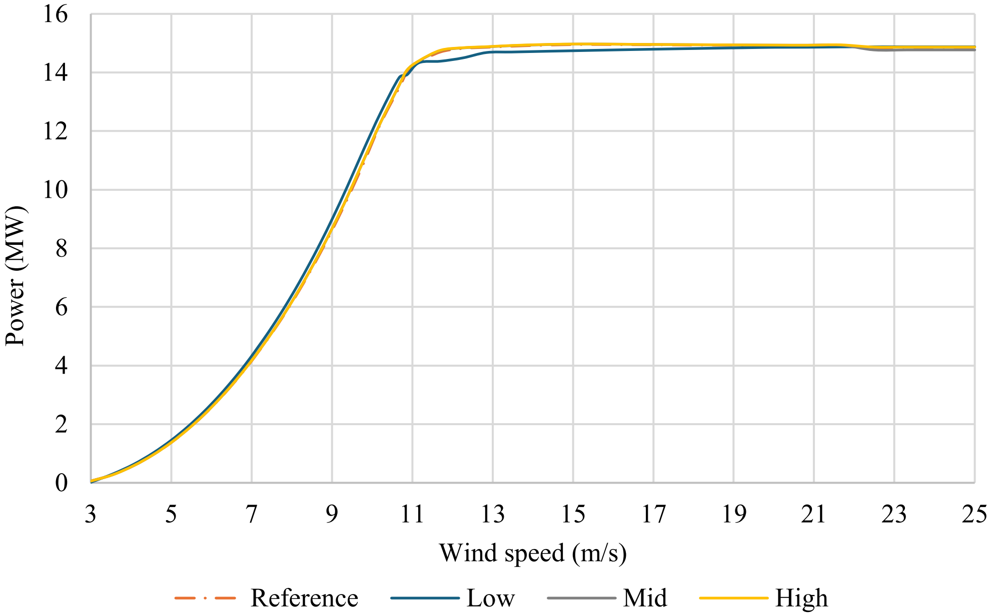

Figure 2.22. Wind turbine power curve for the reference design, and the low, mid, and high case scenarios.

Chapter 3.

Design of a carbon dioxide transportation system

This chapter was first published in the Ocean Engineering journal as:

G. Avellaneda Domene and C. Crawford, “Internal flow effect of a flexible riser system for a floating offshore wind turbine with on-board carbon dioxide capture,” *Ocean Engineering*, vol. 316, p. 119821, Jan. 2025, doi: 10.1016/j.oceaneng.2024.119821. This is an open access article distributed under the terms of the Creative Commons Attribution Non-Commercial License CC BY 4.0.

After publication, we identified two sentences (one in the abstract and one in the conclusions) that were not entirely correct. These have been corrected in the present version and documented for transparency in an erratum appended to the dissertation.

Author contribution

Gerard Avellaneda Domene: conceptualisation, methodology, investigation, modelling, analysis, writing & editing. Curran Crawford: conceptualisation, analysis, supervision, review & editing.

Abstract

This paper designs a flexible riser for transporting carbon dioxide (CO_2) off a floating offshore wind turbine (FOWT)-powered CO_2 capture platform and analyses the internal flow-induced effects caused by the CO_2 on the flexible riser. Internal effects on flexible risers due to the pressurised and internal dynamic flow are a well-studied problem in offshore oil and gas (O&G) applications, which typically requires the use of tools capable of representing their pressurised contents and flows. However, because the flow rates and pressure conditions expected from individual FOWT-CO_2 capture platforms are much lower than those used in O&G installations, we studied the importance of internal flow effects on riser dynamics. To determine their relevance, we designed and modelled the flexible riser in OrcaFlex$^{\text{TM}}$ with different design pressure and flow conditions under normal and extreme environmental events. The results indicate that the riser’s effective tension and curvature are not significantly affected by internal flow, but differences were observed in the von Mises stress arising from the shear stress. As such, as long as the shear term is properly accounted for, these results enable future work to utilise simplified models for the flexible riser system, similar to models for dynamic power cables employed in FOWT farms. This simplification allows us to design and analyse the whole FOWT-CO_2 system alternatively with lower fidelity and open-source offshore wind turbine simulation tools, like OpenFAST, without overlooking relevant riser-dynamics phenomena.

3.1. Introduction

To limit the mean global temperature rise caused by the prolonged combustion of fossil fuels since the Industrial Revolution, the Intergovernmental Panel on Climate Change concluded that national mitigation portfolios need to include some level of negative emission technologies (NETs)[112]. Among these, direct air capture with carbon storage (DACCS) has the potential to permanently sequester many gigatons of carbon dioxide (CO_2), which is several times greater than what is needed to restrict the temperature rise under 2°C, ref.[17]. Due to its energy (1.9-23.1 GJ/tCO_2)[17] and plan-view projected footprint requirements (0.7–5.3 km^2/MtCO_2)[70], some authors have suggested placing DACCS offshore[57,113–115], where competition for grid-energy and land-use can be avoided. Far from shore, DACCS' energy demand can be satisfied by local wind resources, and the CO_2 captured can be injected into reactive rocks (such as basalt), where it can mineralise and permanently adhere to[64].

In previous research[57], we studied the integration of a direct air capture (DAC) system into a floating offshore wind turbine (FOWT) platform. We assessed the impact the addition of the DAC and ancillary systems had on the platform's dynamics, without reporting any substantial negative effect when compared to the baseline FOWT platform without DAC. We focused on the dynamics of the hybrid FOWT-DAC platform and left the transportation of the captured CO_2 to a permanent storage site as future modelling task. For this there are two different CO_2 transportation means: vessel and pipeline. The economics of CO_2 vessel and pipeline transportation have been investigated in several publications[116–118], with a general trend favouring pipelines over vessels when transport distances are less than 200 km. Further, because the operational versus capital expenditures ratio is higher for ships than for pipelines, long duration projects may be benefitted by employing pipelines instead of ships[119]. Also, in open seas, weather conditions limit a vessel's availability, and so a more continuous injection can be achieved when employing pipelines.

3.1.1. Objectives

In this paper, we take a design of a FOWT platform with on-board CO_2 capture proposed by the authors[57] and model a system to transport the CO_2 to a geological reservoir. It is assumed that the FOWT-CO_2 system is placed in the Cascadia Basin region (off the West coast of Canada), where previous studies have assessed the metocean climate for wind-powered CO_2 capture[42], and monitored the basalt resource for CO_2 storage purposes[87,88]. Because of the relative co-location (<200 km) between the CO_2 capture and sequestration sites, as well as their exposure to open seas, the transmission of CO_2 from the FOWT platform is completed with pipelines. The transport may be split into two distinct but connected segments: in the first, the CO_2 is retrieved from the platform and travels along the vertical water column using a riser, terminating at the onset of the second segment; from there a pipeline is employed to cover the largest distance to the injection site. In the present work we are only concerned with the first segment using a riser from the sea surface to the seabed.

In the oil and gas (O&G) industry, production risers have been employed to convey fluids (usually hydrocarbons) from the seabed to platforms and vessels at the sea surface. Several types of risers have been used depending on the project characteristics, with the most well-known being the top-tensioned, free standing, flexible, and steel catenary riser. Because of their flexibility and higher tolerance to motions, lower weight and ease of installation, flexible risers are suitable for a wide range of water depths, seabed conditions and platform motions. Further, their compliant structure allows floating platforms with large motions to be permanently connected to subsea installations. Consequently, they have become the preferred industry option and in 2010 approximately 85% of all installations used flexible risers[120]. For these reasons, we also chose a flexible riser for our FOWT-CO_2 capture system.

Global structural analysis of flexible risers in O&G applications typically requires the use of tools capable of representing the riser's pressurised contents and flows[121–123]. This is because as hydrocarbons' mass flows and pressures increase (up to 6,000 tons/h and 70 MPa, p.497, ref.[124]), so does their inertia effect on the pipe's dynamics. However, it is not clear whether such modelling capabilities are relevant for our flexible riser retrieving CO_2 from the FOWT-CO_2 capture system in ref.[57], with a reported hourly mass flow of 4 tons of CO_2 (tCO_2/h). In other words, there is the question of how important the pressurised internal flow effects on the riser dynamics are.

To determine their relevance, we study how the riser's motions, forces, and stresses are influenced by the CO_2 fluid pressure and flow. If they were not significantly influenced, the riser's modelling could be simplified to resemble that of dynamic power cables employed in FOWT farms[125–127]. This simplification would allow us to design and analyse the whole FOWT-CO_2 system alternatively with lower fidelity and open-source offshore wind turbine simulation tools, like OpenFAST[128], without overlooking relevant riser-dynamics phenomena.

In the remainder of this paper, a flexible riser coupled to the FOWT-CO_2 capture system from ref.[57] is designed and modelled in OrcaFlex™ at two water depths (200 m and 850 m), for normal and extreme environmental conditions. The riser's motion, curvature, forces, and stresses are computed and compared between three cases with different CO_2 conditions: 1) no pressure and no flow, 2) maximum pressure and no flow, and 3) maximum pressure and maximum flow.

3.1.2. The similar case of e-fuels

In addition to NETs, there is a growing interest around the production of electricity-based fuels (e-fuels) to replace the use of fossil fuels in transportation and industry and thus contribute towards the decarbonisation of energy systems. Offshore, the space availability, and the successful commercialisation and cost reduction of wind energy among others have drawn engineers and planners alike to investigate the synthesis of e-fuels at the sea[xxiv]. Among the initiatives, ERM's Dolphyn Hydrogen Project suggested placing all e-fuel production and storage systems together with FOWTs[129], the equivalent to the FOWT-CO_2 system used here. In such configuration, the e-fuel synthesized (i.e. H_2) also needs to be delivered from the FOWT platform and transported to its end-user. To achieve that, ERM is planning on using a flexible riser from the platform to the seabed, and an export pipeline to shore. In their full-scale commercial unit, with a 10 MW WindFloat semisubmersible FOWT, around 150 kgH_2/h are expected[129]. With this configuration it would be

---

[xxiv] See summary of ongoing offshore hydrogen production projects in ref.[69], Table 1.

interesting to ask the same question posed in the previous section and determine the relevance of the H_2 flow in the riser's dynamics. This is explored further in section **3.6**.

3.2. Design

In this section, we outline the relevant aspects of the FOWT-CO_2 capture system, discuss the flexible riser and moorings designs used in the simulations, and present the characteristics and environmental resources of the project site at Cascadia Basin.

3.2.1. FOWT-CO_2 capture system

The FOWT-CO_2 capture platform used in this project was borrowed from ref.[57]. Their design was originally built upon the IEA 15 MW RWT UMaine VolturnUS semisubmersible[72], and adapted to integrate a 1,600-ton solid sorbent-based DAC system together with some on-board CO_2 storage, as well as H_2 production and storage for ancillary services[xxv]. The hydrostatic and inertial properties of the FOWT-CO_2 capture platform are presented in **Table 3.1.**

Table 3.1. Hydrostatic and inertial properties of the FOWT-CO_2 capture platform.

Parameter	Units	Value
Mass	tons	20,611
Draft	m	-19.79
Vertical centre of gravity from SWL	m	-2.74
Vertical centre of buoyancy from SWL	m	-13.41
Roll inertia about centre of gravity	$kg \cdot m^2$	1.333E+10
Pitch inertia about centre of gravity	$kg \cdot m^2$	1.287E+10
Yaw inertia about centre of gravity	$kg \cdot m^2$	2.399E+10

3.2.2. Flexible riser

Flexible risers are made of cylindrical layers of different materials with heterogeneous mechanical properties. In most applications, these layers are non-bonded and can slip past each other when under the influence of loads, giving flexible risers the low relative bending to axial stiffness ratio that makes them ideal for platforms with large motions. In this section, we provide the design basis for the flexible riser, introduce the configuration design, and briefly discuss ancillary components considered for a shallow and deep-water scenario (200 m and 850 m).

[xxv] Three design FOWT-DAC scenarios are used in ref.[57] in which the CO_2 capture capacity varied across them. The middle case, used here, had an annual capture capacity of 34.6 ktCO_2.

3.2.2.1. Design basis

As often seen in CO_2 pipeline transport[130], it is assumed that the fluid is in liquid state and has undergone a dehydration process prior to injection to minimise water corrosion[xxvi]. The CO_2 stream is highly pure and contains no or minimal presence of other particle substances.

The pressure at the riser's inlet is chosen based on a 10-35 MPa range given by Knoope et al.[118] for offshore CO_2 pipeline transport. These high-pressure values were motivated by commonly used direct injection conditions, and by a desire to avoid extra costs associated with additional pumping stations offshore[xxvii]. In this paper, we are interested in studying edge cases that exacerbate the pressurised CO_2 flow effects on the riser's mechanics; for this reason, we chose a pressure value of 35 MPa (5,076 PSI), at the higher end of the range in ref.[118].

With this same motivation in mind, we selected a flexible riser with the smallest inner diameter (ID) commercially available in offshore installations[131], $ID = 0.05$ m (2 inches), and chose as rapid a flow speed as possible that would not cause erosion on the inner riser walls[xxviii]. We postulated that if the effects of the CO_2 fluid on the riser's kinematics and dynamics were negligible for such a small riser, then they should also be so with risers with larger diameter, assuming the mass flow and other riser parameters were kept the same. The maximum allowable velocity in riser systems to avoid pipe-wall thinning due to erosion ($v_{erosion}$) is given by ref.[132] as:

$$v_{erosion} = 1.22C/\sqrt{\rho_{CO_2}} \tag{3.1}$$

where C is an empirical constant equal to $C = 100$ for continuous service[132]**.** With a CO_2 density $\rho_{CO_2} = 964 \text{ kg/m}^3$, the erosional velocity becomes $v_{erosion} = 3.9\ m/s$. With this data, the flow rate (Q) can be determined using equation (3.2), giving $Q = 0.008\ m^3/s$, which corresponds to a mass flow of $\dot{m} = \rho_{CO_2} \cdot Q = 28\ tCO_2/h$.

$$Q = \pi \left(\frac{ID}{2}\right)^2 v_{erosion} \tag{3.2}$$

Note that in ref.[57] the FOWT-DAC platform had a mass flow of ~4 tCO_2/h, whereas the mass flow employed in this case is 28 tCO_2/h. This increased mass flow is meant to account for potential future improvements in CO_2 capture efficiency and technologies, hoping to widen the applicability of our results. If the effects of the CO_2 fluid on the riser's kinematics and dynamics are negligible

---

[xxvi] Corrosion in a riser's metal layers can increase its fatigue and reduce its operational life. However, this should not be a concern in our case since the captured CO_2 has a high purity and is also dehydrated during the compression process.

[xxvii] In fluid flow along pipes, pumping stations may be required to compensate for the pressure drop due to wall friction along the pipe.

[xxviii] When interacting with solid structures, fluid flows can cause material removal known as *erosion*. In flexible risers, erosion produces thinning of the fluid conduit (the so-called carcass), which can lead to rupture or collapse of the riser. Erosion rates are influenced by fluid velocity, the amount and size of produced solid particles (e.g. sand), carcass geometry and material, and presence of corrosive contaminants such as hydrates.

with a mass flow of 28 tCO_2/h, then they should also be so with a lower mass flow of ~4 tCO_2/h, assuming the riser configuration and everything else is kept the same.

The study conditions of the CO_2 flow for both shallow and deep-water scenarios are given in **Table 3.2**. Note that the working pressure has the same value, independent of the water depth scenario. Although a larger pressure drop due to friction with the pipe walls would be expected for the deep-water scenario in comparison to the shallower case, OrcaFlex^{TM} does not model wall friction effects. Moreover, a rough calculation of the drop in pressure for both cases reveals that these are lower than 3% of the working pressure (see Appendices, section **3.7.3**), so it is ignored here.

At our temperature and flow conditions, the CO_2 injected can be considered incompressible[xxix]. This means that the density of the fluid remains, in good approximation, constant. As such, we do not expect to see slugs of different density forming along the riser, and the flow rate will then be the same at all points and over time.

Table 3.2. CO_2 conditions at the flexible riser's inlet.

Characteristic	Units	Value
Temperature	°C	10
Pressure	MPa	35
Density	kg/m^3	964
Mass flow	tCO_2/h	28

3.2.2.2. Configuration

With the design basis specified, this section will present the rest of the riser's design parameters and mechanical properties, and discuss potential layouts.

Cross section

Flexible risers are composite, multi-layered pipes composed of different materials (e.g. polymer, steel, synthetic fibres, and foam) that confer upon them diverse mechanical and thermal properties, such as strength, ductility, wear, creep, and thermal expansion[133]. Whereas a local analysis represents these multiple layers to capture their interactions and effects in the overall riser dynamics, this level of fidelity is not attainable when studying the full-length of a riser. Instead, engineers simplify the layered structure, and risers are modelled as hoses, with dimensions characterised by an inner diameter, an outer diameter and a length. This approach is followed here and the flexible riser is modelled in OrcaFlex^{TM} as a high-pressure hose, which uses the riser's inner diameter (ID) to derive its outer diameter (OD) and some mechanical properties.

Layout

The way a riser is laid connecting the floating platform on the sea surface and the subsea base at the seabed depends on the application (drilling or production), riser type (top tensioned, rigid, or flexible), number of risers, metocean conditions, budget, and seabed characteristics, among others [124]. The most

---

[xxix] A flow can be considered incompressible if the Mach number is smaller than 0.3; at $T = 10°C$, the speed of sound of CO_2 is 802.3 m/s, and the CO_2 flow speed is 3.9 m/s, giving a Mach number of 0.005.

used configurations are catenary, lazy/steep wave, and lazy/steep s; the interested reader can see a schematic representation of these traditional layouts in ref.[134], Figure 9.1. We used a lazy wave riser (LWR) configuration for both water depth cases; thanks to the use of buoyancy modules around the touch down point (TDP), LWRs are less prone to line damage due to the impact and friction with the seabed when compared to catenaries, and are cheaper to install than steep waves and lazy/steep s layouts. Most importantly, buoyancy modules are usually made from floating materials (e.g. foam polymers), which effectively reduce LWRs net submerged weight. For further details on the layout decision process, the reader is directed to the Appendices, section **3.7.1**.

The platform-riser's connection point is chosen below the main column, centred at the base of the hull, and vertically aligned with the centre of gravity of the system, thus reducing the potential for any adverse effects on the platform's stability. This also allows for routing the riser inside the main column, shielding it from external impacts.

The design of the LWR is refined iteratively in OrcaFlex™ by solving the system under static forces[xxx], and testing the candidate configurations with different dynamic conditions (see **Table 3.2**) until a working solution is found. Briefly, the LWR's line length and anchor radius are initially set based on the location of the platform-riser's connection point, water depth, and the line's wet weight. The values are chosen to prevent excessive line bending below the minimum bending radius (MBR) at the hang-off point (HOP), sag bend and hog bend[xxxi], and TDP. The shape of the lazy wave is mainly characterised by the elevation of the sag bend – enough to prevent any impact with the seabed – and the buoyancy of the hog bend, sufficient to decouple the LWR from the platform's motion. The diameter and mass per unit length of the hog bend line section are derived by OrcaFlex™ from the base line's mass and buoyancy modules pitch[xxxii].

The final configurations for the shallow and deep-water cases are shown in **Table 3.3** and **Figure 3.1**. Note that the flexible riser lines for both water depth cases, shown in red, depict a slightly more intense colour around the lazy wave; as will be discussed in section **3.3.1.1**, this is because the density of nodes in that region is greater, which is used to better characterise the line shape and motion.

Table 3.3. Flexible riser dimensions and mechanical properties.

Riser global characteristics	Units	Shallow	Deep
Inner diameter	m	0.05	-
Outer diameter	m	0.07	-
Dry mass per unit length	kg/m	36.3	-
Axial stiffness	MN	140	-
Bending stiffness	kN·m^2	0.188	-
Poisson ratio	-	0.3	-

[xxx] In addition to gravity and buoyancy, the static analysis includes constant currents and internal fluid pressure.

[xxxi] The sag bend and hog bend of a LWR are depicted in **Figure 3.1**.

[xxxii] The buoyancy modules pitch is defined as the average spacing between consecutive buoyancy modules centres. In our model, the properties of lazy wave are spread out evenly along its pitch.

Yield strength[xxxiii]	MPa	650	-
Anchor radial spacing	m	330	675
Unstretched line length (shallow/deep case)	m	483	1,310
Buoyancy module outer diameter	m	0.32	-
Buoyancy module mass per unit length	kg/m	70.0	-
Buoyancy modules length (shallow/deep case)	m	80	225

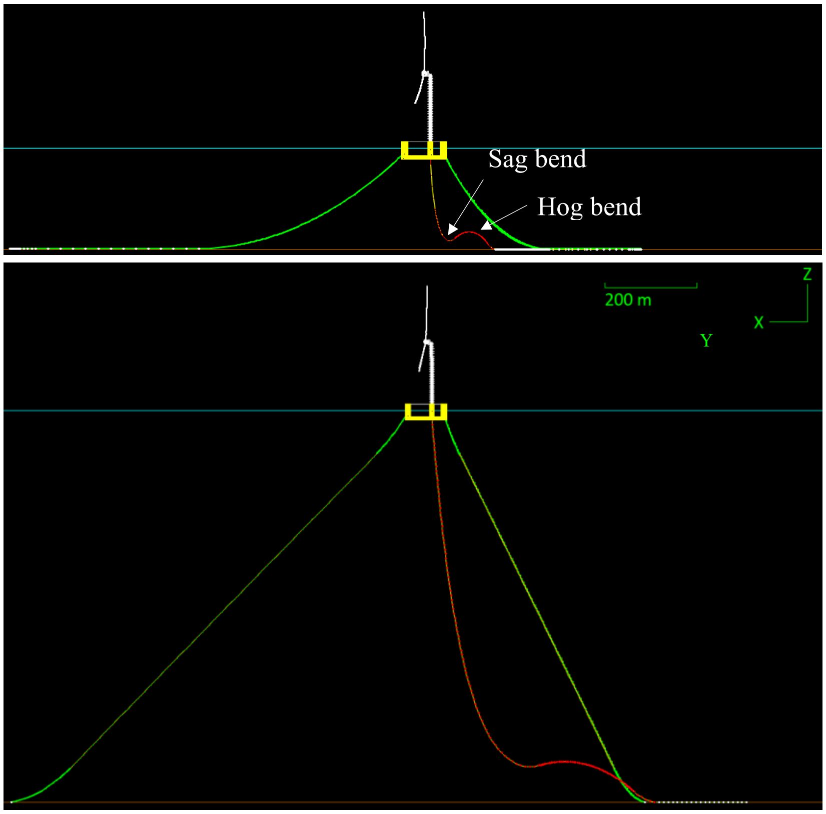

Figure 3.1. FOWT-CO_2 capture platform and flexible riser layout configuration (in red) for the: (top) shallow water case, and (bottom) deep water case.

Ancillary components - bend stiffener

During the preliminary design stages of the riser in the shallow water case, it was observed that the bending radius at the HOP was less than the riser's MBR. This is an undesirable situation to be avoided because of the risk of fatigue cracking, material deformation, and rupture, which can compromise the riser's integrity. In dynamic applications, bend stiffeners are designed to lock the motion of the line beyond its MBR and improve stress distribution over a controlled length[122,124,133]. They are usually made of a polymer material and have a tapered profile along their length, which is designed to provide

---

[xxxiii] The yield strength (σ_y) is an external input by the user. Ref.[133] provides an indicative range for typical flexible risers' yield strengths between 650-1,350 MPa. At this stage, this is a design choice, and we decided to start with the lower value of 650 MPa. Note that this value is very close to the yield strength of rolled carbon steel, a typical material used in tensile armours of flexible risers, which forms one of the main structural layers giving risers their tensile strength.

a gradual stiffness transition at the riser's end termination. For these reasons, we modelled a bend stiffener for our shallow water case, whose properties and profile are given in **Table 3.4** and **Figure 3.2**.

Table 3.4. Bend stiffener mechanical properties and configuration.

Property	Units	Value
ID	m	0.1
Density	tons/m^3	7.85
Young's modulus	GPa	212
Poison ratio	-	0.29
Length	m	10

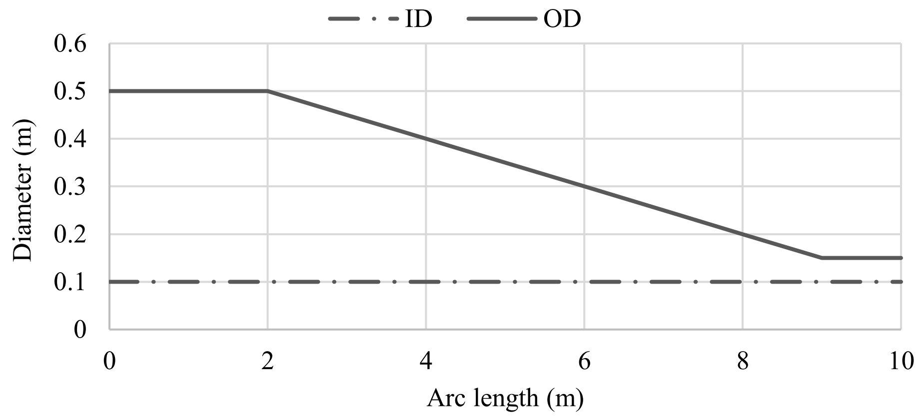

Figure 3.2. Bend stiffener profile along the arc length.

3.2.3. Moorings

For the shallow-water case (200 m), the mooring configuration was taken from the reference design for the IEA 15 MW UMaine VolturnUS platform[72], which used a three-leg catenary chain. For the deep-water case (850 m), no prior reference design was found and thus a mooring configuration was designed. The procedure followed is shown in the Appendices, section B, and here only the final design is provided in **Table 3.5.**

Table 3.5. Mooring line configuration for the deep-water case.

Line	Diameter (m)	Density (kg/m)	Axial stiffness (kN)	MBL (kN)	Arc length (m)
Chain	0.33	685	$3{,}270\cdot10^3$	22,286	100
Dyneema rope	0.04	9.06	2.725	10,771	600
Chain	0.33	685	$3{,}270\cdot10^3$	22,286	150

3.3. Methods

The FOWT-CO_2 capture platform with the riser is modelled in OrcaFlex^{TM} v11.3. To do that, we take existing files from Orcina for the IEA 15 MW RWT UMaine VolturnUS semisubmersible reference design[135] and change its inertial properties to match those of the FOWT-CO_2 mid scenario capture platform in ref.[57], see **Table 3.1**. Orcina used v.1.1.3 of the IEA 15 MW RWT. The published files for the IEA 15 MW RWT in OrcaFlexTM were validated against results with OpenFAST in ref.[57].

In section **3.2.2.1**, we justified how our CO_2 flow could be considered incompressible. As a result, the flow rate is constant over any cross-sectional area and over time (i.e. uniform and steady flow), which is modelled in OrcaFlex$^{\text{TM}}$ by setting a uniform flow.

3.3.1. Riser modelling

The flexible riser is modelled as a high-pressure hose, a category used in OrcaFlex$^{\text{TM}}$ to describe flexible risers with ID between 50-380 mm. Flexible risers in OrcaFlex$^{\text{TM}}$ are represented as lines, which are modelled according to the lumped mass approach (originally in Walton et al.[136]). In this method, lines are modelled as a discretized series of nodes and segments, in which all external forces, internal reactions and mass acting on the massless segments are lumped at the nodes at their ends.

3.3.1.1. Line segmentation

The number of nodes used to segment a line is a modelling decision made by the designer and depends on the complexity of the line's shape and length. For this reason, segmentations are not necessarily distributed evenly along a line's length and refinements may change across its different sections. Because the number of nodes is proportional to the number of differential equations that are required to be solved to characterise a system, it is good practice to optimise the number of nodes employed to model the different lines, this way helping to limit the computational time required. This was done for our flexible riser and mooring lines in both shallow and deep-water scenarios. Briefly, for each scenario, the curvature and effective tension (see section **3.3.1.3**) along the line's arc length were computed for two nodal configurations; one with a high number of nodes evenly distributed along the arc length (constant segment length of 1 m), and one with a lower number of nodes unevenly distributed (segment length varying from 0.5 m to 20 m). In the latter, a higher refinement was set in those regions where the curvature was higher (e.g. at the top, at the lazy wave in the case of the riser, and close to the TDP). To the sides of these, the segmentation was left coarser as the lines remained almost straight throughout the simulations. **Table 3.6** shows these two nodal configurations for the riser in the shallow water case.

Table 3.6. Shallow water case: riser nodal configurations.

Case	No.	Line type	Section length (m)	Segment length (m)	Cumulative no. segments
Finer	1	Riser	10	1	10
	2	Riser	90	1	100
	3	Riser	85	1	185
	4	Lazy wave	80	1	265
	5	Riser	125	1	390
	6	Riser	93	1	483
Coarser	1	Riser	10	0.5	20
	2	Riser	90	20	24
	3	Riser	85	2	66
	4	Lazy wave	80	1	146
	5	Riser	125	1	271
	6	Riser	93	20	276

1845

3.3.1.2. Numerical integration

To solve the equations of motion of the system[xxxiv], OrcaFlex^{TM} implements two numerical integration techniques: a semi-implicit Euler[137], and an implicit Generalized-α method[138]. By default, the OrcaFlex^{TM} files for the IEA 15 MW RWT UMaine VolturnUS semisubmersible reference design, upon which this work is developed, used the Generalized-α method. To determine which method would perform best for our FOWT-CO$_2$ platform, we compared both methods for the two water depth scenarios, with a tolerance of 0.0025 and a maximum of 100 iterations. When using the semi-implicit Euler, we found that the integration time step had to be on the order of 10^{-5} s, or three orders of magnitude smaller than the time step for the Generalized-α method (0.01-0.025 s), to converge to the same solution. Consequently, for the shallow water scenario, the semi-implicit Euler took over 1.5 days to run, while the Generalized-α took approximately an hour. Since both methods reached the same solution, but the Generalized-α was much faster, the remainder of this work is carried out using the Generalized-α method.

3.3.1.3. Pressurised steady flow

The influence the internal CO$_2$ pressure and flow have on our flexible riser is quantified here using its effective tension (T_e), von Mises stress (σ_{VM}), and curvature (κ).

Effective tension

The effective tension (T_e) is the resultant axial force acting on the flexible riser wall, including the contents and the displaced fluid column. In the case of a flexible riser with wall tension T_w, outer (A_o) and inner (A_i) cross-sectional areas, subject to external (p_o) and internal (p_i) pressures, respectively, and with an internal flow velocity (v_i) with a density ρ_i, the effective tension is formulated as[134]:

$$T_e = T_w - A_i p_i + A_o p_o - \rho_i A_i v_i^2 \tag{3.3}$$

Although expression 3.3 is convenient to understand the concept of effective tension of a pipe segment, this is often determined most simply by considering, at any point z, the equilibrium of the segment with the riser top end, and taking its top tension (T_{top}) and apparent weight[139–144]:

$$T_e(z) = T_{top} - \sum_{z}^{top} \left(W_a^{riser} + W_a^{fluid} \right) - \rho_i A_i v_i^2 \tag{3.4}$$

[xxxiv] The dynamics of the FOWT-CO$_2$ platform depend on the action of the external (e.g. wind, waves, current) and the internal forces (e.g. hydrostatic, fluid flow, rotor control) on the rotor, nacelle, tower, platform, and lines. OrcaFlex^{TM} represents this coupled aero-hydro-servo-elastic problem using the forced mass-spring-damper equation[271], which then solves through numerical integration, as described above.

$$M(p,a) + C(p,v) + K(p) = F(p,v,t)$$

Where $M(p,a)$ is the system inertia load, $C(p,v)$ is the system damping load, $K(p)$ is the system stiffness, and $F(p,v,t)$ is the system external load, with p, v and a being the position, velocity and acceleration vectors, respectively, and t the simulation time.

where W_a^{riser} and W_a^{fluid} are the apparent weights of the riser and internal fluid, respectively[xxxv]. Equation (3.4) reveals that the effective tension does not depend on the internal or external pressures, but on the riser's apparent weight and fluid density. Expression (3.3) is therefore rearranged to calculate the wall tension, T_w, from which one can obtain the tensile strain, $\epsilon_{tensile}$,

$$\epsilon_{tensile} = \frac{T_w}{EA_w} = \frac{T_e + A_i p_i - A_o p_o + \rho_i A_i v_i^2}{EA_w} \tag{3.5}$$

where E is Young's modulus, $A_w = A_o - A_i$ is the wall cross-sectional area, and EA_w is the axial stiffness. Note that equation (3.5) shows that the tensile strain is influenced by the internal and external pressures; indeed, the internal pressure term (which is positive), contributes to the tensile stretching of the pipe wall, whereas the external pressure term (which is negative) exerts a compression stress axially.

In OrcaFlex™, the total strain experienced by the flexible riser is comprised of four different sources; the tensile strain ($\epsilon_{tensile}$), which we just discussed, the bending strain, the expansion strain, and the Poisson effect axial strain ($\epsilon_{Poisson}$). Of relevance to our work, the Poisson effect axial strain is caused, as its name suggests, by the radial and circumferential stresses due to the net of the internal and external pressures,

$$\epsilon_{Poisson} = \frac{2\nu(A_o p_o - A_i p_i)}{EA_w} \tag{3.6}$$

where ν is the Poisson ratio ($\nu = 0.3$ for our flexible pipe[145–147], see **Table 3.3**). Put simply, the stretch/compression in the radial and circumferential directions caused by the internal and external pressures is followed by a compression/stretch axially. An undesired - and admittedly counterintuitive - situation resulting from this can occur when a pipe buckles when subjected only to an internal pressure (see proof by Palmer and Baldry[148]). DNV GL provides guidance on how to prevent buckling due to the influence of hydrostatic pressures[121], which can happen for negative effective tensions.

Comparing (3.5) and (3.6), one can see that the internal pressure can contribute to both the pipe's axial stretching and compression (likewise for the external pressure). However, because equation (3.4) is factored by the Poisson ratio, the Poisson effect axial strain does not contribute as much as the tensile strain.

The internal pressure is set at the inlet according to the value in **Table 3.2**, and varies along the riser only because of the weight of the fluid column (recall that OrcaFlex™ does not model wall friction), see **Figure 3.4**.

A first static estimation of the terms in (3.3) at the riser's top end ($p_o = 202.8\ kPa$) for the case of maximum internal pressure ($p_i = 35$ MPa) and maximum flow ($v_i = 3.9\ m/s$) provides an indication of the relative importance of each component; $T_w = 126.2\ kN$, $A_i p_i = 68.7\ kN$, $A_o p_o = 0.78\ kN$, and $\rho_i A_i v_i^2 = 0.057\ kN$. The force produced by the internal pressure is about half the wall

---

[xxxv] The apparent weight of a body submerged in a fluid is defined as the difference between its true weight and the buoyancy force exerted by the fluid on the body.

tension; two orders of magnitude greater than the external pressure term, and three orders greater than the force produced by the internal flow. While the internal and external pressure terms can vary along the riser with the water depth due to the fluid column weight, the internal flow term remains constant throughout the riser's length for steady flows, such as ours (see next section for additional information). Consequently, the force from the internal flow is not expected to contribute significantly to the riser's effective tension, which we will verify with the simulations in this work.

In summary, given that the effective tension does not depend on the internal pressure, and the force from the flow is not expected to be significant, this means that the three design situations considered – maximum pressure and no flow, maximum pressure and maximum flow, and no pressure and no flow – should all have the same effective tension per each load case.

Internal flow

For pipes with constant cross-section and steady flow speeds, the force due to the internal flow is constant and it does not depend on the curvature or on the flow direction. Similar to the internal pressure, the steady flow causes a stretching force on the pipe walls. When the fluid flows along curved sections of the riser, the change of fluid direction (i.e. momentum change) causes additional forces on the riser walls which are dependent on the change of flow direction[xxxvi]. However, experiments on a U-shaped flexible riser proved these forces to be generally negligible for steady flows[149], and so some standards ignore them[121]. Although likely true for our case too, this is checked in the results sections.

von Mises stress

The von Mises effective stress (σ_{VM}) can be defined as a uniaxial tensile stress producing the same distortion energy as the actual combined applied stresses. It is an equivalent stress widely used as a yielding criterion ($\sigma_{VM} < \sigma_y$) and describes the combined axial (tensile and bending) and shear stresses acting on a structure, which for a pipe can be expressed as:

$$\sigma_{VM} = \sqrt{(\sigma_e + \sigma_b)^2 + 3\tau^2} \tag{3.7}$$

where σ_e accounts for the effective tensile stress ($\sigma_e = \frac{T_e}{A_o - A_i}$), σ_b is the bending stress, and τ is the shear stress ($\tau = \frac{(p_i - p_o)A_i A_o}{(A_o - A_i)A_r}$), with $A_r = \pi r^2$ being the cross-sectional area at a radial distance r from the pipe's centre, $ID < 2r < OD$. Note that the effective tensile stress does not depend on the internal and external pressures, and is constant across the riser's cross section, but the bending and shear stresses are not; the bending stress is maximum at the outer surface, whereas the shear stress is maximum at the inner surface[xxxvii]. To account for that, OrcaFlex™ reports the maximum von Mises stress throughout the cross section, which we also use in the results section.

[xxxvi] These are the centrifugal and Coriolis forces, with the latter only applying when the riser is moving.

[xxxvii] The shear stress is related to the radial and circumferential (i.e. hoop) principal stresses through Lamé's equations for thick-walled pipes. Thick-walled pipes have a wall thickness comparable to its inner diameter – in our case, the wall thickness is 0.02 m, and the inner diameter is 0.05 m, so our riser can be treated as a thick-

Curvature

In OrcaFlex™, the curvature at any node is calculated by taking the ratio of the angle between its two adjacent nodes and the sum of its segment lengths. The reciprocal of the curvature is the bending radius, which is usually checked during design stages to ensure its value stays above MBR. An empirical relation to determine MBR for flexible risers in dynamic operations was provided by ref.[133] as:

$$MBR = 8 - 12 \cdot OD \tag{3.8}$$

Which for our flexible riser with $OD = 0.07\ m$ becomes $MBR = 7.2\ m$, or a maximum curvature of 0.14 m^{-1}.

3.3.2. Site description

The wind and wave resource used to define the load cases in this section was characterised in previous work[57], and corresponds to a location in Cascadia Basin (48.0° latitude and -125.6° longitude), off Vancouver Island (British Columbia, Canada). Although this site is at a water depth of 200 m, and is representative of the shallow water case, for simplicity its environmental resource is also used for the deep-water case, at a depth of 850 m. We acknowledge the limitation of this simplification, however, given the rapid changes in bathymetry in the area and the fact that our objective is not to provide a final riser design for the project sites, this seems a reasonable approximation. In addition, the original wind and wave states were derived for a null wind-wave misalignment, but here different wind directions are employed (see **Table 3.7**). Again, this is deemed acceptable because we are not doing a final design. Note that since ref.[57] did not consider the effects of ocean currents, these are discussed below as a result of their relevance in flexible riser dynamics.

3.3.2.1. Current

In general, ocean current velocity (v_c) has a spatial and temporal dependence, $v_c = v_c(x, y, z, t)$. However, in most cases, the current velocity at a given location (x, y) may be considered as a steady flow field, only dependent on the water depth, and can then be written as,

$$v_c(z) = v_{c,tidal}(z) + v_{c,wind}(z) + v_{c,circulation}(z) \tag{3.9}$$

where the total current velocity has been expressed as a sum of the tidal, wind-induced, and circulation currents. At our project location at Cascadia Basin, most of the current effects are wind-induced (as opposed to tidal or circulation), so from now on whenever we talk about ocean current we are referring to mean wind-induced current. Because of this major influence caused by the wind, it is assumed that both wind and current have the same direction.

---

walled pipe. For these types of pipes, G. Lamé (1852) saw that the circumferential and radial stresses vary with the radial distance, but that their sum remains constant at all points of the cross-section.

Given the value at the sea surface ($z = 0$), the mean wind-induced current along the vertical water column can be derived applying a power law[86], similarly to what would be done in the case of a wind profile:

$$v_{c,wind}(z) = v_{c,wind}(z=0)\left(\frac{d_0 + z}{d_0}\right), \qquad \text{for} - d_0 \leq z \leq 0 \tag{3.10}$$

Because of fluid viscosity, the magnitude of the wind-induced current speed dissipates with water depth, until it completely vanishes at the reference depth d_0, considered $d_0 = -50\ m$, ref.[86]. At the surface, the mean wind-induced current is maximum and is determined as:

$$v_{c,wind}(z=0) = kU_{1h,10m} \tag{3.11}$$

The mean wind-induced current is a function of the sea state, the wind fetch, and the atmospheric stability, which are encapsulated in the wind-current coupling coefficient (k), and a function of the wind speed, characterised by the one-hour sustained wind speed at 10 m height ($U_{1h,10m}$). To err on the conservative side, we took the largest value typically assumed for k in open ocean conditions, or $k = 0.03$. **Figure 3.3** shows the wind-induced vertical current profile for different current models; normal current model (NCM), and extreme current model (ECM) with return periods of one year (1-yr RP) and 50 years (50-yr RP).

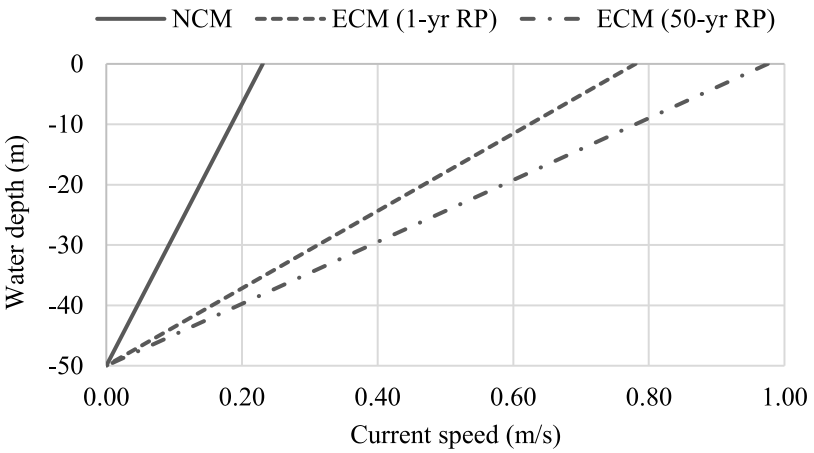

Figure 3.3. Wind-induced vertical current profile for normal and extreme current models.

Note how the current speed progressively decreases from the sea surface at $z = 0\ m$ to the reference depth, $z = d_0 = -50\ m$, at which the current speed was set to vanish.

3.3.2.2. Load cases

In this section, the design load cases (DLCs) used to evaluate the flexible riser dynamics are introduced (**Table 3.7**). These DLCs were selected to cover the most relevant operational and non-operational conditions of the flexible riser after it has been deployed, and were meant to simulate cases that aggravate the effects of the CO_2 flow dynamics.

To achieve that, two environmental regimes were applied: normal, and extreme conditions with a 50-year return period. These correspond to normal operational and parked conditions for the FOWT-CO_2 capture system, respectively. To represent normal conditions, we chose three different wind speeds within the power production regime of the turbine; cut-in speed, close to rated wind speed, and cut-out speed (4, 10, and 24 m/s). Wind and current directions of 0°, 90° and 180° with respect to the x axis (see coordinate system in **Figure 3.1**) were used to study the riser under different configurations, while waves were fixed at 180° for all cases. Note that the directions considered only needed to cover 180° because of the platform geometry. For all conditions, two seeds per wind speed were used, and the environmental conditions were ramped for 30 s. For normal conditions, simulations were run for 600 s, and 3,600 s for extreme conditions to account for the larger return period of the waves.

At the riser's inlet, two values were used for the CO_2 pressure in OrcaFlex^{TM}; zero pressure, and maximum pressure (p = 35 MPa), and two values for the CO_2 flow speed; zero speed, and maximum speed, equal to the erosional velocity, $v_{erosion} = 3.9\ m/s$. Note that, in the zero-pressure case, the pressure inside the riser can still be non-zero due to the weight of the CO_2 column (**Figure 3.4**). Also, even when the platform is parked, CO_2 still flows down the riser. This was done because the FOWT-CO_2 capture platform in ref.[57] was designed to have enough CO_2 storage to allow continued injection for four days (this way maximising injection). The same wind and wave seeds are used between the cases of no pressure and maximum pressure to ensure a fair comparison between scenarios.

Table 3.7. Design load conditions for the flexible riser in the FOWT-CO_2 system.

Config.	CSPD (m/s)	WSPD (m/s)	Hs (m)	Tp (s)	Wind dir. (°)	CO_2 flow	CO_2 pressure	Time
Normal operation	NCM: 0.23	NTM: 4, 10, 24	NSS: 2.14, 2.11, 5.79	NSS: 5.93, 5.89, 9.76	0, 90, 180	0, max	0, max	600 s
Parked, 50-yr RP	ECM: 0.98	EWM: 47.5	ESS: 11.83	ESS: 13.95				3,600 s

Our simulations do not include transient conditions, such as those experienced at the start-up/shutdown of the turbine under extreme events or maintenance activities, and during which the CO_2 flow may be interrupted or considered unsteady. Under these circumstances, the pressure and flow inside the riser may change rapidly, which can contribute to slugging.

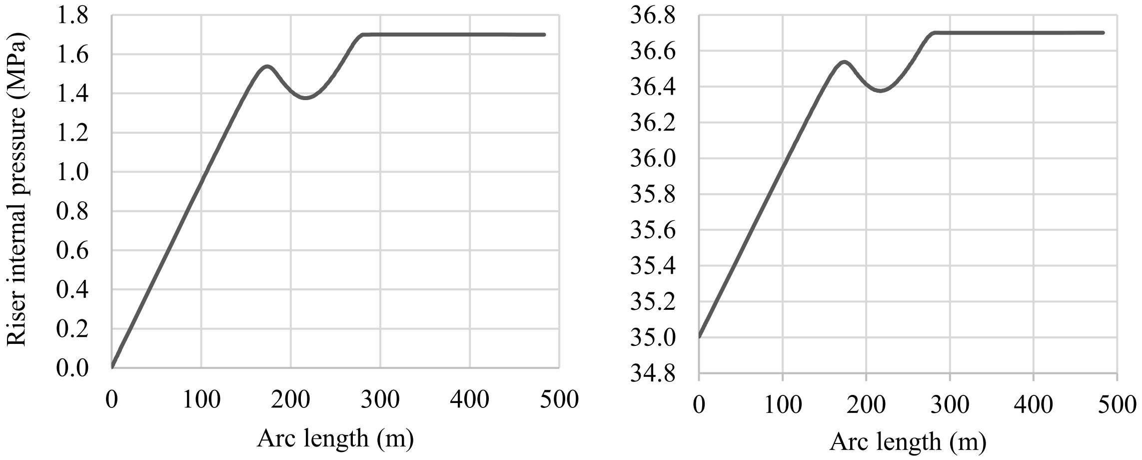

Figure 3.4. Shallow water: internal pressure along the flexible riser length for (left) zero pressure case, and (right) maximum pressure case.

3.4. Results & discussion

In the following sections, we present and discuss the time-averaged results of the different dynamic riser magnitudes (effective tension, von Mises stress, and curvature) for the DLC in **Table 3.7** with wind/current directions of 0 deg and a wind speed of 4 m/s. The results for the other wind/current cases (90 and 180 deg), wind speeds (10, 24, and 47.5 m/s), as well as the minimum and maximum in time of each simulation are not given because they do not provide further insights to the discussion.

3.4.1. Effective tension

Figure 3.5 presents the time-averaged effective tension results for the shallow and deep-water cases for DLC in **Table 3.7** with wind/current directions of 0 deg and a wind speed of 4 m/s.

The effective tension shows a consistent profile across the simulated cases coinciding with the geometry changes of the line, which have been enumerated in **Figure 3.5**, left. From the riser's top end until the beginning of the LWR's sag bend (number 1), the effective tension decreases linearly with the weight of the remaining hanging line. Approaching the hog bend (number 2), the effective tension increases slightly and reaches a local peak which accounts for the hanging line on both sides of it. After this, the additional upthrust supplied by the buoyancy modules in the lazy wave helps to counteract the weight, and the effective tension is slightly reduced throughout (number 3). At the end of it, another local peak marks the point where the buoyancy modules are removed, and the riser's effective tension decreases until the TDP (number 4). From there, the remainder of the riser rests on the seabed, and the effective tension remains constant.

As anticipated in section **3.3.1.3**, in both water depth scenarios, the effective tension for all design cases - maximum pressure and no flow, maximum pressure and maximum flow, and no pressure and no flow - appear identical. The force caused by the dynamic flow is then negligible in comparison to the axial tension.

In addition, the effective tension remains positive at all points along the arc length, which means that no buckling is produced.

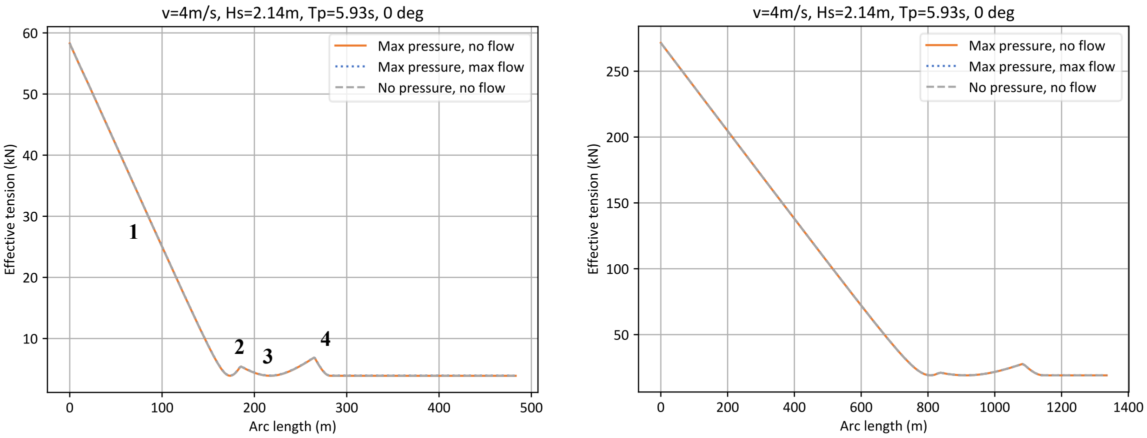

Figure 3.5. Mean riser effective tension for the (left) shallow water case, (right) deep water case. Zero and maximum pressure and flow configurations with 0° wind and current directions, and wind speed of 4 m/s.

3.4.2. von Mises stress

Figure 3.6 presents the time-averaged maximum von Mises stress results for the shallow and deep-water cases for DLC in **Table 3.7** with wind/current directions of 0 deg and a wind speed of 4 m/s.

Unlike the effective tension (equation (3.4)), the von Mises stress depends on the internal and external fluid pressures. As a result, **Figure 3.6** shows very different values for the maximum pressure and no pressure design cases, with a clear gap arising from the shear stress term in equation (3.5). However, both static and dynamic flow cases are seemingly identical, which means that the internal flow does not add a substantial stress to the riser, as anticipated in section **3.3.1.3**.

For both water depth scenarios, and all design and load cases, the von Mises stress curves show similar trends with two distinctive regions along the arc length. In the first stretch, from the riser's top end to the lazy wave section, the von Mises stress decreases linearly with the remaining line hanging weight. It is worthy to note, however, that the von Mises stress decreases at a much faster rate in the no pressure case than in the maximum pressure ones. This can be explained by the internal and external fluid pressures in the shear stress term (equation (3.7)), which increase with the water depth and counteract the decreasing line weight. In the second stretch, from the end of the riser's lazy wave section to its lower end, the von Mises stress is almost constant. In this region, the riser is mostly sitting on the seabed, so the stress caused by the line's own weight is minimal. Moreover, the internal and external pressure remain unchanged together with the water depth, so their contribution to the stress in the pressurised cases also remains constant.

Lastly, all DLCs show a von Mises stress much less than the yield strength ($\sigma_y = 650$ MPa). This means that a lower yield strength could have been chosen, potentially reducing the costs associated with the flexible riser.

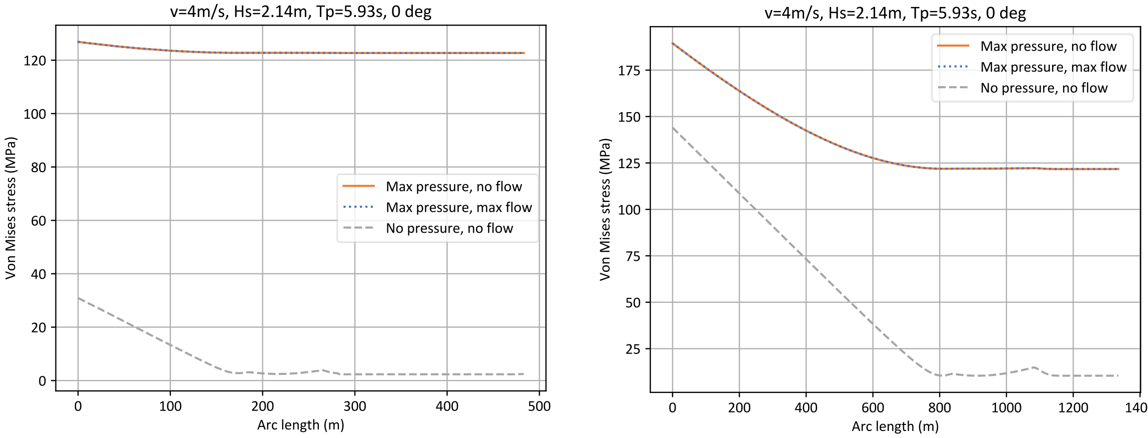

Figure 3.6. Mean riser von Mises stress for the (left) shallow water case, and (right) deep water case. Zero and maximum pressure and flow configurations with 0° wind and current directions, and wind speed of 4 m/s.

3.4.3. Curvature

Figure 3.7 shows the time-averaged curvature results for the shallow and deep-water cases for DLC with wind/current directions of 0 deg and a wind speed of 4 m/s.

As mentioned in **3.3.1.3**, the curvature of a flexible riser depends primarily on the effective tension and the external loads acting on it. The effective tension does not depend on the internal pressure, and we have already shown in the previous sections that the contribution from the internal flow is negligible. As can be readily seen, the curvature results shown in **Figure 3.7** agree with these previous findings since all design pressure and flow cases are identical.

Note that in all DLCs considered, the riser curvature stays well below the maximum curvature of 0.14 m^{-1} allowed (equivalent to a MBR = 7.2 m).

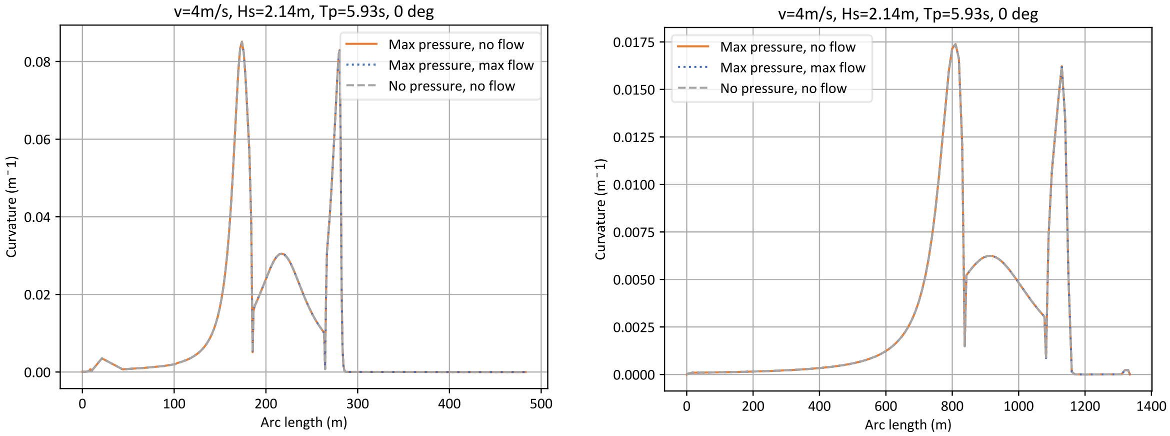

Figure 3.7. Mean riser curvature for the (left) shallow water case, and (right) deep water case. Zero and maximum pressure and flow configurations with 0° wind and current directions, and wind speed of 4 m/s.

3.5. CO_2 riser conclusions

In this paper, we designed and analysed a flexible riser system to transport CO_2 from a floating offshore wind turbine (FOWT) powered carbon capture system published in ref.[57]. Given the low flow rate in ref.[57] and typical maximum CO_2 flow speeds, this paper questioned the relevance of the pressurised internal flow effects on the riser dynamics. This was investigated by simulating the system in OrcaFlex™ at two water depth locations (200 m, and 850 m) and analysing the riser's effective tension, von Mises stress and curvature for a set of design load cases (DLCs); zero and maximum pressure, zero and maximum flow, with normal and extreme environmental conditions (**Table 3.7**). To exacerbate the dynamic effects of the pressurised internal flow, we chose a flexible riser with the smallest inner diameter (ID) available on the market, ID = 0.05 m (or 2 inches).

For all DLCs, it was seen that the flow effects from the circulating CO_2 inside the riser were negligible and had no effect on its dynamics. The effective tension and curvature, by definition, do not depend on the internal pressure, and so showed no variations between design pressures. However, through the shear term - equation (3.7) - the von Mises stress exhibited different values between the maximum pressure and no pressure cases.

The results show that the effective tension along the riser's arc length was always larger than zero, so for the analysis of these cases it could be said that no buckling occurred. Similarly, the von Mises stress met the yielding criterion, with maximum values reported much lower than the yield strength. Finally, the riser's maximum curvature experienced did not threaten its structural integrity, with values reported well below the inverse of the minimum bending radius. For the shallow water case (200 m), this was ensured during the pre-design phases using a bend stiffener at the riser's junction with the floating platform.

Concerning the question of whether the flexible riser for the FOWT-CO_2 capture system could be successfully modelled as a dynamic power cable with lower fidelity offshore wind turbine simulation tools, like OpenFAST, without overlooking relevant riser-dynamics phenomena; we have seen that the behaviour of the riser's effective tension and curvature are the same for the cases of maximum and zero pressure, and maximum and zero flow. In that regard, the results indicate that these main riser dynamics would not be affected were the riser modelled simply as a power cable, without internal pressure or flow. However, it was also shown that the von Mises stress depends on the fluid's internal pressure, and different values were reported for the cases with maximum pressure and no pressure. As such, this term could be easily incorporated into lower fidelity codes with mooring lines modelling capabilities (e.g. OpenFAST[128], HAWC2[150], Bladed), this way completing the stress characterisation of risers with similar configuration as ours.

3.6. Extension to e-fuels risers

In section **3.1.2**, we briefly introduced the potential applicability of our results to other fluids of interest and fundamental to the green transition, such as hydrogen (H_2). This is further elaborated next.

Firstly, we assume the same riser configuration as for the CO_2 shallow water case (ID = 0.05 m, OD = 0.07 m) and determine the transport conditions for H_2. When transported via pipeline, hydrogen is expected to be injected as a gas[xxxviii] and can be done so at a pressure of 10 MPa and temperature of 300 K [151,152], which yields a density of $\rho_{H_2} = 7.6\ \mathrm{kg/m^3}$. Using the known mass flow from the ERM's Dolphyn project ($\dot{m}_{H_2} = 150 \frac{\mathrm{kgH_2}}{\mathrm{h}}$), the H_2 flow speed (v_{H_2}) was calculated by rearranging equation (3.2),

$$v_{H_2} = \frac{4Q_{H_2}}{\pi ID^2} = 2.79\ m/s \tag{3.12}$$

Once the riser and flow configuration were known, we ran the same DLCs as for the CO_2 case, **Table 3.7**. Results for the time-averaged effective tension, von Mises stress and curvature in the shallow water case with wind/current directions of 0 deg and wind speed of 4 m/s are presented below in **Figure 3.8**; the results for the other wind/current cases (90 and 180 deg), wind speeds (10, 24, and 47.5 m/s), as well as the minimum and maximum in time of each simulation are not given because they do not provide further insights to the discussion.

The results for the transportation of H_2 via riser show similar trends to those using CO_2 examined before. Note that both fluids are less dense than seawater, but that the density of the hydrogen injected ($\rho_{H_2} = 7.6\ \mathrm{kg/m^3}$) is more than two orders of magnitude lower than that of the CO_2 case ($\rho_{CO_2} = 964\ \mathrm{kg/m^3}$). As a result, the H_2 effective tension is slightly smaller than that of CO_2, as described by equation (3.2). The effective tension and the curvature plots exhibit identical values between the different design pressure and flow cases, which means that the internal flow effects on the riser dynamics for the H_2 case also appear negligible. The values for the von Mises stress are substantially lower than those for the CO_2 cases, partly because of the reduction on the effective tensile stress (due to the smaller effective tension), but mostly because of the lower internal pressure inside the riser - shear term in equation (3.7). For the same reason, the von Mises stress shows different values for the maximum pressure and no pressure design cases. However, both static and dynamic flow cases are seemingly identical, which means that the internal flow does not add a significant stress to the riser either.

In summary, the same conclusions drawn in the CO_2 cases also apply for the H_2 cases. The results indicate that effective tension and curvature would not be affected were the riser modelled simply as a power cable, without internal pressure or flow. The shear term in the von Mises stress,

---

[xxxviii] Transporting hydrogen as a liquid poses many technical and efficiency problems due to the low temperature conditions needed.

which accounts for the effects of the internal and external pressures, however, needs to be incorporated when modelling the riser with lower fidelity codes.

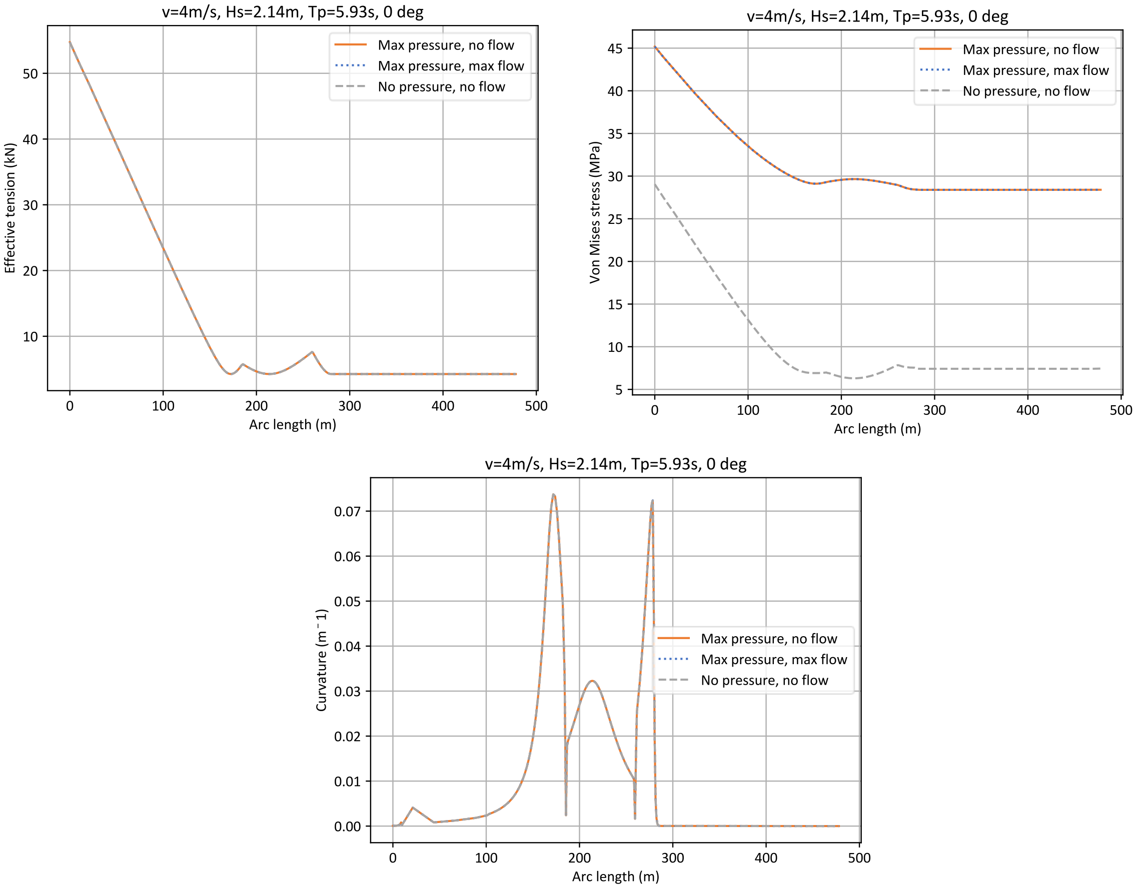

Figure 3.8. Shallow water and H_2 case: mean riser (top left) effective tension, (top right) max von Mises stress, and (bottom) curvature. Zero and maximum pressure and flow configurations with 0° wind and current directions, and wind speed of 4 m/s.

Acknowledgements

The authors would like to thank Heather Norton from the Solid Carbon team for her inputs concerning the riser flow conditions, Spencer Funk and Dr. Brad Buckham from the University of Victoria for their valuable discussions about modelling of lines, Nikki Forde from Flotation Energy Plc for sharing his expertise about design of flexible risers, and Michael Pullinger for taking the time to review this work.

3.7. Appendices

3.7.1. Riser layout

Below we review some of the main layout flexible riser configurations traditionally used in O&G[xxxix] and justify our layout choice.

- Free hanging catenary: it is the simplest and cheapest to install configuration for a flexible riser, suitable for floaters with low to moderate motions, and requiring minimal infrastructure. Because it is freely floating, the riser is more exposed to loading due to floater motions, especially in shallow waters. Around the TDP, the line may experience frequent impact when lifted off and lowered down on the seabed. In deep waters, the tension at the HOP can become greater due to the long, suspended length.
- Lazy/steep wave: in this configuration, buoyancy modules and weights are attached to a section of the riser's length to decouple the motion of the riser's TDP from the floater. The steep wave includes a subsea base to connect the riser to flowlines and a subsea bend stiffener procuring a nearly vertical connection at the seabed, which ensures a stable configuration even under changes in internal fluid density[123,134].
- Lazy/steep S: exhibits a similar line profile as lazy/steep wave, but instead of buoyancy modules clamped to the line, they use subsea buoys or arch systems to raise the riser section close to the TDP[123]. Because of this more complex and expensive equipment, lazy/steep S are usually only used if catenary and wave layouts are not suitable.

3.7.2. Mooring design

This section describes the procedure followed to design the mooring system for the deep-water case. First, using the same number of mooring lines as Allen et al.[72], we opted for a semi-taut mooring configuration rather than the preferred catenary in shallow waters. In deep waters, semi-taut layouts are typically less expensive and have a lower seabed footprint than catenaries.

[xxxix] A schematic representation of these traditional layouts can be seen in ref.[134], Figure 9.1.

Second, in ref.[153], the ratio of anchor radius versus water depth was plotted for different floating offshore platforms. At our water depth of 850 m, the ratio was 1.7 (30° angle with the seabed), which would give an anchor radius of 1,445 m. However, taking into consideration plans to scale up the FOWT-CO_2 capture concept to a farm, we questioned whether a different ratio would be better. Because such a farm will account for a CO_2 piping system (i.e. risers, export pipelines, and manifolds) in addition to the moorings, it may be beneficial to reduce the ratio of anchor radius versus water depth – thus decreasing the seabed footprint for the moorings - and leave a larger available area for the CO_2 piping system. For this reason, we used a unit ratio (45° angle with the seabed), which reduces the seabed footprint per mooring line by over 40%. It is worth noting that this will impose larger vertical loads on the anchors, which may require the use of a different type of anchor with respect to the shallow water case, but this lies outside the scope of this work.

Third, we used the mooring pretension of the shallow water case as a design constraint. This was done to ensure the floater draft and hydrodynamics would be kept as reasonably close as possible to the shallow water case, since this had already been validated in previous work[57].

Last, in the shallow water case, the mooring line was only composed of steel chain, whose weight was the principal mechanism limiting the floater's motion in the catenary configuration. In the deep-water case, however, to keep the same floater draft, the suspended chain section had to be limited due to the longer water column. As a result, chain was only employed at the top and bottom regions of the mooring line, while an AmSteel®-Blue fibre rope[xl] linked the region in between (**Table 3.5**). AmSteel®-Blue is a high-modulus polyethylene (HMPE) made of Dyneema® fibre providing high strength comparable to that of steel but at a fraction of the weight, which makes it buoyant. In contrast to steel chains, AmSteel®-Blue rely on their axial stiffness for their restoring capacity, which allows them to better absorb and dampen the dynamic forces acting on the floater. Being lighter than chains, they are also easier to handle and deploy, however, they are less resistant to abrasion and wear, which is why it is important to still use chain around the hang-off, touchdown and anchor sections of the line, where more damage of this type is expected.

3.7.3. Pressure losses

Because of its own dynamic viscosity, μ, and to frictional effects with the riser walls, the fluid inside the riser may be slowed down. The drop in pressure along the riser can be calculated through the Darcy-Weisbach equation:

$$\Delta p = \rho_{CO_2} f_D \frac{L}{2ID} \langle v \rangle^2 \tag{3.13}$$

Where f_D is the Darcy friction factor, L is the length of the riser across which the pressure drop is calculated, ID is the riser's internal diameter, and $\langle v \rangle$ is the mean flow velocity. The Darcy friction factor f_D is not a constant magnitude, rather it depends on the riser's surface roughness, ε, and the Reynolds number, Re,

---

[xl] https://www.samsonrope.com/commercial-fishing/amsteel--blue.

$$Re = \rho_{CO_2} \langle Q \rangle ID / \mu A_i \tag{3.14}$$

Where $\langle Q \rangle$ is the mean flow rate (0.001 m^3/s), and μ is the kinematic viscosity ($\mu = \rho_{CO_2} \nu$), equal to $\mu = 0.00011167\ \mathrm{Pa \cdot s}$ for CO_2 at 10°C[xli]. For turbulent flows such as ours, f_D is usually found by solving the Colebrook-White equation,

$$\frac{1}{\sqrt{f_D}} = -2 \log_{10} \left(\frac{\varepsilon / ID}{3.7} + \frac{2.51}{Re \sqrt{f_D}} \right) \tag{3.15}$$

This is an implicit expression in f_D and is commonly approached through numerical techniques. However, several approximated explicit forms exist depending on the values of Re and $\frac{\varepsilon}{ID}$. One such approximation was done by Swamee and Jain (1976),

$$f_D = \frac{0.25}{\left[\log \left(\frac{\frac{\varepsilon}{ID}}{3.7} + \frac{5.74}{Re^{0.9}} \right) \right]^2} \tag{3.16}$$

which is applicable in the following ranges:

$$5000 \leq Re \leq 10^8$$

$$0.000001 \leq \frac{\varepsilon}{ID} \leq 0.05$$

For flexible pipes, ref.[121] recommends using $\frac{\varepsilon}{ID} = \frac{1}{250} = 0.004$. Therefore, the Darcy friction factor turns out to be:

$$f_D = \frac{0.25}{\left[\log \left(\frac{\frac{\varepsilon}{ID}}{3.7} + \frac{5.74}{Re^{0.9}} \right) \right]^2} = 0.0055$$

For our flow speed of 3.9 m/s, the pressure drop becomes 0.39 MPa for the shallow-water scenario, and 1.06 MPa for the deep-water scenario, which represents less than 3% of the riser's internal pressure.

[xli] https://webbook.nist.gov/chemistry/fluid/.

Chapter 4.

Offshore Wind-Powered Direct Ocean Capture

This chapter has yet not been submitted to a journal for publication as we are currently assessing the possibility of applying for a patent.

Author contribution

Gerard Avellaneda Domene: conceptualisation, methodology, investigation, modelling, analysis, writing & editing. Curran Crawford: conceptualisation, analysis, supervision, review & editing.

Abstract

In the effort to contribute to the portfolio of solutions aimed at removing carbon dioxide (CO_2) from the atmosphere and reduce the impacts of climate change, we present a novel conceptual design for a direct ocean capture (DOC) system integrated onto a floating offshore wind turbine (FOWT) platform. Direct ocean capture is estimated to have an annual global capture potential of 5-40 $GtCO_2$ and could additionally help mitigate local ocean acidification. To date, improvements in DOC techniques have reduced carbon capture seawater volumetric requirements from 19 to 13 $m^3/kgCO_2$; while more efficient methods may still yield further savings, this paper explores a solution which could offer up to 15% additional gains from a systems approach. By taking advantage of the dissolved inorganic carbon (DIC) gradient in the ocean column, with progressively higher DIC concentrations within the first thousand meters, we design for four scenarios that treat seawater drawn from different depths: 20 m (Case 0), 100 m (Case 1), 200 m (Case 2), and 300 m (Case 3, with 15% higher DIC than Case 0). The energy intensity and levelized cost of carbon (LCC) of each case are then compared. Case 3 is estimated to require the least energy per unit of carbon captured, 3.4 $kWh/kgCO_2$ versus a maximum of 4.0 $kWh/kgCO_2$ in Case 0. However, because the change in DIC between consecutive depths peaks between Cases 0 and 1, and diminishes progressively thereafter, the rising linear costs associated with deeper water withdrawal eventually outweigh these returns. As a result, the estimated LCC is lowest for Case 2 ($1,108/$tCO_2$), which is almost 8% more cost-effective than Case 0 ($1,203/$tCO_2$). In conclusion, in an offshore DOC scenario, the gains from withdrawing deeper oceanwater with higher DIC concentration are expected to diminish with depth. Our findings suggest that the most cost-effective configuration intakes seawater from depths between 100 m to 200 m.

4.1. Introduction

Direct ocean capture (DOC) refers to techniques which remove carbon dioxide (CO_2) directly from ocean water by changing the pH of the treated water. Due to the chemical equilibrium at the air-sea interface, the withdrawal of CO_2 from the ocean enables further removal of CO_2 from the air, thereby ultimately reducing the atmospheric concentration and contributing to climate change mitigation efforts. In addition, DOC can help restore the natural chemistry of the ocean's surface[8], which has experienced declining values of carbonate ion concentration and pH by 25% as a result of the increased uptake and accumulation of anthropogenic CO_2 since the Industrial Revolution[154,155]. Such chemical changes, commonly referred to as ocean acidification, are known to negatively affect the health of marine organisms[156], might also pose a threat to the security of some ecosystem services, such as aquaculture and fisheries[156], and reduce the ocean's capacity as a carbon sink.

When CO_2 enters the oceans, it does not remain free and uncombined for long. It quickly dissolves into bicarbonate and carbonate ions, which together account for about 99% of all dissolved inorganic carbon (DIC) found on the surface, and only 1% of it remains as free CO_2. The rapid conversion of CO_2 into other forms enables the ocean to hold 50 to 60 times as much CO_2 as the atmosphere[157]. The proportion at which each of the DIC compounds is found is driven by, among other factors, seawater pH, which is best represented by a Bjerrum plot (**Figure 4.1**). This plot illustrates two possible pathways for DOC considered in the literature and increasingly by industry: an acid route[22,158–166] and a base route[23,164,167,168]. Here we focus on the acid route[xlii,xliii], in which the pH of seawater is reduced to promote a shift to free CO_2. The free CO_2 can then be stripped from seawater with a gas permeable membrane and near-vacuum pressures[22,162–164,166,169,170]), compressed, piped, and finally sequestered into a permanent geological reservoir such as offshore basalt[16,17,64,115], although the latter is not included in this study. Our estimates suggest that this overall multi-step process requires 3.4 to 4.0 kWh per kgCO_2 captured. In this article we propose to meet such energy requirements with an integrated floating offshore wind turbine-direct ocean carbon capture (FOWT-DOC) solution (section **4.3.5**).

[xlii] Alternatively, in an attempt to reduce the energy expenditure of seawater carbon capture, one may question the need for a pH-swing process at all and aim to remove the CO_2 already present in natural seawater without previously altering its pH[169,172]. However, note that at its naturally occurring surface composition, free aqueous CO_2 only accounts for 1% of the DIC (this increases to 2-3% at 300 m water depth); if the same surface seawater is acidified to a pH = 6, the concentration of CO_2 then increases almost 50 times, just like its mass flow rate. This 50-fold factor compensates for the additional expenses incurred during pH-swing techniques, which are less than 30% of the total seawater capture energy penalty[22]. Rivero et al. reached similar conclusions when employing a hollow fibre membrane contactor to directly strip CO_2 from seawater.

[xliii] In the base route, the pH of seawater is increased to promote the conversion of DIC to carbonate ion (CO_3^{2}), which then may combine with available calcium ion (Ca^{2+}) to form calcium carbonate ($CaCO_3$) and precipitate. The carbon contained in $CaCO_3$ is thus locked in a stable and solid mineral form, therefore achieving negative emissions.

Prior to this research, Patterson et al.[171] conceptualised a stand-alone offshore floating platform powering both DOC and seawater hydrogen (H_2) electrolysis. They considered a floating photovoltaic (FPV) solar farm[xliv] of 120 MW where the CO_2 captured (5.7 ktCO_2/year) through bipolar membrane electrodialysis (BPMED) was utilised to synthesise methanol (15.3 kt/year). The fuel was then retrieved and transported to its final users via tanker ship. Accounting for the carbon emissions of methanol combustion, they estimated that 3.6 ktC/year could be avoided with their FPV methanol facility. More recently, Yoshida et al.[172] combined both direct air capture (DAC) and DOC into a single 10 MW FOWT semisubmersible platform, with a total CO_2 capture capacity of 36 tCO_2/day. Their DOC system also featured a BPMED cell acidifying an electrolyte solution to pH = 6, with properties similar to sampled surface seawater from 5 m deep in the North Pacific[172]. BPMEDs have been investigated with increasing levels of CO_2 capture and energy efficiency[22,23,162,164]; for example, Eisaman et al.[162] achieved 59% capture efficiency at 5.5 GJ/tCO_2, while Digdaya et al.[22] reached 78.91% capture efficiency at 3.4 GJ/tCO_2.

A different approach was followed by Willauer et al.[163], who developed an electrolytic cation exchange module (E-CEM) that simultaneously synthesised H_2 from seawater. The E-CEM's polarity was operated in a reversible manner, thus reducing mineral deposition resulting from calcium and magnesium precipitation on the electrodes' surface and thereby improving electrical efficiency. Most recently, to reduce the cost and lifetime challenges associated with membranes employed in BPMED, Kim et al.[166] operated a membrane-free system made up of a pair of bismuth (Bi) and silver (Ag) electrodes with a chlorine-mediated charge balance. They achieved an 87% capture efficiency at a record low energy consumption of 2.7 GJ/tCO_2 and estimated cost of \$56/tCO_2. Our FOWT-DOC solution is based upon this novel, membrane-free approach.

The estimates quoted from refs.[22,162,166] only accounted for the energy and the costs associated with the electrochemical DOC system, and ignored penalties incurred during seawater intake, pretreatment, gas separation, and cooling. When these additional expenses are considered, the total energy and CO_2 capture cost are expected to increase to 20 GJ/tCO_2 and \$1,800-\$2,000/tCO_2[22,23]. The main factors behind the total system requirements are oceanwater intake (or transport) and pretreatment (filtration processes that remove algae, organic and sand particles, and other smaller impurities in order to guarantee the correct operation of all systems)[xlv]. The pumping work required

---

[xliv] FPV farms show advantages over their land-based counterparts, such as minimal shading and increased PV panel efficiency due to reduced surface temperatures[272]. Despite their rapid growth, with over 1 GW deployed since 2017, FPV farms are still at a lower stage of development than offshore wind farms (OWFs)[273]. This is partly because of the novelty and immaturity of the floating structures used in FPV, whereas OWFs started from a much advantageous position thanks to inherited technology from oil and gas[273,274].

[xlv] To produce fresh-drinking water, desalination plants must pump and pretreat seawater through different systems. Because of the shared infrastructures with DOC applications, many authors in the past have analysed potential DOC removal capacities when coupled with desalination plants[22,23,164]. For example, Eisaman et al.[23] extrapolated the global desalination capacity of 2015 (75 million m^3/day) to 2050 (800 million m^3/day) to estimate an approximated DOC capacity of 50 MtCO_2/year. As the authors point out, however, despite the economic savings, limiting DOC to coexist with desalination plants also limits the carbon removal capacity of DOC, effectively amounting to only "*1% of the estimated 6 GtCO_2/year (likely range of 2–12 GtCO_2/year) of negative emissions required by 2050 to prevent warming beyond 2°C*", ref.[23].

for intake and pretreatment, which ensures system pressures are kept within operational limits, depends on the volume of water needed per unit of carbon captured, herein called carbon capture seawater intensity. In previous works[22,162,166], the carbon capture seawater intensity kept decreasing from 19 to 13 $m^3/kgCO_2$ (assuming oceanwater with surface-like DIC levels of 2.017 mM), thanks to more efficient capture techniques, increasing from 59% to 87%. While there may be capacity for further technical improvements, in this paper we explore a solution that can readily offer up to 15% additional gains; DOC using deeper oceanwater, which has naturally higher DIC concentrations.

The amount of DIC is not constant through the water column, rather it is at its minimum near the ocean surface where photosynthesis and the activity of calcifying organisms is higher and increases with depth as respiration exceeds photosynthesis and organic matter decomposes, until it reaches an approximate constant value at around 1,000 m depth[173,174]. Because the exchange between atmospheric CO_2 and water at those depths is in the order of 1,000 years[155], if DOC is to become a viable tool in the fight against climate change, it must rely on shorter timescales, ideally less than a decade. For instance, the air-sea CO_2 ventilation timescale with the mixed layer can be in the order of one or two years (see Figure 1 in Jones et al.[175]), although this strongly depends on: (1) depth of the mixed layer, which can vary from 20 m to 500 m depending on season and latitude[176]; (2) stratification, where density differences impede vertical water (and CO_2) mixing - see Supplementary Figure S3 by Franco et al.[177]; (3) forced mixing e.g. enhanced by wind speed[xlvi]; and (4) carbonate chemistry. Considering that the ocean mixed layer has sequestered most of the historical anthropogenic CO_2, this encourages the deployment of DOC using oceanwater from this region[178].

To reflect this, our FOWT-DOC platform study draws oceanwater from four different water depths within or in the vicinity of the mixed layer: 20 m, 100 m, 200 m, and 300 m. The first depth is approximately equal to the floater draft, which means that oceanwater intake in this case is facilitated by a sea chest (section **4.3.4.1**). In the other three cases, a vertical pipe (with different lengths depending on the water depth drawing scenario) is attached to the floater hull instead (section **4.3.4.2**). Each increment in pipe length gives access to oceanwater with a larger DIC content per unit volume (up to 15% more at 300 m), but at a greater capital and operational cost. The investigation of such trade-offs is the main contribution of this work, in which we analyse whether the additional CO_2 captured per depth increment justifies the increased associated expenditures.

Measurement, reporting, and verification (MRV) are of paramount importance in any carbon dioxide removal (CDR) method, without which the effectiveness and impact of a CDR solution cannot be transparently assessed, and without which its integrity should be questioned. For example, we consider metered sequestration of CO_2 as opposed to ocean alkalinity enhancement (a base route), which adds alkaline materials to the ocean to shift the equilibrium toward absorbing more CO_2 from the atmosphere, but does not directly meter the carbon sequestered. Our proposed DOC solutions still include some MRV unknowns, which arise from uncertainties around air-sea CO_2 ventilation times (anticipated to being more significant as the depth of the water intake scenario increases), and that

---

[xlvi] The timescale of the air-sea CO_2 mixing is shorter in areas with high winds, favouring the location of DOC activities in these sites which, additionally, are better suited for offshore wind power.

can only be solved by in-situ characterisations (which lies beyond the scope of this research). These limitations are factored in the discussion of the trade-offs from each seawater intake case.

4.2. Direct ocean capture

When CO_2 in the lower atmosphere comes into contact with the upper ocean, it does not remain free and uncombined for long. It quickly dissolves forming carbonic acid (H_2CO_3), which further dissociates into bicarbonate (HCO_3^-) and carbonate (CO_3^{2-}), shown below,

$$CO_2(aq) + H_2O \leftrightarrows H_2CO_3 \leftrightarrows HCO_3^- + H^+ \leftrightarrows CO_3^{2-} + 2H^+ \tag{4.1}$$

The sum of the dissolved carbonate species is defined as the dissolved inorganic carbon (DIC), where the total concentration of H_2CO_3 and $CO_{2(aq)}$ is denoted as $[CO_2^*]$,

$$DIC = [CO_2^*] + [HCO_3^-] + [CO_3^{2-}] \tag{4.2}$$

$$[CO_2^*] = [CO_{2(aq)}] + [H_2CO_3] \tag{4.3}$$

The proportion of each DIC compound is represented in **Figure 4.1** by a Bjerrum plot[xlvii]. The energy consumed and the carbon captured by the DOC system depends partly on the amount of DIC, which is not evenly distributed through the water column. Similarly, thermodynamic parameters (such as oceanwater pH and temperature, density, oxygen and nitrogen concentration, and salinity) and water composition (such as the quantity of suspended solids and dissolved chemicals) also vary with water depth and, to a certain extent, influence the pretreatment and DOC system performance too[xlviii]. In the context of direct ocean capture, these considerations strongly encourage the exploration of different water drawing depths and their trade-offs.

[xlvii] Equations (4.32) to (4.34) in the Appendices, section **4.6.1**, were used to plot the Bjerrum diagram.

[xlviii] Section **4.6.2** in the Appendices provides a brief overview of the relevant thermodynamic magnitudes.

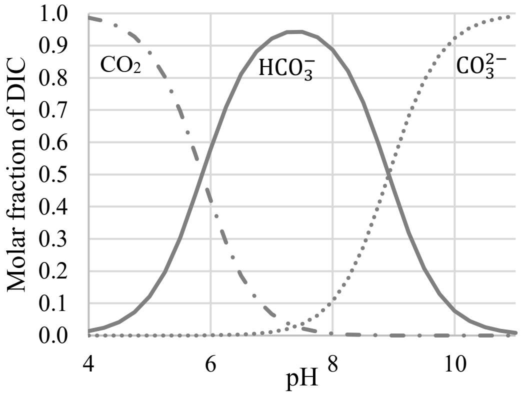

Figure 4.1. Bjerrum plot showing the three main species in the ocean carbonate system; carbon dioxide (CO_2^* = $CO_{2(aq)}$+H_2CO_3), bicarbonate ion (HCO_3^-), and carbonate ion (CO_3^{2-}).

4.2.1. Asymmetric chloride-mediated electrochemical pH swing

Our chosen DOC system is based on the membrane-free concept designed by Kim et al.[166], illustrated in **Figure 4.2** and briefly explained next. The system is comprised of two reversible electrochemical cells operating cyclically: in the first cell, seawater is acidified to a pH = 6 by the release of protons from the bismuth electrode, while the silver electrode releases chloride ions to preserve charge balance. Before entering the second cell, the acidified stream – now with a higher CO_2^* concentration – is degassed under vacuum in a hollow fibre membrane[22,162–164,169,170]. After stripping 87% of the DIC in the form of CO_2^* (known as DIC removal efficiency, η_{DIC}), the effluent stream is sent to the second cell where the bismuth and silver electrodes are regenerated with protons and chloride ions, respectively. The stream is then discharged into the ocean with an increased pH of 10-11, which will be restored to its surface value after capturing more CO_2 from the atmosphere. The system is operated in tandem until the first cell is depleted of protons, which marks the end of the cycle. The oceanwater flow to each cell and electric current between electrodes are then reversed, and the process starts again.

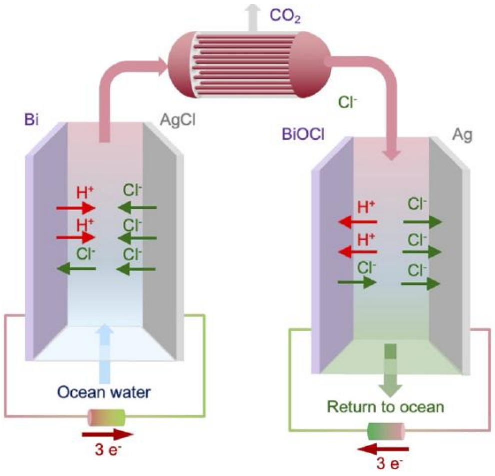

Figure 4.2. Asymmetric chloride mediated pH-swing direct ocean capture system concept by Kim et al.[166].

At typical ocean surface average values (pH = 8.1, DIC = 2.017 mmol/L), the carbon capture seawater intensity is 12.9 m^3/kgCO$_2$, and the total energy consumed by the electrochemical cells themselves, including Ohmic losses, is 174 kJ/mol CO$_2$ (1.1 kWh/kgCO$_2$)[166], equation (3.4). However, these magnitudes depend on seawater DIC and ionic conductivity, among other factors, both of which vary with water depth. Certainly, the higher the DIC per unit volume of seawater, the larger the CO$_2$ captured per unit of energy spent. Further, the higher the seawater ionic conductivity, the lower the resistance hydrogen and chloride ions encounter in the electrolyte (i.e. the lower the Ohmic losses). These two effects are encapsulated in the following expressions:

$$e_{cells} = e_{echem} + e_{Ohmic} \tag{4.4}$$

$$e_{echem} = \frac{1}{\dot{m}_{CO_2}}\left(V_{acid} I_{acid}^{H^+} + V_{alkal} I_{alkal}^{H^+}\right) \tag{4.5}$$

$$e_{Ohmic} = \frac{2rFi_{cell}\delta_{cell}}{\eta_{FE}\lambda_{ow}M_{CO_2}} \tag{4.6}$$

Equation (4.5) describes the electrochemical energy (e_{echem}) necessary to acidify and alkalinize the input seawater stream[xlix]. In (4.5), $\dot{m}_{CO_2}$ is the mass flow rate of CO$_2$ captured, V_{acid} and V_{alkal} are the voltage difference between electrodes in the first (acidifying) and second (alkalizing) cells, respectively, and $I_{acid}^{H^+}$ and $I_{alkal}^{H^+}$ are the absolute partial current carried by protons in the first (acidifying) and second (alkalizing) cells, respectively. Equation (4.6) describes the Ohmic losses (e_{Ohmic})[166], which refers to the voltage drop that occurs when the ionic current passes through the electrolyte (in this case, seawater).

In (4.6), r is the ratio of electron transfer to protons (equal to 3/2 according to the system represented in **Figure 4.2**), F is the Faraday constant (96,485 C/mol), i_{cell} is the cell current density, δ_{cell} is the distance or gap between the electrodes in each cell, η_{FE} is the Faraday efficiency (equal to 92%[166]), λ_{ow} is the seawater ionic conductivity, and M_{CO_2} is the molar mass of CO$_2$ (44 g/mol). The electric and dimensional characteristics of the acidifying and alkalizing cell used are taken from ref.[166] for their suggested prototype configuration; $V_{acid} = 0.7\,V$, $V_{alkal} = 0.1\,V$, $i_{cell} = 76\,mA/cm^2$, and $\delta_{cell} = 1\,mm$.

The total energy consumed by the electrochemical cells does not account for the energy expenses related to oceanwater intake, pretreatment, gas separation (both for nitrogen and oxygen degassing, and for carbon dioxide stripping), and compression, which we refer to collectively as ancillary energy services. The expressions implemented to calculate them are primarily based on previous work by Matsumiya et al.[179] and are introduced in section **4.3.5.1**. The effects the different water withdrawal depth scenarios have on the ancillary energy services are discussed in section **4.4**.

[xlix] The formulation of (4.5) is not explicitly given in ref.[166], so it is derived from first principles in the Appendices, section **4.6.1.**

4.3. Methods

The previous section gave an overview of the fundamentals and characteristics of the DOC system, which is integrated into and powered by a stand-alone, floating offshore wind turbine (FOWT) platform. Once captured, the CO_2 is compressed on-board and retrieved via pipeline to the subseafloor (**Figure 4.3**), from where it could in principle be exported to a basalt sequestration site. That final step, however, lies beyond the scope of this study. The next section describes the process followed to size the DOC system and presents the water intake depth scenarios studied.

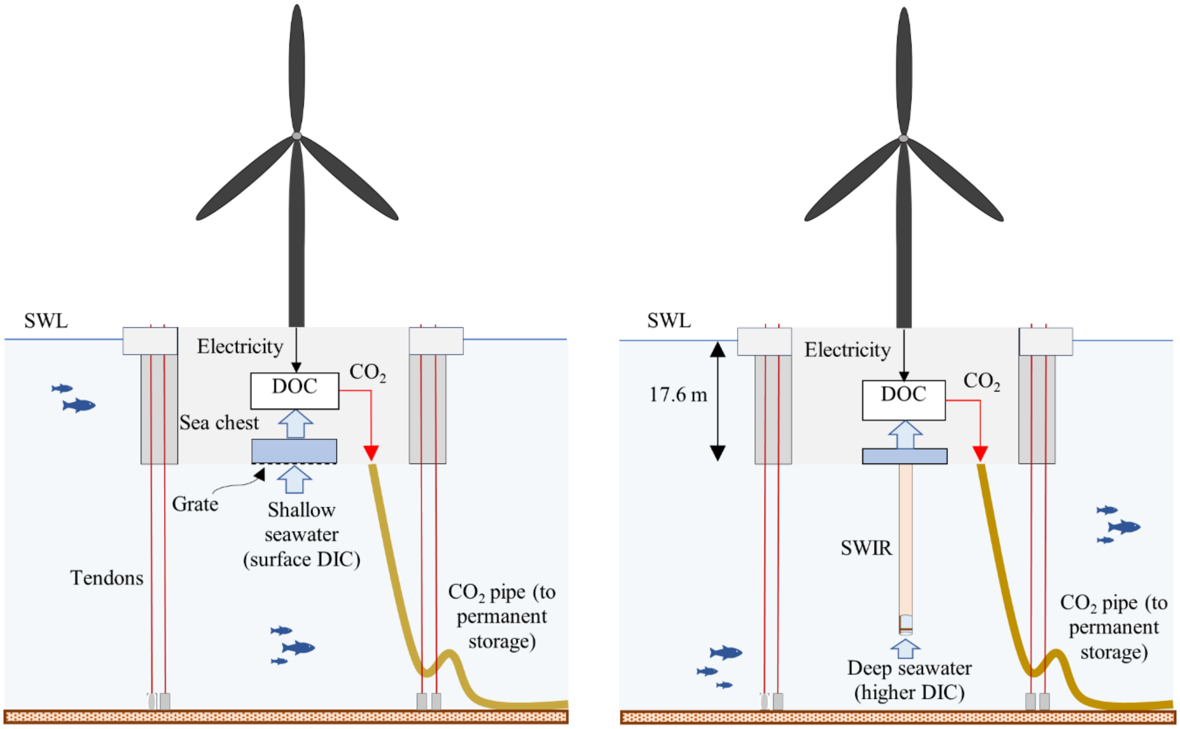

Figure 4.3. Depiction of the conceived FOWT-DOC system using (left) seawater from 20 m depth, at the vicinity of the platform bottom (Case 0), and (right) seawater withdrawn from 100, 200, and 300 m water depth (Cases 1, 2, and 3, respectively). The DOC equipment is placed at the base of the hull (with an assumed concrete thickness of one meter), at around 16.6 m water depth.

4.3.1. Design approach

The rated power of the DOC system is designed to match the wind turbine's, which is based on the IEA 15 MW RWT[73]. The energy available for DOC is equalled to the annual energy production from the turbine (AEP), which is the sum over all working wind speeds ($v_i = 3$ to $25\ \mathrm{m/s}$) of the product of the turbine's power ($P_{WT}(v_i)$), the probability of occurrence of each wind speed ($p(v_i)$) at the project site[1], the number of hours in a calendar year (equal to 8,766 for a year with 365.25 days), and

---

[1] Determined by a Weibull distribution.

an availability factor (assumed as $A_{wind} = 82.5\%$ as per ref.[180]), which accounts for mechanical inefficiencies, electrical losses, and turbine downtime due to planned and unplanned maintenance.

$$AEP = 8{,}766 \cdot A_{wind} \sum_{i}^{N} p(v_i) P_{WT}(v_i) \tag{4.7}$$

At the project site (47.614˚N, -125.771˚W), this yields a capacity factor of 60%. Knowing AEP and the aggregated carbon capture energy intensity of all elements in the DOC system (e_{DOC}) – including ancillary energy services[li] – the annual carbon captured and sequestered ($m_{year}^{CO_2}$) can be calculated as the quotient of both:

$$m_{year}^{CO_2} = \frac{AEP}{e_{DOC}} \tag{4.8}$$

The scenarios considered here explore how e_{DOC} varies when drawing seawater from different water depths. This is computed as the sum of all individual carbon capture energy intensities (total energy intensity consumed by the electrochemical cells, seawater pumping, gas separation, and compression):

$$e_{DOC} = e_{cells} + e_{pumping} + e_{degas} + e_{compression} \tag{4.9}$$

4.3.2. Design scenarios

The FOWT-DOC platform is assumed to sit in a water depth of 350 m, and draws oceanwater from different water depths: from the vicinity of the platform at around 20 m depth, and then subsequently from deeper points at 100 m, 200 m, and 300 m – the different intake systems are presented in section **4.3.4**. In situ and modelled oceanographic data for each depth were retrieved from the Global Ocean Data Analysis Project (GLODAPv2.2023) and the Thermodynamic Equation Of Seawater (TEOS-2010)[181,182] for a site in Cascadia Basin (47.614˚N, -125.771˚W), in the Pacific Northeast, where the Solid Carbon team is assessing the viability of CO_2 sequestration in deep-sea basalt. The data collected and derived is shown in **Table 4.1**.

Table 4.1. Oceanographic data from different water depths (20 m, 100 m, 200 m, 300 m) at a point in the Pacific Northeast (47.614˚N, -125.771˚W)[181,182].

	Units	Case 0	Case 1	Case 2	Case 3
Water intake depth	m	20	100	200	300
Water intake temperature	˚C	14.3	8.5	7.2	6.2
Density	kg/m^3	1,023	1,026	1,027	1,027
(Practical) salinity	-	31.5	33.7	33.9	34.0
Salinity	g/kg	31.66	33.87	34.12	34.17
Ionic conductivity	S/m	3.84	3.55	3.45	3.37
DIC concentration	mmol/L	2.02	2.24	2.31	2.33

[li] See section **4.3.5.2**; an energy storage system is used to deal with short-term wind power fluctuations and control the variable energy influx.

pH	-	7.86	7.50	7.38	7.37
Concentration of oxygen	mol/m^3	0.275	0.137	0.0758	0.0725
Concentration of nitrogen	mol/m^3	1.64	7.14	13.9	20.9

Despite almost equal depth increments between each case, the largest variation for any of the oceanographic magnitudes reported is observed between Cases 0 and 1 (for DIC and pH, this is illustrated in **Figure 4.4**). This layer of significant temperature, salinity and density variations is called pycnocline. Immediately below the pycnocline, the rate of change slows considerably, hence the minor differences between Cases 1, 2, and 3.

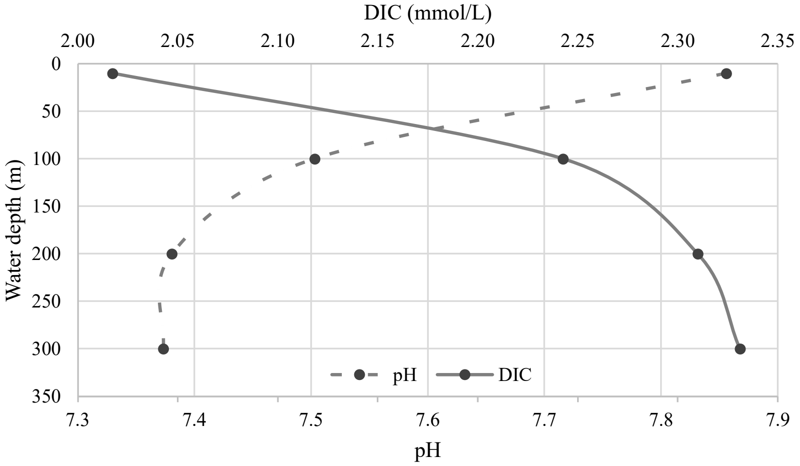

Figure 4.4. Variation of pH and dissolved inorganic carbon (DIC) with water depth for the four cases analysed [181].

As explained in section **4.6.2** in the Appendices, in mid latitudes salinity increases with depth, while temperature and ionic conductivity decrease. When brought to the surface where the FOWT-DOC platform sits, the salinity of the parcel of water for Cases 1, 2, and 3, which is a conservative property, does not change. However, since temperature and ionic conductivity are not conservative, their values are only preserved if transported adiabatically. This opens up the possibility of two further scenarios: adiabatic (AD) and nonadiabatic (NAD) transport, in which the seawater intake pipe prevents or permits heat exchange with the surroundings, respectively. As a result, the seawater intake temperature at the collection point (**Table 4.1**, at the lower end of the intake pipe) and at the platform entry point (**Table 4.2**, at the upper end of the intake pipe) are the same when transported adiabatically. The consequences both types of transport have on the system costs are analysed in the results section.

Table 4.1 also shows how the concentration of dissolved O_2 and N_2 vary throughout the water intake depths considered. As expected, the concentration of O_2 decreases while that of N_2 increases. Therefore, their aggregate effect on the gas separation energy intensity (e_{degas}) cannot yet be anticipated, additionally depending on water temperature and CO_2 mass flow rate.

Table 4.2. Thermodynamic values at the platform entry point for the design scenarios, and for the adiabatic (AD) and nonadiabatic (NAD) transports[181,182].

	Units	Case 1	Case 2	Case 3

	-	AD	NAD	AD	NAD	AD	NAD
Temperature	˚C	8.5	14.3	7.2	14.3	6.2	14.3
Density	kg/m^3	1,026.3	1,025.2	1,026.7	1,025.4	1,026.8	1,025.4
Ionic conductivity	S/m	3.55	4.08	3.45	4.11	3.37	4.12

4.3.3. Floating wind turbine (FOWT) platform

In previous research, the authors designed a direct air capture (DAC) system integrated into a FOWT platform[57]. Given the spatial footprint of DAC, its necessity to operate in open environments, and encouraged by previous initiatives in offshore wind-powered hydrogen production[67], the authors surmised that a semisubmersible floater-type with a large, exterior platform deck area would be best suited for the application. In comparison, the space claims of DOC may be less significant, and it does not need to be placed out in open-air to operate. As a result, other floating platform typologies, such as spars or tension-leg platforms (TLPs), with less waterplane area and potentially cheaper than semisubmersibles[183,184], may be more suitable for our current DOC purposes. To decide on the best typology, we assess the advantages and disadvantages of typical spars and TLPs (Appendices, section **4.6.4**) based on the recent exhaustive review by Edwards et al.[184]. Briefly, thanks to their high-stiffness tendons, TLPs experience less motion and accelerations than semisubmersibles and spars. To date, we ignore what accelerations a DOC system can sustain under normal performance levels, however, it seems reasonable to assume that minimising the accommodations required for optimal DOC operation strengthens our business case. In this regard, TLPs become more attractive alternatives than spars.

Amongst the FOWT TLPs reviewed[185–190], the CT-BOS TLP[190] is preferred for its readily available internal space, where all components of the DOC system can be accommodated, and for its inherent stability during transport and installation (which has traditionally been a major drawback of TLPs). The CT-BOS TLP, compatible with the IEA 15 MW RWT[73], is a nearly rectangular floater made of concrete, with a side length and a breadth of 45 m, a height of 19.6 m (with a freeboard of 2 m), and a mass of 20,000 tons. Concrete is less expensive than steel and, in general, FOWT floaters made of concrete have a lower carbon footprint than steel ones[191], which could be further reduced if combined with CO_2 sequestration in the concrete formulation (see e.g. CarbonCure[192]). That said, the final choice of concrete- or steel-built foundations requires a multi-variable approach, in which options for site recovery (returning project sites to a similar state as before the project) and recyclability, among many other factors, ought to be evaluated[lii].

Considering the CT-BOS TLP floater mass and dimensions, and assuming a uniform concrete distribution (density of 2.5 tons/m^3) with a material thickness of one meter, the useful internal volume is estimated as 32,169 m^3. In comparison, the DOC system has an approximated mass of 500 tons (or 2.5% of the CT-BOS TLP) and a volume of 2,500 m^3 (see description of the main components in the next sections). Therefore, the integration of the DOC equipment onto the CT-BOS TLP is not anticipated to have major impacts on the dynamics of the system worth pursuing any further giving the current conceptual stage (see similar discussion for our previous FOWT-DAC concept[57]).

[lii] See Velenturf[275] for a discussion on implementing a circular economy framework in offshore wind.

4.3.4. Seawater intake system

As the name indicates, the seawater intake system enables the entry of oceanwater into the DOC system. The seawater intake system employed in Case 0 is different to that for Cases 1, 2, and 3. In Case 0, seawater is drawn directly from the vicinity of the platform bottom via a sea chest. In the three other cases, a vertical pipe - formally known as seawater intake riser, or SWIR - is attached to the floater hull instead.

4.3.4.1. Sea chest

Sea chests are recesses built below the water line in the hull of ships that facilitate pumping seawater into internal pipe systems (**Figure 4.5**), typically for temperature control and water provision purposes. Their entry area is protected by bolted or welded grates (15-35 mm gaps) used to block large debris, followed by removable strainers (5-20 mm holes)[193]. Grates are made of hard stainless steel, with grades specifically designed for the marine environment and best suited to reduce corrosion (e.g. 316 L). Low oceanwater speeds, such as those expected in our moored FOWT-DOC platform, make sea chests and their piping systems an ideal environment for biofouling (i.e. the undesired accumulation of organisms on immersed structures). Biofouling in sea chests and seawater piping systems may reduce operational flow speeds, increasing pumping needs and ultimately economic costs. Marine Growth Preventive Systems (MGPS) are the best strategy to initially reduce their appearance, as reactive management is costlier, more labour-intensive, and time-consuming[194]. For example, on surfaces and piping systems, the International Maritime Organisation[195] recommends the installation of antifouling coatings, sacrificial anodic copper and chlorine-based dosing systems[liii]. Regular on-site annual inspections and maintenance activities are still highly recommended.

4.3.4.2. Seawater intake riser (SWIR)

Seawater intake risers (SWIRs) are regularly installed on floating offshore oil and gas (O&G) vessels and platforms to withdraw cold seawater from deeper layers, thereby helping to regulate the temperature of equipment and working fluids, and improving process efficiencies[196]. Similar grates to those employed in sea chests (15-35 mm gaps) are usually installed at the deeper end of SWIRs to prevent the entry of large debris. To protect the SWIR inner walls from erosion, the flow speed (v_{ow}) is limited by the following empirical relationship[132]:

$$v_{ow} < \frac{122}{\sqrt{\rho_{ow}}} \tag{4.10}$$

At the respective seawater densities (ρ_{ow}) for Cases 1, 2, and 3 (**Table 4.1**) and after applying a 1.25 safety factor, the resulting flow speed is $v_{ow} = 3.0\ m/s$. Together with the design flow rate ($\dot{V}_{ow}$), this determines the SWIR internal diameter (ID_{SWIR}),

---

[liii] When exposed to seawater, copper anodes undergo galvanic corrosion (sacrificial dissolution), releasing copper ions that inhibit the settlement and growth of marine organisms. Chlorine-based dosing systems release chlorine in situ via electro-chlorination which kills organisms. Note that this may affect the chemical reactions of chlorine-mediated DOC systems, such as the present case, but a full investigation of these lay outside our scope.

$$ID_{SWIR} = 2\sqrt{\frac{\dot{V}_{ow}}{\pi v_{ow}}} \tag{4.11}$$

With the required DOC system flow rates (27,700-28,350 m^3/h), the internal diameter (ID) of the SWIR then becomes $ID_{SWIR} = 1.5 - 1.6$ m. Although typical IDs used in floating O&G range from 0.50 to 0.75 m, from an engineering and economic perspective, it is preferable to employ one single yet larger pipe than multiples ones[196]. Certainly, with their free lower end and to reduce bending loads induced by waves and currents, certain sections of SWIRs are constructed using lightweight, low stiffness materials. However, this also increases their deflections and raises the likelihood of interference when multiple SWIRs are installed in close proximity. Moreover, the internal flow in narrow pipes experiences larger frictional forces and thus larger head losses. Lastly, capital and operational expenditures for a single, larger pipe are lower than for multiple, smaller ones. For these reasons, we proceed with our conceptual design assuming a single SWIR with $ID_{SWIR} = 1.5 - 1.6$ m, leaving for future work additional design for manufacture exercises. For stability purposes and to prevent interference with the CT-BOS tendons, the pipe is located at the geometrical centre of the floater base. The SWIR's length differs between Case 1, 2, and 3, and is calculated as the pertinent water intake depth minus the platform draft, yielding $L_{SWIR}^{Case\ 1} = 82.4\ m$, $L_{SWIR}^{Case\ 2} = 182.4\ m$, $L_{SWIR}^{Case\ 3} = 282.4\ m$.

4.3.5. FOWT-DOC design

A detailed illustration of the DOC system processes, including the main ancillary services, is shown in **Figure 4.5**. For simplicity, the sea chest is depicted as the seawater intake system but note that the main operating blocks would still be the same with the SWIR. Grates and strainers as previously described stop the entry of large debris into the system. One-way valves are placed before the pumps to prevent the pressure at the suction side from decreasing excessively due to wave motion and causing cavitation. At the discharge side, seawater is pressurised enough to overcome the drop through the pretreatment system ($\Delta p_{PF} = 3.5\ bar$, as per Digdaya et al.[22]) and the electrochemical cells (Δp_{CELL}). To increase the purity of the CO$_2$ captured, the pretreated seawater is subjected to near-vacuum pressure ($p_{VP} = 0.08\ bar$) in a hollow fiber membrane (HFM) to remove most of the dissolved nitrogen (N$_2$) and oxygen (O$_2$) naturally present in seawater (at the surface, their partial pressure is $pN_2 = 0.79\ bar$, $pO_2 = 0.21\ bar$, respectively). The effluent seawater solution is then sent to the DOC cells, which capture the CO$_2$ present in it following the process laid out in section **4.2.1**. After capturing and stripping the CO$_2$ in gas form from seawater, it is compressed in multiple stages up to 350 bar[liv], and retrieved from the platform with a flexible riser down to the seabed. This would follow an additional subsea export pipe to an offshore geologic carbon reservoir (e.g. basalt), but this is not included in our analysis. In turn, the high-pH, CO$_2$-depleted seawater is pumped back to the ocean through the floater's bottom.

[liv] This pressure is at the higher end of the range recommended for offshore CO$_2$ pipeline transport (100-350 bar)[130].

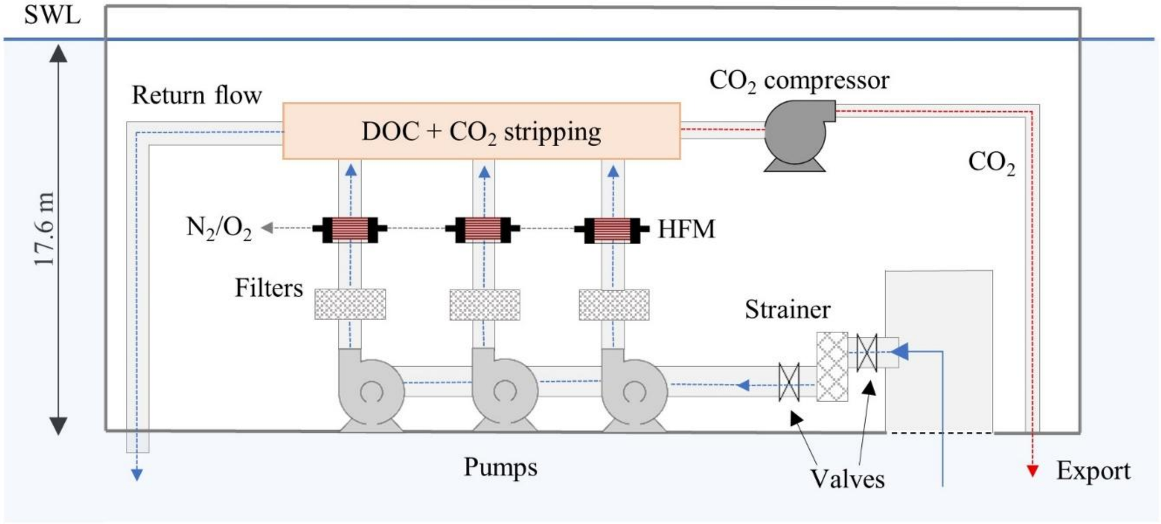

Figure 4.5. Schematic illustration of the main DOC system processes integrated into the floating platform. Blue arrows represent seawater flows, while the red arrow indicates captured CO_2 flow.

Previously, **Figure 4.3** showed the FOWT-DOC system for the architectures of Case 0, and Cases 1, 2, and 3. The latter configuration features a SWIR (coloured in orange) hanging from the floater's base along the water column. As seawater ascends through the SWIR, the friction between the inner pipe surface[lv] and the water flow produces a pressure drop (Δp_{SWIR}). Added to this are the pressure losses across the pretreatment filters ($\Delta p_{PF} = 3.5\,bar$), the hollow fiber membrane ($\Delta p_{HFM} = 0.55\,bar$[22]), and the aggregated pressure drop[lvi] through the first and second electrochemical cells (Δp_{CELL}). The sum of Δp_{SWIR}, Δp_{PF}, Δp_{HFM}, and Δp_{CELL} equals the pressure the seawater pumps must provide. The total dynamic head (TDH) or pressure (in units of distance) required by the pumps is then modelled as,

$$TDH = \frac{\Delta p_{SWIR} + \Delta p_{PF} + \Delta p_{HFM} + \Delta p_{CELL}}{\rho_{ow} g} \tag{4.12}$$

4.3.5.1. Energy penalties

The ancillary processes mentioned above (pumping, vacuum gas stripping, and gas compression) consume energy provided by the wind turbine. The energy consumed by the pumps ($e_{pumping}$) depends on TDH and on the carbon capture seawater intensity[22], $\dot{V}_{ow}/\dot{m}_{CO_2}$,

$$e_{pumping} = \frac{\dot{V}_{ow} \rho_{ow} g TDH}{\dot{m}_{CO_2} \eta_{pump} \eta_{motor}} \tag{4.13}$$

[lv] The SWIR's inner surface roughness is assumed 15 mm, taken as the average of the values studied by ref.[203].

[lvi] The pressure loss or drop due to friction along a pipe or duct is most often described via the Darcy-Weisbach equation. This is used to model separately the pressure loss through the SWIR (Δp_{SWIR}) and across the electrochemical cells (Δp_{CELL}), see section **4.6.3** in the Appendices.

Where η_{pump} and η_{motor} are the pump and motor efficiencies, respectively. As seen in ref.[22], the energy consumed by the pumps is typically the largest ancillary energy service, even larger than the total DOC electrochemical energy. In section **4.4**, we present how this figure is reduced by employing deeper, denser, rich-DIC seawater for DOC.

When stripping a dissolved gas (e.g. CO_2, N_2, O_2) through a hollow fibre membrane, the pressure inside the membrane (the lumen side) must be lowered to near vacuum with the help of a pump. To increase its efficiency, a heat exchanger using a fraction of the drawn seawater at temperature T_{in} is placed at the vacuum side of the pump. The work done by the vacuum pump, including the additional pressure to flow through the heat exchanger, can then be characterised as[179]:

$$e_{degas} = \frac{F_{m,gas} R T_{in} \kappa_{gas}}{(1-\kappa_{gas})\eta_{VP}\eta_{motor}\dot{m}_{CO_2}} \left[\left(\frac{p_{VP,in}}{p_{VP,out}}\right)^{\frac{\kappa_{gas}-1}{\kappa_{gas}}} - 1\right]\left(\frac{1}{1-0.054\eta_{VP}}\right) \tag{4.14}$$

Where $F_{m,gas}$ is the molar flow rate of the dissolved gas saturated with water vapor (mol/s), R is the universal gas constant ($Jmol^{-1}K^{-1}$), κ_{gas} is the adiabatic constant of the gas, $p_{VP,in} = 0.08\ bar$ is the near-vacuum pressure employed, $p_{VP,out}$ is the ambient pressure, and η_{VP} is the efficiency of the vacuum pump, which is expressed as follows[179]:

$$\eta_{VP} = 0.1058\ ln\left(\frac{p_{VP,in}}{p_{VP,out}}\right) + 0.8746 \tag{4.15}$$

Once stripped from seawater, CO_2 is compressed to high-pressure before being withdrawn from the platform. For simplicity, an idealized isothermal compression with a carbon capture energy intensity $e_{compression}$ is assumed:

$$e_{compression} = \frac{RT_{in}}{M_{CO_2}} ln\left(\frac{p_{CP,out}}{p_{CP,in}}\right) \tag{4.16}$$

4.3.5.2. Energy storage

Wind power is inherently variable throughout different time (seconds to decades) and spatial scales. As a result, the power produced by FOWTs is also variable. For the DOC system to operate optimally, however, the power supplied should be continuous and stable, guaranteeing minimum power levels and with fluctuations compatible with the electronic system. This can be achieved with a combination of load management (LM) and energy storage systems (ESS), where the balance between both is often cost-driven. The solutions available to cope with wind power fluctuations depend not only on cost, but on the time span considered. Turbulence effects, within the second to minute region, are harder to predict than hourly or daily variations, within the two-hour to 24-hour period. LM strategies can have time responses in the order of hours, so are not appropriate to handle turbulence effects. Instead, ESS such as batteries can provide the buffering required in a timely and controlled manner. Chabaud[197] used a battery system to deal with wind turbulences of the IEA 15MW RWT under normal operating conditions. They found that turbulence within ten-minute, one-hour and two-hour windows can be tackled with battery capacities of around 60 kWh, 620 kWh, and 1700 kWh, respectively. To err on the conservative side, we consider a two-hour Sungrow ST battery with a capacity up to 5,015 kWh and 2,500 kW[198].

4.3.6. Cost estimation

To understand and compare the benefits and drawbacks of each design scenario studied, the levelized cost of carbon (LCC) of the FOWT-DOC platform system is estimated. For a project lifetime of 25 years and a discount rate r, the LCC ($\$/tCO_2$) is then defined as,

$$LCC = \frac{\sum_{t=0}^{25} \frac{C_T^t}{(1+r)^t}}{\sum_{t=1}^{25} \frac{m_{t-year}^{CO_2}}{(1+r)^t}} \tag{4.17}$$

Where C_T^t is the total cost of the FOWT-DOC platform at year t, and $m_{t-year}^{CO_2}$ is the CO_2 captured by the platform at year t. The sum index t in the nominator starts at 0 to denote that all capital expenditure (CapEx) occurs before the start of operation. The total costs are comprised of CapEx and operational expenditure (OpEx), and can be further divided into costs related to the FOWT CT-BOS platform (C_{FOWT}) and costs related to the DOC (C_{DOC}). To account for the increased costs of operating offshore, all OpEx is multiplied by a marinization factor ($f_{mar} = 2.5$), which is derived by comparing the typical annual OpEx of offshore-based floating wind turbines and land-based wind turbines[199]. The CapEx and OpEx of the FOWT CT-BOS platform over its lifetime are calculated as the average levelized cost of electricity ($LCOE$) of typical FOWT TLPs[200] and the amortized AEP of the FOWT platform,

$$C_{FOWT} = LCOE \frac{AEP}{(1+r)^t} \tag{4.18}$$

The total costs of the DOC system account for the costs of the oceanwater intake system (C_{OWI}), pretreatment system (C_{PF}), water pumps and electric motors (C_{pump}), electrochemical cells (C_{cell}), vacuum pumps and condensers (C_{degas}), CO_2 compressors ($C_{compression}$), and CO_2 riser (C_{riser})[lvii].

$$C_{DOC} = C_{OWI} + C_{PF} + C_{pump} + C_{cell} + C_{degas} + C_{compression} + C_{riser} \tag{4.19}$$

The costs from oceanwater pumping and pretreatment, and vacuum pumps and condensers are estimated following the processes detailed by Digdaya et al.[22]. All costs are expressed in USD ($) and converted to a base year of 2024 using Producer Price Index (PPI)[201] through equation (4.20). The main financial and technical assumptions behind the cost analysis are given in **Table 4.3**.

$$Cost_{2024} = Cost_{yearX}\left(\frac{Index_{2024}}{Index_{yearX}}\right) \tag{4.20}$$

[lvii] NOTE: the cost of the CO_2 riser includes the line from the floating platform to the seabed, but not the export pipe to the injection site.

4.3.6.1. Seawater intake system

For Case 0, two sea chests are installed at the bottom of the CT-BOS platform, and for simplicity it is assumed that their capital cost is driven by the grates. The two grates are identical and made of marine grade stainless steel (316 L), with a material density of 8,000 kg/m^3, ref.[202]. Each grate has an open area equal to half the SWIR's section, and its volume is computed as the product of the section, its open area ratio (taken as 50%), and its average material thickness (taken as 100 mm). The unit cost of stainless steel is \$7,998/ton, and that includes material, labour, and construction[202]. This is multiplied by the total weight of grates to give the CapEx. To err on the conservative side, the OpEx of the sea chests are assumed the same as the SWIR's for Case 1, which is explained next.

For Cases 1, 2, and 3, a single SWIR fabricated with 50% HDPE, 27% reinforced rubber, and 20% steel is used. Such a configuration, as well as the lifetime costs per unit length are approximated from ref.[203] from their 137 m SWIR. The capital expenses ($CapEx_{SWIR}$) are calculated as a combination of the installation costs, and the material and fabrication costs,

$$CapEx_{SWIR} = L_{SWIR}\left(c_{inst_{SWIR}} + \frac{c_{mfab_{SWIR}}\pi(OD_{SWIR}^2 - ID_{SWIR}^2)}{4}\right) \tag{4.21}$$

Where L_{SWIR} is the SWIR's length, $c_{inst_{SWIR}} = \$400/m$ is the cost of installation per unit length[204], and $c_{mfab_{SWIR}} = \$73{,}630/m^3$ is the volumetric material and fabrication cost[203]. The total operational expenditures ($OpEx_{SWIR}$), assuming four maintenance services throughout the project lifetime, are assumed as $OpEx_{SWIR} = 14\%\ CapEx_{SWIR}$, ref.[203].

4.3.6.2. Electrochemical cells

The CapEx of the commercial-scale, bismuth-silver electrochemical cells was estimated by Kim et al.[166] as \$23/tCO$_2$. In addition to this, we assume that the cells must be replaced every 10 years, and that the annual OpEx is 3% of the CapEx.

4.3.6.3. Compressors

Before exporting, the CO$_2$ captured in gas form is compressed to 350 bar in several stages using multiple compressors: Stage 1) from its capture pressure at 0.08 bar to 10 bar, Stage 2) from 10 bar to 100 bar, Stage 3) from 100 bar to 250 bar, and Stage 4) from 250 bar to 350 bar. Each stage is better suited to a particular compressor type (Stage 1: screw, Stages 2 and 3: reciprocating, Stage 4: diaphragm). During and after each stage, CO$_2$ is cooled with heat exchangers to maintain its temperature away from its critical point (31˚C, and 73.8 bar). The CapEx of the compressors used is computed as a function of the power ($P_{compressor}$, in horsepower units) using empirical relations (22.37)-(22.38) from Seider et al.[205], which use a 2006 cost index of 500.

$$CapEx_{screw} = \exp\left(8.1238 + 0.7243 \ln P_{compressor}\right) \tag{4.22}$$

$$CapEx_{reciprocating/diaphragm} = exp\left(7.9661 + 0.8\, ln\, P_{compressor}\right) \tag{4.23}$$

The annual OpEx is defined as the sum of the annual operating costs of electricity, maintenance, insurance, and labour, following Digdaya et al.[22].

4.3.6.4. CO₂ export riser

The flexible riser retrieves the CO_2 captured in liquid form, which descends the water column until reaching the interface with the exporting pipe at the seabed. The length, profile, and material composition are assumed the same across design scenarios, but not the inner (ID_{riser}) and outer (OD_{riser}) diameters, respectively, as they vary slightly with flow rate (0.36 m to 0.39 m). Consequently, the flexible riser $CapEx_{riser}$, which depends on ID_{riser} and OD_{riser}, is different for each design scenario.

$$CapEx_{riser} = L_{riser}\left(c_{inst_{riser}} + \frac{c_{m_{riser}}\pi\left(OD_{riser}^2 - ID_{riser}^2\right)}{4}\left(1 + cf_{fab_{riser}}\right)\right) \qquad (4.24)$$

In equation (4.24) ref.[206], $L_{riser} = 801\ m$ is the riser's length, $c_{inst_{riser}} = \$400/m$ is the cost of installation per unit length[204], $c_{m_{riser}} = \$100/m^3$ is the volumetric material cost[206], and $cf_{fab_{riser}} = \$6{,}200/m$ is a cost factor for fabrication[59]. The annual OpEx is taken as 1% of the CapEx[59].

Table 4.3. Base FOWT-DOC main financial and technical assumptions used in the cost estimation.

Finances & project specifics	Units	Value	Ref.
EUR to USD currency exchange rate (Avg 2024)	USD/EUR	1.08	207
CAD to USD currency exchange rate (Avg 2024)	USD/CAD	0.73	207
Plant lifetime	years	25	
Marinization factor	-	2.5	199
Discount rate for offshore wind	-	9.2%	208
Discount rate for DOC	-	6.5%	22
Wind turbine rated power	MW	15	73
Wind availability factor	-	82.5%	180
FOWT capacity factor	-	60%	
FOWT TLP LCOE	EUR/MWh	150	200
DOC capacity factor	-	90%	22
PPI of pumps and compressors (av. 2024)	-	224.896	201
CapEx - electrochemical cell	USD/tCO_2	230	166
CapEx - Sungrow ST battery (5,015 kWh/2,500 kW)	USD/kWh	132	209

4.4. Results and discussion

Each design scenario draws oceanwater from a different depth, with corresponding naturally occurring oceanographic values as per **Table 4.1**. For example, in the first 1,000 m in the Pacific Ocean, DIC increases with depth and it progressively slows down (**Figure 4.10**). A similar pattern is observed in the carbon capture seawater intensity ($\dot{V}_{ow}/\dot{m}_{CO_2}$) for the design scenarios considered (**Figure 4.6**), illustrating diminishing returns associated with each depth increase.

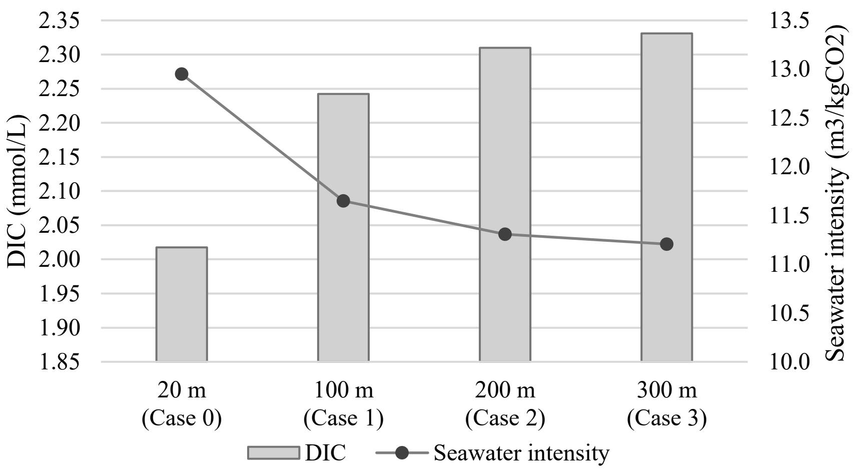

Figure 4.6. Carbon capture seawater intensity as a function of dissolved inorganic carbon (DIC) for the design scenarios.

Since the carbon capture energy intensity of most system components - equations (4.5), (4.13), and (4.14) - depends on $\dot{m}_{CO_2}$, it is no surprise to see that total system energy intensity (e_{DOCCS}) follows an equivalent trend (**Table 4.4**): it is lowest when $\dot{V}_{ow}/\dot{m}_{CO_2}$ is a minimum in Case 3 (at 3.40 kWh/kgCO$_2$), and highest when $\dot{V}_{ow}/\dot{m}_{CO_2}$ is a maximum in Case 0 (at 4.02 kWh/kgCO$_2$). Further, its rate of change between consecutive scenarios progressively decreases, with a maximum observed between Case 0 and 1, and a minimum between Cases 2 and 3. To highlight this, the total system energy intensity (e_{DOCCS}) for Cases 1, 2, and 3 is accompanied by a percentage between parenthesis, which indicates the energy savings of Cases 1, 2, and 3 with respect to Case 0.

The results of e_{DOCCS} for Cases 1, 2, and 3 are given for the nonadiabatic transport case, which is 1% to 2% lower than for the adiabatic transport case. Certainly, as seawater travels up through the SWIR exchanging heat with the environment (nonadiabatic transport), it warms up. Although warmer seawater temperatures have a detrimental effect on the energy expenditure of the gas stripping (e_{degas}) and compression ($e_{compression}$) systems, equations (4.14) and (4.16), respectively, this is overall compensated by reduced Ohmic losses thanks to higher ionic conductivities, equation (4.6). Consequently, all results reported hereafter assume nonadiabatic transport conditions, with a SWIR with no or minimal thermal insulation.

Table 4.4. Carbon capture energy intensities (in kWh/kgCO$_2$) of the main DOC processes for the design scenarios and for the nonadiabatic transport through the SWIR case. The percentage between parenthesis indicates the energy savings of Cases 1, 2, and 3 with respect to Case 0.

	Case 0	Case 1	Case 2	Case 3
Total system energy expenses, e_{DOC}	4.02	3.54 (11%)	3.43 (14%)	3.40 (14%)
Electrochemical energy, e_{echem}	0.63	0.56	0.54	0.54
Ohmic losses, e_{Ohmic}	0.39	0.40	0.40	0.41
Ancillary services	2.99	2.61	2.52	2.49
Pumping, $e_{pumping}$	2.79	2.41	2.32	2.29
Vacuum stripping, e_{degas}	0.07	0.07	0.07	0.07
Compression, $e_{compression}$	0.13	0.13	0.13	0.13

As previously anticipated, of all energy intensive processes, seawater pumping ($e_{pumping}$) is the largest contributor to the total system energy consumption, representing 70% of e_{DOCCS}. Notably, $e_{pumping}$ is reduced with each depth iteration, from Case 0 (2.79 kWh/kgCO$_2$) to a minimum in Case 3 (2.29 kWh/kgCO$_2$, or 18% less). Such a difference can be explained, almost in its entirety, by the linear dependence of the energy intensities to DIC, which increases by up to 15% between Case 0 and Case 3. The remaining 3% difference arises from the influence of the pressure head on $e_{pumping}$, specifically due to the pressure drop along the electrochemical cells (Δp_{CELL}), which is maximum for Case 0 and minimum for Case 3 (**Table 4.5**). The variations observed can be attributed to slower seawater flow speeds through the electrochemical cells (as described by the Darcy-Weisbach equation, see **4.6.3** in the Appendices), possible because of higher DICs with each depth increment.

We note some significant differences between our system energy expenses (**Table 4.4**) and those published by ref.[22]. For its stand-alone DOC plant, Digdaya et al.[22] determined a total carbon capture energy intensity of 5.82 kWh/kgCO$_2$, of which 1.22 kWh/kgCO$_2$ was consumed by their BPMED cells, and 4.6 kWh/kgCO$_2$ was due to ancillary services (oceanwater intake, pretreatment, pumping, vacuum stripping, and cooling). Leaving aside the discrepancies arising from the increased DIC of the input seawater in Cases 1, 2, and 3, our total system energy expenses are 4.02 kWh/kgCO$_2$, the total energy consumed by the cells (electrochemical energy plus Ohmic losses) is 1.02 kWh/kgCO$_2$, and the ancillary services require 2.99 kWh/kgCO$_2$ (all with respect to Case 0). The differences in the total energy consumed by the electrochemical cells can be explained because of the more energy efficient method published by Kim et al.[166], upon which our system is based. The discrepancies in the ancillary services arise from the total pressure head considered, 5.9 bar in our case (**Table 4.5**), and 9.6 bar in Digdaya et al.[22], where the 3.7 bar gap results mostly from the difference between our initial negative elevation ($z_{elevation} = -13.8\, m$) and their initial positive intake head of 50 m, a direct result of our proposed offshore FOWT integrated system layout.

Table 4.5. Pressure heads (in bar) across system components for the design scenarios. The percentage between parenthesis indicates the difference with respect to Case 0.

	Case 0	Case 1	Case 2	Case 3
Across SWIR (Δp_{SWIR})	0.00	0.05	0.11	0.17
Across pretreatment (Δp_{PF})	3.52	3.52	3.52	3.52
Across HFM (Δp_{HFM})	1.10	1.10	1.10	1.10
Across cells (Δp_{CELL})	1.36	1.12 (18%)	1.06 (22%)	1.05 (23%)
TOTAL	5.98	5.79	5.79	5.84

Of all pressure heads identified in **Table 4.5**, the pressure that must be overcome across the pretreatment system (Δp_{PF}) is responsible for the largest share, up to 59% (or 3.52 bar) of the total. This pressure, assumed for a BPMED DOC application by Digdaya et al.[22], assumes three types of water purification levels: disc filters (0.22 bars), cartridge filters (0.3 bar), and ultrafiltration membranes (3 bar). The pressure of each filtering system is associated with its pore size, from 5-50 micrometres in disc (DFs) and cartridge (CFs) filters[lviii], to 0.01-0.1 micrometres in ultrafiltration (UF) membranes. DFs and CFs block the entry of suspended solids with characteristic dimensions as small as 5 micrometres, which in certain environments (e.g. subsurface intakes) can provide high quality feedwaters, enough to make UF membranes redundant[210]. This would considerably reduce the pressure head through the pretreatment system from 3.52 bar to 0.52 bar, and save 35% of the total system energy expenses, down to 2.3-2.7 kWh/kgCO_2. Nevertheless, in open ocean intakes such as ours, UF membranes are still recommended to reduce fouling and scaling of HFMs[lix], thereby extending their lifetime and reducing their maintenance costs.

We saw above how greater DICs can lead to slower flow speeds; however, this can also be achieved by increasing the gap between the cell's electrode (δ_{cell}). This would in turn exacerbate the resistance experienced by ions passing from one electrode to the other (or Ohmic losses), resulting in overall increased energy expenses and lowered carbon captured. As **Figure 4.7** shows, of the range of cell gaps modelled, $\delta_{cell} = 1\ mm$ yields the lowest energy expenses and the highest annual carbon captured, which coincides with the findings previously published by Kim et al.[166]. Most importantly, **Figure 4.7** illustrates how each design scenario captures increasing amounts of CO_2 annually, from 16.9 ktCO_2/year in Case 0 to a peak of 19.5 ktCO_2/year (18% higher) in Case 3 for a cell gap $\delta_{cell} = 1\ mm$.

[lviii] Enough to meet inlet quality requirements of seawater pumps, such as Andritz's ASP700-860A 16 S single-stage, axial split case pump, according to Micha Thormann, Technical Sales and Project Manager at Andritz.

[lix] Membrane fouling, such as in hollow fibre membranes, takes place when matter present in seawater adheres to the surface of the membrane (i.e. adsorption). Membrane fouling can be of organic or inorganic origin, the latter more popularly known as scaling.

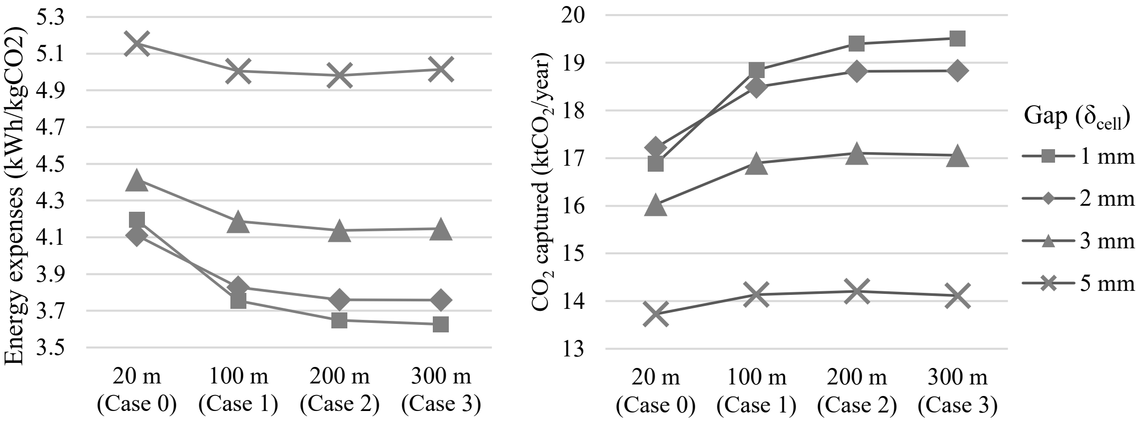

Figure 4.7. (Left) Total system energy expenses, and (right) annual CO$_2$ captured with different gaps between cell's electrodes (δ_{cell}) per each design scenario.

To best assess the profitability and thus complete the analysis of each design configuration, the discounted individual and total costs of the main components of the FOWT-DOC system, together with the levelized cost of carbon (LCC), are given in **Table 4.6**. Observe that the total costs increase from Case 0 (at \$258.6 million) to Case 3 (at \$285.7 million), with an average of \$273.5 million. The largest cost centre is the FOWT platform, representing on average 46% of the total costs, followed by the CO$_2$ flexible riser (24%), and the seawater pumping and pretreatment system (21%). The average cost per unit of carbon captured of each component across design scenarios is presented in **Figure 4.8** (top).

The variation of costs between scenarios is dominated by the costs of the CO$_2$ flexible riser - with a minimum change of \$6.5 million between Case 0 and 1, and a maximum of \$8.3 million between Case 0 and 3 - and by the costs of the seawater intake system, with a peak difference of \$8.6 million between Case 0 and 3. On one hand, because the same CO$_2$ export riser length is assumed for every scenario, according to equation (4.24) the differences displayed can only arise from its linear mass; indeed, as the carbon captured increases with each deeper water intake case, so does the flow rate that is exported through the riser. As a result, since the CO$_2$ flow speed through the riser is considered the same between cases[lx], the higher flow rate must be accommodated by widening the riser's inner and outer diameters, thus increasing its linear mass. On the other hand, the cost of the seawater intake system for Cases 1, 2, and 3 is linear with the SWIR's length, which is equal to the water intake depth minus the platform draft. As the increment in depth is the same between consecutive scenarios, the additional cost per case is also constant. Consequently, because the extra carbon captured diminishes with each depth iteration (which stems from the DIC vertical profile, as shown in **Figure 4.6**), the additional costs of capturing CO$_2$ from deeper points eventually outweigh the gains. This can most clearly be observed with the LCC in **Table 4.6**, which reaches a minimum

---

[lx] The CO$_2$ flow speed along the riser is set to 3 m/s, determined as the maximum flow speed allowed before pipe erosion occurs, and determined using equation (4.16) with ρ_{CO_2} instead of ρ_{ow}.

in Case 2 (\$1,108/tCO_2), only to resurge in Case 3 (\$1,124/tCO_2) despite capturing the largest amount of CO_2 annually. Notably, Case 0 is the least profitable of all, with the largest LCC (\$1,203/tCO_2) up to 8% more expensive per unit of CO_2 captured than the most profitable configuration, or Case 2.

Between Case 0 and 1, the LCC and the annual carbon captured improve 8% and 12% respectively, whereas between Case 1 and 2, the gains are less than 0.2% and 3%, respectively. As these two design scenarios yield similarly close benefits, it is important to consider other decisive parameters. Recall that, to reduce the number of variables and thus facilitate comparison across scenarios, the same project site water depth (350 m) was chosen between cases (section **4.3.2**). However, since Case 1 draws seawater from 100 m depth, and Case 2 from 200 m depth, the water depth at which the FOWT-DOC system would sit in each configuration would not necessarily be the same. Assuming a margin of 50 m with the seabed to minimise turbidity, Case 1 could sit at 150 m and Case 2 at 250 m – provided a similar DIC distribution as in **Figure 4.6**. Since offshore projects operating in deeper waters are generally more expensive[211], this would favour Case 1 over 2. Further, the small additional economic savings provided by Case 2 relative to Case 1 (at \$3/tCO_2), or even with respect to Case 0 (at \$94/tCO_2), may be offset by longer air-sea CO_2 ventilation times associated with bringing up deeper seawater. These longer times complicate MRV activities and ultimately undermine the true effectiveness and impact of this CDR approach. In this sense, Case 0 is therefore more likely to succeed.

Note that because we do not know if or how the DIC removal efficiency published by Kim et al.[166] ($\eta_{DIC} = 87\%$) depends on the input DIC, we assumed η_{DIC} constant for all cases. This is a limitation of our study with a major consequence explained next. Given that the ocean's surface uptake capacity of atmospheric CO_2 depends in part on the CO_2 concentration gradient through the air-sea interface, any DOC approach seeking to draw the most CO_2 must also reduce the DIC the most. However, when assuming η_{DIC} constant across the design scenarios, the discharged, depleted-DIC stream will have different DIC values. For example, in Case 0, the DIC in the effluent stream is reduced from an initial value of 2.02 mmol/L to a final value of $(1-\eta_{DIC})\cdot 2.02 = 0.26$ mmol/L; while in Case 3 (with the largest naturally occurring DIC), the DIC in the discharged stream is reduced from an initial value of 2.33 mmol/L to a final value of $(1-\eta_{DIC})\cdot 2.33 = 0.30$ mmol/L. Although Case 3 removes more DIC from seawater than Case 0, the end point DIC of the former (at 0.30 mmol/L) is slightly larger than for the latter (at 0.26 mmol/L). Consequently, the amount of CO_2 that the ocean may draw from the atmosphere may be lower in Case 3 than in Case 0 and mediated by mixing times.

Table 4.6. Discounted individual and total costs (in million dollars, \$M) for the main FOWT-DOC system components, and levelized cost of carbon (in \$/tCO$_2$) for each design scenario, with a gap between cell's electrodes of $\boldsymbol{\delta_{cell}}$ = 1 mm.

System component	Case 0	Case 1	Case 2	Case 3	Avg
FOWT platform	123.4	123.4	123.4	123.4	123.4 (46%)
CO$_2$ riser	58.7	65.2	64.1	67.0	64.6 (24%)
Oceanwater pumping and pretreatment	54.5	55.2	55.3	55.3	55.1 (21%)
Vacuum pump and condenser	12.1	12.1	12.1	12.1	12.1 (5%)
CO$_2$ compressor	7.1	7.4	7.4	7.4	7.3 (3%)
Seawater intake system	0.3	2.6	5.8	8.9	4.4 (2%)
Electrochemical cells	0.9	1.0	1.0	1.0	0.9 (0.4%)
Wind battery system	0.7	0.7	0.7	0.7	0.7 (0.4%)
TOTAL discounted costs (\$M)	258.6	270.6	279.0	285.7	273.5
Levelized cost of carbon (\$/tCO$_2$)	1,203	1,111	1,108	1,124	1,136

To account for uncertainties in the cost estimates of the CO$_2$ riser and seawater intake system - whose differences across design scenarios outweigh the cost changes experienced by the rest - and to assess the sensitivity of the observed LCC trend (with Case 0 being the least cost-effective and Case 2 the most), **Figure 4.8** (bottom) shows how the LCC varies with percentage changes in the combined costs of these components. As expected, as the combined costs rise (at 115% and 130% of the base cost) but the carbon captured remains the same, the shallower scenarios become more cost-effective, with Case 1 having the lowest LCC. Conversely, the differences between Case 3, and Cases 1 and 2 are narrowed as the combined costs decrease, at 70% and 85% of the base cost. Most importantly, however, Case 0 is still the least profitable of all cases examined.

Since the cost of the FOWT platform represents the greatest cost share (46% of the total), it can be helpful to present how the estimated LCC figures in **Table 4.6** could decrease with forecasted savings in the floating offshore wind industry. By 2035, the average LCOE for FOWT platforms is estimated to be \$63.9/MWh, or over \$100/MWh less expensive than the LCOE considered in this study (see Figure 7 in ref.[212])[lxi]. Using this predicted LCOE and the wind energy conditions in **Table 4.3**, the potentially reduced FOWT platform costs can be estimated with equation (4.18). Summing over all system costs using equation (4.19), the LCC of our FOWT-DOC system could then be as low as \$786/tCO$_2$ in Case 1, equation (4.17).

Similarly, given that the cost of the CO$_2$ export riser is almost a quarter of all costs, future research should assess potential alternatives. In the context of CO$_2$ storage in offshore basalt, CO$_2$ transportation studies ought to consider the operational lifetime of injection wells – dependent, among others, on the reservoir capacity and the rate of injection – and thus a flexible transport system (such as CO$_2$ shipping) would be preferred. Although, in general, transport via ships is favoured over

---

[lxi] In ref.[212], these cost projections are assumed as developers and supply chains continue to mature and gain experience, and cumulative deployment increases, leading to improved efficiencies.

pipelines at low CO_2 volumes and high distances (see e.g. Figure 9 in ref.[117]), there is not a clear threshold[116–118,213], and the decision for each project may rely upon individual circumstances, such as the existence of built infrastructure or the local availability of vessels.

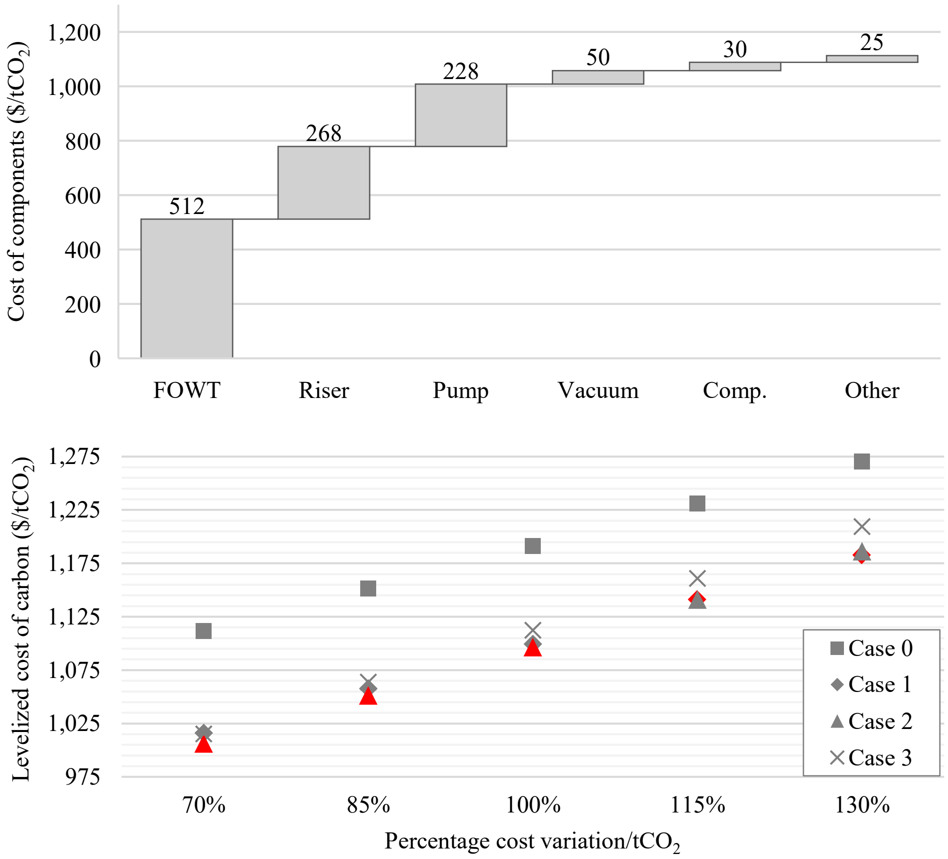

Figure 4.8. (Top) Average system component costs per unit of CO_2 captured across design scenarios. The abbreviated field "Comp." stands for compressor, and the field "Other" comprises the intake system, electrochemical cells, and batteries. (Bottom) Sensitivity of the levelized cost of carbon (LCC, in \$/tCO_2) with ±15% and ±30% percentage changes in the combined cost of the CO_2 riser and seawater intake system for each design scenario. The minimum LCC at every percentage variation across design scenarios is highlighted in red.

The previous cost methodology can be repurposed to determine the costs of a FOWT platform powering a base route DOC. Unlike the acid route, however, the base route configuration does not need vacuum pumps and condensers (to pre-strip dissolved gases), nor CO_2 compression and transportation system, as the treated alkaline seawater is released back to the ocean. Ignoring these pressures, energies, and components, but assuming the same expenses for the rest of the system as in the FOWT-DOC (acid route), the total pressure head required by the pumps and the total system energy expenses are reduced 20%, down to 4.6-4.9 bar and 2.7-3.3 kWh/tCO_2, respectively. In turn, the LCC of the FOWT-DOC (base route) system is reduced to an average of \$653/tCO_2 (over all four design scenarios), or \$480/tCO_2 (40%) cheaper than the FOWT-DOC (acid route), **Table 4.6**. These savings are comparable to those reported by Eisaman et al.[23] for two stand-alone DOC plants, one based on the acid route and the other on the base route, which further underscores the need for additional research on base-route DOC.

Last but not least, one may logically be tempted to look at the cost of other CDR methods (see e.g. Table 1 in ref.[8]) and react either with an air of disapproval or sheer wonder as to why we bother suggesting such expensive distractions. The answer lies in the possibility of coupling this fully autonomous, modular, off-grid solution to the largest and most permanent CO_2 reservoir, which is offshore basalt. As shown by Prado et al.[9], when duration is accounted, "over the long term, almost any form of permanent removal will emerge as being economically preferable to a short-term solution." This is not to suggest that cheaper CDR methods with shorter permanence are to be disregarded, as they can still "buy us time to deploy more durable CDR", ref.[9], however, it puts into perspective their often-overlooked lifetime, all-in costs. This calls for a reconsideration of the quantitative methods employed to determine the true cost of carbon removal, methods which ought to reflect the social costs of carbon emissions and climate mitigation[9,214] and, ideally, be complemented by comprehensive life-cycle assessments (LCAs).

4.4.1. Comparison with FOWT-DAC

This paper presented a conceptual design of a FOWT-DOC system and estimated the associated costs and LCC (\$1,108/tCO_2 to \$1,203/tCO_2, depending on the design scenario). Next, this section conducts a similar but more simplified analysis of a FOWT-direct air carbon capture (FOWT-DAC) system.

To this end, the model presented by the authors in Chapter 2 is employed[57], which assumed a floating semisubmersible rather than a TLP. On average, the LCOE of FOWT semisubmersible platforms is €35/MWh more expensive than TLPs at €185/MWh[183]. In contrast, DAC is less energy intensive than DOC, with total (heat and electricity) requirements comprised between 0.97-2.8 kWh/kgCO_2 depending on whether solid or liquid sorbents are used (see Figure 8 in ref.[21]). We assume a total energy demand of 2.1 kWh/kgCO_2, which corresponds to the value used in previous work[57] and includes compression expenses. At this energy intensity, one 15 MW wind turbine with a 60% capacity factor can generate 78.9 GWh of electricity and capture 33.8 ktCO_2 on a regular year of 8,766 hours (assuming a 90% DAC plant capacity factor). The LCC of the FOWT semisubmersible can then be determined by multiplying its LCOE with the discounted annual power generated and dividing it by the discounted captured CO_2, giving \$370/tCO_2 (assuming a euro-to-dollar currency exchange rate of \$1.08/€)[lxii]. The combined CapEx and OpEx of DAC vary widely, between €80/tCO_2 to €1,133/tCO_2, with an average of €606/tCO_2[215]. Applying a 2.5 marinization factor to the OpEx (which are in turn taken as 5% of all CapEx), we obtain an LCC for DAC between \$93/tCO_2 to \$1,314/tCO_2, with an average of \$703/tCO_2. Adding the LCC of the FOWT semisubmersible and the DAC, and the LCC for compression and transportation of CO_2 (on average \$30/tCO_2 and \$268/tCO_2, respectively, assuming the same costs from our previous FOWT-DOC analysis), we get a total LCC for the FOWT-DAC system in the range of \$757/tCO_2 to \$1,991/tCO_2, with an average of \$1,371/tCO_2 (**Table 4.7**).

[lxii] The annual energy production and captured CO_2 are discounted over the plant lifetime of 25 years at 9.2% and 6.5% discount rates, respectively.

Both average cost estimates for the FOWT-DAC (\$1,229/tCO_2) and FOWT-DOC (\$1,136/tCO_2) platforms remain well above the ambitious desired \$100/tCO_2 target set by the US government[216]. Nevertheless, this widely cited benchmark is not only unlikely to be achieved at present[31] but also unfairly ignores the much higher true global social cost of carbon, with an estimated median cost of \$417/tCO_2, ref.[214].

The energy intensity of FOWT-DAC is plotted and compared with that of FOWT-DOC in **Figure 4.9**. For reference, the figure also shows the minimum thermodynamic energy required to separate CO_2 from ambient air, and the minimum electrochemical energy to separate CO_2 dissolved in seawater. The former is determined with the enthalpy of mixing following Keith et al.[217] at an ambient temperature of 25°C and a CO_2 concentration of 425.5 ppm, which was the monthly average concentration at Mauna Loa in August 2025[218]. The latter is taken as the base electrochemical energy of the acid route laid by Kim et al.[166], followed in this work.

For the case of CO_2 capture from air, the difference observed between the minimum thermodynamic energy (0.1 kWh/kgCO_2) and the range given by ref.[21] (0.97-2.8 kWh/kgCO_2) is dominated by the thermal regeneration step, with typical required temperatures between 70-200°C for solid sorbents, and up to 900°C for liquid solvents[70,219]. Solid and liquid sorbent-based DAC are commercially mature technologies and make up all but one of all DAC facilities deployed currently[220]. However, emerging technologies such as electro-swing adsorption[221] and membrane-based separation[222] feature more efficient solutions with the potential to reduce DAC's energy demand.

For the case of CO_2 capture from seawater, the difference observed between the minimum electrochemical energy for separation itself (0.20 kWh/kgCO_2 by Kim et al.[166]) and the range estimated from our design cases (3.4-4.0 kWh/kgCO_2) is mainly attributed to ancillary services, with water pumping representing 70% of the total DOC energy requirements, as previously shown in **Table 4.4**. Although our design choices – both lowering the pressure head and increasing the input DIC – enabled a significant reduction in the pumping needs with respect to other published values (e.g. 4.6 kWh/kgCO_2 as estimated by ref.[22]), further improvements are necessary. Future efforts could look at harnessing wave power to provide high-pressure seawater, thus reducing the electricity demand of the pumping system, as has been suggested in some desalination applications. For example, Mi et al.[223] designed an oscillating surge wave energy converter capable of delivering seawater at 5-9 bar of pressure for reverse osmosis, which would almost or completely replace the work done by electric pumps in typical DOC configurations.

Table 4.7. Summary of magnitudes used in the estimation of the levelized cost of carbon (LCC) for the FOWT-DAC configuration, presented for a range of possible values (low, mid, and high).

	Units	Low	Mid	High	Ref
EUR to USD exchange rate	USD/EUR	-	1.08	-	207
Marinization factor	-	-	2.5	-	199
Discount rate for offshore wind	-	-	9.2%	-	208
Discount rate for DAC	-	-	6.5%	-	22
LCOE FOWT semisubmersible	EUR/MWh	-	185	-	183
Turbine rated power	MW	-	15	-	-
Hours on a regular year	hours	-	8,766	-	-
Wind turbine capacity factor	-	-	60%	-	-
Energy intensity of DAC	kWh/tCO_2	-	2,100	-	-
DAC capacity factor	-	-	90%	-	-
LCC of FOWT semisubmersible	USD/tCO_2	-	370	-	-
LCC of CO_2 compression	USD/tCO_2	29	30	33	-
LCC of CO_2 export riser	USD/tCO_2	265	268	273	-
OpEx of DAC (5% CapEx)	EUR/tCO_2	4	29	54	-
OpEx of DAC (after marinization factor)	EUR/tCO_2	10	72	136	-
Cost of DAC	EUR/tCO_2	80	606	1,133	215
Cost of DAC (after marinization factor)	USD/tCO_2	93	703	1,314	-
LCC of FOWT-DAC	USD/tCO_2	757	1,229	1,991	-

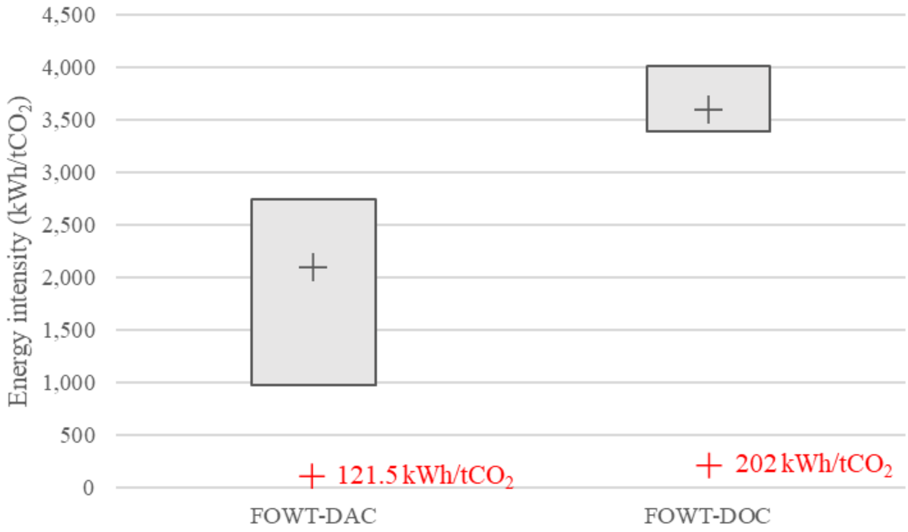

Figure 4.9. Carbon capture energy intensity for the FOWT-DAC and FOWT-DOC systems studied. The minimum thermodynamic energy required for CO_2 direct air capture and minimum electrochemical energy for CO_2 direct ocean capture are included for reference in red.

4.5. Conclusions

Direct ocean carbon capture (DOC) refers to the processes that remove dissolved inorganic carbon (DIC) from oceanwater. Direct ocean capture is a type of carbon dioxide removal (CDR) technique with an annual potential of 5-40 $GtCO_2$ which, in addition to contributing to slowing climate change, can help to reduce local ocean acidification[8]. The IPCC suggests that the largest threat to CDR technologies is land competition with other sustainable activities[224], which provides a strong motivation to place CDR in low energy demand areas, such as the ocean. Another reason comes from the fact that vast and permanent carbon reservoirs are located beneath the seabed, e.g. basalt[16,17,64,115]. Offshore, DOC can be powered by and integrated with floating wind turbines (FOWTs).

The distribution of DIC through the vertical oceanwater column is not uniform, generally accumulating with depth through the first 1,000 m due to the various ocean carbon pumps[225]. The higher the level of DIC in oceanwater processed, the higher the carbon captured per unit of energy spent by the DOC system. This encouraged us to study an offshore FOWT-DOC system with the ability to treat DIC-enriched water located below the ocean surface. We designed four scenarios drawing seawater from different water depths: Case 0 drew seawater from the vicinity of the platform (at around 20 m) using a sea chest, while Cases 1, 2, and 3 featured a vertical intake pipe that drew seawater from 100 m, 200 m, and 300 m, respectively. We then assessed the carbon capture energy intensity, carbon captured, and levelized cost of carbon (LCC) of all scenarios. Case 3 consistently yielded the lowest energy requirements (3.4 $kWh/kgCO_2$) and the highest carbon captured across cases (20.8 $ktCO_2$/year), up to 15% higher than Case 0 (4.0 $kWh/kgCO_2$ and 17.6 $ktCO_2$/year); the difference is attributed to the increased naturally present DIC at 300 m when compared to 20 m in Case 0. Interestingly, because the change in DIC between consecutive scenarios peaks between Cases 0 and 1, progressively diminishing thereafter, the rising, linear costs associated with deeper water withdrawal eventually outweigh the returns on a cost basis. As a result, the estimated LCC is lowest for Case 2 (\$1,108/tCO_2), almost 8% more cost-effective than Case 0 (\$1,203/tCO_2). In conclusion, in an offshore DOC scenario, the gains from withdrawing deeper oceanwater with higher DIC concentration are expected to diminish with depth. Our findings suggest that the most cost-effective configuration intakes seawater from depths between 100 m to 200 m. However, these benefits may be outweighed by longer air-sea CO_2 ventilation times (associated with bringing up deeper seawater), which challenges the effectiveness of this CDR approach. In this sense, Case 0 is more likely to succeed but further research is warranted to explore local mixing-depth and carbon re-absorption considerations in concert with MRV and market valuations.

The cost methodology was repurposed to determine the costs of a FOWT platform powering a base route DOC. Due to a combination of lowered pressure needs and equipment, the LCC of the FOWT-DOC (base route) system was reduced to an average of \$653/tCO_2, or \$480/tCO_2 (40%) cheaper than the FOWT-DOC (acid route). These savings were comparable to those reported by Eisaman et al.[23] for two stand-alone DOC plants, which further underscores the need for additional research on base-route DOC.

The global installed capacity of offshore wind is forecasted to continue expanding, from 228 GW in 2030 to 1,000 GW by 2050[226]. This industry growth is to be accompanied with corresponding savings in the levelized cost of energy (LCOE) of FOWT platforms - by 2035, the average LCOE could be \$100/MWh cheaper than the one considered in this study. Consequently, the LCC of our FOWT-DOC system could decrease to \$786/tCO_2 on that basis alone.

Acknowledgements

The authors would like to specially thank Saeid Hassankhani Dolatabadi from the University of Victoria for his expertise and guidance on offshore equipment, Dr. Richard Dewey from Ocean Networks Canada, and Dr. Lawrence Coogan and Dr. Roberta C. Hamme from the School of Earth and Ocean Sciences at the University of Victoria for their invaluable insights on oceanography. We also appreciate the technical support received from Micha Thormann (Andritz Pump Division) and Bruce Kehler (Atlas Copco Compressors Canada).

4.6. Appendices

4.6.1. Base electrochemical energy

This section lays out the procedure followed to derive the expression used to estimate the base electrochemical energy of the DOC concept by Kim et al.[166]. Most of the steps followed can also be seen in the Supplementary Information from Digdaya et al.[22].

Let G_{H^+} be the generation rate of protons (H^+, in mol/s) due to the electrical current:

$$G_{H^+} = \frac{I_{H^+}}{nF} \tag{4.25}$$

where I_{H^+} is the absolute partial current carried by H^+ (in A), n is the number of participating electrons per generation of one H^+ (3/2=1.5 in our case) and F is the Faraday constant. The number of H^+ that is added (in mol/L) in the acidified stream is given by the rate of generated H^+ divided by the rate of the oceanwater flow ($\dot{V}_{ow}$, in L/s) in the acidified compartment of the cell,

$$[H^+]_{added} = \frac{G_{H^+}}{\dot{V}_{ow}} \tag{4.26}$$

Which can be rewritten as follows using (4.25):

$$[H^+]_{added} = \frac{I_{H^+}}{nF\dot{V}_{ow}} \tag{4.27}$$

The electric current applied between the electrodes can then be estimated based on the number of H^+ added,

$$I_{H^+} = nF\dot{V}_{ow}[H^+]_{added} \tag{4.28}$$

Without loss of generality, the energy consumed per unit of CO_2 captured can be calculated as,

$$e_{echem} = P/\dot{m}_{CO_2} \tag{4.29}$$

Where P is the power consumed by the electrodes and $\dot{m}_{CO_2}$ is the mass flow rate of CO_2 captured (kg/s). Because P is nothing but the product of the voltage difference between electrodes ($V_{acidification} = 0.7\,V,\ \ V_{alkalinization} = 0.1\,V$) and the electric current applied ($I_{H^+} = nF\dot{V}_{ow}[H^+]_{added}$), we can express the total energy consumed for the two steps (acidification and alkalinization) as,

$$e_{echem} = \frac{V_{acidification} I_{H^+}}{\dot{m}_{CO_2}} + \frac{V_{alkalinization} I_{H^+}}{\dot{m}_{CO_2}} \tag{4.30}$$

$$e_{echem} = \frac{V_{acidification} nF\dot{V}_{ow}[H^+]_{added}^{acidification}}{\dot{m}_{CO_2}} + \frac{V_{alkalinization} nF\dot{V}_{ow}[H^+]_{added}^{alkalinization}}{\dot{m}_{CO_2}}$$

Where the ratio $\frac{\dot{V}_{ow}}{\dot{m}_{CO_2}}$ is given by the efficiency of the CO_2 capture process. A key quantity in the equation above is the number of H^+ added to oceanwater, $[H^+]_{added}$. This is related to the change in ionic concentrations of HCO_3^-, CO_3^{2-}, OH^- and H^+ from the initial values, and can be determined as,

$$[H^+]_{added} = \Delta[HCO_3^-] + \Delta 2[CO_3^{2-}] + \Delta[OH^-] - \Delta[H^+] \tag{4.31}$$

With,

$$[CO_2] = \frac{[H^+]^2}{[H^+]^2 + K_1[H^+] + K_1K_2} DIC \tag{4.32}$$

$$[HCO_3^-] = \frac{K_1[H^+]}{[H^+]^2 + K_1[H^+] + K_1K_2} DIC \tag{4.33}$$

$$[CO_3^{2-}] = \frac{K_1K_2}{[H^+]^2 + K_1[H^+] + K_1K_2} DIC \tag{4.34}$$

$$[OH^-] = \frac{K_{ow}}{[H^+]} \tag{4.35}$$

Where K_1 and K_2 are the first and second dissociations constants for carbonic acid, respectively, and K_{ow} is the ion-product constant of liquid water. Note that DIC is lowered due to the reaction, which removes 87% of it. As a result, the DIC value used in (4.32) and (4.33) is different in the acidification and alkalinization steps,

$$DIC_{initial} = 2.2\,mM, \qquad DIC_{final} = (1 - 0.87) \cdot 2.2\,mM \tag{4.36}$$

According to Kim et al.[166], in the first reaction (i.e. acidification), the pH is lowered from the inlet value to pH = 6. Assuming surface oceanwater at a typical value of pH=8.1, expression (4.30) would be explicitly written as:

$$[H^+]_{added}^{acidification} = \left([HCO_3^-]_{pH=8.1} - [HCO_3^-]_{pH=6}\right) + 2 \cdot \left([CO_3^{2-}]_{pH=8.1} - [CO_3^{2-}]_{pH=6}\right) + \left([OH^-]_{pH=8.1} - [OH^-]_{pH=6}\right) - \left([H^+]_{pH=8.1} - [H^+]_{pH=6}\right)$$

While for the second reaction (i.e. alkalinization), the pH is raised from the acidified pH = 6 to pH = 11,

$$[H^+]_{added}^{alkalinization} = \left([HCO_3^-]_{pH=6} - [HCO_3^-]_{pH=11}\right) + 2 \cdot \left([CO_3^{2-}]_{pH=6} - [CO_3^{2-}]_{pH=11}\right) + \left([OH^-]_{pH=6} - [OH^-]_{pH=11}\right) - \left([H^+]_{pH=6} - [H^+]_{pH=11}\right).$$

When the initial pH is set to the one used by Kim et al.[166], we correctly get the base electrochemical energy of 750 kWh/tCO$_2$.

4.6.2. Fundamentals of chemical oceanography

4.6.2.1. Dissolved inorganic carbon and pH

In the sunlit surface region of the ocean, phytoplankton uses CO$_2$ during photosynthesis as part of the so-called biological pump[157]. Phytoplankton, which is at the base of the ocean food chain, is then consumed by larger marine organisms, to which the carbon captured by the phytoplankton is fixed. Upon their death, these larger organisms begin to sink and decompose due to the action of bacteria and microbes on their way down to the seabed (i.e. microbial respiration), which consumes oxygen and releases CO$_2$ back into the water, thus increasing the amount of DIC with water depth (**Figure 4.10**). This gradient of DIC is enhanced because of the larger solubility of CO$_2$ at colder temperatures, typical of deeper waters (e.g. in polar waters at 0 ℃, the solubility of CO$_2$ is more than twice the solubility of equatorial waters at 25 ℃, ref.[227]). The re-emission of CO$_2$ during microbial respiration also shifts the carbonate speciation to lower pHs (acidification), which explains the decrease in pH with water depth (**Figure 4.10**).

Note that the geographical characteristics of the gradient of DIC, larger in higher latitudes, conveniently pairs with areas identified for offshore wind-powered CDR with sequestration into deep-sea basalt by Norton et al.[42], most of which are located near the poles. This can provide unique cost-saving opportunities for offshore wind-powered DOCCS into deep-sea basalt.

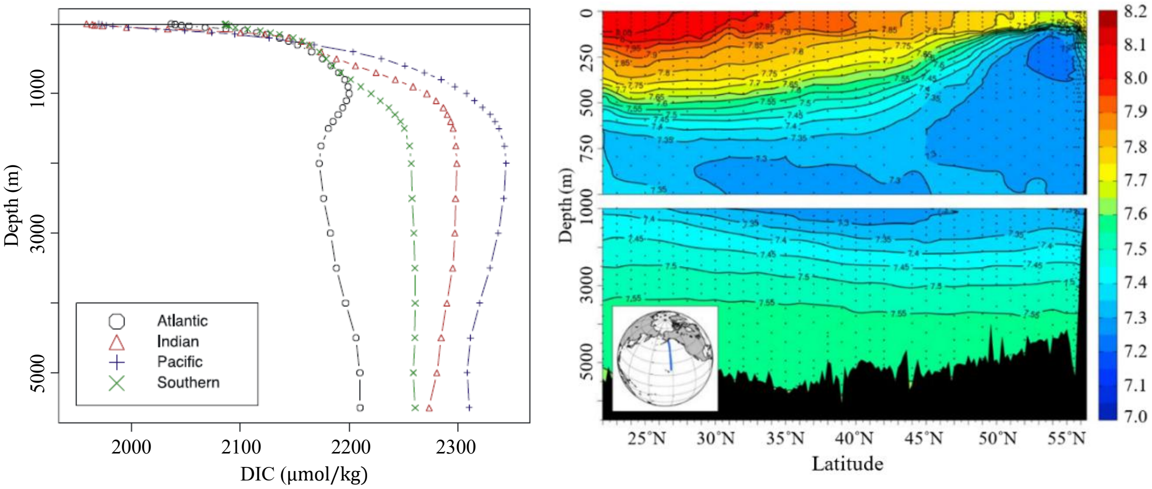

Figure 4.10. Variation with sea water depth of (left) dissolved inorganic carbon by ocean, and (right) pH in the North Pacific along 152°W, modified from refs.[225,228]**.**

4.6.2.2. Oxygen and nitrogen

The concentration of oxygen peaks at the surface because: 1) the air-sea exchange, and 2) photosynthesis, in which primary producers use sunlight to synthesize oxygen. As the depth increases, the exchange with the atmosphere and the light that penetrates the water lessens, and so the amount of oxygen introduced from the former and produced by photosynthesis diminishes too. Organic matter decays and respiration by micro- and macro-marine organisms cause oxygen levels to decrease further. In the North Pacific Ocean, these effects exhibit a minimum oxygen layer between 500 and 1,000 m (**Figure 4.11**). Below this layer, as the water temperature decreases and pressure increases, the partial pressure and the amount of oxygen dissolved also increase (Henry's law). This is enhanced by deep, nutrient- and oxygen-rich waters forming in polar regions and circulating globally throughout ocean basins. These patterns explain the increase in oxygen concentration at depths greater than 1,500 m shown in **Figure 4.11**.

As atmospheric nitrogen enters and dissolves into the ocean surface, it is fixed into ammonium by bacteria, making it more bioavailable to some phytoplankton. Most ammonium, however, is further converted through nitrification into other nitrogenous species, such as nitrate, which is a major nutrient utilised by primary producers. As a result, most surface nitrate is consumed during photosynthesis and is progressively regenerated with the water depth as the organisms that have absorbed it decay (**Figure 4.11**).

4.6.2.3. Salinity and ionic conductivity

Salinity in oceanwater varies due to freshwater addition and removal primarily through the processes of evaporation, precipitation, river run-off, and ice melt; evaporation increases surface ocean salinity, while precipitation, river run-off, and ice melt reduce it. When precipitation dominates over evaporation, it causes surface waters to exhibit lower salinity than deeper waters (**Figure 4.11**). Surface waters tend to show an almost constant salinity due to the constant mixing they are subjected to from wind, waves, and currents. The bottom of the mixed layer is in contact with the halocline, a region which is characterised by rapid changes in salinity.

Oceanwater contains a myriad of dissolved salts or ionic compounds (e.g. chloride, sodium, magnesium, sulfate, calcium, etc.) which are responsible for its salinity. The mobility of these ions is enhanced by seawater temperature, and to a lesser extent by pressure. Both the concentration (i.e. salinity) and mobility (i.e. temperature and pressure) of dissolved salts determine the ionic conductivity of seawater[229]. High-salinity, warm oceanwater with high ionic conductivity thus improves the energy efficiency of electrochemical procedures such as DOC[230]. In mid-latitudes, however, the increase in salinity with depth is greatly diminished by its corresponding temperature drop, overall causing ionic conductivity to decrease with depth.

With some generality, note that the largest variations of DIC, oxygen and nitrogen concentration, and salinity occur between the surface and the first thousand meters (**Figure 4.11**). This should be remembered as our water intake depths (20 m, 100 m, 200 m, 300 m) are within this region.

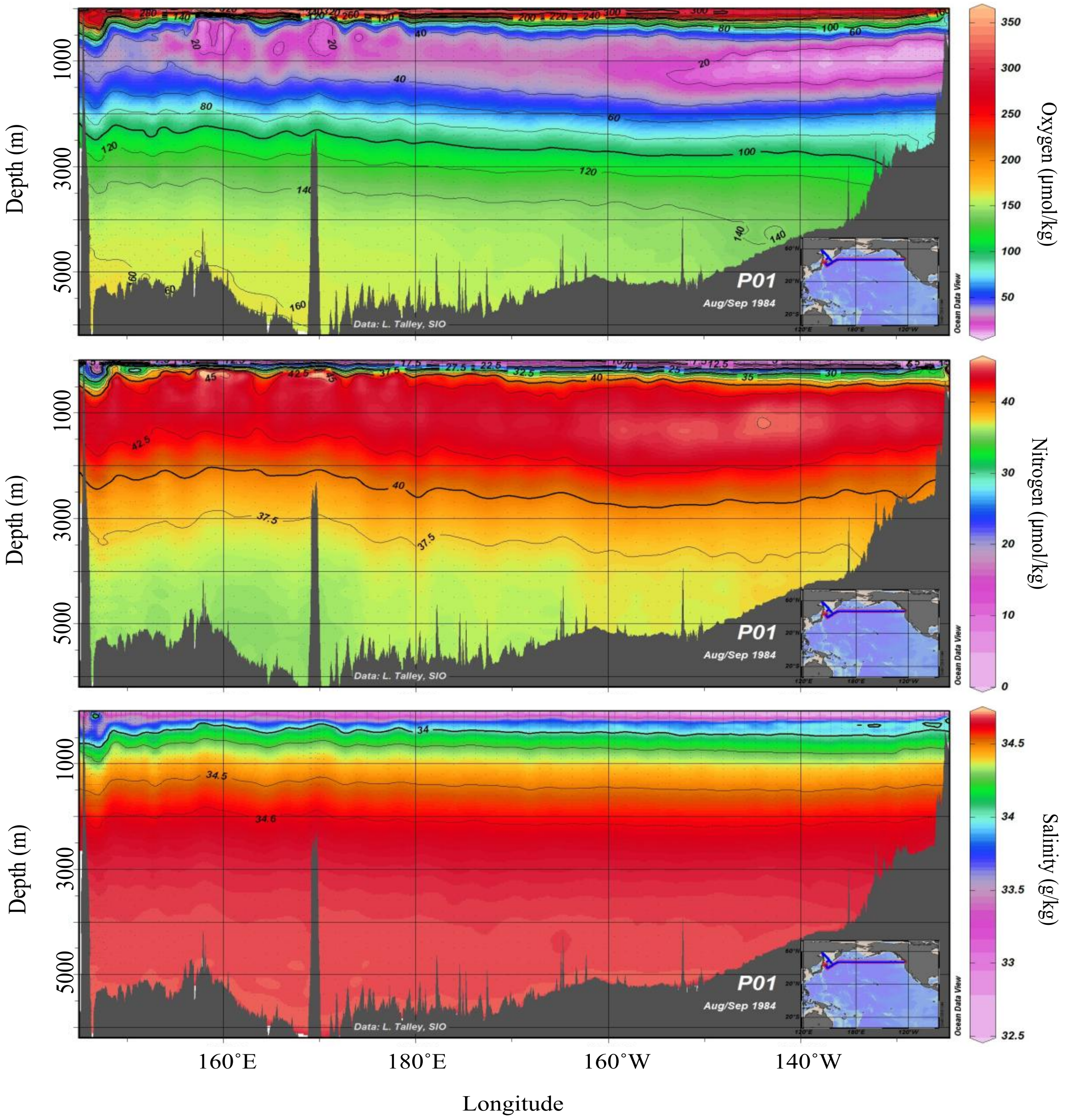

Figure 4.11. Dissolved oxygen (top) and nitrogen (middle) profiles, and salinity (bottom) for the Pacific Ocean (1984) between Japan and USA (40-50˚N) adapted from Schlitzer[231].

4.6.3. Pressure losses

The pressure loss (Δp) experienced by a flow through a channel (either a circular pipe such as the SWIR, or a rectangular duct such as the electrochemical cells) is often characterised by the Darcy-Weisbach equation:

$$\Delta p = \rho f_D \frac{L}{2D_h} \langle v \rangle^2 \tag{4.37}$$

Where ρ is the fluid density, f_D is the Darcy friction factor, L is the channel length, $\langle v \rangle$ is the mean flow velocity, and D_h is the hydraulic diameter of the channel. The Darcy friction factor depends on the channel's surface roughness (ε), and the Reynolds number (Re), and it is most popularly expressed via the implicit Colebrook-White formulation:

$$\frac{1}{\sqrt{f_D}} = -2\log\left(\frac{\varepsilon}{3.7D_h} + \frac{2.51}{Re\sqrt{f_D}}\right) \tag{4.38}$$

For Reynolds values between $5000 \leq Re \leq 10^8$, and relative surface roughness values between $10^{-6} \leq \frac{\varepsilon}{D_h} \leq 0.05$, the Colebrook-White formulation is solved through the Swamee-Jain approximation:

$$f_D = 0.25\left[\log\left(\frac{\varepsilon/D_h}{3.7} + \frac{5.74}{Re^{0.9}}\right)\right]^{-2} \tag{4.39}$$

4.6.4. Floating wind turbine platform

	Advantages	**Disadvantages**
Spar	Inherently stable. Simpler and more inexpensive moorings. Wide range of seabed conditions.	Larger motions and accelerations. Large seabed footprint. Since CoG tends to be below CoB, spars may be more sensitive to the addition of mass close to the water line. Traditionally limited installation and tow-out from ports with sufficient depth (partly addressed by new concepts, e.g. ref.[232]).
TLP	Reduced heave and pitch motion and acceleration. Reduced wear and tear on the turbines due to reduced motions. Reduced seabed footprint. Low sensitivity to waves. Potentially less dynamically sensitive to the integration of DOC system on-board.	The seabed must have sufficient geotechnical strength to hold the anchors securely. Inherently unstable during installation and tow-out (addressed by new concepts, e.g. ref.[190]). Complex and costly installation due to high tensioned tendons and required levels of positioning accuracy. Not suitable for locations with large tidal ranges. Large stresses. High risk in case of line or anchor failure. Tendons are sensitive to high-frequency wave loads.

CoG: centre of gravity, CoB: centre of buoyancy.

4.6.5. Detailed costs

	Units	Case 0	Case 1	Case 2	Case 3	Notes
TOTAL FOWT platform costs	**USD**	**124,347,076**	**126,631,990**	**129,786,369**	**132,940,749**	
TLP floater	USD	123,370,801	-	-	-	Ref. [183]
Seawater intake system + battery	USD	976,275	3,261,189	6,415,568	9,569,948	Refs.[202,203,209]

	Units	Case 0	Case 1	Case 2	Case 3	Notes
TOTAL DOC costs	**USD**	**134,225,018**	**144,007,263**	**149,226,472**	**152,754,820**	**The costs in bold are discounted costs**
Electrochemical cells	**USD**	**884,644**	**1,002,490**	**1,036,481**	**1,046,008**	CapEx+OpEx+Cells replacement
CapEx	USD	388,118	405,343	459,340	474,914	\$23/tCO_2·Annual capture, ref.[166]
Lifetime levelized OpEx	USD	142,026	148,330	168,089	173,788	Discounted annual OpEx (6.5% discount rate), 25-year plant lifetime
Annual OpEx	USD	11,644	12,160	13,780	14,247	3% CapEx
Cells replacement	USD	316,907	330,972	375,061	387,779	Every 10 years
Vacuum pump and condenser	**USD**	**12,057,350**	**12,057,350**	**12,057,350**	**12,057,350**	CapEx+OpEx+Replacement +total (labor, property taxes, and insurance)
CapEx	USD	4,623,679	4,623,679	4,623,679	4,623,679	EPC+contingency+owner's cost
Engineering, procurement, construction (EPC)	USD	3,556,676	3,556,676	3,556,676	3,556,676	Total equipment direct + indirect costs
Total equipment direct cost	USD	3,147,501	3,147,501	3,147,501	3,147,501	Water condenser + vacuum pump + chiller
Water condenser purchase cost	USD	143,917	143,917	143,917	143,917	Supp. Table 6, ref. [22]
Vacuum pump	USD	2,430,409	2,430,409	2,430,409	2,430,409	
Vacuum pump chiller	USD	573,175	573,175	573,175	573,175	
Total equipment indirect cost	USD	409,175	409,175	409,175	409,175	13% Total equipment direct cost
Contingency cost	USD	889,169	889,169	889,169	889,169	25% EPC, ref.[22]
Owner's cost	USD	177,834	177,834	177,834	177,834	5% EPC, ref.[22]
Lifetime levelized OpEx	USD	1,759,651	1,759,651	1,759,651	1,759,651	Discounting annual OpEx (6.5% discount rate), 25-year plant lifetime
Annual OpEx	USD	144,259	144,259	144,259	144,259	3.12% CapEx, ref.[22]
Replacement vacuum pump	USD	1,984,485	1,984,485	1,984,485	1,984,485	Every 10 years
Total levelized labor, property taxes and insurance	USD	3,689,535	3,689,535	3,689,535	3,689,535	Discounted annual labor, property taxes and insurance (6.5% discount rate), 25-year plant lifetime
Total annual labor, property taxes and insurance	USD	302,474	302,474	302,474	302,474	
Annual labor cost	USD	210,000	210,000	210,000	210,000	Ref.[22]
Annual property taxes and insurance	USD	92,474	92,474	92,474	92,474	2% CapEx, ref.[22]
Oceanwater pumping and pretreatment	**USD**	**54,513,335**	**55,167,040**	**55,277,278**	**55,266,627**	CapEx+OpEx
CapEx for oceanwater intake, pretreatment and pumping	USD	36,794,684	37,385,957	37,500,350	37,506,351	Supp. Eq. (59), ref. [22]
Combined oceanwater intake & pretreatment cost	USD	25,172,138	25,582,641	25,662,249	25,666,613	Supp. Eq. (49), ref. [22]
Total pump and electric motor cost	USD	361,993	361,812	361,589	361,389	Supp. Eq. (58), ref. [22]
Total centrifugal pump purchase cost (2006)	USD	444,752	444,477	444,047	443,636	Supp. Eq. (50), ref. [22]
Pump flow rate	GPM	21,226	21,660	21,744	21,749	
Pump head	ft	195	187	185	185	
Pump size factor		296,774	296,515	296,108	295,720	Supp. Eq. (52), ref. [22]
Pump base cost (2006)	USD	18,531	18,520	18,502	18,485	Supp. Eq. (53), ref. [22]
Centrifugal pump purchase cost (2006)	USD	74,125	74,079	74,008	73,939	Supp. Eq. (50), ref. [22]
Number of pumps		6	6	6	6	
Total pump's electric motor purchase cost (2006)	USD	360,050	359,923	359,855	359,821	
Pump's electric motor power	kW	1,393	1,365	1,357	1,353	Supp. Eq. (55), ref. [22]
Pump's motor base cost (2006)	USD	42,863	42,848	42,840	42,836	Supp. Eq. (54), ref. [22]
Pump's motor purchase cost (2006)	USD	60,008	59,987	59,976	59,970	Supp. Eq. (53), ref. [22]

Lifetime levelized OpEx (with marinization factor)	USD	17,718,651	17,781,083	17,776,928	17,760,276	
Total annual OpEx (with marinization factor)	USD	1,452,601	1,457,720	1,457,379	1,456,014	
Annual electricity OpEx	USD	221,761	217,317	215,924	215,313	Supp. Eq. (60), ref. [22]
Annual maintenance OpEx	USD	95,087	97,029	97,407	97,428	Supp. Eq. (61), ref. [22]
Annual insurance OpEx	USD	183,973	186,930	187,502	187,532	Supp. Eq. (62), ref. [22]
Annual labor OpEx	USD	77,529	79,112	79,420	79,437	Supp. Eq. (63), ref. [22]
CO_2 compressor	**USD**	**7,058,573**	**7,368,764**	**7,409,254**	**7,415,387**	CapEx+OpEx
Total CapEx compressors	USD	803,253	933,692	938,546	939,906	
Number of screw compressors (stage 1)		3	3	3	3	
Number of reciprocating compressors (stage 2)		3	3	3	3	
Number of reciprocating compressors (stage 3)		1	2	2	2	
Number of diaphragm compressors (stage 4)		1	1	1	1	
Base purchase cost - screw compressor (stage 1) (2006)	USD	95,177	95,177	95,177	95,177	Eq. (22.38), ref. [204]
Base purchase cost - reciprocating compressor (stage 2) (2006)	USD	162,233	162,233	162,233	162,233	Eq. (22.37), ref. [204]
Base purchase cost - reciprocating compressor (stage 3) (2006)	USD	252,584	252,584	252,584	252,584	Eq. (22.37), ref. [204]
Base purchase cost - diaphragm compressor (stage 4) (2006)	USD	765,692	765,692	765,692	765,692	Eq. (22.38), ref. [204]
Lifetime levelized OpEx (with marinization factor)	USD	6,255,320	6,435,072	6,470,708	6,475,480	
Total annual OpEx (with marinization factor)	USD	512,820	527,557	530,478	530,869	
Annual electricity OpEx for compressors	USD	9,988	11,319	11,702	11,810	Supp. Eq. (60), ref. [22]
Annual maintenance & labor OpEx	USD	190,174	194,059	194,814	194,855	Supp. Eqs. (61),(63), ref. [22]
Annual insurance OpEx	USD	4,016	4,668	4,693	4,700	Supp. Eq. (62), ref. [22]
CO_2 riser	**USD**	**56,254,185**	**62,338,726**	**64,125,932**	**64,478,219**	CapEx+OpEx
Total CapEx riser	USD	50,138,369	55,561,413	57,154,319	57,468,306	Refs. [59,204,206]
Lifetime levelized OpEx (with marinization factor)	USD	6,115,816	6,777,313	6,971,613	7,009,913	
Total annual OpEx	USD	501,384	555,614	571,543	574,683	1% CapEx, ref. [59]

Chapter 5.

Conclusions and future work

> "*Climate change is not so much an emergency as a festering injustice. Your ancestors did not end slavery by declaring an emergency and dreaming up artificial boundaries on "tolerable" slave numbers. They called it out for what it was: a spectacularly profitable industry, the basis of much prosperity at the time, founded on a fundamental injustice. It's time to do the same on climate change.*"
>
> Myles Allen, Professor of Geosystem Science, Leader of ECI Climate Research Programme, University of Oxford, Lead Author of the IPCC WG1 Third Assessment.

This final chapter summarises the study presented in Chapters 2 to 4, underscoring the contributions of this dissertation. It ends the dissertation with a discussion of potential avenues of research arising from it.

5.1. Summary and contributions

Climate change is one of the nine systems and processes identified in the Planetary Boundaries (PB) framework[lxiii] by Rockström et al.[233,234], which quantifies the "safe operating space for humanity", ref. [235]. The PB framework recognises these boundaries as key functions regulating the stability, resilience, and life-support functions of the Earth system, which are three crucial aspects impacting human development. As of 2025, the safe limits of the control variables describing the climate change system – namely, the atmospheric concentration of CO_2 and the total anthropogenic radiative forcing at the top of the atmosphere – have long been transgressed[235]. The atmospheric CO_2 concentration is currently at 423 ppm, exceeding the PB proposed of 350 ppm (equivalent to a global warming of 1.5°C above pre-industrial levels). The increase in atmospheric CO_2 concentration - accompanied by a warming of the atmosphere, ocean, and land - has already intensified weather extremes and threatened the provision of shelter, food and water for the most vulnerable parts of the population[1].

A key factor driving the surge in CO_2 concentration is the human-induced release of CO_2 emitted through the extraction, processing and combustion of fossil fuels. Since these activities are

---

[lxiii] The nine PBs selected are climate change, introduction of novel entities, stratospheric ozone depletion, atmospheric aerosol loading, ocean acidification, biogeochemical flows, freshwater change, land system change, and change in biosphere integrity. For more information, see Rockström et al.[234].

closely linked to major sectors of the economy, such as energy production, transportation, and agriculture, preventing CO_2 concentration from escalating any further requires profound changes of our economic system[lxiv].

In addition to curtailing current CO_2 emissions, historical emissions must be offset by carbon dioxide removal (CDR) methods, resulting in the overall lowering of the concentration of CO_2 in the atmosphere. Estimates suggest[5] that staying below 1.5℃ of global warming with limited or no overshoot requires upscaling CDR so that 100 to 1,000 $GtCO_2$ can be removed by 2100. The Solid Carbon project aims to contribute to that effort by delivering scalable CDR methods and demonstrating the feasibility of CO_2 sequestration in ocean basalt[lxv]. Of the three Activity Areas that compose Solid Carbon, Activity Area 1, within which this dissertation is conducted, focuses on investigating design options for renewably powered CO_2 direct air carbon capture and sequestration (DACCS) and direct ocean carbon capture and sequestration (DOCCS) in subseafloor basalt.

Being located offshore, basalt can be paired with offshore renewable energy sources. Currently, offshore wind turbines are the most competitive technology for generating power in the ocean environment, with multi-billion-dollar, fully developed industries and markets in China and Europe. For this reason, different offshore wind-powered CO_2 DAC (Chapter 2 and 3) and DOC (Chapter 4) designs are proposed and analysed. In particular, we opted for floating offshore wind turbines (FOWTs), which, albeit less developed and more expensive than fixed-bottom turbines, open up the possibility of harnessing winds offshore regardless of the water depth, which is of special interest for those countries with low availability of shallow waters, such as the west coast of Canada.

GOAL AND APPROACH

The goal of the present dissertation was to provide a *first set* of *partial*, *conceptual* solutions to the problem of CDR with offshore sequestration. I used the terms *first set* to highlight, on one hand, the fact that the concepts put forward – namely, the FOWT-DAC (Chapter 2) and FOWT-DOC (Chapter 4) platforms – may not represent final iterations of the design process, and that further research yielding incrementally refined solutions can be expected in this front. I also used the term *partial* to denote that we addressed only the “capture” element of the CDR package and did not explore the injection and sequestration into the reservoir. Foremost, this work is a *conceptual* study and as such is meant to be exploratory, enabling us to sift amongst the myriad possible solutions in the design space and to guide future endeavours.

The research began by exploring configuration typologies for a FOWT-powered DAC system (Chapter 2). Drawing from similar archetypes in offshore wind-powered hydrogen synthesis, we

---

[lxiv] While some high-income countries and regions such as the United States, the European Union, the United Kingdom, Japan, and Korea claim to have reduced their total and per capita CO_2 emissions mainly through rapid growth in clean energy investment and electrification, improved energy efficiency, and reducing coal usage[276], no country is achieving so at a fast-enough rate to be in compliance within their “fair-shares of the global carbon budget for a 50% chance of limiting global warming to 1.5°C”, ref.[261]

[lxv] Basalt reacts with the injected CO_2 to turn it into carbonate rock, providing a permanent way of disposing of it. Ocean basalt has the capacity to store dozens of teratons of CO_2, multiple times larger than what estimates on CDR needs indicate.

chose a decentralised configuration, in which all system equipment is co-located and integrated together with the FOWT platform. We surmised a decentralised approach could remove the need for additional infrastructure to house the DAC equipment, such as extra floating platforms, thus reducing capital and operational costs. Further, given the novelty of a combined FOWT-DAC system, the focus of research was kept on early identification of synergies and cost-reduction pathways of single platforms, rather than arrays of them. However, because CDR must ultimately be scaled up, we stressed the importance of replicable and modular design solutions, which we believed strengthened the case for our decentralised configuration.

These two design philosophies – decentralised and modular configurations – guided the design decision-making process throughout the dissertation, as also reflected in the FOWT-DOC platform (Chapter 4). The design process followed then the next structure:

1) Estimate the CO_2 capture energy intensity (in units of energy per units of CO_2 captured) of the removal method (DAC or DOC) with its corresponding ancillary services (e.g. air fans, pumping water, etc.),
2) Estimate space available in/on the floating platform to house the CO_2 capture and ancillary services, and
3) Determine the CO_2 capture capacity per floating platform.

Step 3 assumed all energy available from the wind turbine was dedicated to power CO_2 capture and ancillary services - that is, no power was exported to the grid or to other non-related activities. Further, to ensure an even comparison between the FOWT-DAC and FOWT-DOC platforms, the same wind turbine rated power and capacity factors were chosen. However, we opted for different platform substructures in each case – a semisubmersible for the FOWT-DAC and a TLP for the FOWT-DOC – to better accommodate their specific dimensional needs and reduce costs where possible.

CONTRIBUTIONS

The principal outcome of this dissertation is the conceptual design and analysis of two integrated floating offshore wind-powered DAC and DOC platforms.

- Chapter 2 designed for the first time a FOWT-DAC platform and highlighted its potential to serve as a viable modular deployment approach. This was accomplished by demonstrating the dynamic (hydrostatic, hydrodynamic, stresses and displacements) and power performance similarities of the FOWT-DAC platform with respect to the FOWT platform reference design (without DAC).
- Chapter 3 extended the scope of Chapter 2 by adding a pipe to transport the CO_2 captured by the FOWT-DAC platform to the seabed. It then analysed the influence the CO_2 internal flow (effective tension, von Mises stress and curvature) had on the dynamics of the flexible pipe. The effective tension and curvature were not affected by the internal flow, but the von Mises stress was due to its dependence on the internal pressure through the shear stress term.
- Chapter 4 turned the attention from DAC to DOC; a more novel CDR concept better suited for the offshore environment. Following the same decentralised and modular philosophy as in Chapter 2, Chapter 4 designed an integrated FOWT-DOC platform and suggested four different scenarios, each drawing seawater from increasingly greater depths with higher DIC

concentrations and correspondingly lower energy intensities. The key finding was showing that the least energy intensive scenario was not the most economical. This was explained by the rising linear costs associated with deeper withdrawal outweighing the benefits from lower energy intensities, whose rate of change was slower than the costs'.

In addition, the two designs proposed were compared in terms of energy intensity, CO_2 capture capacity, and cost (Chapter 4). Below are the main findings:

- The carbon capture energy intensity of DAC was, on average, 1.8 times that of DOC (including all ancillary services), where the main DOC energy cost centre was water pumping. Because the power available for CO_2 capture from each FOWT platform was assumed the same, this difference led the FOWT-DAC platform to capture, on average, twice as much CO_2 than the FOWT-DOC platform on an annual basis.
- In contrast, the average costs of the FOWT-DAC (\$1,229/tCO_2) and FOWT-DOC (\$1,136/tCO_2) platforms did not exhibit such startling differences; in fact, FOWT-DAC was almost \$100/tCO_2 more expensive. This is explained by (1) more intensive capital and operational DAC costs due to sorbent materials and the provision of heat for regeneration, and (2) the choice of floating substructure, as the FOWT-DAC semisubmersible platform's LCOE was €35/MWh more expensive than the FOWT-DOC TLP platform's LCOE.
- However, given the cost range of FOWT-DAC (\$757/tCO_2 to \$1,991/tCO_2), it cannot be concluded on a cost basis alone that FOWT-DOC is preferable to FOWT-DAC in a hypothetical FOWT-powered carbon removal project. In such a case, it will be necessary to additionally consider technical simplicity and technological readiness, industry experience, environmental impacts, societal acceptance and justice, to name but a few considerations.

A PERSPECTIVE FOR CANADA

In Chapter 1, we highlighted the potential role of the solutions presented in this dissertation to develop the offshore wind sector in Canada; this section provides further insight using the cost data derived in Chapter 4.

According to Bushman and Merchant[236], Canada will need around 500 Mt of CO_2 removal per year by 2050 to address historical and residual emissions. The share of removal each CDR method will contribute to is uncertain, bounded pessimistically by industry size and optimistically by technical potential.

For simplicity, let us suppose three CO_2 removal scenarios, in which the FOWT-DAC and FOWT-DOC solutions explored in this dissertation capture each 1% (5 $MtCO_2$/year), 10% (50 $MtCO_2$/year), and 30% (150 $MtCO_2$/year) of Canada's CDR needs by 2050. Given the CO_2 unit capture of each solution (i.e. 29 FOWT-DAC units per $MtCO_2$/year, and 51 FOWT-DOC platforms per $MtCO_2$/year of removal, on average), we can then estimate the total amount of platform units and the corresponding installed capacity (**Table 5.1**). Due to the lower CO_2 unit capture of each FOWT-DOC platform, a greater number of units is required.

Table 5.1. FOWT-DAC and FOWT-DOC unit deployment for three CO_2 removal scenarios by 2050.

Magnitude/Scenario	1%	10%	30%
CO_2 removal ($MtCO_2$/year)	5	50	150
# 15-MW FOWT-DAC platforms (wind capacity, in GW)	145 (2.2)	1,450 (22)	4,350 (65)
# 15-MW FOWT-DOC platforms (wind capacity, in GW)	251 (3.8)	2,510 (38)	7,530 (113)

To do this, we took into consideration how cumulative learning through increased deployment reduces the otherwise linear CapEx per unit (or $CapEx_0$ in equation (5.1)) when scaling up wind power production from X_0 to X. This learning applied to CapEx is expected through experimentation, design optimisation, R&D, and unit-scale economies, and is assumed to have a learning rate (LR) of 8%, as per ref.[237]. The same authors define CapEx as the sum of the development expenditure, turbine supply cost, platform and moorings supply cost, and other project expenses (insurance, project management, and contingencies)[237].

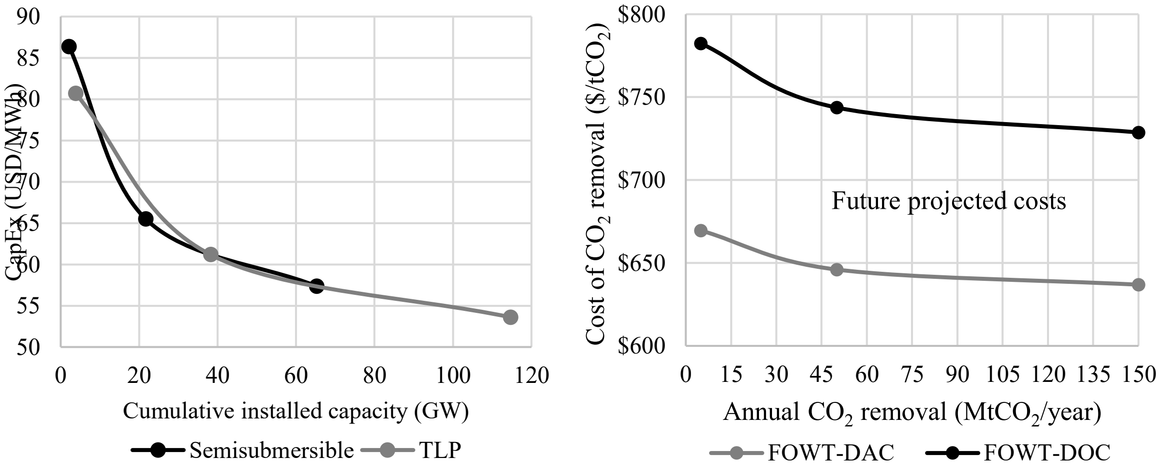

Figure 5.1. (Left) Future projected CapEx for the FOWT platforms (semisubmersible and TLP) used in the FOWT-DAC and FOWT-DOC solutions. (Right) Future projected cost of CO_2 removal via FOWT-DAC and FOWT as a function of the annual CO_2 removal.

The learning rate LR is accounted in equation (5.1) through the experience parameter E, defined in equation (5.2), and its non-linear effects on the CapEx due to learning via cumulative deployment can be visualised in **Figure 5.1.**

$$CapEx_X = CapEx_0 \left(\frac{X}{X_0}\right)^{-E} \tag{5.1}$$

$$LR = 1 - 2^{-E} \tag{5.2}$$

The costs of our FOWT semisubmersible and TLP platforms were initially estimated in section **4.4** using equation (4.18) with LCOE values given by Sykes et al.[183]. In other words, we did not determine the CapEx as the sum of its constituents; for this reason, we now estimate $CapEx_0$ as

78.5% of the LCOE[199], which excludes OpEx and decommissioning expenditures (in compliance with the definition of CapEx used above, ref.[237]).

Table 5.1 also shows the corresponding installed floating offshore wind capacity (in GW) of the different CO_2 removal scenarios by 2050 required to power CO_2 capture via DAC or DOC. The minimum installed power is 2.2 GW (1% scenario) and the maximum is 113 GW (30% scenario). To provide a sense of the scale of the effort, consider the projections of the global installed floating offshore wind capacity by 2050 by DNV[238], approximately 220 GW. Since Canada's present offshore wind capacity is zero, one may deem the required levels of deployment compatible with the 30% scenario as overly ambitious, or even unrealistic. That said, in 2023 Canada added more than 1.7 GW of onshore wind power[239]. If such annual growth were replicated offshore, Canada could comfortably achieve 34 GW of new installed wind power by 2050, assuming construction began by 2030. That would certainly be compatible with the wind power deployment required in the 1% CO_2 removal scenario requirement for both FOWT-DAC and FOWT-DOC. It would also achieve almost 90% of the estimated capacity when using DOC in the 10% CO_2 removal scenario.

Finally, the average cost of CO_2 removal via FOWT-DAC and FOWT-DOC shown in **Figure 5.1** can be compared with the estimated impacts of inaction on the Canadian economy. According to a report by the Canadian Climate Institute[240], by mid-century the loss in real GDP[lxvi] due to climate change with respect to a stable-climate reference case[lxvii] could be between \$77.9 to \$101.2 billion, or 4% to 5% of the real GDP in 2024, ref.[241]. By the end of the century, this could amount to \$391 to \$865 billion, or 18% to 40% of the real GDP in 2024.

5.2. Recommendations for future work

It is not always the case that, as one is finalising their contributions to a project, they are informed that it will be extended for a few more years. This situation places one in a privileged position (accompanied by a sense of responsibility) given the possibility that one's suggestions might shape future research considerations. This is my attempt to describe these recommendations.

FOWT-DAC PLATFORM

In Chapter 2, our FOWT-DAC platform was based on Climeworks' modular DAC unit as designed for and implemented at the Orca plant (Iceland) in 2021. At that time, Climeworks' capture system required 200-300 kWh_{el}/tCO_2 for the fans and control systems, and 1,500-2,000 kWh_{th}/tCO_2 for regeneration[242]. In 2024, Climeworks revealed upgrades to their DAC technology resulting from their integration of Svante's structured adsorbent beds (SABs), composed of low-cost and durable

---

[lxvi] The real GDP is the nominal GDP adjusted for inflation/deflation. For a given year t, it is calculated here as: $real\ GDP_t$(in *t-1* prices)= $\frac{Nominal\ GDP_t}{1+D_t}$, where D_t is the percentage annual GDP deflator.

[lxvii] In their report, the Canadian Climate Institute defines the stable-climate reference case as "the economic structure that existed in Canada in 2015"[240].

substrates onto which amines are immobilised. This configuration increases the amine surface contact area with CO_2, leading to a doubling CO_2 capture capacity per module and a halving of energy consumption. In addition, the immobilisation of the amines on the structured beds helps reducing sorbent degradation over time, thereby increasing material lifetime and lowering the CO_2 adsorption capacity loss[243]. Overall, these advances led Climeworks to claim a cutting of costs of 50 percent, en-route to achieve \$250-350/tCO_2 by 2030[244]. These are substantial advances that merit a reassessment of the costs of our FOWT-DAC platform system, especially considering that Climeworks' DAC technology is one of the two most advanced solutions currently on the market. That said, it is still unclear how the performance and durability of Climeworks' DAC technology would be affected by exposure to more humid and salty air, and by the platform's floating motion, typical of offshore environments.

One of the key performance indicators Climeworks sought to refine was the cyclic loss of CO_2 adsorption capacity - caused by sorbent degradation[lxviii] - achieving a remarkably lower than 10% loss within one year[245]. Despite the improvements, it is imperative that future economic assessments account for the effects of such capacity losses on total costs. Indeed, one modelling study suggests that cost differences could exceed \$600/tCO_2 when comparing an ideal scenario without degradation to one in which 50% of the working capacity remains after one year (Figure 3 in ref.[246]).

CO_2 TRANSPORT

As part of the cost assessment of the FOWT-DOC system presented in Chapter 4, we evaluated the costs of the CO_2 exporting riser, with similar characteristics to the riser designed in Chapter 3. Our analysis revealed that the CO_2 riser accounted for almost one quarter of the total system costs, second only to the FOWT platform itself. This finding motivates the exploration of alternative CO_2 transport methods.

The CO_2 riser enables the transfer of CO_2 from the FOWT-CO_2 capture platform (either through DAC or DOC) at the sea surface down to the seabed. Although not included in our cost estimates, the seabed section of the riser was designed to connect via a manifold to a rigid subsea pipeline, which would then export the CO_2 to the sequestration site. Alternatively, the captured CO_2 could be transported directly from the floating platform to the sequestration site by marine chemical carriers. This configuration was not adopted initially as some studies suggest it could be more expensive at our expected transport distances (<200 km, see e.g. Figure 9 in ref.[117]). That said, there is not a clearly defined distance threshold for when pipeline transport becomes more economical than shipping[116–118,213]. The optimal decision for each project is site-specific and depends among others on: (1) the existence of built-in piping infrastructure or the availability of chemical carriers, (2) metocean conditions, which constrain vessel operation times, and (3) GHG emissions associated with their operation.

[lxviii] Amine-functionalised sorbents, such as Climeworks', degrade over time when exposed to air, humidity, and heat during the adsorption and desorption stages. Depending on the cause, the rate of degradation may be more or less aggressive, for example, decreasing linearly or exponentially over time[246].

With regards to point (1), Norton et al.[42] completed a geospatial analysis investigating global sites for offshore wind-powered CO_2 capture and sequestration into basalt. Listing the criteria to determine candidate locations, they examined the distance between potential sites and major port infrastructures. Future efforts could go one step further by mapping existing subsea pipe networks and characterising existing fleets of chemical carriers.

Concerning (2), vessel downtimes resulting from limited weather windows reduce the frequency of CO_2 retrieval from the FOWT-CO_2 capture platforms. In such cases, rather than slowing down the capture of CO_2, it may be preferable to compensate for vessel downtimes by increasing the on-board CO_2 storage.

Of interest to point (3), in their 2023 strategy[247], the International Maritime Organization aimed to progressively reduce GHG emissions from international shipping - to at least 20% by 2030 and 70% by 2040 when compared to 2008 - and eliminate them completely by 2050. While this is not aimed specifically to chemical carriers, it is plausible to assume that, in broad terms, chemical carriers will not be carbon neutral at least until then.

In the context of CO_2 storage in offshore basalt formations, the design decision should also consider (4) the operational lifetime of the injection wells, which depends, among others, on the reservoir capacity and the rate of injection. This last factor will favour the transport mode flexible enough to accommodate one or multiple site reallocations at the least cost possible.

All the aforementioned considerations should be accounted for in future designs and techno-economic assessments.

FOWT-DOC PLATFORM

In Chapter 4, our FOWT-DOC platform drew oceanwater from four water depths with progressively larger DIC values (Case 0 to 3). The DOC system was based on the electrochemical cell designed by Kim et al.[166], with an estimated $\eta_{DIC} = 87\%$ DIC removal efficiency. Since the dependence of η_{DIC} on the input DIC was unknown, we assumed η_{DIC} to be constant across all DICs (i.e. for Cases 0 to 3). Consequently, the discharged, DIC-depleted stream had different DIC values, with Case 3 (having the highest natural DIC) still retaining the largest DIC value. Because the ocean's surface uptake capacity of atmospheric CO_2 depends, in part, on the CO_2 concentration gradient through the air-sea interface, the amount of CO_2 absorbed by the ocean may be lower in Case 3 than in Case 0. Under these conditions, Case 0 would be, in principle, more effective at removing atmospheric CO_2 and thus preferrable as a CDR approach. Nevertheless, these conclusions remain contingent on the assumed independence between the DIC removal efficiency and the oceanwater DIC. This assumption should be investigated in future studies.

Chapter 4 relied on the natural DIC distribution through the water column, with Cases 1-3 drawing oceanwater from deeper waters (up to 300 m) due to the richer DIC content. However, for these design solutions to be considered viable CDR approaches, it would be necessary to demonstrate that they enhance the ocean's naturally occurring uptake of atmospheric CO_2, and that they do so within a *reasonable* timeframe. The author is not aware of conversations defining what constitutes a reasonable timeframe, although the added technical and economic challenges with long-term monitoring – particularly offshore – are readily apparent. These difficulties are often highlighted by critics of CO_2 sequestration in sedimentary basins, where permanent monitoring may be required to provide adequate guarantees. As a result, some advocate instead for the use of basaltic formations, where CO_2 mineralisation can render long-term monitoring unnecessary.

Of all pressure heads identified, the drop in pressure across the pretreatment system was responsible for the largest share, up to 59% (or 3.52 bar) of the total. The pretreatment train consisted of three main filter types: disc filters, cartridge filters, and ultrafiltration membranes (UFs), each employing increasingly finer pore sizes to yield cleaner seawater, but requiring greater transmembrane pressures (TMPs). Of these, the TMP across the UF membranes (equal to 3.0 bar, after refs.[22,210]), with pore sizes of 0.01-0.1 micrometres, represented over 50% of the total pressure head and 35% of the total energy consumption.

Before such considerable expenses, two questions naturally arise. The first one concerns whether UF membranes are strictly necessary for the operation of DOC systems such as the one under consideration, ref.[166]. The short answer is no; nevertheless, they are highly desirable because they (1) prevent particulate deposition on the electrodes, thereby reducing the reaction's overpotential and associated energy costs, and (2) mitigate fouling of the hollow fiber membranes, extending their lifetime and lowering their maintenance costs. The second question relates to the magnitude of the TMP across the UF membranes. Note that refs.[22,210] assumed an unusually large TMP, significantly greater than values quoted by other authors, which typically lie in the range of 0.2-1 bar, refs.[248,249]. The reason for this discrepancy is not obvious to us and warrants further work; however, there are some apparent and unwanted outcomes that may arise from running such high TMPs that can already be identified. As formulated by Darcy's law, the flux through a porous media – that is, the permeate - is driven by TMP. Since the rate of membrane fouling generally increases with flux, it can be concluded that high TMPs lead to faster membrane fouling rates[250]. This is an undesirable consequence as membrane fouling increases energy consumption and needs more frequent cleaning, ultimately resulting in higher operational and maintenance costs.

As previously noted, the most energy-intensive process of the FOWT-DOC system is the supply of high-pressure seawater by the pumping system (up to 6 bar), which requires over 2.5 kWh per kilogram of CO_2 captured, and represents 70% of the total electricity consumed. An alternative approach is to generate pressurised seawater directly harnessing wave power. For example, Mi et al.[223] designed an oscillating surge wave energy converter capable of delivering seawater at 5-9 bar of pressure for reverse osmosis, which would almost or completely offset the work currently performed by electric pumps.

COST ASSESSMENT

Chapter 4 evaluated the levelized cost of carbon (LCC) of the FOWT-DAC and FOWT-DOC platforms, which indicated how economically efficient the systems were in capturing CO_2 over their lifetime. Owing to the emerging and early stage of development of FOWT platforms, and DAC and DOC technologies, respectively, as well as the limited availability of reliable information to accurately assess the project costs, the LCC estimates presented should be interpreted with appropriate caution. For instance, the LCC approach used ignored typical cost reductions observed with cumulative deployment due to "innovation, learning by doing, learning by using, and economies of scale", ref.[31]. Incorporating these expected savings could yield a truer (and more competitive) LCC, as done by ref.[251].

Last but not least, when comparing our LCC estimates with the costs of other CDR methods (see e.g. Table 1 in ref.[8]), it is essential that the *true* cost of carbon removal be considered. This cost should reflect the social costs of carbon emissions and climate mitigation[9,214] and, ideally, be complemented by comprehensive life-cycle assessments (LCAs). When factoring in the former, one should expect CDR techniques with longer permanence to be preferred, thus underscoring the importance of the types of solutions advocated by Solid Carbon.

When considering the latter, refs.[252,253] reviewed previous CDR LCA studies and made, among others not discussed here, two recommendations: (1) to include multiple environmental impact categories (thus avoiding e.g. the so-called "carbon-tunnel vision" only concerned with CO_2 emissions); and (2) to clearly define the assessment methodology, scope, goal, and system boundaries.

Concerning (1), Terlouw et al.[252] highlighted that some CDR LCA studies failed to include multiple environmental impacts other than GWP, such as human toxicity, freshwater toxicity and eutrophication, and resource depletion. Further, by design LCAs ignore any social justice index[lxix], which should ideally accompany studies aiming to inform about the impacts of global adoption and upscaling of a technology. Finally, with regards to (2), Butnar et al.[253] emphasised the importance to quantify indirect system-wide environmental impacts and benefits caused by the upscaling of CDR, unaccounted in 18 out of the 19 studies they reviewed.

[lxix] For instance, LCAs indicate that electric engine vehicles have a lower GWP than internal combustion engine vehicles; however, they fail to capture how lithium mining in the Global South may at present be replicating exploitative colonial patterns of extractivism[277,278]. This is not to suggest that fossil fuel production relies on more just practices, as it has historically involved equally unjust dynamics. Rather, it highlights the necessity to complement LCAs (and techno-economic assessments) with additional tools.

Erratum

CHAPTER 3: Abstract

Where it says:

> “The results indicate that the riser’s effective tension and curvature are not significantly affected by internal flow effects, but differences were observed in the von Mises stress arising from the shear stress, which is a purely hydrostatic term”

It should say:

> “The results indicate that the riser’s effective tension and curvature are not significantly affected by the internal flow, but differences were observed in the von Mises stress arising from the shear stress.”

Explanation:

> The shear stress is not a *purely hydrostatic term*, but a *purely shear term*. What I meant but failed to convey was that the shear stress only depends on the internal and external pressures. However, this can be confusing considering that there is such a thing as a “hydrostatic stress” (see e.g. Sparks[140]) and it is different from a shear stress. A hydrostatic stress is normally understood as an isotropic stress with equally compressive stresses in all directions and that produces no distortion on the body.

CHAPTER 3: CO_2 riser conclusions

Where it says:

> “However, it was also shown that the von Mises stress depends on the fluid’s internal pressure, and different values were reported for the cases with maximum pressure and no pressure. Their differences arose due to the shear term, which is purely a hydrostatic stress.”

It should say:

> “However, it was also shown that the von Mises stress depends on the fluid’s internal pressure, and different values arising from the shear term were reported for the cases with maximum pressure and no pressure.”

References

1. Calvin, K. *et al. IPCC, 2023: Climate Change 2023: Synthesis Report. Contribution of Working Groups I, II and III to the Sixth Assessment Report of the Intergovernmental Panel on Climate Change [Core Writing Team, H. Lee and J. Romero (Eds.)]. IPCC, Geneva, Switzerland.* (2023) doi:10.59327/IPCC/AR6-9789291691647.

2. Intergovernmental Panel on Climate Change (IPCC). *Climate Change 2021 – The Physical Science Basis*. (Cambridge University Press, 2023). doi:10.1017/9781009157896.

3. IPCC. Summary for Policymakers. in *Climate Change 2021 – The Physical Science Basis. Contribution of Working Group I to the Sixth Assessment Report of the Intergovernmental Panel on Climate Change* (eds. Masson-Delmotte, V. et al.) 3–32 (Cambridge University Press, Cambridge, United Kingdom and New York, NY, USA, 2021). doi:10.1017/9781009157896.001.

4. Armstrong McKay, D. I. *et al.* Exceeding 1.5°C global warming could trigger multiple climate tipping points. *Science (1979).* **377**, eabn7950 (2022).

5. IPCC. *Global Warming of 1.5°C. An IPCC Special Report on the Impacts of Global Warming of 1.5°C above Pre-Industrial Levels and Related Global Greenhouse Gas Emission Pathways, in the Context of Strengthening the Global Response to the Threat of Climate Change, Sustainable Development, and Efforts to Eradicate Poverty*. (2018).

6. IRENA. *Decarbonising Hard-to-Abate Sectors with Renewables: Perspectives for the G7*. www.irena.org (2024).

7. Smith, S. M. *et al.* The State of Carbon Dioxide Removal - 2nd Edition. in *The State of Carbon Dioxide Removal - 2nd Edition* (2024). doi:10.17605/OSF.IO/F85QJ.

8. Cross, J. N. *et al. Strategy for NOAA Carbon Dioxide Removal Research: A White Paper Documenting a Potential NOAA CDR Science Strategy as an Element of NOAA's Climate Interventions Portfolio. NOAA Special Report*. (2023) doi:10.25923/gzke-8730.

9. Prado, A. & Mac Dowell, N. The cost of permanent carbon dioxide removal. *Joule* **7**, 700–712 (2023).

10. Archer, D. *et al.* Atmospheric Lifetime of Fossil Fuel Carbon Dioxide. *Annu. Rev. Earth Planet. Sci.* **37**, 117–134 (2009).

11. Biermann, F. *et al.* Solar geoengineering: The case for an international non-use agreement. *WIREs Climate Change* **13**, (2022).

12. King, S. UK experiments to reflect sunlight one step closer. *BBC* https://www.bbc.com/weather/articles/c5ygydeqq08o (2025).

13. Seifritz, W. CO2 disposal by means of silicates. *Nature* **345**, 486 (1990).

14. Kelemen, P. B. & Matter, J. In situ carbonation of peridotite for CO2 storage. *Proceedings of the National Academy of Sciences* **105**, 17295–17300 (2008).

15. Matter, J. M. *et al.* Rapid carbon mineralization for permanent disposal of anthropogenic carbon dioxide emissions. *Science (1979).* **352**, 1312–1314 (2016).

16. Goldberg, D. S., Takahashi, T. & Slagle, A. L. Carbon dioxide sequestration in deep-sea basalt. *Proceedings of the National Academy of Sciences* **105**, 9920–9925 (2008).

17. Goldberg, D. & Slagle, A. L. A global assessment of deep-sea basalt sites for carbon sequestration. *Energy Procedia* **1**, 3675–3682 (2009).

18. Anderson, J. *et al. IPCC Special Report on Carbon Dioxide Capture and Storage. Chapter 5: Underground Geological Storage*. (2005).

19. Bachu, S., Gunter, W. D. & Perkins, E. H. Aquifer disposal of CO2: Hydrodynamic and mineral trapping. *Energy Convers. Manag.* **35**, 269–279 (1994).

20. Babiker, M. *et al.* 2022: Cross-sectoral perspectives. in *2022: Climate Change 2022: Mitigation of Climate Change. Contribution of Working Group III to the Sixth Assessment Report of the Intergovernmental Panel on Climate Change* (eds. P.R. Shukla et al.) 295–408 (Cambridge University Press, Cambridge, UK and New York, USA, 2023). doi:10.1017/9781009157926.005.

21. Ozkan, M., Nayak, S. P., Ruiz, A. D. & Jiang, W. Current status and pillars of direct air capture technologies. *iScience* **25**, 103990 (2022).

22. Digdaya, I. A. *et al.* A direct coupled electrochemical system for capture and conversion of CO2 from oceanwater. *Nat. Commun.* **11**, (2020).

23. Eisaman, M. D. *et al.* Indirect ocean capture of atmospheric CO2: Part II. Understanding the cost of negative emissions. *International Journal of Greenhouse Gas Control* **70**, 254–261 (2018).

24. IEA. *Global Energy Review 2025*. https://www.iea.org/reports/global-energy-review-2025 (2025).

25. Canada Energy Regulator. Provincial and Territorial Energy Profiles - Canada. https://www.cer-rec.gc.ca/en/data-analysis/energy-markets/provincial-territorial-energy-profiles/provincial-territorial-energy-profiles-canada.html (2024).

26. de Jonge, M. M. J., Daemen, J., Loriaux, J. M., Steinmann, Z. J. N. & Huijbregts, M. A. J. Life cycle carbon efficiency of Direct Air Capture systems with strong hydroxide sorbents. *International Journal of Greenhouse Gas Control* **80**, 25–31 (2019).

27. Jacobson, M. Z. The health and climate impacts of carbon capture and direct air capture. *Energy Environ. Sci.* **12**, 3567–3574 (2019).

28. Deutz, S. & Bardow, A. Life-cycle assessment of an industrial direct air capture process based on temperature–vacuum swing adsorption. *Nat. Energy* **6**, 203–213 (2021).

29. Terlouw, T., Treyer, K., Bauer, C. & Mazzotti, M. Life Cycle Assessment of Direct Air Carbon Capture and Storage with Low-Carbon Energy Sources. *Environ. Sci. Technol.* **55**, 11397–11411 (2021).

30. Musial, W. *et al. Survey and Assessment of the Ocean Renewable Resources in the US Gulf of Mexico*. www.boem.gov/Environmental-Studies-EnvData/, (2020).

31. Young, J. *et al.* The cost of direct air capture and storage can be reduced via strategic deployment but is unlikely to fall below stated cost targets. *One Earth* **6**, 899–917 (2023).

32. Kilpatrick, R. J., Wakim, C. & Caesar, G. *Preliminary Considerations Analysis of Offshore Wind Energy in Atlantic Canada*. https://doi.org/10.4095/331855 (2023) doi:10.4095/331855.

33. Daborn, G., Parsons, S., Whitman, L., Wilkie, A. & Wooder, J. *Regional Assessment of Offshore Wind Development in Nova Scotia. Final Report*. https://iaac-aeic.gc.ca/050/documents/p83514/160595E.pdf (2025).

34. John Dalton. *Creating a Workplan for Offshore Wind Pathways to Market Studies*. (2023).

35. Government of Nova Scotia. *Nova Scotia Offshore Wind Roadmap. Module 1*. https://novascotia.ca/offshore-wind/docs/offshore-wind-roadmap-module-1.pdf (2023).

36. Government of Nova Scotia. *Nova Scotia Offshore Wind Roadmap. Module 2: Supply Chain & Infrastructure*. https://novascotia.ca/offshore-wind/docs/offshore-wind-roadmap-module-2.pdf (2024).

37. Government of Nova Scotia. Province Sets Offshore Wind Target. https://news.novascotia.ca/en/2022/09/20/province-sets-offshore-wind-target (2022).

38. Government of Nova Scotia. Economics and Statistics. https://www.novascotia.ca/finance/statistics/archive_news.asp?id=20669&dg=&df=&dto=0&dti=3 (2025).

39. Canadian Renewable Energy Association. *CanREA's 2050 Vision. Powering Canada's Journey to Net-Zero*. https://renewablesassociation.ca/wp-content/uploads/2021/11/CanREAs2050Vision_Nov2021_web.pdf (2021).

40. Stantec with E3. *Market Opportunities for Offshore Wind in Atlantic Canada*. https://netzeroatlantic.s3.ca-central-1.amazonaws.com/files/2025-06/250609_phase_1_report_osw_grid_integration_and_transmission_print.pdf (2025).

41. Ho, D. T. Carbon dioxide removal is not a current climate solution — we need to change the narrative. *Nature* **616**, 9–9 (2023).

42. Norton, H., Todd, D. & Crawford, C. Storage capacity estimates and site conditions of potential locations for offshore-wind powered carbon dioxide removal and carbon sequestration in ocean basalt. *Carbon Capture Science & Technology* **13**, 100231 (2024).

43. Ocean Networks Canada. Solid Carbon: A rock-solid climate solution. https://solidcarbon.ca/ (2025).

44. Scherwath, M. *et al.* Solid Carbon – a Gigaton-Scale Ocean Rock Solid Climate Solution. *SSRN Electronic Journal* https://doi.org/10.2139/ssrn.5069687 (2025) doi:10.2139/ssrn.5069687.

45. Goldberg, D. *et al.* Geological storage of CO2 in sub-seafloor basalt: the CarbonSAFE pre-feasibility study offshore Washington State and British Columbia. *Energy Procedia* **146**, 158–165 (2018).

46. Davis, E. E. *et al.* Regional heat flow variations across the sedimented Juan de Fuca Ridge eastern flank: Constraints on lithospheric cooling and lateral hydrothermal heat transport. *J. Geophys. Res. Solid Earth* **104**, 17675–17688 (1999).

47. Goldberg, D. S., Lackner, K. S., Han, P., Slagle, A. L. & Wang, T. Co-Location of Air Capture, Subseafloor CO2 Sequestration, and Energy Production on the Kerguelen Plateau. *Environ. Sci. Technol.* **47**, 7521–7529 (2013).

48. Goldberg, D. & Lackner, K. Creating negative emissions at remote CO2 sequestration sites. *Greenhouse Gases: Science and Technology* **5**, 238–240 (2015).

49. Foxall, R., Ishaq, H. & Crawford, C. Design considerations for the marinisation of offshore direct air capture. *Energy* **316**, 133864 (2025).

50. Ishaq, H., Foxall, R. & Crawford, C. Performance assessment of offshore wind energy integrated monoethanolamine synthesis system for post-combustion and potential direct air capture. *Journal of CO2 Utilization* **64**, 102154 (2022).

51. Ishaq, H., Siddiqui, O., Chehade, G. & Dincer, I. A solar and wind driven energy system for hydrogen and urea production with CO2 capturing. *Int. J. Hydrogen Energy* **46**, 4749–4760 (2021).

52. Ishaq, H. & Crawford, C. Review of ammonia production and utilization: Enabling clean energy transition and net-zero climate targets. *Energy Convers. Manag.* **300**, 117869 (2024).

53. Ishaq, H. & Crawford, C. CO2-based alternative fuel production to support development of CO2 capture, utilization and storage. *Fuel* **331**, 125684 (2023).

54. Ishaq, H., Shehzad, M. F. & Crawford, C. Transient modeling of a green ammonia production system to support sustainable development. *Int. J. Hydrogen Energy* **48**, 39254–39270 (2023).

55. Shehzad, M. F., Ishaq, H. & Crawford, C. Offshore wind energy prospects for power-to-direct air capture and power-to-gas. *Int. J. Hydrogen Energy* **48**, 39216–39224 (2023).

56. Shehzad, M. F., Ishaq, H. & Crawford, C. Linear programming model predictive control for offshore wind-direct air capture system using battery storage. in *2023 European Control Conference (ECC)* 1–6 (IEEE, 2023). doi:10.23919/ECC57647.2023.10178329.

57. Avellaneda Domene, G. & Crawford, C. Dynamic analysis of a floating wind turbine platform with on-board CO2 direct air capture. *Ocean Engineering* **308**, 118205 (2024).

58. Avellaneda Domene, G. & Crawford, C. Internal flow effect of a flexible riser system for a floating offshore wind turbine with on-board carbon dioxide capture. *Ocean Engineering* **316**, 119821 (2025).

59. Norton, H., Gillessen, P. & Crawford, C. Techno-economic assessment of supercritical, cold liquid, and dissolved CO2 injection into sub-seafloor basalt. *Carbon Capture Science & Technology* **13**, 100236 (2024).

60. Connolly, P. & Crawford, C. Analytical modelling of power production from Un-moored Floating Offshore Wind Turbines. *Ocean Engineering* **259**, 111794 (2022).

61. Connolly, P. & Crawford, C. Comparison of optimal power production and operation of unmoored floating offshore wind turbines and energy ships. *Wind Energy Science* **8**, 725–746 (2023).

62. Nisa, M. U., Ishaq, H. & Crawford, C. Electrochemical approaches for CO2 point source, direct air, and seawater capture: identifying opportunities and synergies. *Environmental Science and Pollution Research* https://doi.org/10.1007/s11356-025-35890-x (2025) doi:10.1007/s11356-025-35890-x.

63. IEA. Direct Air Capture. Preprint at https://www.iea.org/reports/direct-air-capture (2022).

64. Snæbjörnsdóttir, S. *et al.* Carbon dioxide storage through mineral carbonation. *Nature Reviews Earth and Environment* vol. 1 90–102 Preprint at https://doi.org/10.1038/s43017-019-0011-8 (2020).

65. Sigfússon, B. *et al.* Reducing emissions of carbon dioxide and hydrogen sulphide at Hellisheidi power plant in 2014-2017 and the role of CarbFix in achieving the 2040 Iceland climate goals. *Energy Procedia* **146**, 135–145 (2018).

66. White, S. K. *et al.* Quantification of CO2 Mineralization at the Wallula Basalt Pilot Project. *Environ. Sci. Technol.* **54**, 14609–14616 (2020).

67. D. Caine, M. Iliffe, K. Kinsella, W. Wahyuni & L. Bond. *Dolphyn Hydrogen Phase 1 - Final Report*. www.erm.com (2019).

68. Singlitico, A., Østergaard, J. & Chatzivasileiadis, S. Onshore, offshore or in-turbine electrolysis? Techno-economic overview of alternative integration designs for green hydrogen production into Offshore Wind Power Hubs. *Renewable and Sustainable Energy Transition* **1**, 100005 (2021).

69. Ibrahim, O. S. *et al.* Dedicated large-scale floating offshore wind to hydrogen: Assessing design variables in proposed typologies. *Renewable and Sustainable Energy Reviews* **160**, 112310 (2022).

70. National Academies of Sciences, Engineering & Medicine. *Negative Emissions Technologies and Reliable Sequestration: A Research Agenda*. (The National Academies Press, Washington, DC, 2019).

71. Norton, H., Todd, D. & Crawford, C. A global assessment of potential locations for offshore wind-powered direct air capture and carbon sequestration in ocean basalt. *Unpublished manuscript* (2023).

72. Allen, C. *et al. Definition of the UMaine VolturnUS-S Reference Platform Developed for the IEA Wind 15-Megawatt Offshore Reference Wind Turbine Technical Report*. www.nrel.gov/publications. (2020).

73. Gaertner, E. *et al. Definition of the IEA Wind 15-Megawatt Offshore Reference Wind Turbine Technical Report*. www.nrel.gov/publications. (2020).

74. IEA Wind Task 37. IEA-15-240-RWT VolturnUS-S ontology. https://github.com/IEAWindTask37/IEA-15-240-RWT/blob/master/WT_Ontology/IEA-15-240-RWT_VolturnUS-S.yaml (2020).

75. Sabatino, F. *et al.* A comparative energy and costs assessment and optimization for direct air capture technologies. *Joule* **5**, 2047–2076 (2021).

76. Deutz, S. & Bardow, A. Life-cycle assessment of an industrial direct air capture process based on temperature–vacuum swing adsorption. *Nat. Energy* **6**, 203–213 (2021).

77. Ishaq, H. & Crawford, C. Potential of offshore wind energy for direct air capture. *Int. J. Energy Res.* **46**, 18919–18927 (2022).

78. Wurzbacher, J. A., Gebald, C., Brunner, S. & Steinfeld, A. Heat and mass transfer of temperature–vacuum swing desorption for CO2 capture from air. *Chemical Engineering Journal* **283**, 1329–1338 (2016).

79. Masciola, M., Chen, X. & Yu, Q. Evaluation of the dynamic-response-based intact stability criterion for floating wind turbines. in (OMAE, 2015).

80. DNV GL. *ST-0119 Floating Wind Turbine Structures*. http://www.dnvgl.com, (2018).

81. Newman, J. *Marine Hydrodynamics*. (The MIT press, Cambridge, 2018).

82. DSA Ocean. *ProteusDS Manual*. https://proteusds.com/software-downloads/ProteusDS%20Manual.pdf (2018).

83. ABS. *Guidance Notes on Air Gap and Wave Impact Analysis for Semisubmersibles*. www.eagle.org (2020).

84. DNV GL. *OTG-13 Prediction of Air Gap for Column Stabilised Units*. (2019).

85. Winterstein, S. R. *et al.* Environmental parameters for extreme response: inverse FORM with omission factors. in (ICOSSAR, Innsbruck, Austria, 1993).

86. DNV. *DNV-RP-C205: Environmental Conditions and Environmental Loads*. *Dnv* https://rules.dnv.com/docs/pdf/dnvpm/codes/docs/2010-10/RP-C205.pdf (2010).

87. Goldberg, D. *et al. Integrated Pre-Feasibility Study for CO2 Geological Storage in the Cascadia Basin, Offshore Washington State, British Columbia*. https://www.osti.gov/biblio/1488562 (2018) doi:10.2172/1488562.

88. Scherwath, M., Moran, K. & Goldberg, D. Solid Carbon: Storing CO2 in Deep Water Basalts as a Negative Emission Technology. in *AGU Fall Meeting Abstracts* vol. 2020 (2020).

89. Marine Energy Resource Atlas Canada. S3-NetCDF-API. https://github.com/meracan/s3-netcdf-api/tree/master/example (2020).

90. Copernicus program. ERA5 hourly data on single levels from 1940 to present. https://cds.climate.copernicus.eu/cdsapp#!/dataset/reanalysis-era5-single-levels?tab=form (2018) doi:10.24381/cds.adbb2d47.

91. Burton, N. T., Jenkins, D. & Sharpe, E. B. *Wind Energy Handbook*. (John Wiley & Sons, 2011).

92. Stewart, G. M., Robertson, A., Jonkman, J. & Lackner, M. A. The creation of a comprehensive metocean data set for offshore wind turbine simulations. *Wind Energy* **19**, 1151–1159 (2016).

93. DNV GL. *ST-0437 Loads and Site Conditions for Wind Turbines*. http://www.dnvgl.com (2016).

94. Liu, Y. HAMS: A frequency-domain preprocessor for wave-structure interactions-Theory, development, and application. *J. Mar. Sci. Eng.* **7**, (2019).

95. Ramachandran, G. K. V, Robertson, A., Jonkman, J. M. & Masciola, M. D. Investigation of Response Amplitude Operators for Floating Offshore Wind Turbines. in *The Twenty-third International Offshore and Polar Engineering Conference* (Anchorage, Alaska, 2013).

96. International Electrotechnical Commission (IEC). *IEC 61400-3-2: Wind Energy Generation Systems - Part 3-2: Design Requirements for Floating Offshore Wind Turbines*. (2019).

97. Niranjan, R. & Ramisetti, S. B. Insights from detailed numerical investigation of 15 MW offshore semi-submersible wind turbine using aero-hydro-servo-elastic code. *Ocean Engineering* **251**, 111024 (2022).

98. Keith, D. W., Holmes, G., st. Angelo, D. & Heidel, K. A Process for Capturing CO2 from the Atmosphere. *Joule* **2**, 1573–1594 (2018).

99. Tesla. Tesla Megapack. https://www.tesla.com/megapack (2019).

100. DOE Fuel Cell Technologies Office. Multi-Year Research, Development, and Demonstration Plan. in (2016).

101. Lucas, T. R., Ferreira, A. F., Santos Pereira, R. B. & Alves, M. Hydrogen production from the WindFloat Atlantic offshore wind farm: A techno-economic analysis. *Appl. Energy* **310**, 118481 (2022).

102. Siemens Energy. Silyzer 300 - The next paradigm of PEM electrolysis. https://assets.siemens-energy.com/siemens/assets/api/uuid:a193b68f-7ab4-4536-abe2-c23e01d0b526/datasheet-silyzer300.pdf (2018).

103. Sherif El-Eskandarany, M. Solid-state hydrogen storage nanomaterials for fuel cell applications. in *Mechanical Alloying Energy Storage, Protective Coatings, and Medical Applications* 229–261 (William Andrew Applied Science Publishers, 2020).

104. W. Langmi, H., Engelbrecht, N., M. Modisha, P. & Bessarabov, D. Hydrogen Storage. in *Electrochemical Power Sources: Fundamentals, Systems, and Applications* (eds. Smolinka, T. & Garche, J.) (Elsevier, 2021). doi:10.1016/C2018-0-05096-3.

105. Hyfindr. Hydrogen type 4 cylinder 700 bar 103L. https://hyfindr.com/marketplace/components/hydrogen-tanks/hydrogen-type-4-cylinder-700-bar-103l/.

106. Compass International Inc. *2016 Pipelines, Mining, and Offshore Cost Data Yearbook*. (Compass International Consultants Inc., 2016).

107. Chart. Bulk Storage Systems - Equipment for cryogenic services. Preprint at www.chartbulktanks.com.

108. Haver, S. & Winterstein, S. R. Environmental Contour Lines: A Method for Estimating Long Term Extremes by a Short Term Analysis. in *SNAME Maritime Convention* (SNAME, 2008). doi:10.5957/SMC-2008-067.

109. Sigurdsson, G., Cramer, E., Lotsberg, I. & Berge, B. *Guideline for Offshore Structural Reliability Analysis: Application to Jacket Platforms*. (1996).

110. Mohsen Vazirizade, S., Haldar, A. & Gaxiola-Camacho, J. R. Uncertainty Quantification of Sea Waves - An Improved Approach. *Oceanogr. Fish. Open Access J.* **9**, (2019).

111. Rosenblatt, M. Remarks on a Multivariate Transformation. *The Annals of Mathematical Statistics* **23**, 470–472 (1955).

112. Pathak, M. *et al.* Climate Change 2022: Mitigation of Climate Change. Contribution of Working Group III to the Sixth Assessment Report of the Intergovernmental Panel on Climate Change. in (eds. Shukla, P. R. et al.) (Cambridge University Press, Cambridge, UK and New York, NY, US, 2022). doi:10.1017/9781009157926.002.

113. Ishaq, H. & Crawford, C. Potential of offshore wind energy for direct air capture. *Int. J. Energy Res.* **46**, 18919–18927 (2022).

114. Shehzad, M. F., Ishaq, H. & Crawford, C. Offshore wind energy prospects for power-to-direct air capture and power-to-gas. *Int. J. Hydrogen Energy* **48**, 39216–39224 (2023).

115. Goldberg, D. S. & Moran, K. Offshore wind energy, direct air capture and carbon sequestration in basalt: Solutions for atmospheric CO2 reduction. *The Journal of Ocean Technology* **17**, 30–36 (2022).

116. ZEP. The Costs of CO2 Transport Post-demonstration CCS in the EU 2. Preprint at (2010).

117. Roussanaly, S., Brunsvold, A. L. & Hognes, E. S. Benchmarking of CO2 transport technologies: Part II - Offshore pipeline and shipping to an offshore site. *International Journal of Greenhouse Gas Control* **28**, 283–299 (2014).

118. Knoope, M. M. J., Ramírez, A. & Faaij, A. P. C. Investing in CO2 transport infrastructure under uncertainty: A comparison between ships and pipelines. *International Journal of Greenhouse Gas Control* **41**, 174–193 (2015).

119. Vermeulen, T. N. *Knowledge Sharing Report—CO2 Liquid Logistics Shipping (LLSC), Overall Supply Chain Optimization*. (2011).

120. Hokstad, P., Habrekke, S., Johnsen, R. & Sangesland, S. *Ageing and Life Extension for Offshore Facilities in General and for Specific Systems*. (2010).

121. Det Norske Veritas and Germanischer Lloyd. *DNV-ST-F201 Dynamic Risers*. http://www.dnvgl.com, (2018).

122. American Petroleum Institute. *API 17J: Specification for Unbonded Flexible Pipe*. (2009).

123. American Petroleum Institute. *API 17B: Recommended Practice for Flexible Pipe*. (1998).

124. Bai, Y. & Bai, Q. *Subsea Pipelines and Risers*. (Elsevier, 2005). doi:https://doi.org/10.1016/B978-0-08-044566-3.X5000-3.

125. Young, D. G., Ng, C., Oterkus, S., Li, Q. & Johanning, L. Assessing the mechanical stresses of dynamic cables for floating offshore wind applications. in *Journal of Physics: Conference Series* vol. 1102 (Institute of Physics Publishing, 2018).

126. Sobhaniasl, M., Petrini, F., Karimirad, M. & Bontempi, F. Fatigue life assessment for power cables in floating offshorewind turbines. *Energies (Basel).* **13**, (2020).

127. Schnepf, A., Devulder, A., Johnsen, Ø., Ong, M. C. & Lopez-Pavon, C. Numerical Investigations on Suspended Power Cable Configurations for Floating Offshore Wind Turbines in Deep Water Powering an FPSO. *Journal of Offshore Mechanics and Arctic Engineering* **145**, (2023).

128. Jonkman, B. *et al.* OpenFAST/openfast: v3.5.3. Preprint at https://doi.org/10.5281/zenodo.10962897 (2024).

129. Caine, D. *et al. ERM Dolphyn Hydrogen Phase 2-Final Report*. https://assets.publishing.service.gov.uk/media/61f953e08fa8f53894502152/Phase_2_Report_-_ERM_-_Dolphyn.pdf (2021).

130. Knoope, M. M. J., Guijt, W., Ramírez, A. & Faaij, A. P. C. Improved cost models for optimizing CO 2 pipeline configuration for point-to-point pipelines and simple networks. *International Journal of Greenhouse Gas Control* **22**, 25–46 (2014).

131. Obrien, P. *et al.* Outcomes from the SureFlex Joint Industry Project - An International Initiative on Flexible Pipe Integrity Assurance. in *All Days* (OTC, 2011). doi:10.4043/21524-MS.

132. American Petroleum Institute. Recommended Practice for Design and Installation of Offshore Production Platform Piping Systems. Preprint at (1991).

133. NTNU, 4Subsea & SINTEF Ocean. *Handbook on Design and Operation of Flexible Pipes Joint Industry Project: 'Safe and Cost Effective Operation of Flexible Pipes'-2017 Edition*. (2017).

134. Bai, Y. *Deepwater Flexible Risers and Pipelines*. (Wiley, 2021). doi:10.1002/9781119322740.

135. Orcina. K03 15MW semi-sub FOWT. https://www.orcina.com/wp-content/uploads/examples/k/k03/K03%2015MW%20semi-sub%20FOWT.pdf.

136. Walton, T. S. & Polachek, H. Calculation of Transient Motion of Submerged Cables. *Math. Comput.* **14**, 27 (1960).

137. Niiranen, J. Fast and accurate symmetric Euler algorithm for electromechanical simulations. in *6th International Conference Electrimacs'99, 14.-16.9.1999* 71–78 (Instituto Superior Técnico, Lisboa, Portugal, 1999). doi:10.13140/2.1.4663.0080.

138. Chung, J. & Hulbert, G. M. A Time Integration Algorithm for Structural Dynamics With Improved Numerical Dissipation: The Generalized-α Method. *J. Appl. Mech.* **60**, 371–375 (1993).

139. Sparks, C. P. Mechanical Behavior of Marine Risers Mode of Influence of Principal Parameters. *J. Energy Resour. Technol.* **102**, 214–222 (1980).

140. Sparks, C. P. The influence of tension, pressure and weight on pipe and riser deformations and stresses. *J. Energy Resour. Technol.* **106**, 46–54 (1984).

141. Sparks, C. P. *Fundamentals of Marine Riser Mechanics: Basic Principles and Simplified Analyses*. *Fundamentals of Marine Riser Mechanics* (PennWell, 2018).

142. Patel, M. H. & Seyed, F. B. Internal flow-induced behaviour of flexible risers. *Eng. Struct.* **11**, 266–280 (1989).

143. Seyed, F. B. & Patel, M. H. Mathematics of flexible risers including pressure and internal flow effects. *Marine Structures* **5**, 121–150 (1992).

144. Guesnon, J., Gaillard, C. & Richard, F. Ultra Deep Water Drilling Riser Design and Relative Technology. *Oil & Gas Science and Technology - Revue d'IFP Energies nouvelles* **57**, 39–57 (2002).

145. Lu, H., Vaz, M. A., Caire, M. & Hernández, I. D. Full-scale experimental and numerical analyses of a flexible riser under combined tension-bending loading. *Marine Structures* **86**, 103275 (2022).

146. Liu, Q., Xue, H., Tang, W. & Yuan, Y. Theoretical and numerical methods to predict the behaviour of unbonded flexible riser with composite armour layers subjected to axial tension. *Ocean Engineering* **199**, 107038 (2020).

147. Song, J., Chen, W., Guo, S. & Yan, D. Distortion model design of flexible marine riser. *J. Mar. Sci. Technol.* **27**, 92–103 (2022).

148. Palmer, A. C. & Baldry, J. A. S. Lateral Buckling of Axially Constrained Pipelines. *Journal of Petroleum Technology* **26**, 1283–1284 (1974).

149. SINTEF. *FPS 2000 Flexible Pipes and Risers: Handbook on Design and Operation of Flexible Pipes*. (Sintef Report STF70 A92006, 1992).

150. Larsen, T. J. & Hansen, A. M. *How 2 HAWC2, the User's Manual*. (Risø National Laboratory. Denmark. Forskningscenter Risoe. Risoe-R No. 1597(ver. 3-1)(EN), 2007).

151. Jepma, C., Kok, G., Renz, M., Van Schot, M. & Wouters, K. *North Sea Energy D3.6 Towards Sustainable Energy Production on the North Sea-Green Hydrogen Production and CO2 Storage: Onshore or Offshore, As Part of Topsector Energy TKI Wind & TKI New Gas*. https://north-sea-energy.eu/static/fc2fba594593abe1330f8b80eeaad756/NSE1_D3.6-Towards-sustainable-energy-production-on-the-North-Sea_final-public.pdf (2018).

152. Witkowski, A., Rusin, A., Majkut, M. & Stolecka, K. Comprehensive analysis of hydrogen compression and pipeline transportation from thermodynamics and safety aspects. *Energy* **141**, 2508–2518 (2017).

153. Ma, K.-T., Luo, Y., Kwan, T. & Wu, Y. Mooring design. in *Mooring System Engineering for Offshore Structures* 63–83 (Elsevier, 2019). doi:10.1016/b978-0-12-818551-3.00004-1.

154. Feely, R. A. *et al.* Impact of Anthropogenic CO2 on the CaCO3 System in the Oceans. *Science (1979).* **305**, 362–366 (2004).

155. Zeebe, R. E. History of seawater carbonate chemistry, atmospheric CO2, and ocean acidification. *Annual Review of Earth and Planetary Sciences* vol. 40 141–165 Preprint at https://doi.org/10.1146/annurev-earth-042711-105521 (2012).

156. Doney, S. C., Busch, D. S., Cooley, S. R. & Kroeker, K. J. The Impacts of Ocean Acidification on Marine Ecosystems and Reliant Human Communities. *Annu. Rev. Environ. Resour.* **45**, 83–112 (2020).

157. Devries, T. The Ocean Carbon Cycle. *Annual Review of Environment and Resources Downloaded from www.annualreviews.org. Guest (guest* **21**, 49 (2024).

158. Hardy, D. R., Zagrobelny, M., Willauer, H. D. & Williams, F. W. *Extraction of Carbon Dioxide from Seawater by Ion Exchange Resin Part I: Using a Strong Acid Cation Exchange Resin*. (2007).

159. Willauer, H. D., Ejiogu, C. & Lewis, K. *Extraction of Carbon Dioxide From Seawater by Ion Exchange Resin. Part II. Using Strong Base Anion Exchange Resin*. https://www.researchgate.net/publication/235094624 (2009).

160. Nalco, F. D., Company, E., Willauer, H. D. & Lewis, K. *Extraction of Carbon Dioxide from Seawater by an Electrochemical Acidification Cell. Part 1-Initial Feasibility Studies*. https://www.researchgate.net/publication/235185675 (2010).

161. Willauer, H. D., DiMascio, F., Hardy, D. R., Lewis, M. K. & Williams, F. W. Development of an Electrochemical Acidification Cell for the Recovery of CO2 and H2 from Seawater. *Ind. Eng. Chem. Res.* **50**, 9876–9882 (2011).

162. Eisaman, M. D. *et al.* CO2 extraction from seawater using bipolar membrane electrodialysis. *Energy Environ. Sci.* **5**, 7346–7352 (2012).

163. Willauer, H. D., Dimascio, F., Hardy, D. R. & Williams, F. W. Feasibility of CO2 extraction from seawater and simultaneous hydrogen gas generation using a novel and robust electrolytic cation exchange module based on continuous electrodeionization technology. *Ind. Eng. Chem. Res.* **53**, 12192–12200 (2014).

164. de Lannoy, C. F. *et al.* Indirect ocean capture of atmospheric CO2: Part I. Prototype of a negative emissions technology. *International Journal of Greenhouse Gas Control* **70**, 243–253 (2018).

165. Yan, L., Bao, J., Shao, Y. & Wang, W. An Electrochemical Hydrogen-Looping System for Low-Cost CO2 Capture from Seawater. *ACS Energy Lett.* **7**, 1947–1952 (2022).

166. Kim, S. *et al.* Asymmetric chloride-mediated electrochemical process for CO2 removal from oceanwater. *Energy Environ. Sci.* https://doi.org/10.1039/d2ee03804h (2023) doi:10.1039/d2ee03804h.

167. La Plante, E. C. *et al.* Saline Water-Based Mineralization Pathway for Gigatonne-Scale CO $_2$ Management. *ACS Sustain. Chem. Eng.* **9**, 1073–1089 (2021).

168. Sharifian, R., Boer, L., Wagterveld, R. M. & Vermaas, D. A. Oceanic carbon capture through electrochemically induced in situ carbonate mineralization using bipolar membrane. *Chemical Engineering Journal* **438**, 135326 (2022).

169. Willauer, H. D., Hardy, D. R., Ndubizu, E. C., Williams, F. W. & Lewis, M. K. *Recovery of [CO2]T from Aqueous Bicarbonate Using a Gas Permeable Membrane*. (2008).

170. Yan, L., Bao, J., Shao, Y. & Wang, W. An Electrochemical Hydrogen-Looping System for Low-Cost CO2Capture from Seawater. *ACS Energy Lett.* **7**, 1947–1952 (2022).

171. Patterson, B. D. *et al.* Renewable CO2 recycling and synthetic fuel production in a marine environment. *Proc. Natl. Acad. Sci. U. S. A.* **116**, 12212–12219 (2019).

172. Yoshida, H. *et al.* Conceptual Design of an Underwater Direct Seawater Capturing for Enhanced Ocean Carbon Storage. in *OCEANS 2023 - MTS/IEEE U.S. Gulf Coast* 1–6 (IEEE, 2023). doi:10.23919/OCEANS52994.2023.10337220.

173. Feely, R., Sabine, C., Takahashi, T. & Wanninkhof, R. Uptake and Storage of Carbon Dioxide in the Ocean: The Global CO2 Survey. *Oceanography* **14**, 18–32 (2001).

174. Kleypas, J., Langdon, C. & Chris, S. *Impacts of Ocean Acidification on Coral Reefs and Other Marine Calcifiers: A Guide for Future Research, Report of a Workshop 18–20 April 2005, St. Petersburg, FL, Sponsored by NSF, NOAA, and the U.S. Geological Survey*. https://www.researchgate.net/publication/248700866 (2006).

175. Jones, D. C., Ito, T., Takano, Y. & Hsu, W. Spatial and seasonal variability of the air-sea equilibration timescale of carbon dioxide. *Global Biogeochem. Cycles* **28**, 1163–1178 (2014).

176. Monterey, G. I. & Levitus, S. Seasonal Variability of Mixed Layer Depth for the World Ocean. Preprint at https://repository.library.noaa.gov/view/noaa/49153 (1997).

177. Franco, A. C. *et al.* Anthropogenic and Climatic Contributions to Observed Carbon System Trends in the Northeast Pacific. *Global Biogeochem. Cycles* **35**, (2021).

178. Arroyo, M. C. *et al.* Dissimilar Sensitivities of Ocean Acidification Metrics to Anthropogenic Carbon Accumulation in the Central North Pacific Ocean and California Current Large Marine Ecosystem. *Geophys. Res. Lett.* **49**, (2022).

179. Matsumiya, N., Teramoto, M., Kitada, S. & Matsuyama, H. Evaluation of energy consumption for separation of CO2 in flue gas by hollow fiber facilitated transport membrane module with permeation of amine solution. *Sep. Purif. Technol.* **46**, 26–32 (2005).

180. Lotovskyi, E., Teixeira, A. P. & Guedes Soares, C. Availability Analysis of an Offshore Wind Turbine Subjected to Age-Based Preventive Maintenance by Petri Nets. *J. Mar. Sci. Eng.* **10**, 1000 (2022).

181. Lauvset, S. K. *et al.* GLODAPv2.2022: the latest version of the global interior ocean biogeochemical data product. *Earth Syst. Sci. Data* **14**, 5543–5572 (2022).

182. McDougall, T. J. & Barker, P. M. Getting started with TEOS-10 and the Gibbs Seawater (GSW). *Scor/Iapso Wg127* 28 (2011).

183. Sykes, V., Collu, M. & Coraddu, A. A Review and Analysis of the Uncertainty Within Cost Models for Floating Offshore Wind Farms. *Renewable and Sustainable Energy Reviews* **186**, 113634 (2023).

184. Edwards, E. C. *et al.* Trends in floating offshore wind platforms: A review of early-stage devices. *Renewable and Sustainable Energy Reviews* vol. 193 Preprint at https://doi.org/10.1016/j.rser.2023.114271 (2024).

185. Adam, F., Myland, T., Dahlhaus, F. & Großmann, J. Scale Tests of the GICON®-TLP for Wind Turbines. in *Volume 9A: Ocean Renewable Energy* (American Society of Mechanical Engineers, 2014). doi:10.1115/OMAE2014-23216.

186. Melis, C., Caille, F., Perdrizet, T., Poirette, Y. & Bozonnet, P. A Novel Tension-Leg Application for Floating Offshore Wind: Targeting Lower Nacelle Motions. in *Volume 6: Ocean Space Utilization; Ocean Renewable Energy* (American Society of Mechanical Engineers, 2016). doi:10.1115/OMAE2016-54961.

187. Vita, L. *et al.* Comparison of Numerical Models and Verification Against Experimental Data, Using Pelastar TLP Concept. in *Volume 9: Ocean Renewable Energy* (American Society of Mechanical Engineers, 2015). doi:10.1115/OMAE2015-41874.

188. Urbán, A. M., Voltà, L., Lio, W. H. & Torres, R. Preliminary assessment of yaw alignment on a single point moored downwind floating platform. *J. Phys. Conf. Ser.* **2018**, 012043 (2021).

189. Oguz, E. *et al.* Experimental and numerical analysis of a TLP floating offshore wind turbine. *Ocean Engineering* **147**, 591–605 (2018).

190. Pierella, F. *et al.* Numerical simulations of a 15MW wind turbine on a concrete TLP with rigid pipe tendons. *J. Phys. Conf. Ser.* **2362**, 012030 (2022).

191. DNV. *Comparative Study of Concrete and Steel Substructures for FOWT*. https://windworks-jelsa.no/app/uploads/2022/01/Comparative-study-of-concrete-and-steel-substructure-for-FOWT_final-for-distribusjon.pdf (2022).

192. CarbonCure Technologies Inc. CarbonCure. https://www.carboncure.com/ (2025).

193. Davidson, I. *et al.* A Review of Biofouling of Ships' Internal Seawater Systems. *Frontiers in Marine Science* vol. 8 Preprint at https://doi.org/10.3389/fmars.2021.761531 (2021).

194. Growcott, A., Kluza, D. & Georgiades, E. *Review: In-Water Systems to Reactively Manage Biofouling in Sea Chests and Internal Pipework*. (2017).

195. International Maritime Organization. *2023 Guidelines for the Control and Management of Ships' Biofouling to Minimize the Transfer of Invasive Aquatic Species*. (2024).

196. Chakkarapani, V. & Chaudhury, G. Concept to design: a novel seawater intake riser. in *Proceedings of the ASME 2014 33rd International Conference on Ocean, Offshore and Arctic Engineering OMAE2014* (San Francisco, California, USA, 2014).

197. Chabaud, V. *Power Fluctuations Caused by Wind Turbulence on a 15MW Floating Offshore Wind Turbine*. https://www.sintef.no/en/publications/publication/2329880/ (2024).

198. Sungrow. ST5015kWh-2500kW-2h-US. https://en.sungrowpower.com/productDetail/4448/energy-storage-system-st5015kwh-2500kw-2h-us (2023).

199. Stehly, T., Duffy, P. & Mulas Hernando, D. *Cost of Wind Energy Review: 2024 Edition*. https://www.energy.gov/eere/wind/wind-market-reports-2024-edition (2024).

200. Sykes, V., Collu, M. & Coraddu, A. A Review and Analysis of the Uncertainty Within Cost Models for Floating Offshore Wind Farms. *Renewable and Sustainable Energy Reviews* **186**, 113634 (2023).

201. Federal Reserve Bank of St. Louis. Producer Price Indexes. https://fred.stlouisfed.org/categories/31 (2025).

202. Compass International Inc. *2023 Pipelines, Mining, and Offshore Cost Data Yearbook*. https://compassinternational.net/wp-content/uploads/2024/01/Compass_2024PipelinesMiningOffshoreCostDatabase_Watermark_01-24.pdf (2023).

203. Craig, I. Seawater intake risers for floating liquified natural gas (FLNG) vessels. (University of Sunderland, 2018).

204. Keprate, A. & Ratnayake, R. M. C. Riser Concept Selection for FPSO in Deepwater Norwegian Sea: A Case Study. in *Volume 5: Pipelines, Risers, and Subsea Systems* (American Society of Mechanical Engineers, 2018). doi:10.1115/OMAE2018-78344.

205. Seider, W. D. *et al. Product and Process Design Principles: Synthesis, Analysis and Evaluation, 4th Edition*. (Wiley, 2016).

206. Tanaka, R. L. & de Arruda Martins, C. A Genetic Algorithm Approach to Steel Riser Optimization. in *Volume 1: Offshore Technology; Offshore Wind Energy; Ocean Research Technology; LNG Specialty Symposium* 271–277 (ASMEDC, 2006). doi:10.1115/OMAE2006-92257.

207. Exchange-rates.org. World currency exchange rates and currency exchange rate history. https://www.exchange-rates.org/ (2025).

208. Malleret, S., Jansen, M., Laido, A. S. & Kitzing, L. Profitability dynamics of offshore wind from auction to investment decision. *Renewable and Sustainable Energy Reviews* **199**, 114450 (2024).

209. Mauler, L., Duffner, F., Zeier, W. G. & Leker, J. Battery cost forecasting: a review of methods and results with an outlook to 2050. *Energy Environ. Sci.* **14**, 4712–4739 (2021).

210. Shahabi, M. P., McHugh, A. & Ho, G. Environmental and economic assessment of beach well intake versus open intake for seawater reverse osmosis desalination. *Desalination* **357**, 259–266 (2015).

211. Maienza, C., Avossa, A. M., Picozzi, V. & Ricciardelli, F. Feasibility analysis for floating offshore wind energy. *Int. J. Life Cycle Assess.* **27**, 796–812 (2022).

212. Shields, M., Beiter, P. & Nunemaker, J. *A Systematic Framework for Projecting the Future Cost of Offshore Wind Energy*. https://www.osti.gov/biblio/1902302 (2022) doi:10.2172/1902302.

213. Holm, S. E., Winther, M. S., Straus, J. & Roussanaly, S. How to best transport CO2 to offshore storages? *Carbon Capture Science & Technology* **15**, 100416 (2025).

214. Ricke, K., Drouet, L., Caldeira, K. & Tavoni, M. Country-level social cost of carbon. *Nat. Clim. Chang.* **8**, 895–900 (2018).

215. Chauvy, R. & Dubois, L. Life cycle and techno-economic assessments of direct air capture processes: An integrated review. *Int. J. Energy Res.* **46**, 10320–10344 (2022).

216. US Department of Energy. Secretary Granholm Launches Carbon Negative Earthshots to Remove Gigatons of Carbon Pollution from the Air by 2050. Preprint at https://www.energy.gov/articles/secretary-granholm-launches-carbon-negative-earthshots-remove-gigatons-carbon-pollution (2021).

217. Keith, D. W., Ha-Duong, M. & Stolaroff, J. K. Climate strategy with CO2 capture from the air. *Clim. Change* **74**, 17–45 (2006).

218. NOAA. Global Monitoring Laboratory. Carbon Cycle Greenhouse Gases. Trends in CO2. https://gml.noaa.gov/ccgg/trends/mlo.html (2025).

219. Ozkan, M., Akhavi, A.-A., Coley, W. C., Shang, R. & Ma, Y. Progress in carbon dioxide capture materials for deep decarbonization. *Chem* **8**, 141–173 (2022).

220. Li, G. & Yao, J. Direct Air Capture (DAC) for Achieving Net-Zero CO2 Emissions: Advances, Applications, and Challenges. *Eng* **5**, 1298–1336 (2024).

221. Voskian, S. & Hatton, T. A. Faradaic electro-swing reactive adsorption for CO2 capture. *Energy Environ. Sci.* **12**, 3530–3547 (2019).

222. Fujikawa, S., Selyanchyn, R. & Kunitake, T. A new strategy for membrane-based direct air capture. *Polym. J.* **53**, 111–119 (2021).

223. Mi, J. *et al.* Experimental investigation of a reverse osmosis desalination system directly powered by wave energy. *Appl. Energy* **343**, 121194 (2023).

224. IPCC. Summary for Policymakers. in (ed. H.-O. Pörtner, D. C. R. E. S. P. K. M. M. T. A. A. M. C. S. L. S. L. V. M. A. O.) 3–33 (Cambridge University Press, Cambridge, UK and New York, 2022). doi:10.1017/9781009325844.001.

225. Key, R. M. *et al.* A global ocean carbon climatology: Results from Global Data Analysis Project (GLODAP). *Global Biogeochem. Cycles* **18**, (2004).

226. IRENA. *Future of Wind: Deployment, Investment, Technology, Grid Integration and Socio-Economic Aspects (A Global Energy Transformation Paper)*. www.irena.org/publications. (2019).

227. Weiss, R. F. Carbon dioxide in water and seawater: the solubility of a non-ideal gas. *Mar. Chem.* **2**, 203–215 (1974).

228. Byrne, R. H., Mecking, S., Feely, R. A. & Liu, X. Direct observations of basin-wide acidification of the North Pacific Ocean. *Geophys. Res. Lett.* **37**, (2010).

229. IOC, SCOR & IAPSO. *The International Thermodynamic Equation of Seawater – 2010: Calculation and Use of Thermodynamic Properties*. (2010).

230. Oschlies, A., Bach, L. T., Fennel, K., Gattuso, J.-P. & Mengis, N. Perspectives and challenges of marine carbon dioxide removal. *Frontiers in Climate* **6**, (2025).

231. Schlitzer, R. Electronic atlas of WOCE hydrographic and tracer data now available. *Eos, Transactions American Geophysical Union* **81**, 45–45 (2000).

232. INTEGRATED TELESCOPIC TOWER AND EVOLVED SPAR FLOATING SUBSTRUCTURE FOR LOW-COST DEEP OFFSHORE WIND AND NEXT GENERATION OF 10MW+ TURBINES. Preprint at https://doi.org/10.3030/654634 (2015).

233. Rockström, J. *et al.* Exploring the Safe Operating Space for Humanity. *Ecology and Society* **14**, (2009).

234. Rockström, J. *et al.* Planetary Boundaries guide humanity's future on Earth. *Nat. Rev. Earth Environ.* **5**, 773–788 (2024).

235. Sakschewski, B. *et al. Planetary Health Check 2025: A Scientific Assessment of the State of the Planet*. https://publications.pik-potsdam.de/pubman/item/item_32589 (2025) doi:10.48485/pik.2025.017.

236. Bushman, T. & Merchant, N. *Ready for Removal: A Decisive Decade for Canadian Leadership in Carbon Dioxide Removal*. (2023).

237. Santhakumar, S., Heuberger-Austin, C., Meerman, H. & Faaij, A. Technological learning potential of offshore wind technology and underlying cost drivers. *Sustainable Energy Technologies and Assessments* **60**, 103545 (2023).

238. DNV. *Energy Transition Outlook 2024. A Global and Regional Forecast to 2050*. https://www.dnv.com/energy-transition-outlook/ (2024).

239. Lafreniere, K. & Kilpatrick, R. *IEA Wind Annual Report TCP. Canada 2023*. https://iea-wind.org/wp-content/uploads/2024/11/Canada-2023.pdf (2024).

240. Sawyer, D., Ness, R., Lee, C. & Miller, S. *Damage Control: Reducing the Costs of Climate Impacts in Canada*. https://climateinstitute.ca/reports/damage-control/ (2022).

241. World Bank. World Bank Data, Canada. https://data.worldbank.org/country/canada?most_recent_value_desc=false (2025).

242. Fasihi, M., Efimova, O. & Breyer, C. Techno-economic assessment of CO2 direct air capture plants. *J. Clean. Prod.* **224**, 957–980 (2019).

243. Chi, Y. Exploring DAC Methods for Carbon Dioxide Removal. *MATEC Web of Conferences* **410**, 02002 (2025).

244. Climeworks. Next generation tech powers Climeworks' megaton leap. https://climeworks.com/press-release/next-gen-tech-powers-climeworks-megaton-leap (2024).

245. Jelen, D. *Direct Air Capture Using Novel Structured Adsorbents (DE-FE0031959 Final Technical Report)*. https://www.osti.gov/biblio/2267573 (2023).

246. Holmes, H. E. *et al.* Tuning sorbent properties to reduce the cost of direct air capture. *Energy Environ. Sci.* **17**, 4544–4559 (2024).

247. IMO. 2023 IMO Strategy on Reduction of GHG Emissions from Ships. Resolution MEPC.377(80). Preprint at https://www.imo.org/en/ourwork/environment/pages/2023-imo-strategy-on-reduction-of-ghg-emissions-from-ships.aspx (2023).

248. Jezowska, A., Bottino, A., Capannelli, G., Fabbri, C. & Migliorini, G. Ultrafiltration as direct pre-treatment of seawater – a case study. *Desalination* **245**, 723–729 (2009).

249. Brover, S., Lester, Y., Brenner, A. & Sahar-Hadar, E. Optimization of ultrafiltration as pre-treatment for seawater RO desalination. *Desalination* **524**, 115478 (2022).

250. Bolton, G. R., Boesch, A. W. & Lazzara, M. J. The effects of flow rate on membrane capacity: Development and application of adsorptive membrane fouling models. *J. Memb. Sci.* **279**, 625–634 (2006).

251. Roussanaly, S. *et al.* Towards improved cost evaluation of Carbon Capture and Storage from industry. *International Journal of Greenhouse Gas Control* **106**, 103263 (2021).

252. Terlouw, T., Bauer, C., Rosa, L. & Mazzotti, M. Life cycle assessment of carbon dioxide removal technologies: a critical review. *Energy Environ. Sci.* **14**, 1701–1721 (2021).

253. Butnar, I. *et al.* A Review of Life Cycle Assessment Methods to Inform the Scale-Up of Carbon Dioxide Removal Interventions. *WIREs Energy and Environment* **13**, (2024).

254. Shindell, D. *et al.* The methane imperative. *Frontiers in Science* **2**, (2024).

255. Paul Rosane, Baysa Naran, Angela Ortega Pastor, Jake Connolly & Dharshan Wignarajah. *The Landscape of Methane Abatement Finance*. https://www.climatepolicyinitiative.org/publication/the-landscape-of-methane-abatement-finance/ (2022).

256. Friedlingstein, P. *et al.* Global Carbon Budget 2025. *Earth System Science Data Discussions* **2025**, 1–139 (2025).

257. Riahi, K. *et al.* The Shared Socioeconomic Pathways and their energy, land use, and greenhouse gas emissions implications: An overview. *Global Environmental Change* **42**, 153–168 (2017).

258. Hickel, J. & Kallis, G. Is Green Growth Possible? *New Political Economy* **25**, 469–486 (2020).

259. Wiedenhofer, D. *et al.* A systematic review of the evidence on decoupling of GDP, resource use and GHG emissions, part I: bibliometric and conceptual mapping. *Environmental Research Letters* **15**, 063002 (2020).

260. Haberl, H. *et al.* A systematic review of the evidence on decoupling of GDP, resource use and GHG emissions, part II: synthesizing the insights. *Environmental Research Letters* **15**, 065003 (2020).

261. Vogel, J. & Hickel, J. Is green growth happening? An empirical analysis of achieved versus Paris-compliant CO2–GDP decoupling in high-income countries. *Lancet Planet. Health* **7**, e759–e769 (2023).

262. Gilfillan, S. M. V. *et al.* Solubility trapping in formation water as dominant CO2 sink in natural gas fields. *Nature* **458**, 614–618 (2009).

263. Kelemen, P., Benson, S. M., Pilorgé, H., Psarras, P. & Wilcox, J. An Overview of the Status and Challenges of CO2 Storage in Minerals and Geological Formations. *Frontiers in Climate* **1**, (2019).

264. Alcalde, J. *et al.* Estimating geological CO2 storage security to deliver on climate mitigation. *Nat. Commun.* **9**, 2201 (2018).

265. IRENA. *Renewable Capacity Statistics 2024*. https://www.irena.org/-/media/Files/IRENA/Agency/Publication/2024/Mar/IRENA_RE_Capacity_Statistics_2024.pdf (2024).

266. IRENA. *Renewable Power Generation Costs in 2023*. https://www.irena.org/-/media/Files/IRENA/Agency/Publication/2024/Sep/IRENA_Renewable_power_generation_costs_in_2023.pdf (2024).

267. Northland Power Inc. Offshore wind. https://www.northlandpower.com/en/assets-and-infrastructure/offshore-wind.aspx (2025).

268. Government of Nova Scotia. Canada’s First Offshore Wind Energy Areas Designated. https://news.novascotia.ca/en/2025/07/29/canadas-first-offshore-wind-energy-areas-designated (2025).

269. Cambridge Econometrics. *Future UK Employment in the Offshore Wind Industry. A Report Commissioned by the University of Hull on Behalf of Aura.* https://aura-innovation.co.uk/wp-content/uploads/2020/04/Cambride-Econometrics-Future-UK-Employment-in-Offshore-Wind-June-2017.pdf (2017).

270. Meier, K. Hydrogen production with sea water electrolysis using Norwegian offshore wind energy potentials: Techno-economic assessment for an offshore-based hydrogen production approach with state-of-the-art technology. *International Journal of Energy and Environmental Engineering* **5**, 1–12 (2014).

271. Orcina. OrcaFlex documentation v11.4d. https://www.orcina.com/webhelp/OrcaFlex/ (2024).

272. Charles Lawrence Kamuyu, W., Lim, J., Won, C. & Ahn, H. Prediction Model of Photovoltaic Module Temperature for Power Performance of Floating PVs. *Energies (Basel).* **11**, 447 (2018).

273. Ali, F. *et al.* Co-located offshore wind and floating solar farms: A systematic quantitative literature review of site selection criteria. *Renewable Energy Focus* vol. 50 Preprint at https://doi.org/10.1016/j.ref.2024.100611 (2024).

274. Fan, S., Ma, Z., Liu, T., Zheng, C. & Wang, H. Innovations and development trends in offshore floating photovoltaic systems: A comprehensive review. *Energy Reports* **13**, 1950–1958 (2025).

275. Velenturf, A. P. M. A Framework and Baseline for the Integration of a Sustainable Circular Economy in Offshore Wind. *Energies (Basel).* **14**, 5540 (2021).

276. IEA. The relationship between growth in GDP and CO2 has loosened; it needs to be cut completely. Preprint at https://www.iea.org/commentaries/the-relationship-between-growth-in-gdp-and-co2-has-loosened-it-needs-to-be-cut-completely (2024).

277. Chaudary, M. S. A. Lithium dreams, local struggles: Navigating the geopolitics and socio-ecological costs of a low-carbon future. *Energy Res. Soc. Sci.* **121**, 103952 (2025).

278. Cabaña, G. & Richter, K. Green extractivism in Colombia: A scoping review on indigenous rights and livelihood impacts, and policy and social movement responses. *Extr. Ind. Soc.* **25**, 101808 (2026).